Design of Thermal Control Systems for Testing of Electronics

by

Matthew Sweetland

B.S. Mechanical Engineering,
Purdue University (1993)

and

M.S. Mechanical Engineering,
Massachusetts Institute of Technology (1998)

Submitted to the Department of Mechanical Engineering
in partial fulfillment of the requirements for the degree of

Doctor of Philosophy in Mechanical Engineering

at the

MASSACHUSETTS INSTITUTE OF TECHNOLOGY

May 2001 [June 2001]

BARKER

© Massachusetts Institute of Technology 2001. All rights reserved.

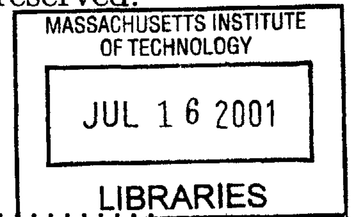

Author ....
Department of Mechanical Engineering
May 5, 2001

Certified by ....
John H. Lienhard V
Professor of Mechanical Engineering
Thesis Supervisor

Accepted by ....
Ain Sonin
Chairman of Graduate Studies
Department of Mechanical Engineering

Design of Thermal Control Systems for Testing of Electronics

by

Matthew Sweetland

Submitted to the Department of Mechanical Engineering
on May 5, 2001, in partial fulfillment of the
requirements for the degree of
Doctor of Philosophy in Mechanical Engineering

Abstract

In the electronic component manufacturing industry, most components are subjected to a full functional test before they are sold. Depending on the type of components, these functional tests may be performed at room temperature, at cold temperature, or at high temperature (−50°C to 160°C) depending on the type of component and intended market. The thermal management of these components during testing forms two basic issues that need to be addressed. The first issue is the heating or cooling of devices to the desired temperature prior to being tested, and the second issue concerns temperature control during the actual functional test.

This thesis covers the design, modeling and testing of two prototype systems. One system uses a low cost IR heating system to preheat bulk devices to a target temperature, prior to the actual functional test. Theory shows that the limits on temperature ramp rates are imposed by the device package configuration and carrier configuration. The results from the prototype system show that the IR heating chamber is an effective low cost, low volume system for uniformly heating a wide range of device and carrier types.

The second prototype system uses high performance jet impingement coupled with laser heating to actively control the temperature of a high power density device during a functional test. Experimental results from the prototype system are presented and design guidelines for future systems are developed. The theory for temperature control is developed and the effects of package design and test sequence design on the temperature control limits are studied.

Thesis Supervisor: John H. Lienhard V
Title: Professor of Mechanical Engineering

Thesis Committee:

Prof. John Lienhard V

Prof. Alex Slocum

Prof. Bora Mikic

Prof. George Barbastathis

Acknowledgements

Needless to say, there are a large number of people that I wish to thank for assistance in the completion of this thesis and my doctoral degree. This project was sponsored by Teradyne Inc., and I wish to thank Andy Pfahnl and Ray Mirkhani at Teradyne for answering too many questions and for putting up with a very grumpy contract researcher. Pooya Tadayon at Intel has been very supportive with answers to technical questions about testing requirements and Intel provided the thermal test vehicles used in the prototype system. I want to thank the gracious patience of my thesis committee (John Lienhard, Alex Slocum, Bora Mikic, George Barbastathis) for putting up with way too many committee meetings in far too short of a period. My two advisors, John Lienhard and Alex Slocum, have been very helpful whenever I needed it, but also had the forebearance to leave me alone most of the time and allowed me to pursue the research as I found fit.

I also want to thank all my friends that have provided the necessary distractions over the past two years to prevent me from going nuts in the basement of MIT. Pat and Scott for the oversize trucks and water skiing. Millie and Buster for paddling, hiking and biking. All the others that suckered me into every possible sport requiring a helmet, body armor and/or enhance health insurance. I'm glad James was around for most of my stay. Always nice to have someone to bounce ideas off over a couple of beers (OK, so more than a couple). MJ and FB who provided the motivation to get done fast. Most of all I want to thank Virginie, who made the final year so much more bearable and enjoyable.

Contents

1 Introduction **25**

2 Infrared Heating Theory **29**

2.1 Radiant Heating . . . 30

2.2 IR Heating Model . . . 34

2.2.1 Component Heating . . . 34

2.2.2 Device Modeling Results . . . 39

2.2.3 Carrier Heating . . . 43

2.2.4 Device/Component Coupling . . . 47

2.2.5 Degradation of Plastics . . . 52

3 Infrared Heating Experimental Results **53**

3.1 Prototype Description . . . 53

3.1.1 IR Source Selection . . . 54

3.1.2 Heating Chamber Design . . . 56

3.1.3 Carrier Holder and Mounting . . . 56

3.1.4 Instrumentation . . . 58

3.2 Design Example . . . 59

3.2.1 Low Conductivity Carrier Design Example . . . 59

3.2.2 High Conductivity Carrier Design Example . . . 63

3.3 Experimental Data . . . 67

3.4 Conclusion . . . 74

3.4.1 Design Guidelines . . . 74

4 Temperature Control of Active Device **77**

4.1 Description of an Electronic Device Under Test . . . 78

4.2 Device Descriptions for Prototype System . . . 79

4.3 Model of Device Under Test 83
4.4 Model Data from Experimental Results 84
4.5 System Model for Control of a Device Under Test 88

5 Laser/Convection Experimental Apparatus 93
5.1 Laser/Convection System 93
5.1.1 Nozzle Cooling System 94
5.1.2 Lasers and Optics 96
5.1.3 System Assembly 99
5.2 Data Acquisition System 99
5.3 Power Supply and Control System 101
5.4 Calibration and Test Procedures 102
5.4.1 TTV Calibration 102
5.4.2 Test Procedures 108

6 Convective Cooling 109
6.1 Convective Cooling Theory 109
6.2 Convective Cooling Experimental Prototype 111
6.3 Experimental Data 115
6.3.1 Impingement Surface Convection 115
6.3.2 Side Edge Convection 116
6.3.3 Effect of Device Holder 120
6.3.4 System Noise 123
6.4 Error Propagation and Analysis 125
6.5 Conclusions 127

7 Laser/Convection System Experimental Results 129
7.1 Baseline Data 129
7.1.1 Pinetop TTV 131
7.1.2 P858ACY TTV 132
7.2 Temperature Control Data 137
7.2.1 Pinetop TTV 137
7.2.2 P858ACY TTV 140
7.3 Control Limits 144
7.3.1 Five Second Average Power Sequence. 144
7.3.2 One Second Average Power Sequence 152

7.3.3 Remainder Power Sequence 156
7.4 Control Sequence Generation 157
7.5 Conclusions 163

8 Thermal Model 165
8.1 Isothermal Die Temperature 165
8.2 Surface Absorption of Incident Radiation 167
8.3 Control Limits 170
8.3.1 Die Cut Off Frequency 170
8.3.2 Die Power to Control Power Estimation 173
8.4 Transient Control Limits 177
8.4.1 Temperature Response to Die and Control Inputs 177
8.4.2 Model Confirmation 191
8.5 Control of Non-Sinusoidal Die Power Profile 194
8.6 Limits to Control with known Die Power Profile 198
8.7 Feedback Control Limits 200
8.8 Transient Lateral Conduction 205
8.9 Steady State Temperature Profile 213
8.9.1 Control Input Steady State Response 213
8.9.2 Die Input Steady State Response 215
8.9.3 Combined Steady State Solution 218
8.10 Solution Approach 218
8.11 Conclusions 221

9 Theoretical versus Experimental Results 223
9.1 Control Plots for Intel Thermal Test Vehicles 223
9.2 Experimental Data Correlation to Control Limit Model 225
9.2.1 1 Second and 5 Second Decomposed Power Profile 225
9.2.2 Remnant Power Profile 231
9.3 Conclusions 233

10 Conclusions and Future Work 235
10.1 IR Heating of Bulk Devices 235
10.1.1 Conclusions 235
10.1.2 Future Work 236
10.2 Laser/Convection Thermal Control of an Active Device 236

10.2.1 Conclusions 236
10.2.2 Future Work 237

A Derivation of Temperature Solution **243**
A.1 Temperature response to control input 243
A.2 Temperature response to die input 245
A.3 Combined temperature response 247

List of Figures

2-1 Cross section view of proposed IR chamber. 33
2-2 Isometric view of IR chamber. 35
2-3 Areas for view factor calculations. 36
2-4 Average device temperature for a 10 mm QFP package with high reflectivity chamber walls. 38
2-5 Average device temperature for a 10 mm QFP package with low reflectivity chamber walls. 39
2-6 Average device temperature for a 10 mm QFP package with a 5 mm side wall height and low wall reflectivity. 40
2-7 Average device temperature for a 10 mm QFP package with a large diffuse to collimated radiation intensity ratio. 41
2-8 Average device temperature for a 10 mm QFP package with a small diffuse to collimated radiation intensity ratio. 42
2-9 Temperature response inside a 10 mm QFP package for specified surface flux. 44
2-10 Temperature profile for low conductivity carrier. 46
2-11 Temperature profile for high conductivity carrier. 46

3-1 Section of an industry standard carrier tray for 10 mm QFP devices. 54
3-2 Section of strip carrier. Carrier on right is original metal lead frame, carrier on left has been overmolded. Width of frame is 5.84 cm. . . . 55
3-3 IR heating chamber assembly. 57
3-4 Photograph of assembled IR heating system. 58
3-5 Temperature profile in 10 mm QFP device at exit of heating chamber. 61
3-6 Temperature profile through a plastic carrier after exiting heater section. 62
3-7 Temperature profile along strip carrier metal frame for $I_0 = 65.7$ kW/m^2 and $V = 0.8$ cm/sec. 64

3-8 Resistance model for encapsulated strip device. The hatched area represents the region where conductivity is assume to be infinite. 66
3-9 Experimental data for testing lateral heating uniformity with high reflectivity chamber walls. Data is for 10 mm QFP device mounted on leading row of plastic carrier. Temperature measured on integral heat spreader. 68
3-10 Experimental data for testing lateral heating uniformity with low reflectivity chamber walls. Data is for 10 mm QFP device mounted on leading row of plastic carrier. Temperature measure on integral heat spreader. 69
3-11 Experimental and simulation data for 10 mm QFP on carrier centerline. 70
3-12 Temperature profile for high conductivity carrier. 71
3-13 Temperature profile for heating of strip carrier. 72
3-14 Settling time for device in center of carrier compared to surrounding metal frame. 72
3-15 Heating of strip carrier at two different carrier velocities. 73
3-16 Temperature profile for heating of 10 mm QFP devices. 75

4-1 Cross-section of typical high power density device. Some components may not be present in some devices. 78
4-2 Intel P858ACY TTV 80
4-3 Intel Pinetop TTV 81
4-4 Baseline Intel power profile 82
4-5 Baseline transient model of a typical device under test. 83
4-6 Experimental and simulation data for a P858ACY TTV subject to a 93.2 W Intel power profile. 86
4-7 Experimental and simulation data for a P858ACY TTV subject to a 70 W step power profile. 87
4-8 Experimental and simulation data for a Pinetop TTV subject to a 23.3 W Intel power profile. 89
4-9 Physical model of system updated to include lateral conduction in the integrated heat spreader. 90
4-10 Diagram for calculation of conduction resistance between ring segments on the IHS. 91

4-11 Experimental and simulation data for a Pinetop TTV device subject to the Intel test sequence. 92
4-12 Expanded view of the data in Fig. 4-11. 92

5-1 Single and stacked nozzle modules. 95
5-2 Side view and cross sectional view of assembled laser/convection system. Manifold system and base support structure not shown. 100
5-3 Schematic diagram of control and data acquisition system for laser/convection prototype system. 102

6-1 Test apparatus for measuring convective transfer coefficients on a simulated electronic device. 112
6-2 Schematic drawing of nozzle test system. 112
6-3 Detailed view of the heater section of the nozzle test assembly. Views are shown with and without a device holder. 114
6-4 Correlation and experimental data for Reynolds number versus the convection coefficient $\overline{h}_c$ for the nozzle test rig. Error bars show the experimental measurement errors in $\mathrm{Re_d}$ and $\overline{h}_c$. Data is for a flat face conduction plate configuration (no side edges exposed) with no device holder present. 116
6-5 Measured values of h for increasing power dissipation levels at $\mathrm{Re_d} =$ 14500. Correlation value is $\overline{h}_c = 1400$ W/m^{2}K. Flat face configuration with no device holder present. 117
6-6 Correlation and experimental $\overline{h}_c$ values for multiple H/D ratios. Experimental data is for no exposed side edges and no holder present. . 118
6-7 Average side edge convective heat transfer coefficients for various exposed side face heights. 119
6-8 Detailed view of simulated die holder for convection experiments. The recessed grooves mount on the four corners of the copper block. . . . 121
6-9 Effective heat transfer coefficient for various side edge exposure heights with no device holder and with PEEK device holder present. 122
6-10 Percent decrease in $\overline{h}_e$ when a PEEK device holder is added for a specified exposed edge height. 123
6-11 Measured $\overline{h}_e$ for various holder materials and flat plate configuration with no holder. 124
6-12 Noise level at a position 1 cm from the nozzle assembly. 124

7-1 Manifold pressure versus $\overline{h}_c$ for the prototype system. 130

7-2 Volumetric flow rate under standard conditions versus manifold pressure. 130

7-3 Die temperature for Pinetop TTV subject to a 23.3 W Intel test sequence. 131

7-4 Single channel data for Pinetop TTV subject to 23.3 W Intel test sequence. 132

7-5 Temperature response of Pinetop TTV subject to a 14 W Intel power sequence with no forced convection. 133

7-6 Temperature response of Pinetop TTV to scaled Intel test sequences with constant manifold pressure. 134

7-7 Temperature response of Pinetop TTV for a 23 W Intel test sequence at multiple manifold pressures. 135

7-8 Die temperature for a P858ACY TTV subject to a 46.7 W Intel test sequence. 136

7-9 Uncontrolled and controlled temperature response of a Pinetop TTV to a 46.7 W Intel test sequence. 137

7-10 Controlled temperature response of a Pinetop TTV to a 23.3 W Intel test sequence. 138

7-11 Control power sequence for Pinetop die temperature response shown in Fig. 7-10. 139

7-12 Controlled die temperature response to 23.3 W Intel test sequence at multiple manifold pressures. 140

7-13 Uncontrolled and controlled temperature response of a Pinetop TTV to a 46.7 W Intel test sequence. 141

7-14 Controlled temperature response of a P858ACY TTV to a 46.7 W Intel test sequence. 142

7-15 Control power sequence for P858ACY TTV die temperature response shown in Fig. 7-14. 143

7-16 Decomposition of Intel test sequence. 145

7-17 Uncontrolled and controlled temperature profile of a Pinetop TTV to the 5 second average power profile with a peak power at 50.2 W. . . . 146

7-18 Experimental limits of temperature control for 5 second power average with Pinetop TTV. 146

7-19 Peak control power versus peak die power for 5 second average power sequence on a Pinetop TTV. 147

7-20 Temperature variation across the die for controlled and uncontrolled 5 second average test sequences. 147
7-21 Die power and laser power as a function of time for temperature control of a Pinetop TTV with a 5 second average power sequence. 148
7-22 Uncontrolled and controlled temperature profile of a P858ACY TTV to the 5 second average power profile with a peak power at 53.2 W. . 149
7-23 Experimental limits of temperature control for 5 second power average with P858ACY TTV. 150
7-24 Peak control power versus peak die power for 5 second average power sequence on a P858ACY TTV. 150
7-25 P858ACY TTV temperature variation across the die for controlled and uncontrolled 5 second average test sequences. 151
7-26 Die power and laser power as a function of time for temperature control of a P858ACY TTV with a 5 second average power sequence. 151
7-27 Uncontrolled and controlled temperature profile of a Pinetop TTV to the 1 second average power profile with a peak power at 36.0 W. . . . 152
7-28 Experimental limits of temperature control for the 1 second power average with Pinetop TTV. 153
7-29 Peak control power versus peak die power for the 1 second average power sequence on a Pinetop TTV. 153
7-30 Die power and laser power as a function of time for temperature control of a Pinetop TTV with a 1 second average power sequence. 154
7-31 Uncontrolled and controlled temperature profile of a P858ACY TTV to the 1 second average power profile with a peak power at 48.0 W. . 155
7-32 Experimental limits of temperature control for the 1 second power average with a P858ACY TTV. 156
7-33 Peak control power versus peak die power for the 1 second average power sequence on a P858ACY TTV. 157
7-34 Die power and laser power as a function of time for temperature control of a P858ACY TTV with a 1 second average power sequence. 158
7-35 Detailed view of remainder power sequence. 159
7-36 Controlled and uncontrolled temperature response of Pinetop TTV die to the remainder power sequence. 160
7-37 Controlled and uncontrolled temperature response of P858ACY TTV die to the remainder power sequence. 161

8-1 Comparison models for proof of isothermal die assumption. 166
8-2 Magnitude of temperature fluctuation for distributed generation and surface flux on adiabatic die structure. 168
8-3 Phase shift of IHS side temperature for surface flux case. 169
8-4 Die cut off frequency for the Intel P858ACY TTV at various temperature tolerance levels and power levels. 171
8-5 Die cut off frequency for the Intel Pine-Top TTV at various temperature tolerance levels and power levels. 172
8-6 Physical model for die power to control power ratio calculation. . . . 173
8-7 Control power to die power ratio versus exponential settling times of the die power for the Intel Pinetop TTV. 175
8-8 Die power and control power for dual mass model based on $\tau = 0.025$ sec. 176
8-9 Schematic diagram of simplified device for transient analysis. Q_c is the magnitude of the control input and a is the phase shift of the control input. Q_d is the magnitude of the die power profile. 179
8-10 Schematic drawing of decomposition for solution to transient temperature profile in integrated heat spreader. 180
8-11 Graphical solution for phase shift and magnitude of control power profile. 183
8-12 Temperature response of IHS to a 10 Hz die power profile with $Q_d =$ 10 W/cm^2. For this system, $h_c = 1200$ W/cm^2 and the IHS is 1.8 mm thick. 184
8-13 Temperature response of IHS to a 10 Hz die power profile with $Q_d =$ 10 W/cm^2 and a control power profile imposed on the front face. . . . 185
8-14 Solution for phase shift and control magnitude for ideal temperature control of die. 187
8-15 IHS temperature profile for ideal control of die temperatures. 188
8-16 Magnitude and phase shift of control profile to maintain die temperature within 4 K for a 10 Hz die power profile with $Q_d = 10$ W/cm^2. . 191
8-17 Temperature profile in die and IHS for 10 Hz die power profile with magnitude of 10 W/cm^2 with $\Delta T = 4$ K. 192
8-18 Incremental segment break-down for finite difference confirmation model. 193
8-19 Calculated die temperature using finite difference model to confirm analytic solution for control input. 195
8-20 Control input and die temperature for square wave die power profile. 196

8-21 Control input and die temperature for triangular wave die power profile. 197
8-22 Control limits for specified die power profile. 198
8-23 Control limits for specified die power profile. 199
8-24 Limits of control for multiple values of the convective heat transfer coefficient h_c. 200
8-25 Effect of die to IHS thermal resistance on control limits. 201
8-26 Effect of IHS thickness on control limits. 201
8-27 Effect of die thickness on control limits. 202
8-28 Solution for temperature profile propagation time for integrated heat spreader. 203
8-29 Minimum changed in die temperature for under ideal feedback control conditions. 204
8-30 Device to device variation in temperature response for common power sequence. 206
8-31 Segmentation of IHS for lateral conduction calculations. 208
8-32 Transient fin temperature profile for Pinetop TTV 209
8-33 Lateral conduction into Pinetop TTV IHS for multiple frequencies with $h_c = 1200$ W/m^{2}K. Q represents the total energy loss due to transient conduction into the edges of the IHS. ΔT_b represents the magnitude of the fluctuation of the temperature of the IHS directly over the die structure. 210
8-34 Lateral conduction (Q) into Pinetop TTV IHS for a range of h_c values for a 10 Hz base temperature fluctuation of ΔT_b. 211
8-35 Transient fin temperature profile for Pinetop TTV with $\Delta T_b = 4$ K at 40 Hz. Top plot represents temperature profile at base, middle, and tip of fin. Bottom plot represents maximum temperature defect along the length of the fin. 212
8-36 Steady state temperature profile for Pinetop TTV. 214
8-37 IHS temperature as a function of h_c for 20 W control power input. . . 214
8-38 Steady state temperature profile for P858ACY TTV. 215
8-39 IHS temperature distribution for small illumination spot size on the Pinetop TTV. 216
8-40 IHS temperature profile for Pinetop TTV with 20 W die input. 217
8-41 IHS temperature profile for P858ACY TTV with 20 W die input. . . 217

8-42 IHS temperature profile for Pinetop TTV with 20 W die and 20 W control input. 219
8-43 IHS temperature profile for P858ACY TTV with 20 W die and 20 W control input. 220

9-1 Control limit plot for Intel Pinetop TTV and P858ACY TTV for 46.7 W peak power and $\Delta T = 2°C$. 224
9-2 Comparison of temperature control limits of Pinetop TTV and P858ACY TTV for a 46.7 W Intel test sequence. 226
9-3 Results of a discrete Fourier transform on each of the decomposed power profiles. 228
9-4 Experimental data for P858ACY TTV and Pinetop TTV for comparison with control limit theory. 229
9-5 Experimental data versus control limit theory for 1 second and 5 second power profile sequences. 230
9-6 P858ACY TTV uncontrolled temperature response to scaled remnant power profiles. 231
9-7 Uncontrolled temperature limits for P858ACY to scaled remnant power profile. 232

Nomenclature

Symbol	Description
$a,\ b,\ c$	geometric factors in conduction resistance calculation [m]
a_t	thermal diffusivity $[\frac{m^2}{s}]$
$A,\ A_1,\ A_2$	integration constant
A_{CU}	cross sectional area of heated copper block $[m^2]$
A_{device}	total device surface area exposed to radiation $[m^2]$
A_{face}	top surface area exposed to convection $[m^2]$
A_p	apparent contact area between device and carrier $[m^2]$
A_{ped}	pedestal cross sectional area $[m^2]$
A_{side}	side surface area exposed to convection $[m^2]$
b	integrated heat spreader thickness [m]
b	RTD calibration intercept
$B,\ B_1,\ B_2$	integration constant
Bi	Biot number - Eqn. 8.2
Bi_R	modified Biot number - Eqn. 8.3
c_p	specific heat $[\frac{J}{kgK}]$
C	integration constant
$C_1,\ C_2$	Planck's constants
C_n	constant in infinite sum
D	internal nozzle diameter [m]
$D,\ D_1$	integration constants
$E,\ E_1$	integration constants

$E_{b\lambda}$	black body spectral distribution $[\frac{\mathrm{W}}{\mathrm{m}^2\mu\mathrm{m}}]$
f	nozzle geometry factor - Eqn. 6.2
F_1	integration constant
F_{dA-1}	view factor from small area dA to area 1
Fo	Fourier number
$\overline{h}_c$	average convective transfer coefficient $[\frac{\mathrm{W}}{\mathrm{m}^2\mathrm{K}}]$
$\overline{h}_{face}$	convective transfer coefficient on top surface of target $[\frac{\mathrm{W}}{\mathrm{m}^2\mathrm{K}}]$
$\overline{h}_{side}$	convective transfer coefficient on side surface of target $[\frac{\mathrm{W}}{\mathrm{m}^2\mathrm{K}}]$
H	nozzle to target plate spacing [m]
i	imaginary number - $\sqrt{-1}$
I_0	incident surface radiation intensity $[\frac{\mathrm{W}}{\mathrm{m}^2}]$
I_a	absorbed radiation intensity $[\frac{\mathrm{W}}{\mathrm{m}^2}]$
I_c	collimated radiation intensity $[\frac{\mathrm{W}}{\mathrm{m}^2}]$
I_d	diffuse radiation intensity $[\frac{\mathrm{W}}{\mathrm{m}^2}]$
k	thermal conductivity $[\frac{\mathrm{W}}{\mathrm{mK}}]$
k_{air}	thermal conductivity of air $[\frac{\mathrm{W}}{\mathrm{mK}}]$
k_{PEEK}	thermal conductivity of PEEK pedestal $[\frac{\mathrm{W}}{\mathrm{mK}}]$
K	thermal mass of die $[\frac{\mathrm{J}}{\mathrm{K}}]$
L	interstitial gap length [m]
L	frequency coefficient - Eqn. 8.25
L_t	orthogonal nozzle spacing [m]
L_{TC}	thermocouple spacing in PEEK pedestal [m]
m	mass [kg]

m	RTD calibration slope
M	energy transfer correction factor - Eqn. 8.51
M_1	integration constant
M_c	thermal mass of carrier $[\frac{\mathrm{J}}{\mathrm{K}}]$
M_d	thermal mass of device $[\frac{\mathrm{J}}{\mathrm{K}}]$
n	index of refraction
N_1	integration constant
Nu	Nusselt number - Eqn. 6.1
P	fin perimeter [m]
P_1	integration constant
P_{TTV}	power applied to thermal test vehicle [W]
Pr	Prandtl number
$P.P.$	pumping power - Eqn. 6.13
PS_1, PS_2	integration constants
Q_{CU}	power conducted through copper block [W]
$Q_{pedestal}$	power conducted through PEEK pedestal [W]
Q_{sq}	square wave die power [W]
Q_{tr}	triangular wave die power [W]
Q_d	die power density $[\frac{\mathrm{W}}{\mathrm{m}^2}]$
Q_c	control power density $[\frac{\mathrm{W}}{\mathrm{m}^2}]$
r_1	control power illumination radius [m]
r_2	outer IHS radius [m]
r_3	die radius [m]

R_0	TTV die resistance at 0°C [Ω]
R_1	integration constant
R_f	calibrated TTV die resistance [Ω]
R_m	measured TTV die resistance [Ω]
R_t	thermal contact resistance [$\frac{\mathrm{Km}^2}{\mathrm{W}}$]
Re_D	Reynold's Number
s	Laplace operator
s	material depth [m]
t	time [sec]
t_c	carrier thickness [m]
t_{ss}	steady state settling time [sec]
T_0	initial temperature [K]
T_{air}	air temperature [K]
T_{BF}	IHS die side temperature [K]
T_{CU}	copper surface temperature [K]
T_{LC}	pedestal lower thermocouple temperature [K]
T_{UT}	pedestal upper thermocouple temperature [K]
U_1	integration constant
V_1	integration constant

Greek Symbols

α	phase shift [radians]
α	shaped fin geometry factor
α	surface absorptivity

α_n	infinite series constant
β	phase shift [radians]
δ	error term
ϵ	emissivity
κ	absorption coefficient [cm^{-1}]
λ	integration constant
λ	wavelength [μm]
λ_n	infinite series constant
Θ	temperature defect [K]
ρ	surface reflectivity
σ	rms surface roughness [m]
ω	sinusoidal frequency [$\frac{rad}{s}$]

Chapter 1

Introduction

In the electronic component manufacturing industry, most components are subjected to a full functional test before they are sold. Depending on the type of components, these functional tests may be performed at room temperature, at cold temperature, or at high temperature (−50°C to 160°C) depending on the type of component and intended market[1] [1, 2]. The thermal management of these components during testing forms two basic issues that need to be addressed. The first issue is the heating or cooling of devices to the desired temperature prior to being tested, and the second issue concerns temperature control during the actual functional test.

Thermal conditioning of devices prior to testing is becoming more important as test equipment technology enables increased parallel testing and reduces required test times. The actual time required for electrical test of some components can be less than 1 second, while traditional air convection soak chambers may take 20 to 60 minutes [2] to bring devices up to the test temperature. The time required for testing is only a very small fraction of the total test cycle time. This is especially true in the case of parallel testing where up to 64 components can be tested at a time. In order to reduce the total test cycle time and make the testing process more efficient, a new method is required to rapidly bring multiple components to test temperature. This thesis will describe a new method that utilizes infrared radiation to heat components. Target ramp rates of ±6°C/sec to ±60°C/sec have been set, but as will be shown, the main limitation in device heating is due to the physical design of the package. The problem then becomes a case of calculating the maximum heating rate based on

[1]Under the hood automotive components and military components tend to be tested at the temperature extremes.

component packaging and then designing the system around the upper limit.

Temperature control of devices during the functional test is primarily an issue for high power microprocessor devices. With increasing levels of integration, reduced component size, and increasing clock speeds, the total thermal power dissipated and power density of microprocessors is rapidly increasing. During the testing process, device manufacturers specify a minimum device temperature. The higher the temperature deviation over this temperature, the higher the risk of classifying a device in the wrong category[2]. With increasing power dissipation levels, it is becoming more difficult to keep the temperature of the device under test (DUT) constant using only passive methods. Some form of active temperature control is required for managing the thermal drift during testing. Typical functional tests on a microprocessor make last 1-2 minutes with the power cycling from almost zero power to full power on a very rapid basis.

There are two primary methods that have been proposed for thermal control of an active device during testing. One method described in a UNISYS patent [3] utilizes a large thermal mass with embedded heaters and cooling channels in direct contact with the device. The temperature of the thermal mass can be controlled very tightly, thereby controlling the temperature of the device under test. This method requires physical contact between the device and control mass, and the thermal contact resistance can vary significantly due to low contact pressures and variations in surface conditions. This variation in contact resistance makes reliable thermal control difficult. The contact resistance variation can be significantly reduced through use of a thermal interface material (liquid or soft solid interface), but electronic manufacturers are very resistant to this idea because it will required an additional step to clean the devices after testing[3] and will increase the cost and time of the testing process.

An alternate approach utilizes radiation and convective cooling to control the temperature of the device under test. The convection system is capable of handling the full thermal load produced at 100% device power, but due to capacitance and flow resistance, the convective cooling cannot be controlled at a sufficiently rapid rate to control the temperature of the device by itself. Instead, the convective cooling is held constant, and constant die temperature will be obtained through use of a controllable

[2]For example, classifying a 1 GHz microprocessor as a 950 MHz device. Increasing device temperatures can reduce signal propagation speed within a device.

[3]Solid thermal interfaces generally have liquid silicon or some other liquid imbedded in them and will leave a residue when removed.

radiation source. This system requires no contact between the device and control system so variable thermal contact resistance is no longer a problem. A prototype system has been developed that utilizes high performance impingement cooling and laser heating to control the temperature of a device. The system will be described in this thesis, as well as experimental test results from the prototype system.

The mathematical theory for the temperature control system will be developed. Critical parameters will be identified and theory will show the impact of the test sequence design on the fundamental limits of temperature control for a device under test conditions.

Chapter 2

Infrared Heating Theory

Three possible methods are available for rapidly heating and cooling multiple components: convection, conduction, and radiation. Convection is the most common method currently used in industry, but there are significant limits to this technology. In order to increase the heating rate of a group of devices, either the air temperature needs to be increased or the convective transfer coefficient needs to be increased. Increasing the air temperature increases the risk of overheating devices, and it can be fairly complicated to obtain small zones of high temperature convective heating due to baffling requirements. Increasing air temperatures also results in lower system efficiency as more energy is wasted in air loss and external convection/conduction losses. Increasing air velocities can cause loose mounted devices to be blown out of the carrier, which limits this approach to increasing the convective heat transfer coefficient. Also high air velocities on a large scale can cause significant noise problems that would required additional insulation on the test handler.

Conductive heating is difficult to implement for multiple devices. Manufacturers do not want to use interface materials that leave a residue or require a secondary cleaning process, so all thermal interfaces are dry contact. Without high contact pressures, which have the potential to damage devices, the thermal interface resistance between a heater and device can vary significantly. This means each device temperature must be measured and a form of feedback control must be implemented to bring components to a uniform temperature. This is possible with single device testing and can even be implemented for several devices at once, but with large parallel testing[1], this can be very difficult and expensive. Just trying to obtain an even pressure be-

[1]Up to 64 components at a time.

tween multiple devices and a heating chuck can be difficult, let alone measuring and controlling the temperature of each device. Granted, the heating chuck can be kept at the target temperature, but because the temperature difference between a component and the chuck decays exponentially, this doesn't fulfill the requirement for rapid heating.

Radiant heating provides one of the best options for rapid heating of multiple components, but a number of factors must be considered. The device packaging and material will dictate the usable wavelengths. Uniform heating of multiple components requires proper selection of the radiant source and heating chamber in order to produce a uniform radiation field. The final temperature of the device will depending on the heating of the component and the heating of the carrier, and an accurate device model is required to avoid overheating of the device surface. The proposed system for heating of multiple components is composed of an off-the-shelf IR heater with shields to block the end effect of the IR bulb and a high reflectivity heating chamber to produce a uniform radiation field. To model the heating of devices, a basic background in radiation is required.

2.1 Radiant Heating

The heating of a device using infrared radiation is a function of the radiation field and the radiation properties of the device. Assuming a uniform radiation field intensity I_o, the energy reflected from the surface is simply given by $I_r = \rho \cdot I_o$ where ρ is the surface reflectivity [4]. Unfortunately, ρ is a function of the incident wavelength λ, surface conditions, material type, material temperature and incident angle of radiation. The energy that is not reflected is either absorbed by the material or transmitted through the material. The radiation absorbed over a material thickness s is given by

$$I_a = (1 - \rho)\, I_o \left(1 - e^{-\kappa s}\right) \tag{2.1}$$

where κ is the absorption coefficient of the material and is generally specified in units of cm^{-1}. Again, κ is a function of wavelength, material and temperature.

For infrared heating of devices, it is desirable to have a low surface reflectivity to increase the effective heating rate. Also, all the energy should be absorbed in the device encapsulant with little or no radiant energy propagating through to the active die region of the device. Radiation that propagates through to the active die has the potential to interact with active components to create photocurrents that can cause

Table 2.1: Reflectivity and absorption coefficients for common device materials.

Material Type	Short Infrared 800 nm	Short Infrared 1.06 μm	Long Infrared 10.6 μm
Silicon [5]	$\rho \sim .3$ $\kappa \sim 10^4$ cm^{-1}	$\rho \sim .3$ $\kappa \sim 1.5$ cm^{-1}	$\rho \sim .2 - .7$ [a] $\kappa \sim 1.5$ cm^{-1}
Al_2O_3[b] [5]	$\rho \sim .8 - .9$ $\kappa \sim .009$ cm^{-1}	$\rho \sim .9 - 1$ $\kappa \sim .009$ cm^{-1}	$\rho \sim .1 - .15$ $\kappa \geq 100$ cm^{-1}
SiO_2[c] [5]	$\rho \sim .8 - .9$ $\kappa \sim .004$ cm^{-1}	$\rho \sim .9 - .95$ $\kappa \sim .004$ cm^{-1}	$\rho \sim .1 - .2$ $\kappa \geq 100$ cm^{-1}
Polyimide Plastics[d] [6]	$\rho \sim .2$ $\kappa \sim 10 - 20$ cm^{-1}	$\rho \sim .2$ $\kappa \sim 10 - 20$ cm^{-1}	$\rho \sim .1$ $\kappa \sim 300 - 700$ cm^{-1}
Ni coated Cu[e] [7]	$\rho \sim .6$ $\kappa \sim 10^5$ cm^{-1}	$\rho \sim .8$ $\kappa \sim 10^5$ cm^{-1}	$\rho \sim .95$ $\kappa \sim 10^5$ cm^{-1}

[a]Highly dependent on doping type and quantitiy.
[b]Crystalline.
[c]Fused.
[d]Representative values only. Actual values strong function of specific plastic composition.
[e]ρ values are a strong function of surface conditions.

erroneous results in the testing process, or if the radiation intensity is sufficiently high, the potential exists to actually damage active components on the device. The wavelengths that must be considered for IR heating extend from the near ultraviolet $\lambda \approx 300$ nm to the far infrared $\lambda \approx 15$ μm. There are four common types of packaging material that must be considered over these wavelengths: metals, plastics, ceramics and silicon. Selection of a radiation source now becomes a matter of selecting an operating wavelength region over which the device has low reflectivity with a high absorption coefficient. Both requirements cannot always be fulfilled simultaneously, so selection of a radiation source becomes a compromise between low reflectivity and high absorptivity. Table 2.1 presents representative reflectivity and absorption data for some common packaging materials at three different wavelengths. For the majority of materials, with material thicknesses of 1 mm or greater, the materials are effectively opaque at all wavelengths, or in other words, all of the radiation is effectively absorbed and very little is transmitted through the layer. For this reason, all devices will be treated as non-transparent for modeling purposes.

The characteristics of the radiation incident on the surface of a device are dependent on the operating temperature and emissive properties of the IR source. The general distribution of energy for a black body can be calculated from

$$E_{b\lambda} = \frac{C_1 \cdot n^3 \cdot T^5}{(n \cdot \lambda \cdot T)^5 \left[exp\left(\frac{C_2}{n \cdot \lambda T}\right) - 1\right]} \tag{2.2}$$

where $C_1 = 3.7914 \times 10^{-16}$ Wm^2, $C_2 = 14388$ μm K, and n is the refractive index and is taken equal to 1 for gases. The total emissive power over a wavelength region can be calulated by integrating eqn. 2.2 over the specified wavelength. This integral is tabulated in most radiation heat transfer text books [4, 8]. This can be useful for calculating how much of the incident energy is in the visible, IR, and ultraviolet regions and for calculating heat transfer rates.

The system developed for heating of multiple components consists of a single quartz-tungsten bulb mounted in a parabolic reflector assembly. Multiple devices on a carrier are passed under the output of the bulb-reflector assembly. Figure 2-1 shows a typical cross section of a proposed heating system. Two main challenges arise in heating components using this method, both of which involve heating components in different positions on the carrier to the same temperature. The first problem is to hold a uniform temperature for all devices along a line perpendicular to the direction of carrier motion. This requirement is not generally a problem if there are only 1–2 components across the carrier, but, for situations with 3 or more components, it is harder to keep the edge components at the same temperature as the central components. This problem can be addressed by suitable selection of the radiant heater, surface properties, and geometry of the thermal chamber, so that the radiation field is uniform across the device carrier.

The second challenge in producing uniform device temperatures is in heating a device on the leading edge of the carrier to the same target temperature as a device on the trailing edge of the carrier. This problem is solely a function of the carrier type. For low conductivity carriers with high thermal resistance between the device and carrier, such as plastic trays with loose mounted devices or polymer-sheet strip carriers, conduction along the carrier does not have to be considered, and leading-edge and trailing-edge devices are easily heated to the same temperature without additional thermal control. For high conductivity carriers, such as lead-frame strip carriers and metal transport trays, conduction along the carrier can cause trailing-edge devices to be heated to a higher temperature than leading-edge devices. Under

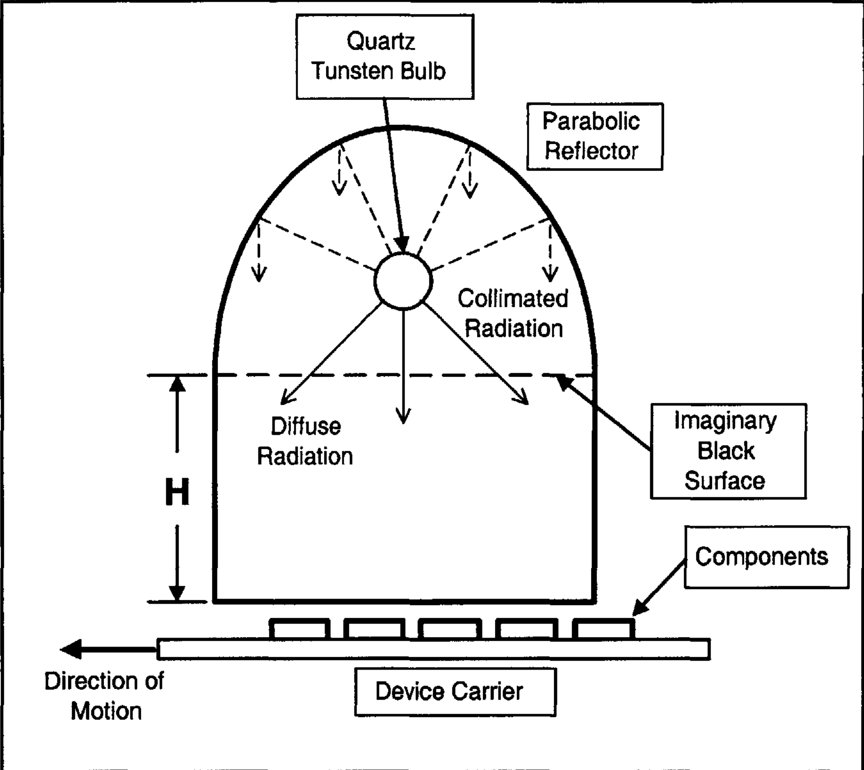

Figure 2-1: Cross section view of proposed IR chamber.

final steady state conditions, the temperatures of trailing and leading-edge devices will be the same, but the transient effect of carrier conduction must be analyzed to prevent overheating of components and to minimize the settling time after exiting the IR heating system.

2.2 IR Heating Model

Three parts are involved in modeling the heating of devices using an IR source. One part is associated with the heating of the actual devices, another with the heating of the device carrier, and the third is associated with the coupling between the carrier and the devices. The main objectives of the modeling are to determine the feasibility of obtaining uniform device temperatures and to determine the parameters that are critical to the final design.

2.2.1 Component Heating

The radiant heat transfer from the IR source to an individual device can be calculated using traditional resistance network methods, but the method must be modified in order to account for the effect of collimating reflectors on the radiation field. Figure 2-1 shows a cross-sectional view of a proposed heating chamber and Fig. 2-2 presents an isometric view of the heater and carrier. To keep the size of the heating system to a minimum, the heater is assumed to be the same width as the carrier. Rather than analyzing the IR source and parabolic reflector, the emitted radiation from the IR bulb is separated into a diffuse and collimated component. The IR bulb and reflector assembly can then be treated as an imaginary surface with two specified radiant fluxes, one collimated and the other diffuse. The ratio of collimated to diffuse radiation will depend on the design and reflectivity of the parabolic mirror and the placement of the bulb. The radiant intensity from the bulb can be assumed uniform around its circumference. Then, if a parabolic reflector with the bulb set deep inside the reflector is used, the majority of the emitted radiation will intersect with the reflector and will be reflected as collimated radiation. Conversely, for a very shallow reflector surface, most of the radiation will be diffuse with only a small fraction of the total emission intersecting the reflector surface and becoming collimated. The position of the bulb and reflector are generally fixed for a given design, and the ratio of collimated to diffuse radiation cannot easily be changed. Modeling will be used to

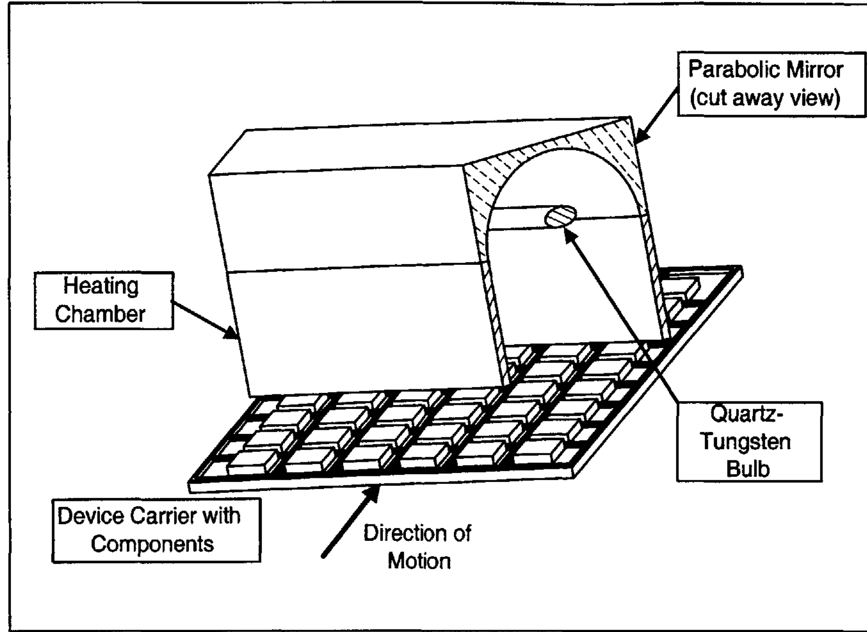

Figure 2-2: Isometric view of IR chamber.

evaluate the effect of various collimated/diffuse ratios, but a good starting baseline is to assume half is diffuse and half is collimated. The radiation emitted from the bulb is also assumed to be uniform over the entire width of the heating chamber[2].

View factors between a device and all surrounding surfaces can be easily calculated for parallel surfaces using

$$F_{dA-1} = \frac{1}{2\pi}\left[\frac{A}{\sqrt{1-A^2}}\tan^{-1}\frac{B}{\sqrt{1+A^2}} + \frac{B}{\sqrt{1+B^2}}\tan^{-1}\frac{A}{\sqrt{1+B^2}}\right] \tag{2.3}$$

where $A = a/c$, $B = b/c$, and a and b are the dimensions of the wall, and c is the distance between the small area and one corner of the wall [4]. For perpendicular surfaces, the view factor can be calculated from

$$F_{dA-1} = \frac{1}{2\pi}\left[\tan^{-1}\frac{1}{Y} - \frac{Y}{\sqrt{X^2+Y^2}}\tan^{-1}\frac{1}{\sqrt{X^2+Y^2}}\right] \tag{2.4}$$

where $X = a/b$, $Y = c/b$, a is the height of the wall, b is the width, and c is the horizontal distance between the lower corner of the wall and the center of the small area dA [4].

These view factor calculations are valid for radiation transfer between a small surface and a parallel or perpendicular surface with one corner in line with the center

[2]The end effects of the bulb are neglected.

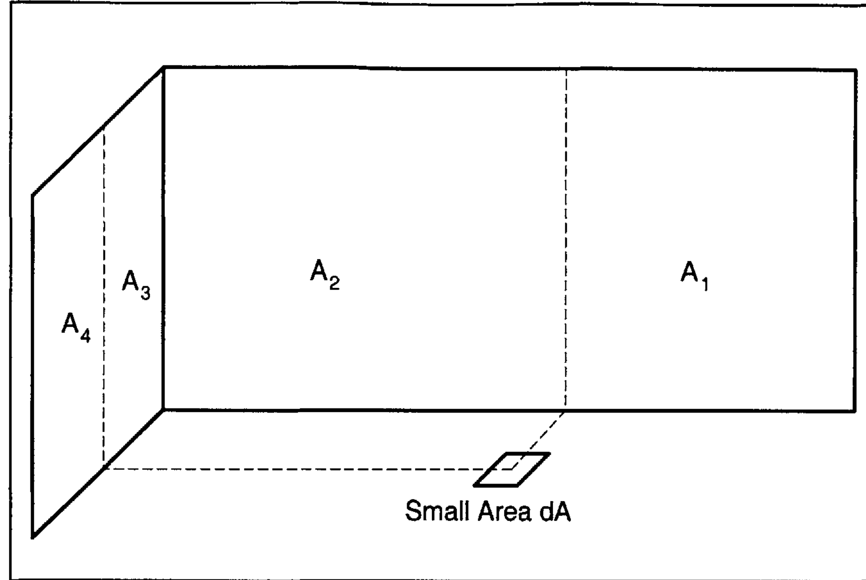

Figure 2-3: Areas for view factor calculations.

of the small area. Based on the position of the device, the surrounding surfaces were broken up into rectangular segments such that one corner of each segment was in line with the center of the small area dA as shown in Fig. 2-3 for two of the four side walls. The device was broken into a number of small sections whose area is much smaller than any single wall section and the total view factors were found by discrete integration over the entire component surface to the surrounding segmented surfaces. With all view factors known, the total energy transfer from collimated and diffuse radiation can be calculated. Heat transfer from the collimated radiation is simply given by

$$Q_c = \alpha A_{\text{device}} I_c \tag{2.5}$$

where A_{device} is the component surface area exposed to the radiation field, α is the device absorptivity, and I_c is the collimated radiation intensity. Heat transfer to the device from diffuse bulb radiation can be combined with radiant exchange between the device and the chamber walls, and the total heat flux can be found using a traditional resistance network. In the resistance model, the imaginary surface in Fig. 2-1 is treated as a black surface at the same temperature as the component, but with a specified radiant emissive power (i.e. there is no loss from the device to the imaginary surface, but the imaginary surface has a specified flux). This assumption of a black surface neglects the higher intensity directly under the bulb, but this effect

is reduced due to an imperfect parabolic reflector surface and the bulb is not a true line source at the focus of the parabola[3].

The devices are assumed to be flat with no interaction between adjacent devices and no exposed edges. For any given position within the heating chamber, all view factors can be calculated and the total heat transfer to a device can be found as the sum of the collimated heat transfer and the diffuse heat transfer. Each chamber wall is assumed to be a diffuse isothermal surface with specified emissivity and reflectivity. The temperature of each wall can be set independently. The collimated radiation is assumed to have no secondary effects on energy transfer to the devices[4]. By breaking the progress of a device through the heater as a series of small discrete steps, the heat transfer at each position in the heating chamber can be calculated, and the device temperature may be found from

$$M_D \frac{d\overline{T}}{dt} = Q_c + Q_d \tag{2.6}$$

where $M_D = m_d C_p$ is the thermal mass of a device, Q_c is the heat transfer from the collimated radiation, Q_d is the heat transfer from the diffuse radiation and interaction with chamber walls at each position, m is the component mass, c_p is the specific heat, t is the time elapsed since entering the chamber, and $\overline{T}$ is the average temperature of the component. Entrance and exit effects are treated by assuming partial shielding of each device. The diffuse radiation transfer Q_d is a function of the component temperature as this term contains radiant transfer between the device and the walls. The component temperature used in this calculation is the device temperature from the previous step.

A computer simulation was constructed using this method to analyze the effects of various heater geometries and other physical parameters on the temperatures of components across a carrier. Of main interest is a comparison of the temperature rise of a component on the edge of a carrier to that of a component in the middle of the carrier. The standard component selected for the simulation is a plastic encapsulated 10 mm QFP[5] device. This device consists of a silicon die mounted on a 0.5 mm thick integrated copper heat spreader with 1 mm of plastic encapsulant on the top surface

[3]Higher intensity directly under the bulb will affect final device temperature, but will have a limited effect on temperature uniformity across the carrier.

[4]Primary and secondary reflections of the collimated radiation are neglected. The collimated radiation is assumed to have no interaction with the chamber walls.

[5]Quad Flat Package - 10 mm by 10 mm square.

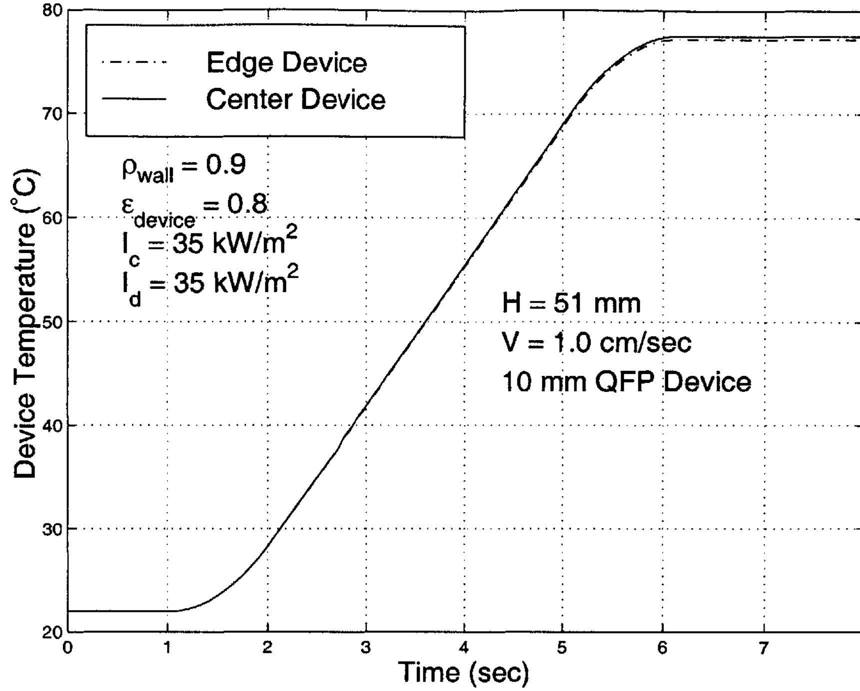

Figure 2-4: Average device temperature for a 10 mm QFP package with high reflectivity chamber walls.

of the device and 0.5 mm of plastic encapsulant on the bottom surface. The radiation intensity for the collimated radiation and diffuse radiation was set at a representative output of 70 kW/m^2 with a constant carrier velocity of 1.0 cm/sec.

While the absolute values of the radiation intensity and carrier velocity will affect the final temperature of the device, of interest is their effect on the temperature difference of devices across a carrier. This means one of the parameters of interest is the ratio of the collimated to diffuse radiation intensity. Other parameters that can affect the temperature difference between components is the height of the heating chamber[6], the wall side reflectivities and temperatures, and the collimated/diffuse intensity ratio. All devices are assumed to be at an initial uniform temperature with uniform radiation properties. Weed and Kirkpatrick [9] have estimated the emissivity of a plastic encapsulated QFP package as $\varepsilon \approx 0.9$. The QFP package is assumed to be a grey body with $\varepsilon = \alpha$.

[6]While the height of the chamber can be modified, the depth of the chamber in direction of motion and width of the heater are assumed fixed.

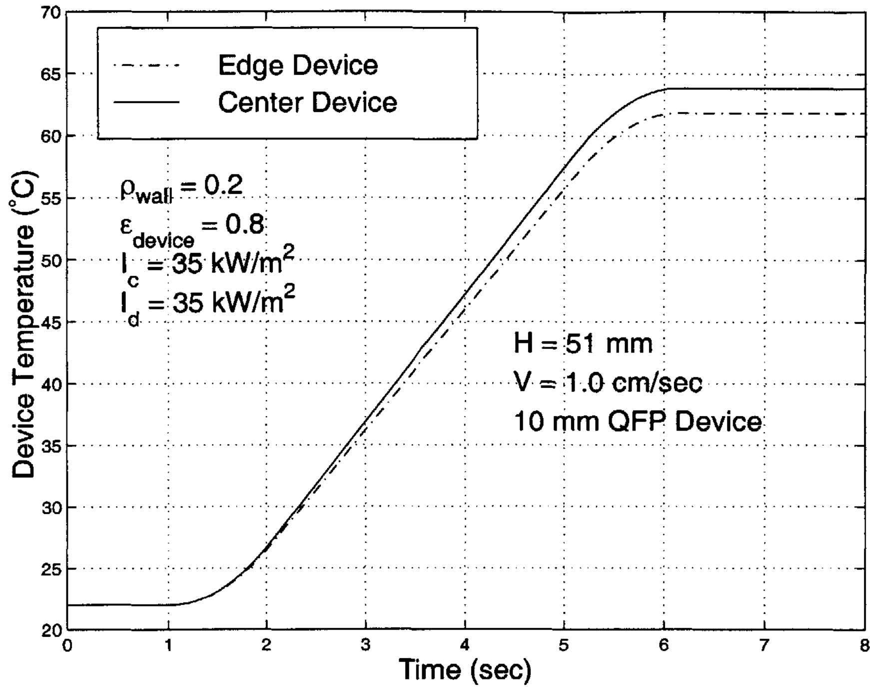

Figure 2-5: Average device temperature for a 10 mm QFP package with low reflectivity chamber walls.

2.2.2 Device Modeling Results

Figure 2-4 shows the average temperature response of two devices, one on the edge of the carrier, one at the center. This figure is for the case with wall reflectivity of 0.8, wall temperatures of 27°C on the two side walls and one end wall, and a wall temperature of 77°C on the remaining wall. The chamber dimensions are 150 mm wide by 41 mm deep by 51 mm high. As can be seen, the edge and center devices are at almost identical temperatures. Figure 2-5 presents data for the same parameter values, but with the wall reflectivity changed from 0.8 to 0.2. Two main effects can be observed from reducing the wall reflectivity while keeping all other parameters the same. The final component temperature is reduced and there is now about 3°C difference between the edge device and the center device. This shows that from a pure efficiency perspective, high reflectivity walls are preferred to increase the fraction of radiant power that is transferred to the components and to keep the chamber walls at a lower temperature.

Figure 2-6 presents the simulation results for the case where the wall height is

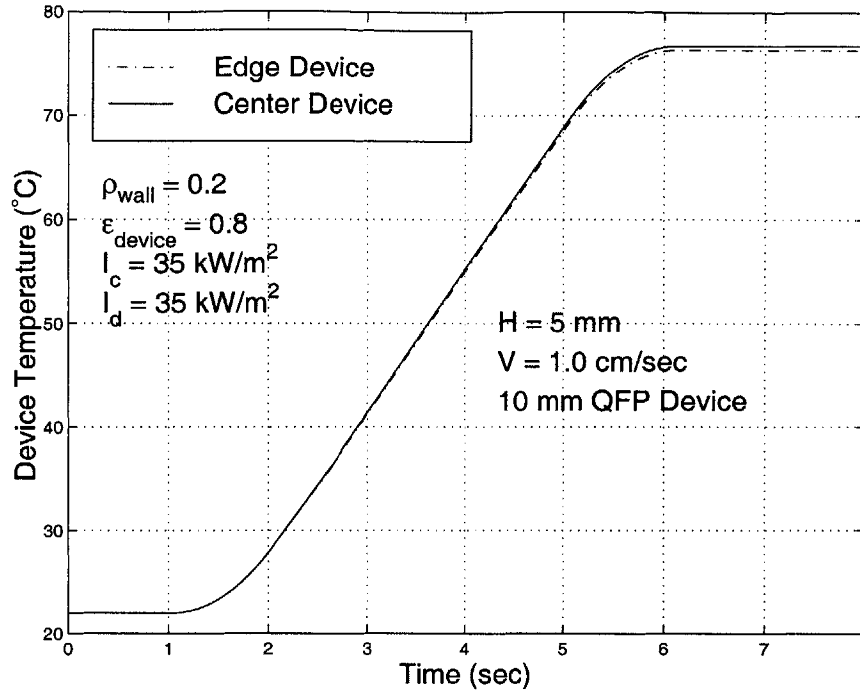

Figure 2-6: Average device temperature for a 10 mm QFP package with a 5 mm side wall height and low wall reflectivity.

reduced to 5 mm with low reflectivity. As is expected, when the side walls are almost eliminated, reflection effects no longer matter and there is very low absorption by the walls, so the device temperatures are more uniform and the final temperature is close to the case with high reflectivity walls. Figure 2-7 presents the results for a high ratio of diffuse/collimated radiation, and Fig. 2-8 presents the results for a low diffuse/collimated ratio. Both sets of results are for low reflectivity walls ($\rho = 0.2$) with a wall height of 51 mm. These results demonstrate that under the assumption that end effects of the IR bulb can be neglected and that output is uniform across the width of the chamber, rapid uniform heating of multiple component is possible with the best results obtained for high reflectivity walls with small distances between the devices heater surfaces. The physical implementation of the assumption to neglect bulb end effects will be discussed in the apparatus section.

Equation 2.6 illustrates another factor that must be considered in the analysis of component heating using IR radiation. Very high heat fluxes are possible at the surface of the device, so conduction through the device must be considered. While eqn. 2.6 will provide information about the average temperature of a component as

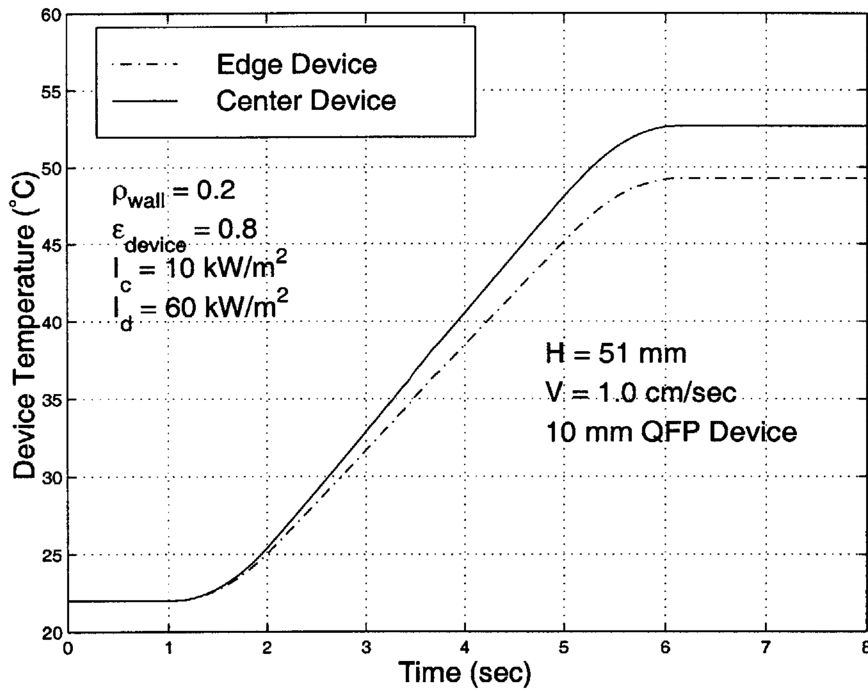

Figure 2-7: Average device temperature for a 10 mm QFP package with a large diffuse to collimated radiation intensity ratio.

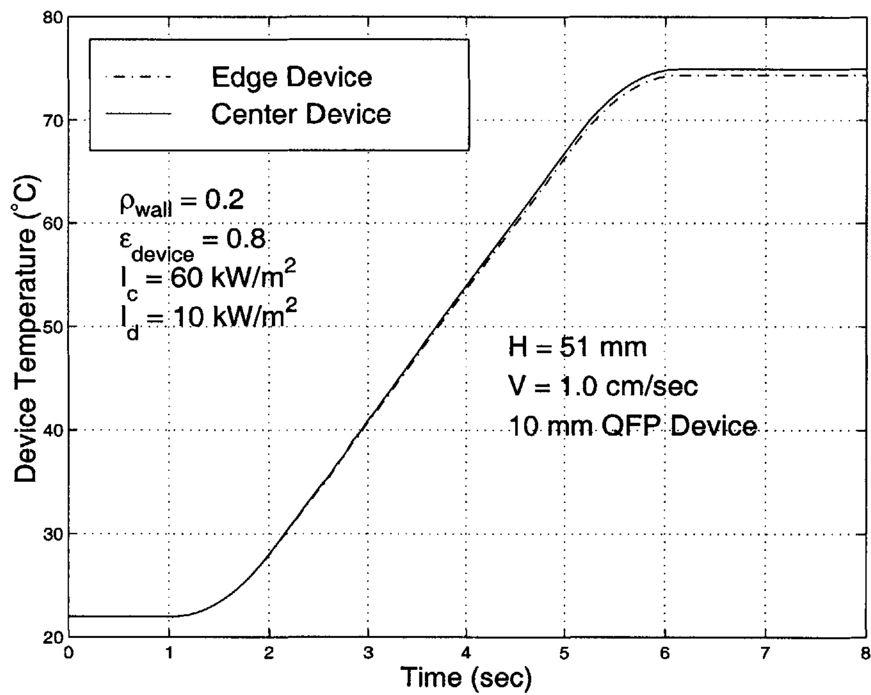

Figure 2-8: Average device temperature for a 10 mm QFP package with a small diffuse to collimated radiation intensity ratio.

a function of position in the heating chamber, it does not describe the temperature distribution within the device. This becomes especially important in plastic encapsulated devices where conduction resistances are very high. To prevent high thermal stresses or material overheating, the conduction through a device must be analyzed.

A typical component will consist of a die, substrate, an encapsulant, and sometimes an integral heat spreader. The die and substrate can be considered a single thermal mass at uniform temperature, so the problem can be effectively reduced to an analysis of multiple plane layers subject to a specified surface flux. Transient analysis can be simplified by assuming a constant surface flux and no lateral conduction and by combining the die and substrate with the integral heat spreader to form a single isotropic thermal mass[7]. Contact resistances between the layers are also neglected. The model now consists of three layers: top layer of encapsulant, integrated heat spreader, and base layer of encapsulant.

The solution to this transient problem does not have a compact closed form solution, so an implicit finite difference model was generated to calculate the temperature profile throughout a device. Each material layer was broken into multiple layers, and the temperature at each layer was calculated for a given time step, accounting for surface flux and conduction between layers. The time step in the model was progressively reduced until the quasi-steady state temperature difference between the surface temperature and center die temperature changed by less than 0.5% for a factor of two reduction in time step. An analysis of the 10 mm QFP device illustrates how large the temperature difference between the surface and die temperature can become. Figure 2-9 presents the temperature at three points within a device as it travels through a heating chamber. Under these conditions, the surface temperature of the device reaches a higher temperature than the die/substrate. These results are for the 10 mm QFP package which has 1 mm of plastic encapsulant, a 0.5 mm copper heat spreader on which the die is mounted, and a bottom layer of 0.5 mm of plastic encapsulant.

2.2.3 Carrier Heating

To determine the temperature distribution in a device carrier, an approach similar to that for component heating can be used. View factors for any given section of carrier to the surroundings can be calculated and used in a finite difference model to

[7]The die and substrate have very small mass and thickness compared to the other layers.

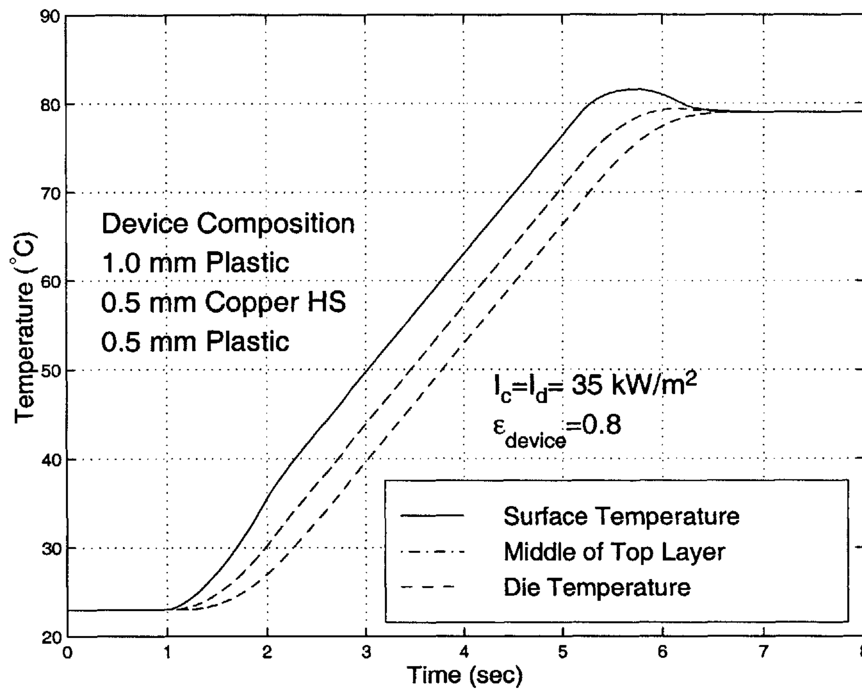

Figure 2-9: Temperature response inside a 10 mm QFP package for specified surface flux.

determine the temperature distribution in the carrier. With low conductivity carriers, the effect of conduction along the tray can be completely neglected, and the trailing edge of the carrier will be brought to the same temperature as the leading edge. For high conductivity carriers, the trailing edge of the carrier can potentially end up at a higher temperature than the leading edge owing to conduction along the carrier, potentially bringing the trailing devices above maximum temperature limits.

An implicit finite difference model was developed for calculating the temperature distribution in the carrier. This type of model allows easy definition of changing boundary conditions[8] over the entire length of the carrier. For any given incremental length of the carrier, the total radiant heat transfer can be calculated in a manner identical to the component heating method. This surface flux over an incremental length was combined with conduction effects to calculate the temperature distribution in the tray as it traveled through the heater. Convection from the carrier to the surrounding environment was neglected. Figure 2-10 demonstrates that, for a low conductivity carrier, the temperature along the carrier remains fairly uniform. Figure 2-11 shows the results for a high conductivity[9] carrier. Obviously, high conductivity carriers present the additional problem of a non-uniform temperature distribution along the carrier after exiting the heating chamber.

Like the devices themselves, low conductivity carriers will have a large temperature difference across the thickness of the carrier. Calculation of this temperature profile is easier to determine in closed form than a component profile because there is a single material layer. Assuming an adiabatic back face and no temperature gradients in the lateral directions, the temperature profile within the device can be calculated from [8]

$$T(x) = \frac{Q_T t_c}{k}\left[\frac{x^2}{2t_c^2} - \frac{1}{6} + \mathrm{Fo} + \frac{2}{\pi^2}\sum_{n=1}^{\infty}\frac{(-1)^n\cos(\lambda_n x)\exp^{-\lambda_n^2 a t}}{n^2}\right] \tag{2.7}$$

where x is measured from the back (adiabatic) surface of the carrier, t_c is the carrier thickness, k is the thermal conductivity, $\mathrm{Fo} = a_t t/t_c^2$ is the Fourier number, and $\lambda_n = n\pi/t_c$. Again, the maximum temperature will occur at the irradiated surface $(x = t_c)$. This analysis yields the worst case profile, as actual carriers are not 1-D and lateral conduction into side ribs and sections of the carrier that are shielded from the radiation by the components will lower the actual maximum carrier temperature, but this model helps to identify the maximum allowable heating rate.

[8]Conditions on given incremental length of the carrier change from no radiation to radiation exposure, and back to no radiation as a function of time and position.

[9]Cast aluminum carrier.

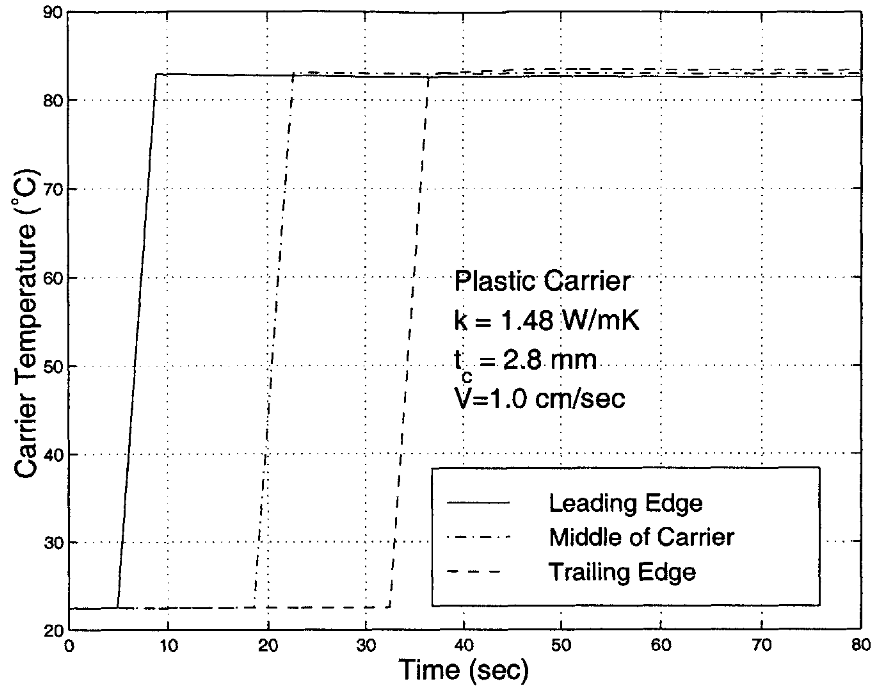

Figure 2-10: Temperature profile for low conductivity carrier.

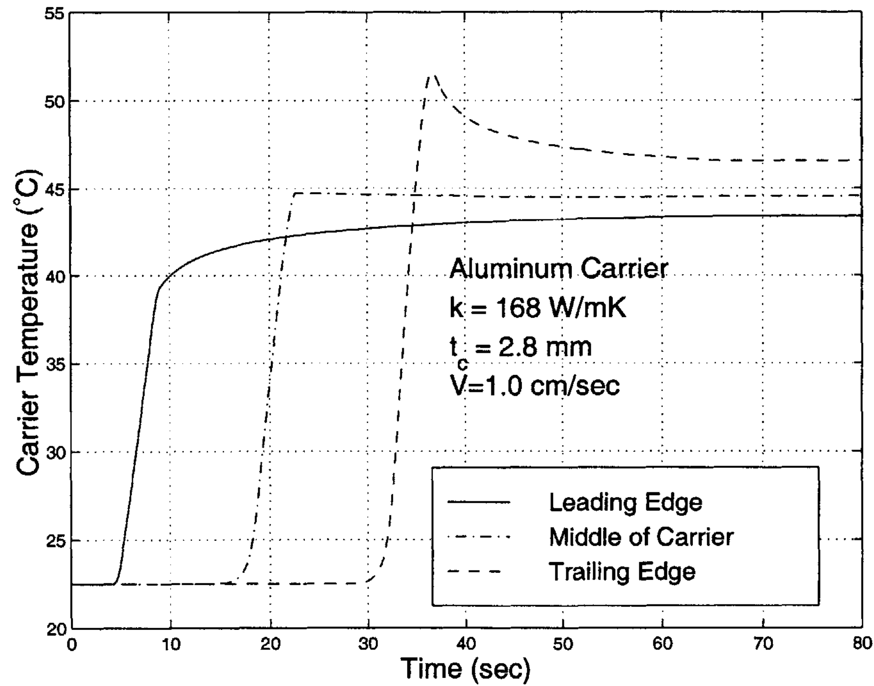

Figure 2-11: Temperature profile for high conductivity carrier.

2.2.4 Device/Component Coupling

The final temperature of the components is a function of both the heat transfer to the individual devices and the heat transfer to the carrier. In cases where the majority of the thermal mass is associated with either the components or the carrier, the final temperature will be driven by that thermal mass. In cases where the thermal masses are more evenly distributed, a full analysis of the energy transfer to all parts is required to determine the final temperature of the components. For situations where either the carrier or the components drive the final temperature, the heat transfer to the other side must be analyzed to ensure that maximum temperature limits are not exceeded. The time required to establish final steady state equilibrium between the carrier and components will vary depending on component type, type of mounting (loose mounted, hard wired, etc.), and initial temperature difference after exiting the heater. The more uniform the temperature profile when exiting the heater, the less time required to reach steady state. The final, steady state temperature can be found through a simple energy balance.

The time required to reach steady state can be estimated by combining the model results from component modeling and carrier modeling. The temperature of each component and along the carrier can be used as an input to another model that uses a resistance/capacitance network to examine the temperature settling times. This approach will provide an upper bound on the time required to reach steady state, as the components and carrier will tend towards equilibrium even while inside the heating chamber. The type of carrier and component dictates the level of complexity required in the model. For low conductivity carriers, where the exiting temperature of the carrier is uniform along its length, the model only needs to include one or two devices and a short section of a carrier. These carriers are generally implemented using loose mounted components and there is a large uncertainty in estimating the thermal contact resistance between the carrier and device. A more detailed model in this case does not make sense due to the uncertainty in the resistance values.

In the case of high conductivity carriers, these are typically strip carriers where the components are hard wired onto a metal frame. In this case, since the temperature varies so much along a carrier, the model needs to cover the entire length of the system. In both cases, low and high conductivity carriers, the model must also include convection to the surrounding environment. The value of the convective transfer coefficient will affect the time to steady state, and can be modified in the

model to represent various conditions in the hot chamber.

Low Conductivity Carrier/Device Coupling

If the thermal contact resistance between a device and the carrier is very large, then non-uniform temperature distributions in the device and the carrier can be neglected, and the system can be modeled as two isothermal masses connected through a thermal resistance. The transient solution to this system is quite easy and can be expressed as

$$T_D = \frac{M_C}{M_C + M_D}\left(T_{D_i} - T_{C_i}\right)\exp\left(\frac{-t}{\beta}\right) + T_{ss} \tag{2.8}$$

where $M_C = m_C C_{p_C}$ and $M_D = m_D C_{p_D}$ are the thermal masses of the carrier and device. The effective time constant β is given by

$$\beta = \frac{M_C \cdot M_D}{(M_C + M_D)\cdot R_C} \tag{2.9}$$

where R_C is the thermal contact resistance between the carrier and device. The final steady state temperature can be found from a simple energy balance and can be calculated from

$$T_{ss} = \frac{M_C T_{C_i} + M_D T_{D_i}}{M_C + M_D} \tag{2.10}$$

where T_{C_i} and T_{D_i} are the initial temperatures of the carrier and device upon exiting the heater.

If convection from the device and carrier to the surroundings is considered, the temperature of the device can be determined by solving the differential equation:

$$\frac{d^2T_D}{dt^2} + \left[\frac{R_C M_C + M_D}{M_C \cdot M_D} + \frac{hA_D M_C + hA_C M_D}{M_C \cdot M_D}\right]\frac{dT_D}{dt} + \frac{hR_C\left(A_C + A_D\right) + h^2 A_C A_D}{M_C \cdot M_D} T_D = \left[\frac{hR_C\left(A_D + A_C\right) + h^2 A_C A_D}{M_C \cdot M_D}\right] T_\infty \tag{2.11}$$

The convective heat transfer coefficient h is assumed to be the same for the device and carrier, and A_C and A_D are the convective surface areas of the carrier and device respectively. The solution to this second order differential equation is fairly straight forward, but the final form of the solution depends on the relative values of the coefficients. If R_C is very large, then the solution is simply that of two independent masses subject to convective conditions. If convection is very small, then the solution approaches the earlier solution of two isolated thermal masses connected through a thermal resistance (eqn. 2.9). For intermediate cases where convective heat transfer is

of the same order of magnitude as conduction between the masses, the actual values of all parameters are needed to determine final form of the the solution.

For this intermediate case, if $\Theta = T_D - T_\infty$, eqn. 2.11 can be rewritten as

$$\frac{d^2\Theta}{dt^2} + b\frac{d\Theta}{dt} + c\Theta = 0 \tag{2.12}$$

where the parameters b and c are simply the coefficients in front of the dT_D/dt and T_D terms respectively. This equation is a simply second order differential equation. The general solution for this equation is derived in Lienhard and Lienhard [10], and can be expressed as the sum of two exponentials:

$$\begin{aligned}\frac{T_D - T_\infty}{T_D\,(t=0) - T_\infty} &= \frac{b/2 + \sqrt{(b)^2 - c}}{2\sqrt{(b/2)^2 - c}} \exp\left[-\frac{b}{2} + \sqrt{\left(\frac{b}{2}\right)^2 - c}\right] t \\ &\quad + \frac{-b/2 + \sqrt{(b)^2 - c}}{2\sqrt{(b/2)^2 - c}} \exp\left[-\frac{b}{2} - \sqrt{\left(\frac{b}{2}\right)^2 - c}\right] t \end{aligned} \tag{2.13}$$

The problem now becomes a question of the magnitude of the parameters. While the values of the masses, specific heats, and even convective transfer coefficients can be determined fairly easily, the value of the thermal contact resistance is not known. Estimation of the value can be made based on some published data, but the error in this value can be expected to be quite large due to low contact force with no interfacial material (i.e. dry contact). The contact resistance between the device and carrier will depend on a number of factors including [11]: geometry of contacting surfaces (surface roughness, asperity slope and waviness), interstitial fluid (air properties), thermal conductivities of solids, and elastic properties of the materials. In order to create a usable engineering model some very simplifying assumptions will be made.

Assuming the temperature difference between the two surfaces is less than 550 K, radiation heat transfer can be neglected [12] and the thermal contact resistance can be separated into two parts. One part is associated with the thermal resistance from direct contact of the two surfaces and the other part is associated with conduction through air in the interstitial gap between the two surfaces. The actual contact area between a device and the carrier is much smaller than the apparent contact area due to surface roughness effects on both parts[13]. Because the contact force between the two surfaces in so low ($\simeq 4.5 \times 10^{-3}$ N for 10 mm QFP), there will be very little or no plastic deformation at the contacting points and actual contact area will be very

low. This factor combined with the low conductivity of the plastic encapsulant and carrier means that the flux through direct contact points will be very small and can be neglected. Now assuming all of the heat transfer takes place through conduction through the air in the interstitial gap, the problems become the case of estimating the thickness of this gap.

General surface finish data is available for die molded parts. Oberg et.al. [14] states die finishes in the range of 3.2 to 0.8 μm. Using the roughest surface finish[10] and assuming the component and die have the same surface characteristics, the effective rms surface roughness can be calculated from[12]

$$\sigma = \sqrt{\sigma_1^2 + \sigma_2^2} = \sigma_1 \cdot \sqrt{2} \tag{2.14}$$

where $\sigma_1 = 1.6$ μm. The mean gap thickness is now simply $L = \sigma/2$ and the thermal contact resistance can be calculated from

$$R_c = \frac{L}{k_{air} \cdot A_p} \tag{2.15}$$

where A_p is the apparent contact area. For the 10 mm QFP device resting on the plastic carrier, this yields a thermal contact resistance of 0.8 K/W. To put this value in perspective, assuming a convective heat transfer coefficient of 50 W/m^{2}K on the top of the QFP device yields a thermal resistance of 200 K/W, so assuming the temperature defects in the hot side chamber between the device and carrier and the device and air are of the same order of magnitude, most of the heat transfer will be between the device and carrier, not between the device and air. Therefore it is important to design the system so that the components and carrier are heated to the same temperatures.

High Conductivity Carrier/Device Coupling

In the case of a high conductivity carrier, the analysis for calculation of steady state becomes a little more complicated, as the entire carrier and all devices need to be included in the model to estimate steady state settling time. Since the main point of interest is the time required for the system to reach equilibrium and not the temperature profile of the system while reaching equilibrium, a number of modeling assumptions can be made that lead to a simplified estimate of the longest possible time to reach steady state.

[10]Use of the roughest finish will result in the largest interstitial gap thickness and largest thermal contact resistance. This results in a worst case analysis yielding the longest possible settling time.

The previous analysis developed for low conductivity carrier to device coupling can be used at two places on the high conductivity carrier to determine a pair of bounding times. The two time constants calculated should be for a leading edge device and a trailing edge device, as these represent the maximum and minimum temperature defects between the carrier and components. The leading edge carrier temperature will be the closest to the component temperature, and the trailing edge of the carrier will have the largest temperature defect with respect to an adjacent component. Along with calculating the settling time for these two extreme components, the time required for reaching steady state within the carrier can also be calculated.

Rather than trying to calculate the settling time from the actual temperature distribution in the carrier after exiting the heater, a linear temperature distribution can be assumed between the leading edge and trailing edge temperatures on the carrier. This will allow a closed form estimate of the settling time. Assuming the ends of the carrier are adiabatic and assuming no convection, the temperature profile along the carrier can be calculated from

$$T(x,t) = T_L + \frac{T_H - T_L}{2} - \frac{4\left(T_H - T_L\right)}{\pi^2} \sum_{n=0}^{\infty} \exp\left(\frac{-\left(2n+1\right)^2 \pi^2 a_t}{L^2} t\right) \cos\left(\frac{\left(2n+1\right)\pi x}{L}\right) \tag{2.16}$$

where x is the position from the leading edge of the carrier, L is the length of the carrier, a_t is the thermal diffusivity of the carrier, T_L is the leading edge temperature after exiting the heater, and T_H is the trailing edge temperature. This equation may not seem useful in providing information on the decay time due to the infinite sum, but the decay time can actually be found from the first term in the infinite expansion with $n = 0$. All remaining terms, $n = 1, 2, 3...$, will yield a more rapidly decaying time response due to the $-(2n+1)^2$ term in the exponential.

Analysis now yields three separate settling times based on two different time constants for a high conductivity carrier. One settling time is for the carrier itself, one is for the component on the leading edge of the carrier, and one is for the component on the trailing edge of the carrier[11]. These two characteristic times are given by:

[11] The characteristic time constant for the leading edge and trailing edge component is the same, but the settling time required for the temperature to reach a specified tolerance region is different since the initial temperature defects of the components are different.

Carrier Time Constant	Component Time Constant
$t_c = \frac{L^2}{\pi^2 a_t^2}$	$t_c = \frac{M_C \cdot M_D}{R_c \cdot (M_C + M_D)}$

The worst of the settling times for each condition can be calculated based on a final temperature tolerance.

2.2.5 Degradation of Plastics

A brief discussion of the effect of radiation on the mechanical properties of the plastic encapsulant and plastics carriers needs to be covered. In general, the degradation of properties (electrical insulation, mechanical strength, color) of plastics is due to interaction with ultraviolet radiation[12] [15]. For the IR source used, the peak wavelength at maximum power is $\lambda = 1.15$ μm from an operating temperature of 2227°C. By integrating eqn. 2.2 over the UV bandwidth, the proportion of energy present in the UV range can be calculated. Using the tabulated data in Modest [4], all energy below 0.4 μm represents only .032% of the total incident energy. This means that for a radiation intensity of 100 kW/m^2 on the surface of a device, only 3.2 W/m^2 of the energy is contained within the UV bandwidth. This illustrates another reason for utilizing an IR source versus a higher output radiation source, such as a QTH[13] bulb, which operates at a higher filament temperature and emits more radiation in the UV band. Very little of the energy from an IR source is contained in the UV band, and degradation of the plastics in not important. Some plastics are degraded by light in the visible and near IR region, but these are not generally utilized for electronics packaging. Many sources, such as the paper by Chanda and Roy [16], specify the durability of plastics to sunlight, and these can be used as a good indication of degradation due to IR and visible radiation.

[12] 100 $\text{Å} \leq \lambda \leq 4000$ Å

[13] Quartz tungest halogn bulb. These are the primary sources in RTP chambers and operate with filament temperatures on the order of 3000-3200 K.

Chapter 3

Infrared Heating Experimental Results

A prototype system was built to test the theoretical model of Chapter 2 and to obtain heating data for various types of devices and carriers.

3.1 Prototype Description

The main goal in the design of a component heating system is to raise all devices to a uniform temperature. Modeling has demonstrated that uniform heating across the width of the heater can be obtained under the assumption that bulb end effects can be eliminated. One method of meeting this condition is to use a bulb that is much longer than the width of the carrier; however, IR bulb sizes and shapes are limited, and using a radiation source that is much larger than the tray is inefficient in terms of energy and space utilization. Another possible solution is to use multiple bulbs arranged so as to provide a uniform radiation field, but this can be very difficult in practice, requiring ray tracing over multiple reflections for the full emission from each bulb. The problem cannot be solved in reverse, starting from a uniform flux and working backwards to a bulb arrangement, so the problem becomes one of repeated experimental analysis.

A third option exists in the selection of an IR source. By choosing a bulb that is slightly longer than the width of the carrier, the heating chamber and mounting system can be designed so that output from the ends is shielded from the components and carrier. This can be done fairly easily with edge reflectors that extend up to the

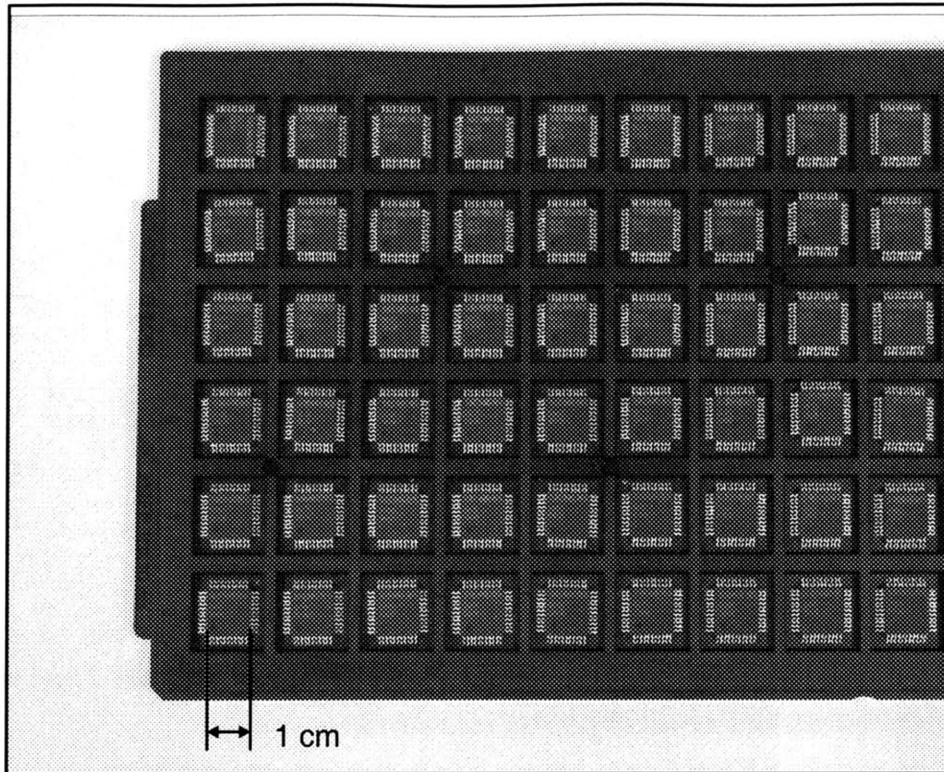

Figure 3-1: Section of an industry standard carrier tray for 10 mm QFP devices.

bulb surface and by putting radiation absorbing surfaces beneath the ends of the bulb assembly. This method was chosen for construction of a prototype system.

The system was designed around industry standard plastic carrier trays. A picture of a typical tray is shown in Fig. 3-1. The system was also designed to be adaptable to running strip carriers. Only a very limited number of strip devices were available for testing purposes, so tests were also run on flat aluminum trays to help evaluate the effect of conduction along the carrier. Figure 3-2 shows an image of a strip carrier including the metal lead frame assembly before the die is installed and molding is added. The lead frame assembly is stamped from 0.24 mm thick copper and the final device is 2.3 mm thick including the lead frame, die and overmolded plastic encapsulant.

3.1.1 IR Source Selection

The characteristics of the radiation are dependent on the generating materials (i.e. filament type), the designed operating temperature, and any filtering elements such

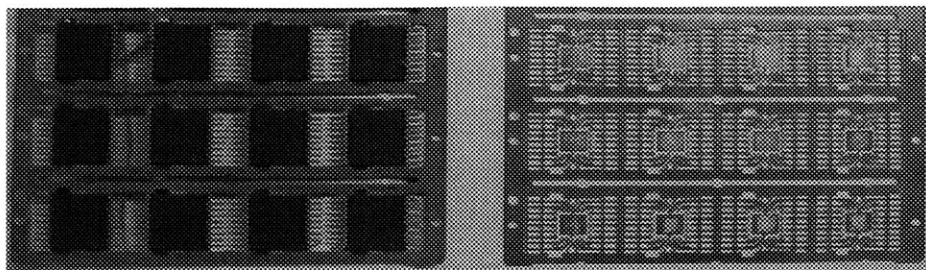

Figure 3-2: Section of strip carrier. Carrier on right is original metal lead frame, carrier on left has been overmolded. Width of frame is 5.84 cm.

as gases and bulb materials. The bulb chosen is a quartz-tungsten bulb, 9.5 mm in diameter and 254 mm in total length[1] with a maximum filament temperature of 2227°C and a peak wavelength of 1.15 μm. Bulb life is estimate at 3000 hrs with a response time of 3 seconds for 90% of full operating temperature from a cold start. The chosen assembly is a model 5305-10 strip heater from Research Inc. The system includes a parabolic mirror assembly with integral water cooling channels. A short wavelength IR source was chosen because the response time is much faster than traditional long wavelength systems.

The system output is adjustable from zero power to full power using an adjustable voltage supply. Actual radiant power of the system is not precisely known, nor is it of critical importance. Final temperatures are selected by making several runs at multiple power levels and then using this to develop a correlation to find the set point for the desired temperature. There is sufficient uncertainty in the radiant properties (emissivities, radiant intensities, etc.) that absolute determination of final temperature just from modeling and design calculations is not practical without some form of calibration procedure.

[1]Includes electrical connections.

3.1.2 Heating Chamber Design

The IR chamber must be designed around the bulb type and carrier component configuration. The main goal in design of the chamber is to obtain high reflectivities and prevent bulb end effects from affecting the radiation field. End reflectors were custom fit to extend up into the parabolic reflector section with a very small gap left between the reflector and surface of the bulb. The heating chamber was constructed with a 0.2 mm layer of aluminum foil over an 8 mm thick high temperature calcium silicate millboard insulating layer to reduce external losses. The height of the heating chamber was kept to a minimum, but physical mounting requirements forced a minimum height of 51 mm. The analytical model shows this is not a problem as long as the wall reflectivity is kept high. At the peak wavelength of the IR bulb, the aluminum has a reflectivity on the order of 0.90–0.95 [17]. The entire reflector/insulator assembly was supported by an aluminum box frame. Copper shields with low reflectivity surfaces were installed below the bulb sections outside of the heating chamber. The absorbed radiant energy from the end sections of the bulb was conducted through the copper shields to be dissipated to the environment through external heat sinks with integral fan units. Figure 3-3 shows a view of the assembled IR system without the motor drive and without a carrier installed. Also not shown are the base reflector unit and the integral fan heat sinks mounted on the end of the copper shields.

3.1.3 Carrier Holder and Mounting

The carrier was mounted on thin black-anodized aluminum cross bars supported on linear bearings. The bearings were mounted on a pair of linear rails and the whole system was moved using a lead screw and variable speed motor assembly. Only a very thin section of the supporting aluminum structure is exposed to the radiant energy, with all bearings, mounts and drive components operating outside the radiation field. The base of the heating chamber was lowered to within 1 mm of the component/carrier surface to reduce external losses, and an aluminum reflector was mounted below the heating chamber with just enough separation to allow the carrier to pass. The carrier travels from open air, through the heater, and into a low volume insulated delivery chamber. The inside of the delivery chamber was lined with polished aluminum to reduce radiant losses between the components and the chamber. The assembled system is shown in Fig. 3-4. The velocity of the tray was measured with a contacting digital tachometer accurate to ± 0.1 rpm. The output of the drive motor was measured

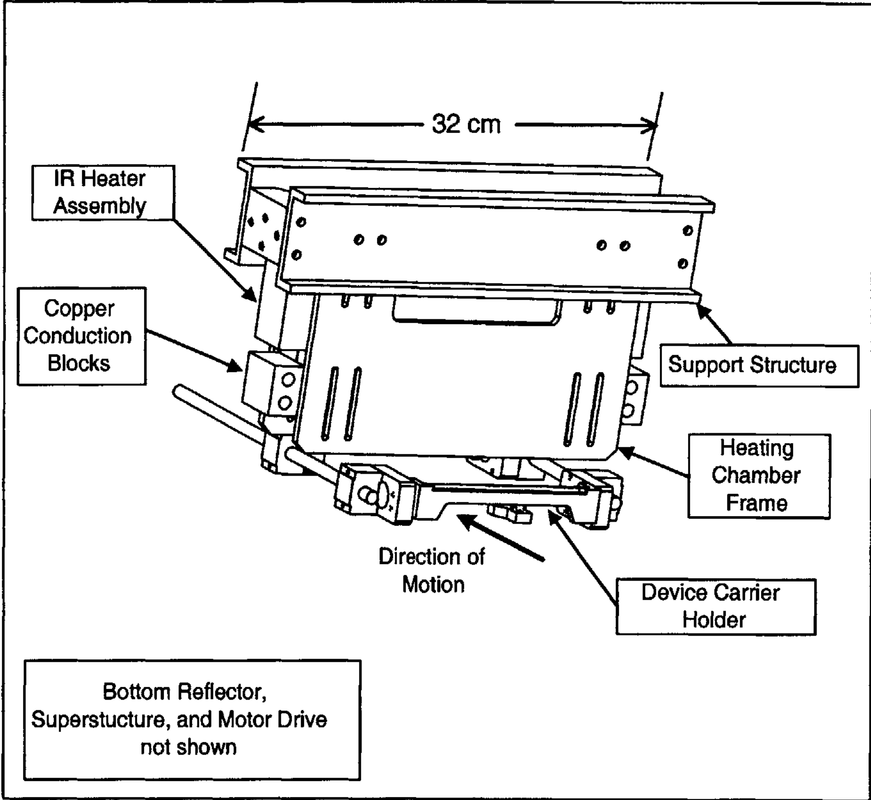

Figure 3-3: IR heating chamber assembly.

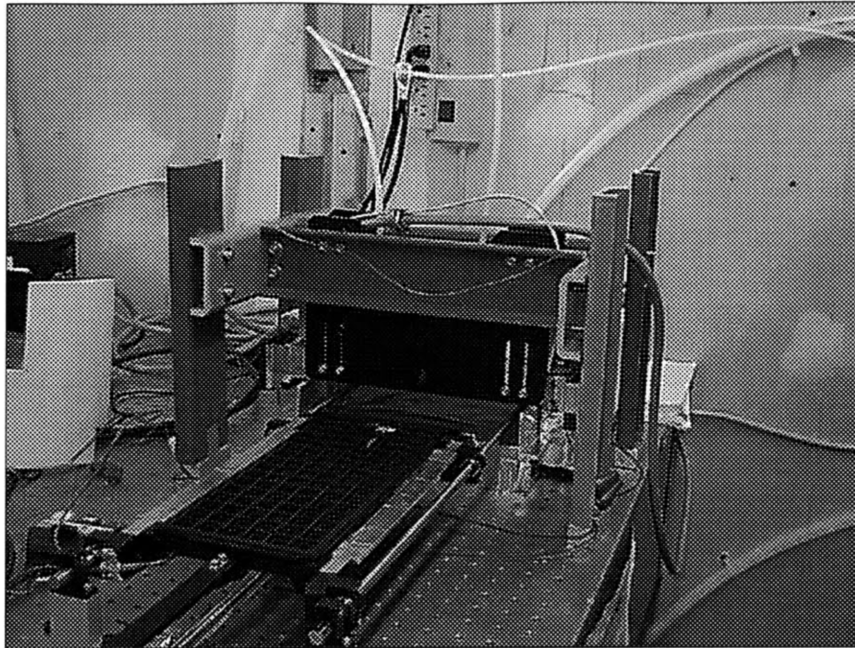

Figure 3-4: Photograph of assembled IR heating system.

on the center shaft. This output was reduce through a 10:1 transmission onto a 2 tpi precision lead screw.

3.1.4 Instrumentation

All temperature measurements for infrared heating were obtained using T type thermocouples. The data was collected using a National Instruments PCMCIA DAQ card, capable of acquiring 6 channels of data with build in cold junction reference. The precision of the absolute temperature measurements is only ±2°C, but of more interest in this work is the resolution and repeatability for a change in temperature. For the T type thermocouples used and the associated DAQ system, single channel repeatability is within ±0.5°C. To reduce the error for testing of uniform heating across the carrier, the same device was used at each position over multiple runs. This reduces the error associated with attempting to instrument each component at the exact same point and eliminates variability in contact resistance values.

3.2 Design Example

The actual selection of IR source, radiation intensity, carrier velocity, and required settling time after exiting the heater must be evaluated for each type of component and carrier. To make the method more clear, two examples will be worked through to estimate the required parameters.

3.2.1 Low Conductivity Carrier Design Example

This example is based on the plastic carrier shown in Fig. 3-1 with 10 mm QFP devices. The carrier dimensions are 13.6 cm wide by 32.1 cm long and is capable of carrying 96 components. The mass of the carrier is 141 grams. While the geometry of the carrier is fairly complex, the largest thickness of solid plastic is 1.95 mm. The 10 mm QFP device consists of a 1 mm layer of plastic over a 0.5 mm thick copper heat spreader with 0.5 mm of plastic on the bottom of the heat spreader. The devices rest loosely in the carrier with the 1 mm layer of plastic on top. The devices are 10 mm square with 11 lead frame contacts to a side. Each contact is 0.15 mm thick, 0.33 mm wide and approximately 2.3 mm long and manufactured from Kovar Alloy 42. Material properties for the device are listed in Table 3.2.1. The carrier is assumed to be manufactured from the same polyimide material as the encapsulant.

Table 3.2.1: Material properties for typical component.

Material	Density	Specific Heat	Thermal Conductivity
Polyimide Encapsulant	1850 kg/m^3	1185 J/kg K	1.48 W/m K
Copper IHS	8950 kg/m^3	385 J/kg K	386 W/m K
Silicon	2330 kg/m^3	699 J/kg K	148 W/m K
Lead Frame (Kovar Alloy 42)	8200 kg/m^3	447 J/kg K	16 W/m K

The devices rest in the carrier with contact area on the back face, and no contact between the lead frames and carrier. Contact area depends on the position on the carrier with some sites having a solid contact face, and with others having a 1.5 mm contact strip around the sides of the base of a component. The first step is to determine the ratio of thermal masses between the carrier and the components. The thermal mass of the carrier is simply $M_C = m_C C_p = 0.141 \cdot 1185 = 167$ J/K. The thermal mass of a single component can be estimated by combining the multiple

layers into a uniform thermal mass. The mass of the integrated copper heat spread is $\sim 1.6 \times 10^{-4}$ kg and the mass of the plastic encapsulant is $\sim 3.3 \times 10^{-4}$ kg. The effect of the lead frame and die are neglected compared to the relative mass of the IHS and encapsulant. This yields a thermal mass for a single component of $M_d \simeq 0.5$ J/K. The total thermal mass of all components is $M_D = n_D M_d = 96 \cdot 0.5 = 48$ J/K, so the thermal mass of the carrier will be the driving factor in the final temperature.

Take the target temperature to be 85°C and the initial room temperature as 23°C. Assume the maximum limiting temperature on the carrier and components is 100°C. The width of the heater is 41 mm (fixed) and the output of the bulb can be varied from zero to 100 kW/m^2. From the analysis section, it was shown for high reflectivity walls, the edge devices and centerline devices are heated uniformly, so variations across the heater will not be considered. Figure 2-10 shows that for the case with a low conductivity carrier the temperature variation along the carrier is minimal and can also be neglected.

Start the analysis by calculating a radiation intensity and carrier velocity that will yield a component final temperature of 85°C. An infinite number of combinations will yield the required final temperature, but, from a practical stand point, the tradeoff becomes a selection between speed and degree of surface overheating. Take the velocity to be 1 cm/sec. With a surface absorptivity of 0.9 [9], the required radiation intensity for the 4.1 seconds of exposure is

$$I_0 = \frac{M_D \Delta T}{\varepsilon A_s t} = \frac{0.5 \text{ J/K} \cdot 63 \text{ K}}{0.9 \cdot 1 \times 10^{-4} \text{ m}^2 \cdot 4.1 \text{ sec}} = 85.3 \text{ kW/m}^2 \tag{3.1}$$

where A_s is the surface area of the device exposed to the radiation and is taken as simply the top projected area of the 10 mm QFP. This value of I_0 is within the limits for the intensity. The next step is to evaluate the final temperature of the carrier at this intensity. The residence time of the carrier in the radiation field is approximately 32 seconds and the projected area at any given time is 41 mm by 136 mm, but this needs to be corrected for a shielding factor due to the presence of components on the surface of the carrier. For this carrier, 75% of the surface is exposed to the radiation. The final temperature of the carrier can be found from

$$T_C = T_0 + \frac{I_0 \varepsilon A_p t}{M_C} = 23 \text{ K} + \frac{85.3 \text{ kW/m}^2 \cdot 0.9 \cdot 4.182 \times 10^{-3} \text{ m}^2 \cdot 32 \text{ sec}}{167 \text{ J/K}} = 84.5°\text{C} \tag{3.2}$$

where A_p is the projected area. In this case, the final temperatures of the carrier and components are almost identical, but this will not always be the case. In situations

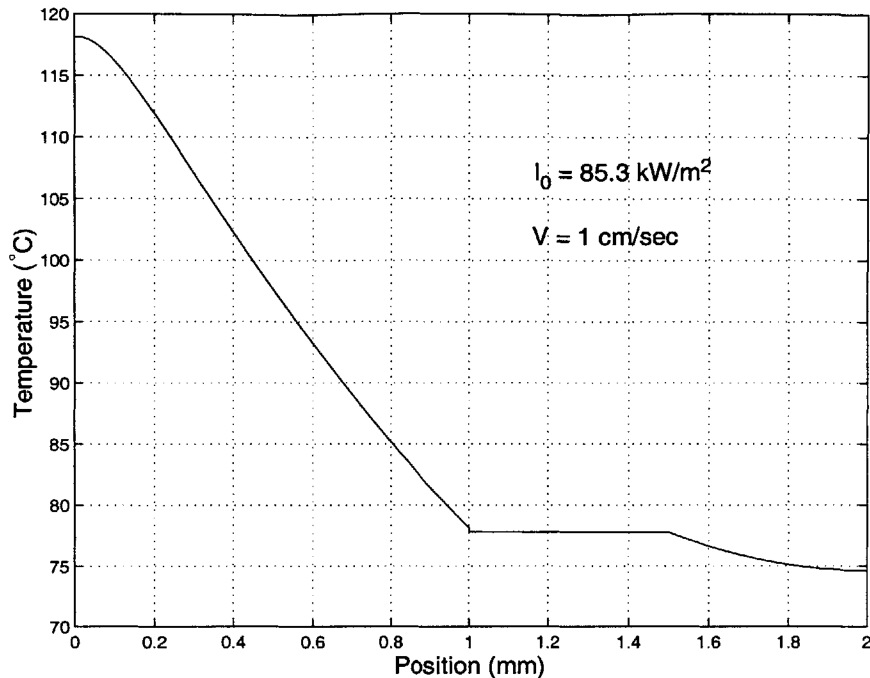

Figure 3-5: Temperature profile in 10 mm QFP device at exit of heating chamber.

where the carrier and components are manufactured from different materials, or in cases where there is significant shielding of the carrier by the components, the final temperatures could be very different. Since the final temperatures of the components and carriers are so close in this case, the settling time between the carrier and components does not need to be considered.

Now the maximum temperatures in the component and carrier need to be evaluated to ensure the maximum temperature limit is not exceeded. The temperature profile in the device must be calculated using the implicit finite difference method developed in the modeling section. For the stated conditions (I_0 = 85.3 kW/m^2, V = 1 cm/sec, 10 mm QFP device) the temperature profile within the device is given in Fig. 3-5. As can be seen, the maximum surface temperature as the device exits the heater is greater than the allowed maximum of 100°C. Before recalculating a new velocity and intensity, calculate the profile in the carrier using eqn. 2.7. The results for a carrier thickness of 1.95 mm is given in Fig. 3-6. These results are very similar to the temperature profile in the component. The maximum temperature is over the 100°C limit by almost the same amount as the surface of the carrier.

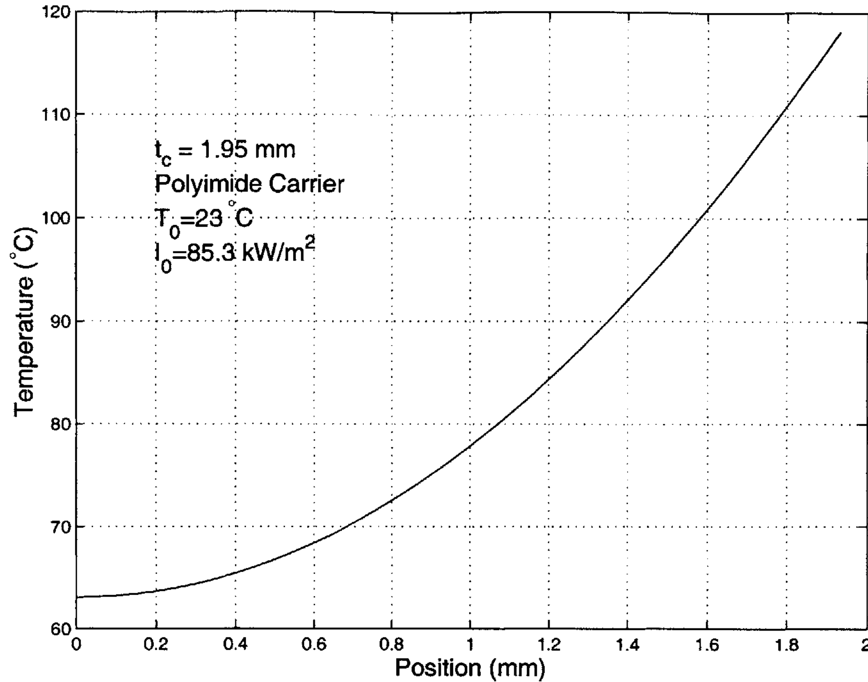

Figure 3-6: Temperature profile through a plastic carrier after exiting heater section.

So now a new velocity and radiation intensity needs to be considered to reduce the maximum surface temperatures of the components and carrier. By using a slower velocity and lower intensity, the same final temperature can be obtained, but with lower corresponding maximum surface temperatures. Selecting a new velocity of 0.7 cm/sec, the new intensity can be calculated as $I_0 = 59.8\ \text{kW/m}^2$. Using these new values for intensity and carrier velocity, the maximum surface temperature for a component becomes 94°C, and the maximum temperature of the carrier is 106°C. The component surface temperature is below the limiting factor, but the surface of the carrier appears to be too hot. The calculation used for the surface temperature of the carrier is a worst case scenario, assuming perfect 1-D slab conduction with 100% radiation absorption at the surface of the device. The carrier is actually subject to 3-D conduction effects into shielded areas and the absorption takes place over a finite length from the surface. Both of these factors will tend to reduce the temperature gradient across the depth of the carrier, so this set of operating conditions[2] is acceptable

[2]The final temperatures calculated at this point are not exact because radiant transfer between the components and chamber walls has not been considered, but these calculations provide a good baseline starting point and it is assumed that a number of calibration runs will be made to fine tune

($I_0 = 59.8$ kW/m^2, $V = 0.7$ cm/sec) as an initial design point.

3.2.2 High Conductivity Carrier Design Example

Now an example will be worked through that covers a high conductivity carrier. In particular, the strip carrier device shown in Fig. 3-2 will be used in this example. As stated earlier, the strip carrier is 5.8 cm wide, 21.3 cm long and the metal lead frame is 0.24 mm thick copper. The final encapsulated device is 2.3 mm thick, 7.4 mm wide, and 11.5 mm long. Encapsulation thickness is approximately even on both side and is equal to 1 mm. There are 48 encapsulated devices per strip carrier. The metal lead frame assembly weighs 16 grams and an assembled strip is 32 grams. Neglecting the mass of the die and die/lead frame interconnects as small[3] compared to the mass of the encapsulant and carrier frame, the relative thermal masses of the carrier and encapsulant can be calculated.

The thermal mass of the metal lead frame is 6.16 J/K and the thermal mass of the encapsulant is approximately 18.9 J/K, so the dominant thermal mass is the encapsulant, not the lead frame assembly. Again, take the target temperature to be 85°C with an initial temperature of 23°C. Start with an initial velocity of 0.8 cm/sec. The required radiation intensity for the encapsulant is

$$I_0 = \frac{M_D \Delta T}{\varepsilon n A_D t} = \frac{18.9\text{J/kg} \cdot 62\text{K}}{0.9 \cdot 48 \cdot 8.1 \times 10^{-5}\text{m}^2 \cdot 5.1\text{ sec}} = 65.7\text{ kW/m}^2 \tag{3.3}$$

which can now be used to estimate the temperature profile in the carrier. Putting the stated conditions into the implicit finite difference model, the resulting temperature profile along the carrier is given in Fig. 3-7. The average temperature of the carrier upon exiting the heater is 108°C, so the final steady state temperature of the entire system will be

$$T_{final} \simeq \frac{T_C M_C + T_D M_D}{M_D M_C} = \frac{85 \cdot 18.9 + 108 \cdot 6.16}{18.9 + 6.16} = 90.6°\text{C} \tag{3.4}$$

which is slightly higher than the target value of 85°C. The value is approximate because not all the surface area of the lead frame is exposed to the radiation[4].

The time required to reach steady state can be estimated by looking at a leading edge device, trailing edge device and conduction along the carrier. Using eqn. 2.16,

---

the final velocity and intensity settings.

[3]Mass of die ~ 1.9 mg.

[4]Some of the mass of the lead frame is masked by the encapsulant.

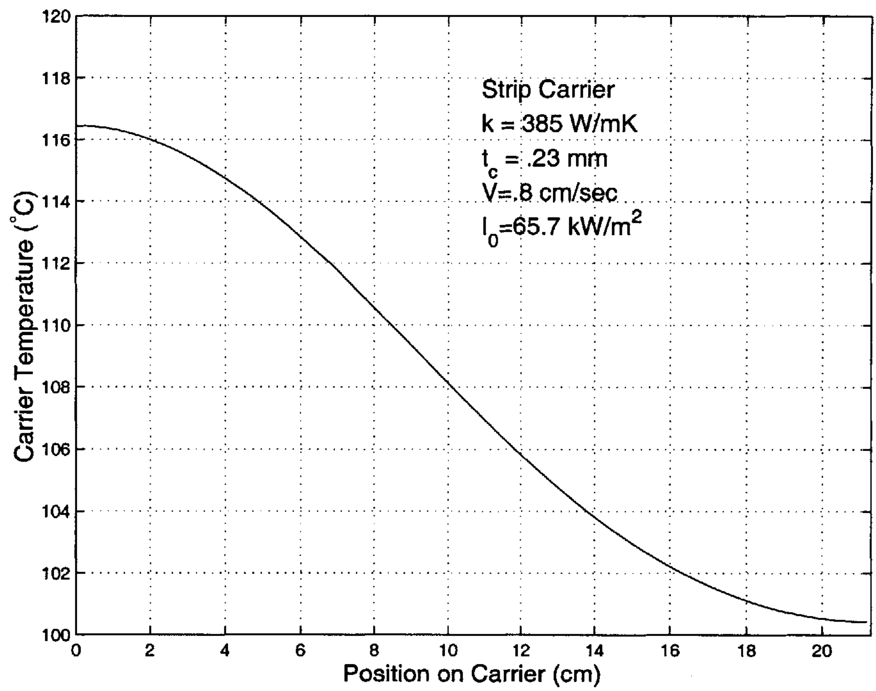

Figure 3-7: Temperature profile along strip carrier metal frame for $I_0 = 65.7$ kW/m^2 and $V = 0.8$ cm/sec.

the time constant for the conduction along the carrier can be estimated as

$$t_{ss} = \frac{L^2}{\pi^2 a_t} = \frac{(0.213 \text{ m})^2}{\pi^2 \cdot 112 \times 10^{-6} \text{ m}^2/\text{sec}} = 41 \text{ sec} \tag{3.5}$$

which can be used to estimate the time required for the two ends of the carrier to come within 3°C of each other. For an exponentially decaying temperature defect with an initial temperature difference[5] of 8°C, this requires approximately a single time constant, or $\sim$ 40 seconds.

The other two time constants can be estimated by looking at a device and the coupling to the surrounding lead frame. The die structure inside an encapsulated device is connected to the lead frame through two small metal structures on either end. The dimensions of this connection are 3.8 mm long, 0.36 mm wide, and 0.25 mm deep. An effective conduction resistance can be calculated for these structures between the exposed lead frame and center die mount, but this isn't really the resistance that is needed. Most of the thermal mass is contained in the encapsulant, so the point of interest is how long it takes the surrounding lead frame and encapsulant to reach equilibrium. Again, this is not a system that lends itself well to closed form solution: two non-isothermal masses in contact over a small area with complex geometries. In order to get a rough time estimate, some simplifying assumptions need to be made.

Consider just the encapsulated device. Since the item of interest is an upper bound on the time to steady state, a minimum flux can be used to estimate this time. The minimum flux can be calculated by considering an effective minimum[6] temperature difference of 6°C. The flux associated with this temperature defect can be calculated assuming the lead frame is isothermal and the encapsulant is adiabatic on all sides except at the contact point with the lead frame. The end of each device is in full contact with a strip of the lead frame. This strip is the only direct contact between the component and the strip carrier structure as the side lead frame contacts are sheared and disconnected from the lead frame after the plastic overmolding is added. Neglecting contact resistance between the lead frame and encapsulant, the flux from

[5]The temperature defect of interest is from initial temperature to the final steady state temperature, not from one end temperature to the other.

[6]Temperature limits are specificed to within ±3°C of the target temperature. Assuming the encapsulant is at one extreme and the lead frame at the other, effective steady state is reached when both are within the limits of the target temperature, or 6°C apart. Use of this temperature defect will provide an upper limit on the minimum required time to approach steady state.

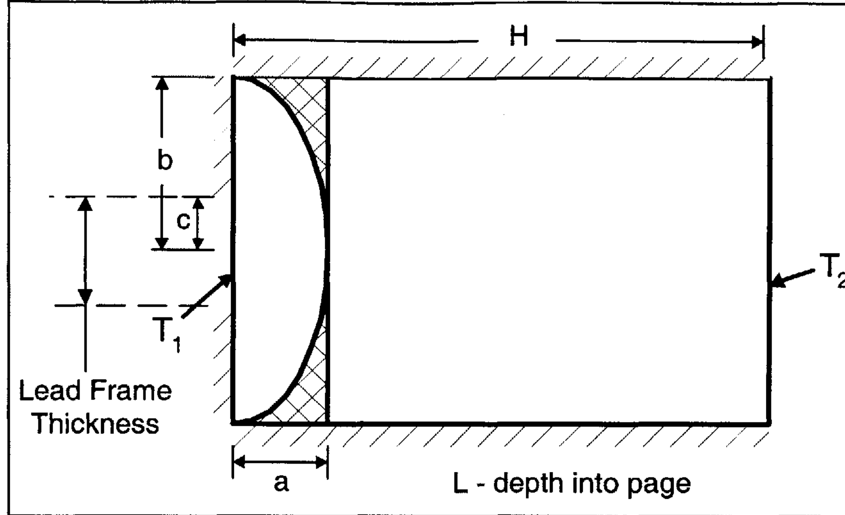

Figure 3-8: Resistance model for encapsulated strip device. The hatched area represents the region where conductivity is assume to be infinite.

the lead frame to the encapsulant can be calculated from

$$Q = \frac{T_2 - T_1}{\left[\frac{H-a}{2kbL} + \frac{\ln\left(\frac{b+a}{c}\right)}{\pi k L} \right]} \tag{3.6}$$

and where the geometric terms are taken from Fig. 3-8, and $T_2 - T_1$ is the 6°C temperature defect. In Fig. 3-8, the a dimension is given by $a = \sqrt{b^2 - c^2}$ and L is the depth of the device into the page. This resistance model can be used to simulate the strip device. Assuming the device is symmetric and modeling only half of the device, the thickness $2 \cdot c$ is the thickness of the lead frame, $2 \cdot b$ is the thickness of the device, H is half the length of a device, and L is the width. This model will slightly overestimate the heat transfer due to the assumption that the hatched area has infinite conduction. For the encapsulated strip device under consideration, this yields a heat transfer of $Q = 8.96 \times 10^{-3}$ W. This heat transfer calculation can now be used to estimate the time required for steady state. For a change in temperature

of the device[7] of approximately 5°C, the time required for steady state becomes

$$t = \frac{M_D \Delta T}{Q} = \frac{\rho C_p (2b) L H \Delta T}{Q}$$
$$= \frac{1850 \text{ kg/m}^3 \cdot 1185 \text{ J/kgK} \cdot 2 \cdot 0.0011 \text{ m} \cdot 0.0023 \text{ m} \cdot 0.0058 \text{ m} \cdot 5 \text{ K}}{8.96 \times 10^{-3} \text{ m}^3} = 36 \text{ sec} \tag{3.7}$$

which is of the same order of magnitude as the time required for the carrier to come to equilibrium. This settling time is a very rough order of magnitude estimate that provides a reference to make sure the component settling time is not much greater than the carrier settling time.

3.3 Experimental Data

A number of experiments have been run, focused on the heating of 10 mm QFP devices in a plastic carrier and on the heating of a plane aluminum carrier without any devices. The QFP plastic carrier has 6 components mounted across the width of the carrier, with 16 rows of devices along the length of the carrier.

Figure 3-9 shows the results for multiple runs through the heater in all lateral positions. As can be seen, the final temperatures are within a range of 3°C for all runs. This data is for a heating chamber height of 51 mm, a heater width[8] of 41 mm, a carrier velocity of 1.04 cm/sec, and aluminum foil coated walls with a reflectivity of 0.9. Some of the variation can be explain through uncontrolled convection conditions and instrumentation errors, but even discounting these factors, the final temperature is very uniform and well within the ±3°C that is often specified for thermal conditioning systems in electronic test handlers. In comparison, Fig. 3-10 presents data for the case where the walls have low reflectivity ($\rho \simeq 0.2$). The radiation intensity setting is exactly the same as for Fig. 3-9. As is expected, there is a larger range of final component temperatures, and the low reflectivity wall case has a lower final temperature despite the same radiant intensity and almost identical carrier velocities[9]. This demonstrates the benefit of high reflectivity walls in the heating chamber, even if temperature uniformity across all devices in not critical.

[7]Temperature change of interest is from initial component temperature once exiting the heater to the final steady state temperature once the components and strip are at the same temperature.

[8]Heater width is fixed for all runs.

[9]The final temperatures in Fig. 3-10 would have an even bigger range if the end bulb effects were

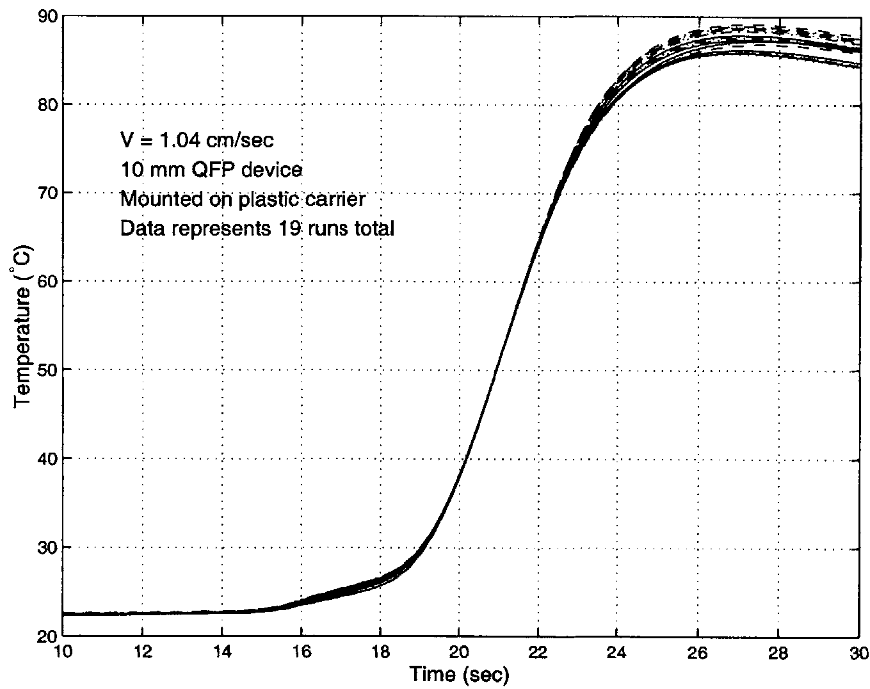

Figure 3-9: Experimental data for testing lateral heating uniformity with high reflectivity chamber walls. Data is for 10 mm QFP device mounted on leading row of plastic carrier. Temperature measured on integral heat spreader.

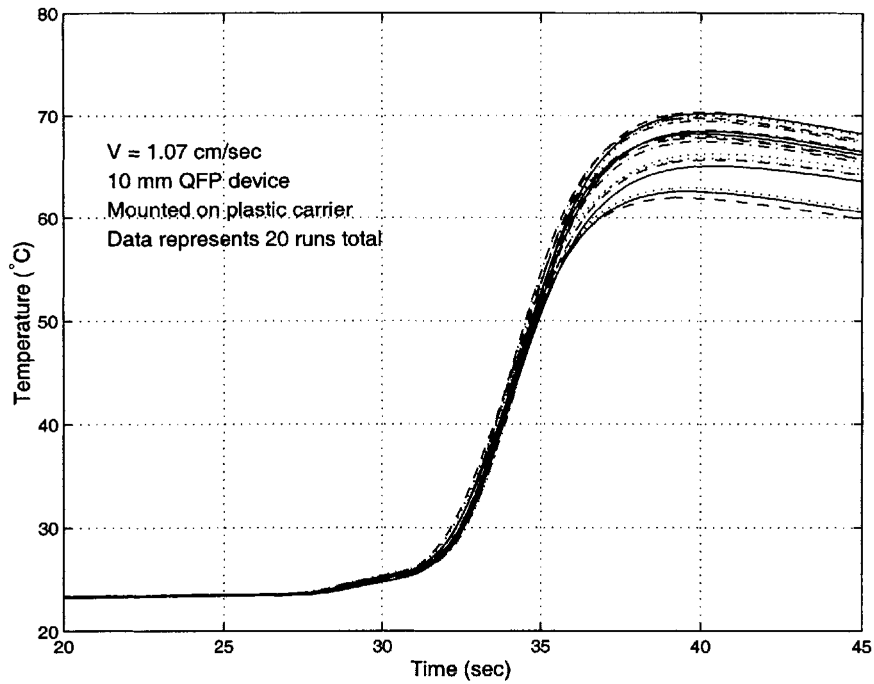

Figure 3-10: Experimental data for testing lateral heating uniformity with low reflectivity chamber walls. Data is for 10 mm QFP device mounted on leading row of plastic carrier. Temperature measure on integral heat spreader.

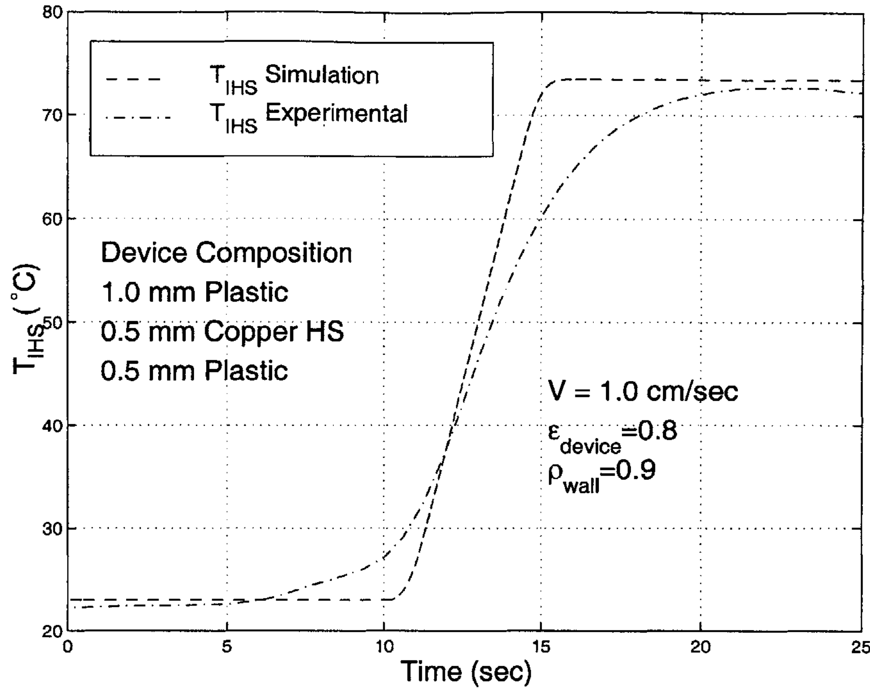

Figure 3-11: Experimental and simulation data for 10 mm QFP on carrier centerline.

A comparison of experimental data to the simulation can been seen in Fig. 3-11. The initial heating of the experimental device compared to the simulation is due to radiation leakage outside the heating chamber. The experimental data shows a slower response than the simulation indicating that the conduction resistance is higher in the actual case than in the model. This may be due to interfacial resistance between the layers that was not included in the model, or it may be that the conductivity of the plastic encapsulant is lower than believed, or it may be the result of an instrumentation problem where the temperature is being sensed at a point just below the QFP's heat spreader.

Experimental measurements of the effect of conduction along the carrier are presented in Fig. 3-12 for a 2.8 mm thick flat aluminum carrier. As predicted, the trailing edge temperature is significantly higher than the leading edge temperature. This demonstrates the importance of considering conduction along the carrier in calculating the peak and steady state temperature profiles in the carrier. This is especially true for strip carriers. Figure 3-13 presents data for heating of the strip carrier shown in Fig. 3-2. Type T thermocouples were attached to the center metal frame on three

added (i.e. no heating chamber whatsoever.

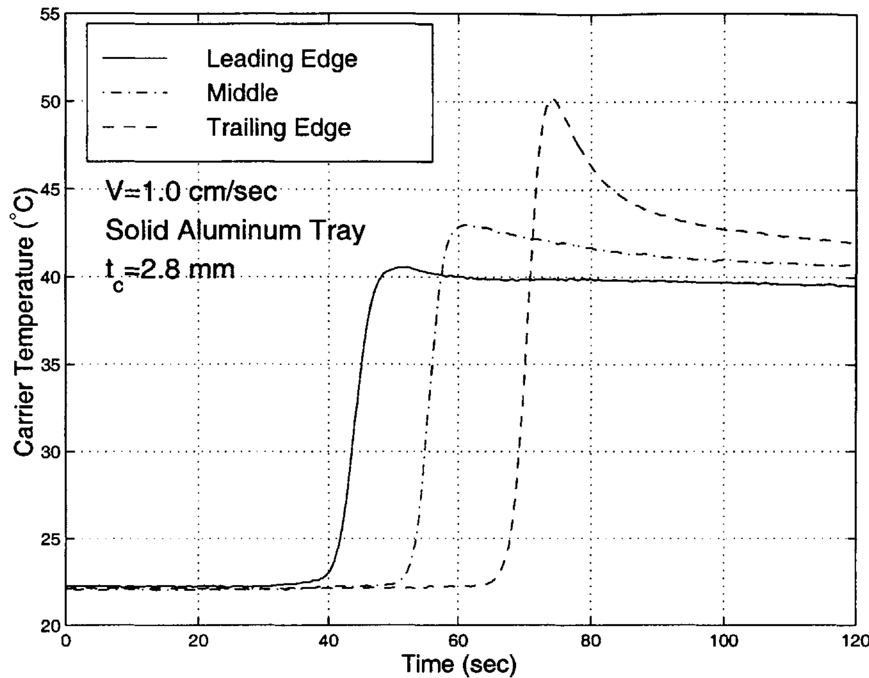

Figure 3-12: Temperature profile for high conductivity carrier.

devices using high conductivity[10] epoxy. Thermocouples were also attached to the edge and middle of the metal frame using low melting point solder. The strip carrier was delivered into a heated chamber with air temperatures as stated on the plots. The convection state in the hot side chamber had only limited controllability resulting in the leading device settling to a higher final temperature than the devices in middle and trailing edge of the frame. Figure 3-14 shows the temperature profile of a device in the middle of the strip carrier and the surrounding frame temperatures during and after the heating process. As was stated in the design example for the strip carrier, there are multiple carrier velocity/radiation intensity combinations that will produce the desired final temperature. Figure 3-15 shows temperature profiles for heating the strip carrier at two different carrier velocities.

Error Analysis

The output from the IR bulb was held constant between runs by securing the controller setting at an initial fixed value. Limited information is currently available on

[10]High conductivity is very relative. Nominal conductivity for epoxy is 3.5 W/m K.

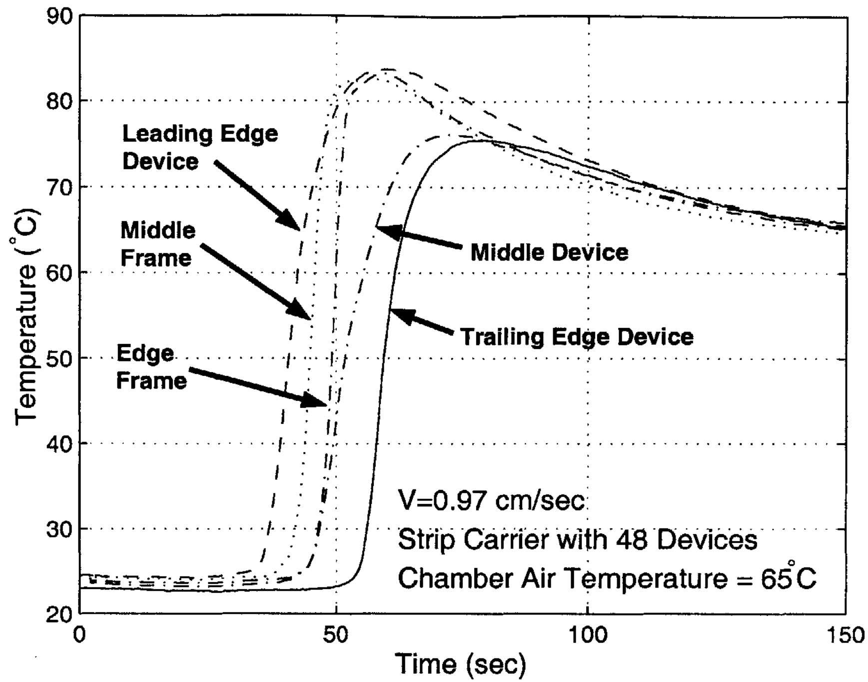

Figure 3-13: Temperature profile for heating of strip carrier.

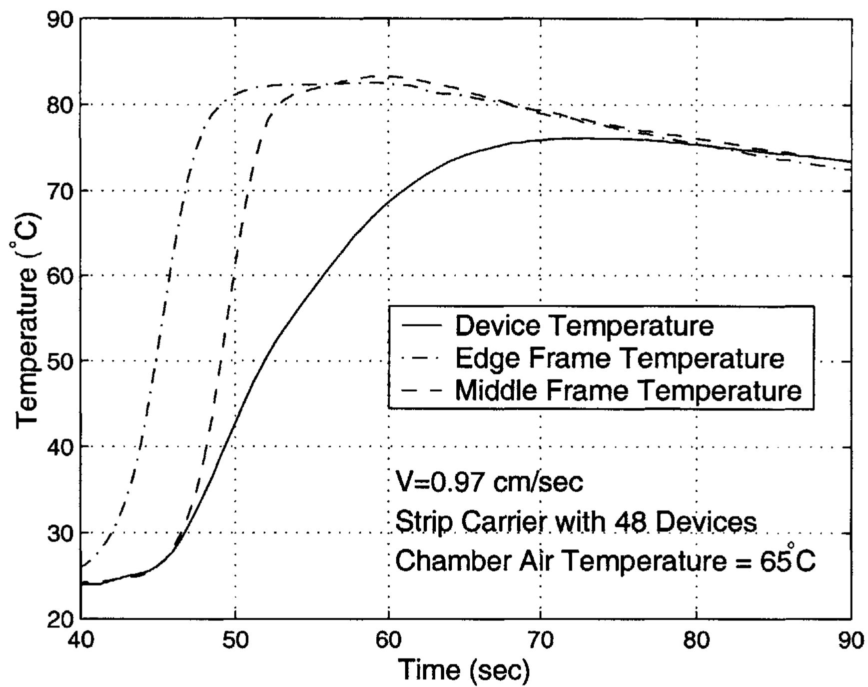

Figure 3-14: Settling time for device in center of carrier compared to surrounding metal frame.

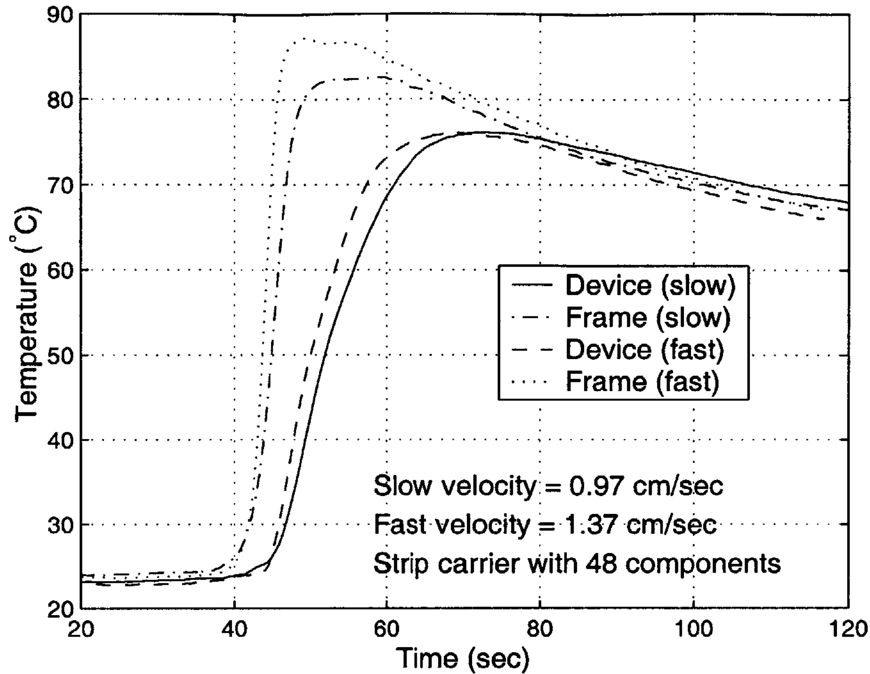

Figure 3-15: Heating of strip carrier at two different carrier velocities.

the variability of the IR output, but initial estimates put repeatability at ±0.5% of a given fixed output. The IR source was allowed to heat up for 5 seconds before a data run was started. Manufacturer specifications state the 90% rise time at 3 seconds for the IR bulb utilized.

As stated earlier, the carrier velocity was measured using a hand held digital tachometer on the output shaft from the motor, before reduction through a fixed ratio gear transmission. Accuracy of the tachometer is specified as ±0.5 rpm, but measured variation of the motor during a run is over ±10 rpm. For a 10:1 gear ratio and a 2 tpi precision ground lead screw, this corresponds to a velocity variation of ±0.02 cm/sec.

For these conditions, a standard propagation of error method (at 95% confidence levels) can be used to estimate the expected variation in temperature change for a given component. Since the errors in the IR flux and carrier velocity are independent, and since the total temperature change of a device can be estimated from $\Delta T = Q_a t/mc_p$ where Q_a is an average flux and t is the effective residence time in the

heater, the expected variation in temperature change can be calculated as

$$\frac{\delta \Delta T}{\Delta T} = \sqrt{\left(\frac{\delta Q_a}{Q_a}\right)^2 + \left(\frac{\delta t}{t}\right)^2} \tag{3.8}$$

This will yield an expected variation of $\pm 2.1\%$ of ΔT for a carrier velocity of 1 cm/sec at any Q value. For the data in Fig. 3-9, this represents an expected variation of $\pm 1.2°C$, which is over twice as large as the repeatability of the thermocouple. This helps explain the variation in the data in Fig. 3-9.

Simultaneous temperature measurements on multiple devices have large variations due to instrumentation problems. Even trying to instrument the same device with two thermocouples mounted onto the integral heat spreader. The data shown in Fig. 3-16 illustrates this problem. The data presented are for a 10 mm QFP devices, where one device has been instrumented with two T type thermocouples, mounted directly onto the integral heat spreader using high conductivity epoxy. There is no flux across the lateral direction of the heat spreader and there should be no temperature gradient, but even in this case, the maximum temperatures measured are different by 3°C due to differences in contact resistance and thicknesses of epoxy between the thermocouples and the heat spreader.

3.4 Conclusion

It has clearly been shown that IR heating of multiple devices is a possible means of rapidly bringing the components to test temperature. Both the components and carrier must be considered in the system design process, as they both have an affect on the final component temperature. The maximum heating rate is generally limited by conduction into the device, and care must be taken to avoid exceeding material temperature limits on a local basis.

3.4.1 Design Guidelines

The following is a list of basic design guidelines that need to be considered in the implementation of IR heating of devices.

- Select an IR heater/bulb assembly such that the entire width of the carrier can

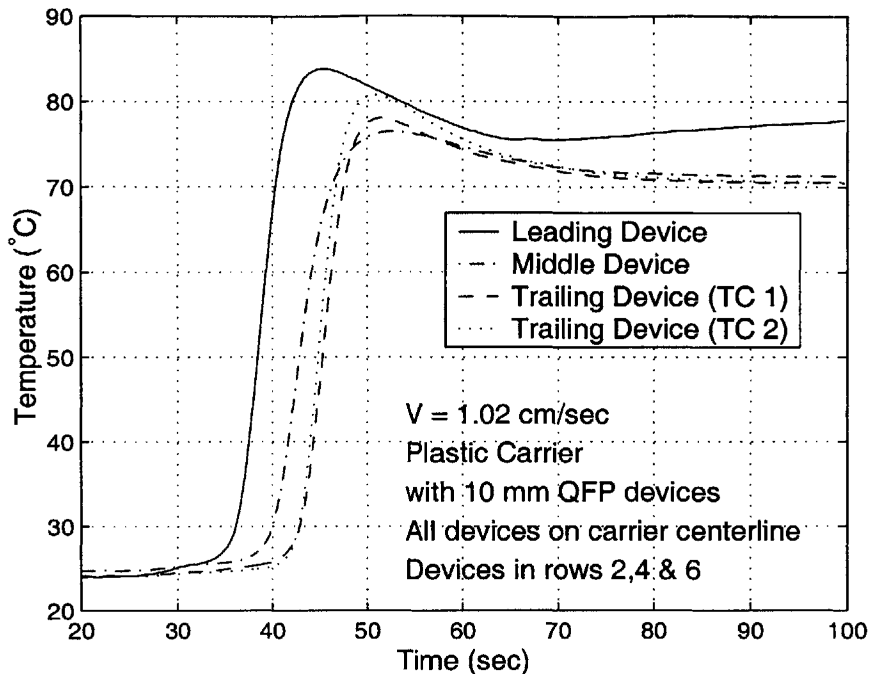

Figure 3-16: Temperature profile for heating of 10 mm QFP devices.

be covered by the central 80–90% of the bulb length[11].

- Make sure the devices are not transparent to the emission band of the source.
- Calculate relative thermal masses of components and carrier. If either mass dominates, design the IR system to bring that mass to test temperature. If masses are of same order of magnitude, design system around the components and then calculate settling times.
- Evaluate the maximum component and carrier temperatures. If maximum exceeds specified limits, reduce radiation intensity and reduce velocity or increase exposure distance (i.e. add a second heater).
- The design of the reflectors can be an important component in the system design. For low cost, standard parabolic reflectors are useful and provide a fairly uniform collimated radiation field. Hyperbolic reflectors are also generally available, but use of these systems are of limited for this application. Hyperbolic

[11]90% is a minimum, depending on the IR manufacturer specification, 80% may be more appropriate.

reflectors can focus the output of a IR bulb into a smaller area than a parabolic reflector, but this will generally lead to material overheating for plastic encapsulated devices and plastic carriers[12]. If the target is sufficiently far away from a hyperbolic reflector, the radiation field will cover more area than a parabolic reflector, but the intensity will not be constant over the field and very careful analysis will be required to eliminate the possibility of localized over heating. Custom made reflectors are an option, but the economics of such a decision will have to be considered on a case by case basis.

[12]Higher heating rates without any real system space savings. Hyperbolic reflectors are generally useful for very high localized heating, not the uniform heating required in the handling of bulk devices.

Chapter 4

Temperature Control of Active Device

As stated in the introduction, the two main thermal problems in functional testing of electronics are to heat multiple components to a uniform test temperature and temperature control of high power devices during the actual test sequence. Rapid heating of multiple components has already been covered, so now the focus will change to thermal control of high power devices during the actual functional test. The UNISYS [3] method for temperature control was described in the introduction, along with its inherent problem of requiring contact with the device under test (DUT). The main goal of this thesis was to develop a non-contacting system that utilizes convection and radiation to actively control the temperature of the device.

The convective cooling system must be capable of handling the full thermal load of the device, but is not generally capable of the rapid response required for temperature control due to capacitance and flow friction effects. A radiation source can be used to supplement the cooling system and provide a method of temperature control in the presence of rapidly changing thermal conditions on a device. This chapter will describe the characteristics of a typical high power device, the cooling and heating requirements for the thermal control system, and a dynamic model to characterize the behavior of a device under test. The physical implementation of the cooling and heating systems and a detailed analysis of the control system will be covered in the next chapters.

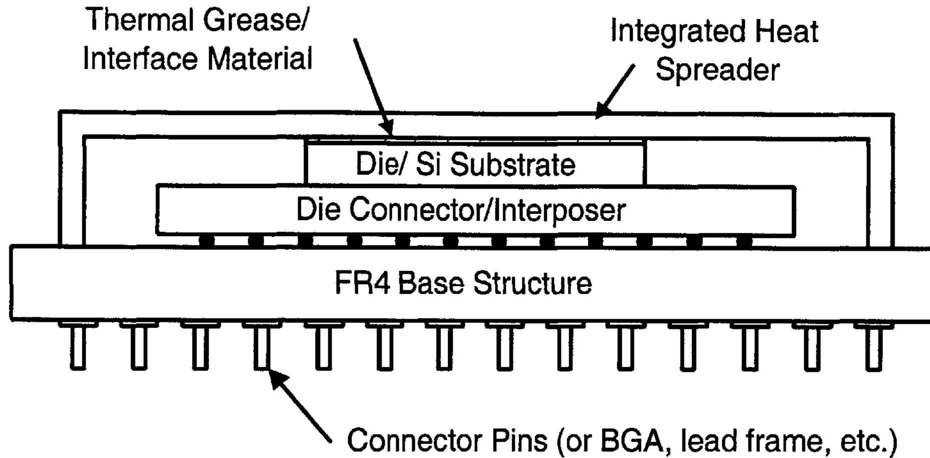

Figure 4-1: Cross-section of typical high power density device. Some components may not be present in some devices.

4.1 Description of an Electronic Device Under Test

A typical device consists of several components. Figure 4-1 shows the cross section of a typical high power device. There are a large number of variations of this basic device and not all elements are present in all configuration, but this model is representative of a majority of devices. The pin connections on the base of the device may take many forms, from pins to ball grid arrays (BGA) to edge mounted lead frames. Not all devices have integrated heat spreaders and there may be multiple interposer layers with no base structure, but this device offers a good basis for developing a model.

In a testing configuration, this device will be held using a suitable fixture and pressed against a test contactor. The test socket in mounted to a Handler Interface Board (HIB) that routes each pin to the appropriate testing channel. The back side of the device (HIB side) is not generally accessible for temperature control during testing due to the presence of the interconnects and electronics, so all temperature control methods must be applied to the front face of the device[1]. The handling fixture is custom for each type of device and must be capable of exerting enough force on the device to ensure reliable contact with the test socket and is also responsible for device/socket alignment. The handler and tester are generally not manufactured by the same company, with the HIB being the primary component that requires

[1]With component sizes shrinking, devices that may have had open areas on the back side are becoming covered with external interconnects.

interaction between the tester company and the handler manufacturer. Any active thermal control system that uses signals or timing from the test head, must also be able to interface with a wide variety of handler systems with only minor modifications for mounting hardware and interfaces.

Generally the only information provided about a given device is the thermal resistance between the die and the heat spreader. This information can come from calibration data, but can also be a best guess that is not backed up by any hard data. Even less information is available on thermal resistances between the die and the interposer/base support structures.

4.2 Device Descriptions for Prototype System

Two devices were selected for testing with a prototype temperature control system. Both devices are thermal test vehicles (TTV) provided by Intel. These devices are exact physical copies of actual devices, but instead of active components on the silicon die structure, a set of thin film heaters and RTD temperature sensors are manufactured on the silicon die. All remaining components are the same. The P858ACY TTV is a multi-die assembly designed for testing high power levels at low to medium power densities. It consists of four thin film heaters on a single monolithic silicon die. There is a single nickel coated copper integrated heat spreader (IHS) on top of the silicon die and the base of the die is connected to an interposer structure. The interposer is mounted on a FR-4 base structure that has pin-out connections routed to the thin film heaters and RTD sensors. The other TTV is the Intel Pinetop thermal test vehicle. This is designed for low to medium power levels at high power densities. There is a single thin film heater on a silicon die with a nickel coated copper heat spreader. There is no interposer structure on the Pinetop TTV and the die is mounted directly to the FR-4 support structure.

The integrated heat spreader on each TTV is 1.8 mm thick. A picture of the P858ACY TTV is shown in Fig. 4-2 and a picture on the Pinetop TTV is shown in Fig. 4-3. The die and IHS sizes and resistances are given in Table 4.2.

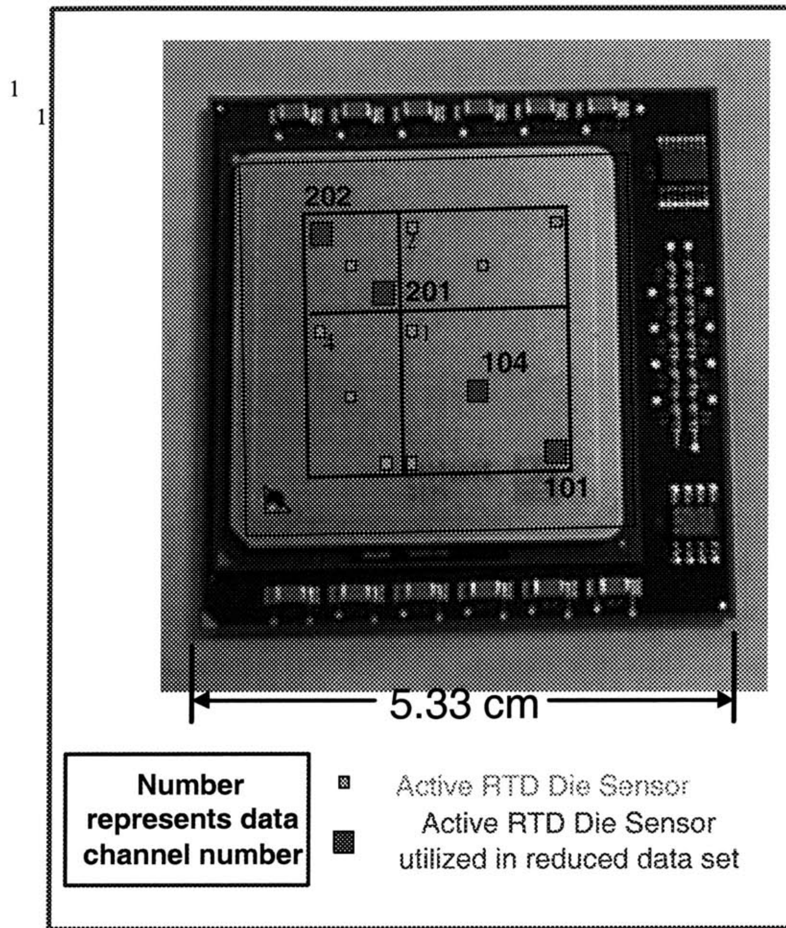

Figure 4-2: Intel P858ACY TTV. Squares indicate individual dies.

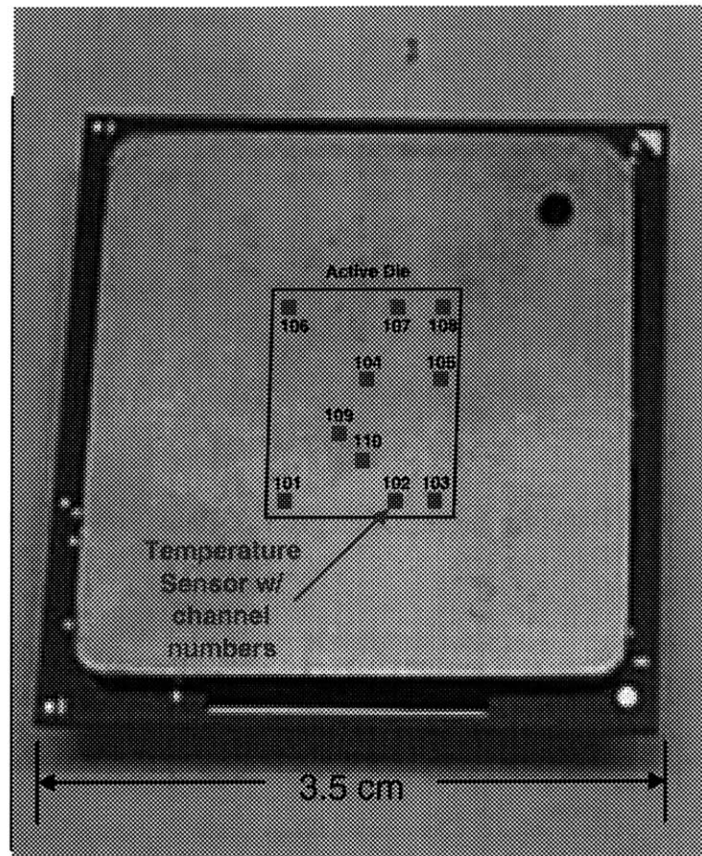

Figure 4-3: Intel Pinetop TTV

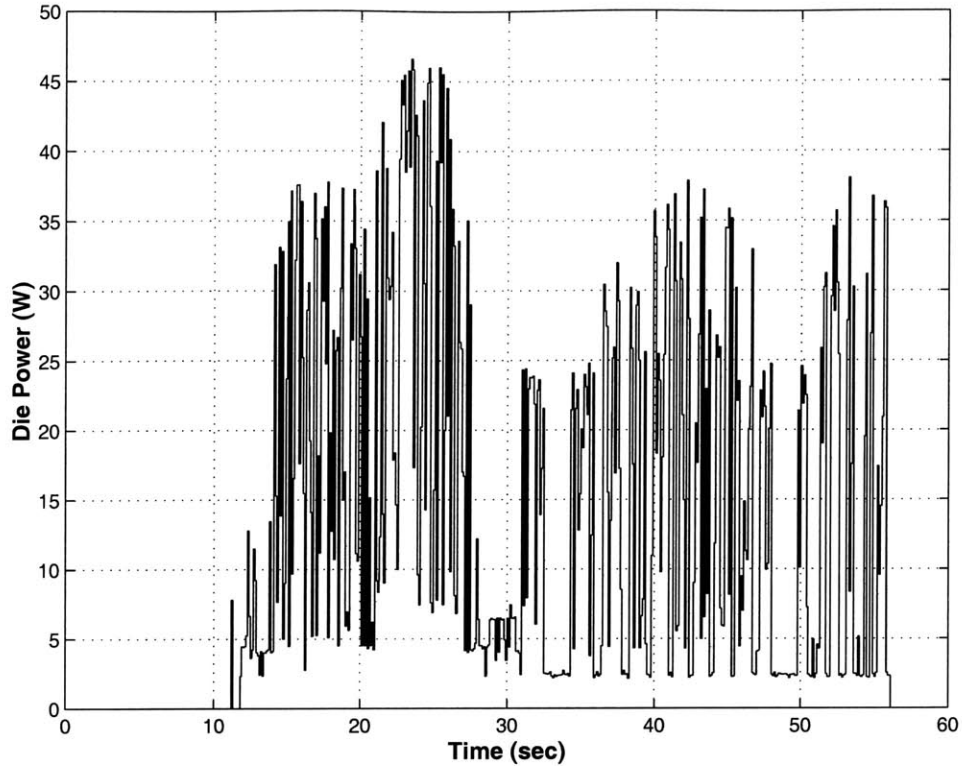

Figure 4-4: Baseline Intel power profile. Peak power is 46.6 W.

Table 4.2: Thermal Test Vehicle Description.

	P858ACY TTV	Pinetop TTV
IHS Surface Area	14.9 cm^2	9.6 cm^2
Die 1 Size	1.53 cm^2	1.17 cm^2
Die 2 Size	1.05 cm^2	-
Die 3 Size	0.97 cm^2	-
Die 4 Size	0.65 cm^2	-

Each device has RTD's mounted directly on the die structure for monitoring of die temperature. Each RTD is a four wire system with connections routed to the pin-outs on the base structure.

A baseline test profile that lists power as a function of time is shown in Fig 4-4. This profile is scaled up or down to obtained the desired peak power magnitude. The profile consists of 0.1 second square waves.

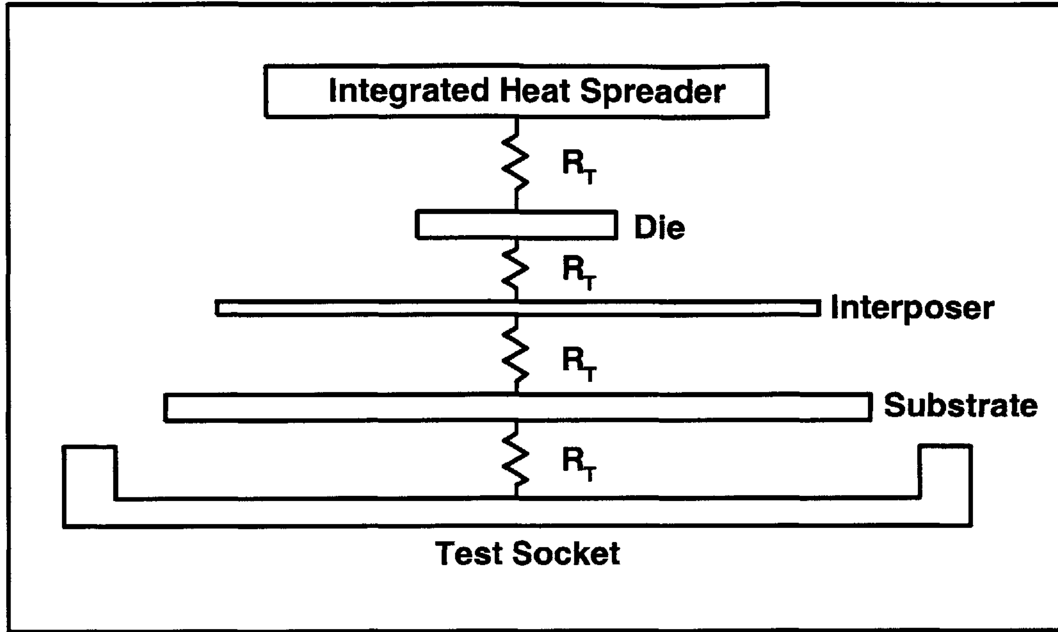

Figure 4-5: Baseline transient model of a typical device under test.

4.3 Model of Device Under Test

In order to estimate the effectiveness of various control methods on a device under test, a model needs to be developed that includes the dynamic aspects of the device. On the most basic level, a simple resistance-capacitance model can be constructed that assumes each mass is isothermal. A schematic drawing of this thermal model is shown in Fig. 4-5. While the mass and specific heat of each individual component is known, as was stated earlier, the thermal resistance between the components in generally not known except for the contact resistance between the die and the integrated heat spreader. Also in this case there is the additional contact resistance between the device and the test socket that must be considered.

The system shown in Fig. 4-5 can be described by a system of coupled first order differential equations. The resulting equations for the integrated heat spreader and die are as follows[2]:

$$m_1 c_{p_1} \frac{dT_1}{dt} = Q_1 + \frac{T_2 - T_1}{R_{1-2}} - h_c \cdot A_1 \left(T_1 - T_{air}\right) \tag{4.1}$$

$$m_2 c_{p_2} \frac{dT_2}{dt} = Q_2 + \frac{T_1 - T_2}{R_{1-2}} + \frac{T_3 - T_2}{R_{2-3}} \tag{4.2}$$

[2]Assumes lumped capacitance.

Subscript 1 in this case indicates the integrated heat spreader and subscript 2 indicates the die. Similar equations can be written for the interposer, support base, and test socket in Fig. 4-5. The resulting system of equations can be written in matrix form.

$$\frac{d}{dt}[\mathbf{T}] = [\mathbf{A}] \cdot [\mathbf{T}] + [\mathbf{H}] \tag{4.3}$$

The matrix **A** is the characteristic matrix of the system and **H** is the forcing function. For a specified set of boundary and initial conditions, this system of equations can be quite easily solved [18]. Let **M** be the a matrix whose columns are the eigenvectors of **A** and let **Y** be a new matrix such that $\mathbf{T} = \mathbf{MY}$. Then eqn. 4.3 can be rewritten as

$$\mathbf{Y}' = \left(\mathbf{M}^{-1}\mathbf{AM}\right)\mathbf{Y} + \mathbf{T}^{-1}\mathbf{H} \tag{4.4}$$

where it can be shown that the resulting system of equations is now a system of uncoupled first order differential equations in y_1, y_2, ..., y_n. Each equation can be solved separately and the final solution is simply $\mathbf{T} = \mathbf{MY}$.

4.4 Model Data from Experimental Results

The model developed in the previous section is very useful for calculating the response of the system to a given die power profile. Even more important, the model from the previous section can be used in conjunction with experimental data to determine the thermal resistances between all of the components. This can be done by comparing the experimental results at multiple times over a range in die power profiles. Very short times provide information about contact resistances between the die and the IHS and the die and first interposer. Intermediate times provide information about thermal resistances between interposer layers, the base structure, and test socket. Long term or steady state results provide information about die to IHS resistance as well as confirmation of convective boundary conditions. The procedure for determining these values becomes an iterative process of matching experimental data and model results.

The thermal capacitance of each layer can be estimated with a reasonable degree of accuracy. For the P858ACY TTV, there are 5 layers that must be estimated. The die and the IHS are both fairly easy to estimate as the volumes, densities and material types are all known. The mass of the the IHS is 21.77 g with a specific heat of c_p = 385 J/kg K. The mass of the die is 0.20 g with a specific heat of c_p = 712 J/kg K [19]. Defining the properties of the interposer and support structure

is not as simple. Both of these parts consist of layers of multiple materials, with embedded interconnects, signal paths and also some surface mount components. The mass of each component was found using a balance scale, but the effective thermal capacitance of each is not known. The specific heat of the epoxy glass structure in both the interposer and support base is $c_p = 879$ J/kg K [20], but the percent of each structure which is other material such as copper, plastic, gold and stainless steel is unknown. The mass of the interposer structure on the P858ACY TTV is 7.608 g and the mass of the base structure is 8.17 g. It is assumed that half of the mass of each of these structures is copper and the other half is glass/epoxy. This results in an average specific heat of $c_p = 632$ J/kg K. The mass of the test socket is 125 g and is mostly polyethylene so the specific heat is taken as $c_p = 2090$ J/kgK [17].

By matching experimental data and simulation results, the values of the thermal resistances between layers can now be estimate. Figures 4-6 and 4-7 show experimental and simulation data for the Intel power profile scaled up to 93.2 W peak power and for a step power profile. As can be seen, the simulation and experimental data can be matched very well using this procedure. The results of matching the simulation and experimental provide the following values for thermal resistances:

1. R_T from die to IHS is 0.42 Kcm^2/W. This is very close to the target value of 0.40 Kcm^2/W as estimated by Intel for the thermal resistance between die and heat spreader.

2. R_T from die to interposer is 3.44 K/W while the resistance between the interposer and base structure is 2.92 K/W, and the resistance between the base structure and test socket is 1.04 K/W. This shows that the resistance from the die to the interposer/base structure assembly is an order of magnitude higher than from the die to the IHS.

3. The estimated $\overline{h}_c$ value is 1100 W/m^{2}K. This is lower than estimated from the correlation equation 6.1. This is due to two reasons. The assumed surface area in the simulation includes the side edges of the IHS where the convection value is known to be significantly less than on the impinging surface. Also this estimated value assumes that the temperature over the entire surface of the IHS is uniform, but the center temperature will actually be at a higher temperature than the edges. Both of these effects cause the simulation $\overline{h}_c$ value to be less than the calculated value.

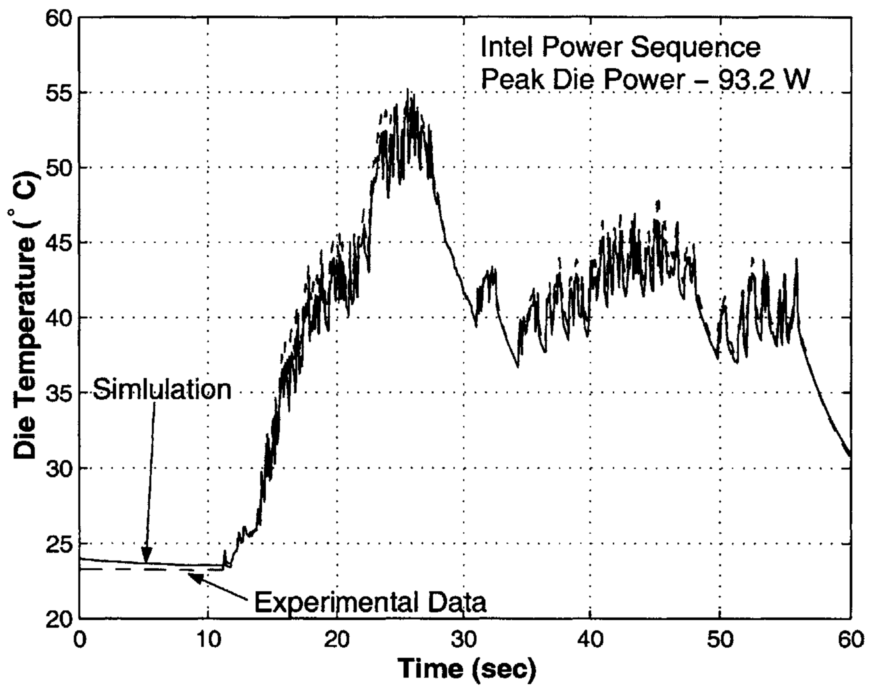

Figure 4-6: Experimental and simulation data for a P858ACY TTV subject to a 93.2 W Intel power profile.

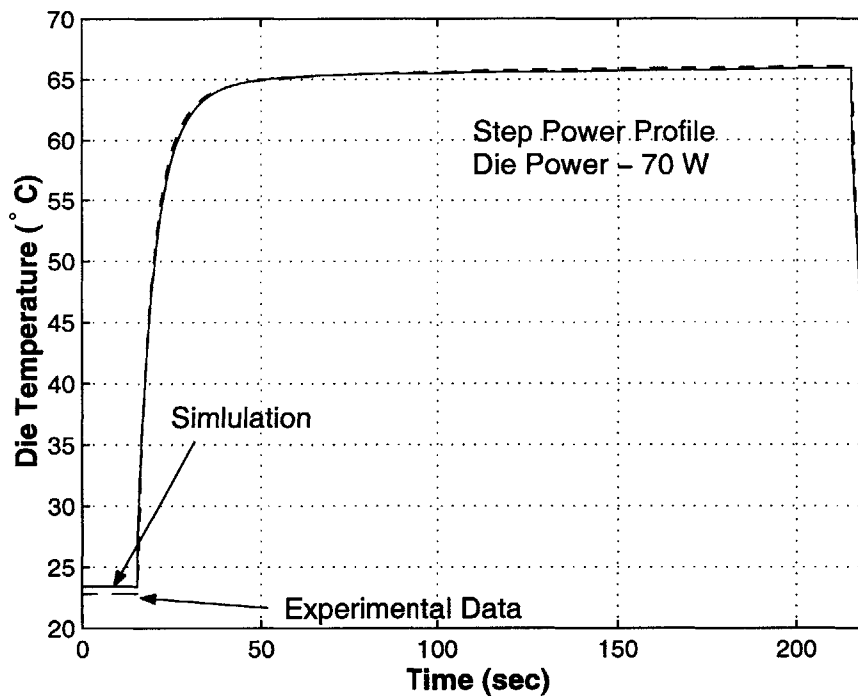

Figure 4-7: Experimental and simulation data for a P858ACY TTV subject to a 70 W step power profile.

There were a number of approximations that were made in building this simulation, all of which affect the accuracy of the results. All masses are assumed isothermal. This is the single largest source of error in the model. Clearly there is the potential for large gradients across both the heat spreader, and the interposer/base structure. While the problem with temperature variations across the heat spreader will be address in the next section where the model is adapted for use with the laser control method, the assumption of isothermal interposer/base structure will not be changed. The properties of these structures is not known (e.g. conductivity), and the two structures are attached to each other over multiple points. The edges of both structures are subject to convective transport, but the actual h_c values are not known. All these factors will contribute to the errors in using this simulation to evaluate the thermal resistances, but this method does provide a powerful and quick method to make order of magnitude estimates of the resistances within the devices, and even this order of magnitude estimate is better than the complete lack of available information without the simulation.

A similar type of analysis can be performed on the Pinetop TTV. The mass of the IHS is 9.22 g, the mass of the die is .05 g, and the mass of the base structure is 8.99 g. There is no interposer assembly on the Pinetop TTV so this layer is removed from the model. The results of matching the simulation to experimental data results in a thermal resistance between the die and base structure of 4.28 K/W and a resistance between the base structure and socket of 2.13 K/W. The resistance between the die and heat spreader is 0.42 Kcm^2/W. A plot of the matched simulation and experimental data is shown in Fig. 4-8.

4.5 System Model for Control of a Device Under Test

The device model developed so far is very useful for predicting the temperature response of the system based on an input to the die, but the model fails to accurately predict the temperature response of the system when both die power and control power are applied. The cause of this is the assumption that the integrated heat spreader is an isothermal mass. For a given control power, the model assumes all this power is evenly distributed over the IHS so the time response for a step change in control power is much slower than actual. In the actual case, the control power is

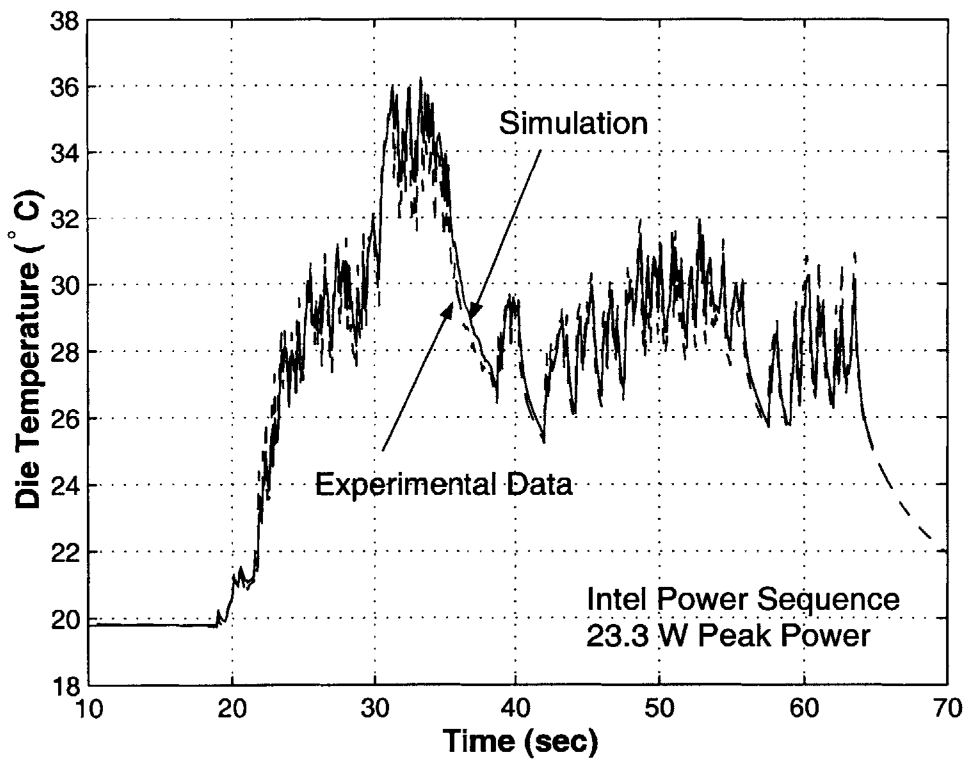

Figure 4-8: Experimental and simulation data for a Pinetop TTV subject to a 23.3 W Intel power profile.

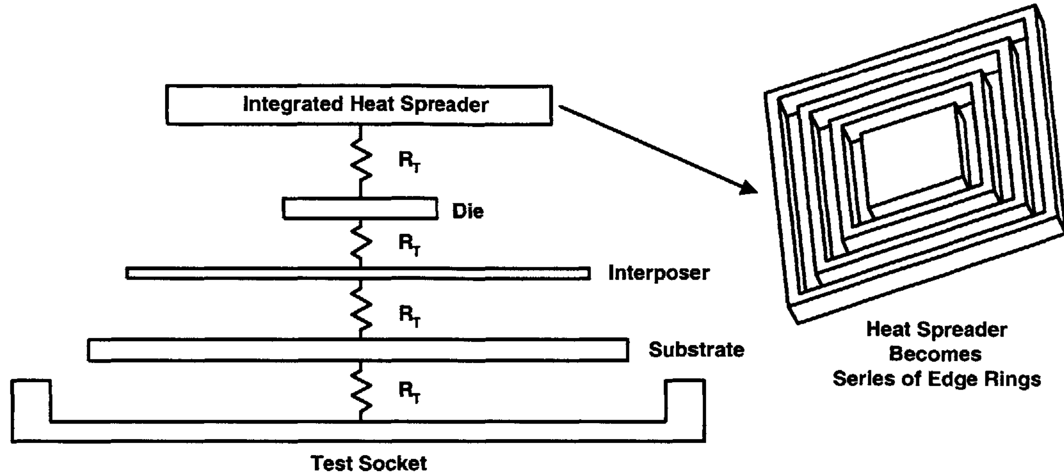

Figure 4-9: Physical model of system updated to include lateral conduction in the integrated heat spreader.

focused in a region directly above the die, which may be only 20-30% of the actual IHS surface area. The control power heats up this impingement section much faster than the rest of the IHS, with some conduction or leakage occurring to the surrounding material. The model developed up to this point is very useful for estimating the internal thermal resistances of the device, but needs to be updated in order to account for lateral conduction effects if the model is to predict the temperature response of the die to a control input.

This can be done by breaking the IHS into a series of edge rings, each of which is at a set temperature with a specified resistance between surrounding rings. A detailed view of this can be seen in Fig. 4-9. The conduction resistance between each segment has to be calculated. Since the system is symmetric, only one quarter of the system needs to be considered. The conduction resistance between any two segments in Fig. 4-10 can be calculated from [21].

$$R = \frac{1}{k} \int \frac{dx}{A_x} \tag{4.5}$$

where k is the conductivity and the integral is over the length from the center of one segment to the next segment. In this case, $A_x = 2 \cdot x \cdot b$ where b is the thickness of the heat spreader and the integral becomes

$$R_{1-2} = \frac{1}{2k} \ln \frac{x_2}{x_1} \tag{4.6}$$

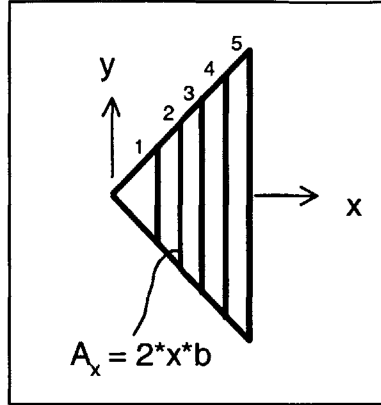

Figure 4-10: Diagram for calculation of conduction resistance between ring segments on the IHS.

for the resistance between any two segments. Since there are 4 segments to each ring and the resistances are in parallel, the total resistance is simply 1/4 this value, or $R_{1-2} = (1/8k) \cdot \ln(x_2/x_1)$.

A new set of linear differential equations can now be written in matrix form in the same way as eqn. 4.3, but with more components. The solution is straight forward and the results are very good predictions of the temperature response of the die for a given die and control input. Figure 4-11 shows experimental and simulation data for a Pinetop TTV device using this model. Figure 4-12 shows an expanded section of the simulation and experimental data. This model is very useful as it allows the simulation of test sequences that cannot currently be run on the prototype system. The prototype system is limited in power availability, but more importantly it is limited in the frequency at which the laser input can be controlled. The current control system is only capable of running about 10 commands a second, but much faster speeds are needed to test some of the more highly developed control sequences. This model provides a method for performing these simulations with a good confirmation that the baseline results are accurate at 10 Hz. Errors between the simulation and actual system will increase as the control frequency increases, but the model can still provide useful information and feedback.

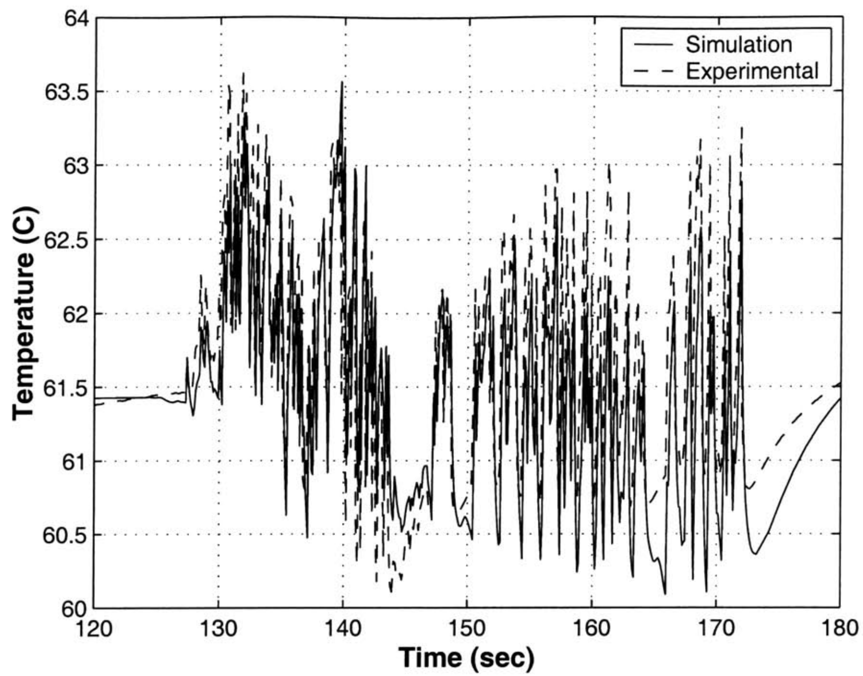

Figure 4-11: Experimental and simulation data for a Pinetop TTV device subject to the Intel test sequence.

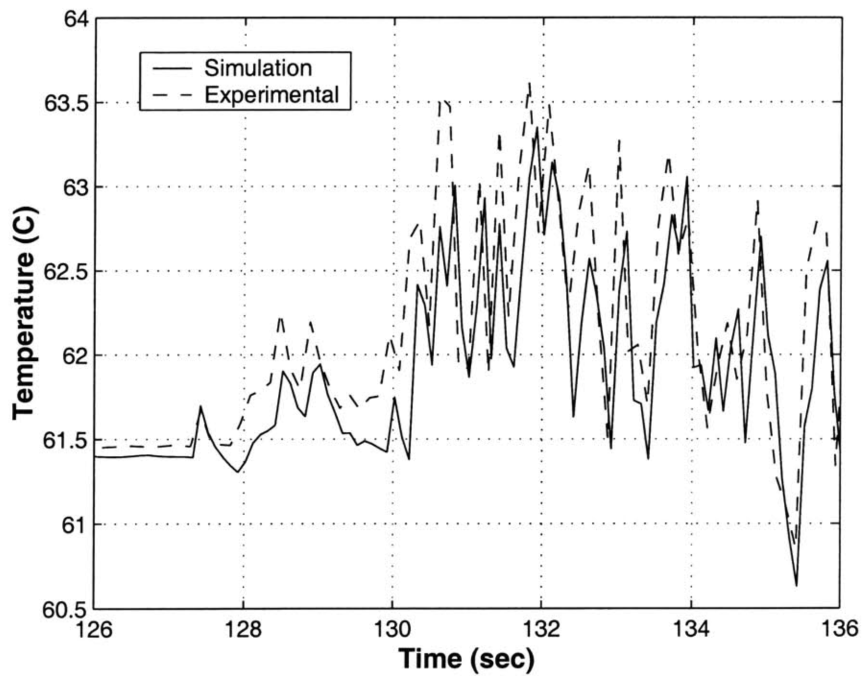

Figure 4-12: Expanded view of the data in Fig. 4-11.

Chapter 5

Laser/Convection Experimental Apparatus

This chapter describes the prototype laser/convection system that was assembled along with the data acquisition and control systems.

5.1 Laser/Convection System

The prototype system was design to operating around two Intel thermal test vehicles. The P858ACY thermal test vehicle is used for multi-die operation and higher power tests (up to 100 W total power) at lower power densities, and the Pinetop thermal test vehicle for lower total powers at higher densities. Both devices are connected to power supplies and data acquisition systems using clam-shell connection type burn-in sockets. The burn-in socket for each test vehicle is mounted on a black anodized aluminum base. The sockets are held in place using four 3.0 X 6M screws and are separated from the aluminum base using 2 mm thick teflon washers. This provides a level of thermal isolation between the socket and base structure. The aluminum base is supported using three leveling feet, about 5 cm high. This allows a space underneath the aluminum base where the wiring from the burn-in socket could be routed to external connections. Four threaded rods are mounted in the top of the aluminum base to provided the support structure for the nozzle cooling assembly.

5.1.1 Nozzle Cooling System

The jet impingement cooling system was assembled using PEEK[1] capillary tubing for the nozzles. The PEEK tubing is easily handled and cut, insulating, and semi-rigid, which makes the nozzles very resistant to accidental damage. The nozzle array geometry was optimized for maximum cooling performance with minimum pumping power based on a fixed nozzle diameter using eqn. 6.1. The nozzle I.D. is 1.07 mm, which yield an optimum nozzle to nozzle spacing of 4.2 mm in an orthogonal array. The nozzle array is constructed from modules. Each module was manufactured from copper with two main thru holes, one for air and one for water. Seven small holes were drilled through the base of each copper block into the main air channel for mounting the PEEK nozzles. The nozzles are mounted in the copper block using Loctite® 222 which is a removable liquid adhesive, making the removal and replacement of nozzles very easy. A figure of a single module is shown in Fig. 5-1 as well as 3 modules stacked together. These modules can be stacked together to form an array of nozzles 7 wide by any length. The array width can be reduced to less than 7 nozzles by removing the unnecessary nozzles and sealing the holes with aluminum tape. These modules are held together by threaded rods that pass through the two side holes in each module. Support mounts on either side clamp the modules together and provide a mounting base for attachment to the base structure. When clamped together, since the ends of each module are wider than the center section, a 3.05 mm slot is formed between each module. These slots provide spent air exits for the nozzle air and act as an access point for fiber optics and radiation sources. Copper tubing was silver soldered into the air and water channels on each end of each module. The end of each copper tube was fitted with a Swagelok® fitting to allow connection to distributed air and water systems. The actual number of nozzle used depended on which type of device was mounted in the test socket. For the P858ACY TTV, the nozzle array was reduce to a 5 by 5 array of nozzles, centered over the IHS. For the Pinetop TTV, the nozzle array was further reduced to a 3 by 3 array, center over the IHS. While more cooling capability was available, including being able to establish impingement cooling on the edges of the interposer/base structure and test socket, it was found that these limited arrays were more than capable of handling any thermal load generated in the prototype system.

Distribution manifolds were mounted on either side of the test assembly. Two

[1]Polyether Ether Ketone

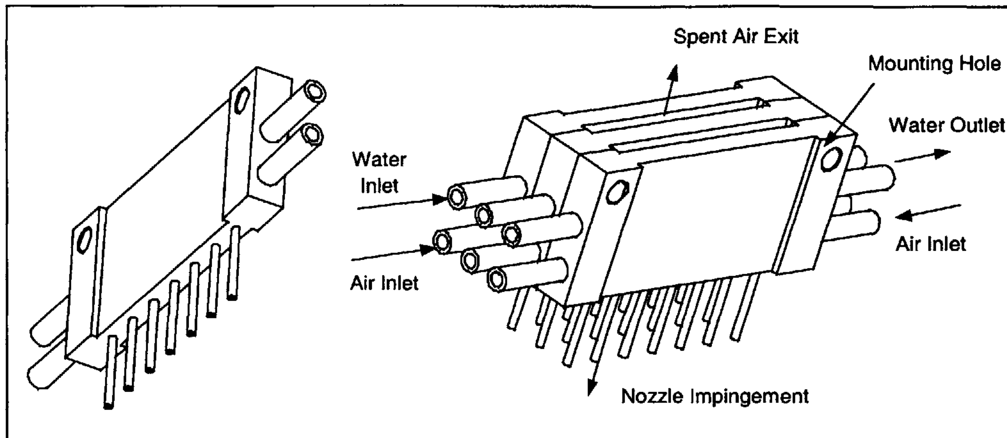

Figure 5-1: Single and stacked nozzle modules.

air supply manifolds were used, each supplying the air connections to one side of the copper modules using 1/4" polypropylene flexible lines. This allows air to be supplied to both sides of each module in order to reduce the pressure difference across a row of nozzles. The two air manifolds are connected to each other using 3/4" piping. One end of one manifold is connected to the air supply using 3/4" tubing, while the remaining end of the other manifold was used for mounting a pressure bulkhead for a T-type thermocouple which allows real time measurement of the manifold air temperature. The system operating pressure was measured from a line tap in the middle of the first manifold using a 0–103.4 kPa (0–15 psi) calibrated dial gauge pressure sensor. Compressed air was supplied from the laboratory air system. The air was filtered through a particle filter and dessicant air dryer before being passed through a pair of high flow air regulators. The lab air supply pressure varied from 827–1034 kPa (120–150 psi), and it was found that two regulators were required for holding the manifold pressure constant with the variations in up stream supply pressure. One regulator is rated for 68.9 to 551.6 kPa (20-80 psi) output pressure, while the secondary regulator is rated for 13.8-206.8 kPa (2-30 psi) output pressure. This combination of regulators allowed the manifold pressure to be held constant within ±344 kPa for a given flow configuration.

Two manifolds were also used for the water supply, but unlike the air system, one was used for the supply manifold and one was used for the drain line. The supply

manifold was connected back to the laboratory cold process water line through a particle filter and series of control valves. The drain manifold was connected to a floor drain in the test bay. The water channels in the copper modules were installed as contingency. The water lines are there to provide a method of cooling in the case where temperature variations in the copper module became important. Initial design calculations indicated that these channels would not be needed except in the case of very high device powers ($\sim 150 - 200$ W with low air velocities), but it was believed that it would be much easier to machine these features into the modules at the same time as all the other feature, rather than trying to rework the parts after the need arose. In the worst case, this simply provided more flexibility with a small amount of additional machining effort and cost. As it turned out, the water channels have never been used.

5.1.2 Lasers and Optics

Due to economic considerations, only a few wavelengths are available at which high power thermal radiation sources can be purchased. These sources are CO_2 lasers, Nd:YAG lasers, high output diode laser bars, and non-coherent sources (Tungsten lamps, QTH bulbs, arc-lamps). The last choice, non-coherent sources, are not really practical for application to thermal control of a device under test for a couple of reasons. The output from an IR bulb or arc-lamp is diffuse and must be concentrated on the target using large reflector assemblies, and even then it is very hard to focus the energy down to a point and still have room for mounting a nozzle assembly. IR bulbs also have slow response times[2]. Arc-lamps have very fast response times by changing the cycle rate, but these systems tend to be extremely noisy (RF noise) and will interfere with the electrical tests on the device under test. The only viable choices for this application at this time are collimated radiation sources (lasers).

For some types of devices, there is an obvious choice for optimal radiation source. Silicon, for example, is semi-transparent to wavelengths above 1 μm, but has a very high absorption coefficient below 1 μm. This makes a diode laser the obvious choice for heating exposed silicon devices. Table 5.1.2 summarizes basic reflectivity and absorption properties of common devices at available wavelengths. Desired values for the best performance are a very low reflectivity and an absorption coefficient that will distribute the energy absorbed over the entire encapsulating layer. In all

[2] A fast IR bulb typically has a 1-3 second settling time to reach 90% of steady state.

Table 5.1.2: Reflectivity and absorption coefficients for common device materials.

Material Type	Diode Laser 790 – 980 nm	Nd:YAG Laser 1.06 μm	CO_2 Laser 10.6 μm
Silicon [5]	$\rho \sim 0.3$ $\kappa \sim 10^4$ cm^{-1}	$\rho \sim 0.3$ $\kappa \sim 1.5$ cm^{-1}	$\rho \sim 0.2 - 0.7$ [a] $\kappa \sim 1.5$ cm^{-1}
Al_2O_3[b] [5]	$\rho \sim 0.8 - 0.9$ $\kappa \sim 0.009$ cm^{-1}	$\rho \sim 0.9 - 1.0$ $\kappa \sim 0.009$ cm^{-1}	$\rho \sim 0.1 - 0.15$ $\kappa \geq 100$ cm^{-1}
SiO_2[c] [5]	$\rho \sim 0.8 - 0.9$ $\kappa \sim 0.004$ cm^{-1}	$\rho \sim 0.9 - 0.95$ $\kappa \sim 0.004$ cm^{-1}	$\rho \sim 0.1 - 0.2$ $\kappa \geq 100$ cm^{-1}
Polyimide Plastics[d] [6]	$\rho \sim 0.2$ $\kappa \sim 10 - 20$ cm^{-1}	$\rho \sim 0.2$ $\kappa \sim 10 - 20$ cm^{-1}	$\rho \sim 0.1$ $\kappa \sim 300 - 700$ cm^{-1}
Ni coated Cu[e] [7]	$\rho \sim 0.6$ $\kappa \sim 10^5$ cm^{-1}	$\rho \sim 0.8$ $\kappa \sim 10^5$ cm^{-1}	$\rho \sim 0.95$ $\kappa \sim 10^5$ cm^{-1}

[a]Highly dependent on doping type and quantity.
[b]Crystalline.
[c]Fused.
[d]Representative values only. Actual values strong function of specific plastic composition.
[e]ρ values are a strong function of surface conditions.

situations, the propagation of the radiation through the encapsulant or substrate to the active components on the die must be avoided. If this happens, there is the potential for causing permanent damage to the device, or the radiation could interact with the device to generate photocurrents. These photocurrents will interfere with device operation and cause failure during the testing cycle. Either of these options (photocurrents or thermal damage) is undesirable and care is required to avoid this problem (i.e. limiting I_o values for thin or low absorbing layers).

Metals have very high absorption coefficients, but generally also have very high reflection losses making laser heating of large areas more difficult. Actual ρ values are strongly dependent on surface conditions and can vary by 40 – 50% for a given material. The energy that is not reflected is absorbed over a very small region near the surface. Other factors must also be considered in the selection of the radiation source. A high efficiency is desired to reduce the waste heat that must be removed. CO_2 and Nd:YAG lasers are both around 20% efficient, while diode lasers can be up to 35 – 40% efficient. Size, cost, and type of optics must also be considered in the final design.

The lasers selected for the prototype system were a pair of 60 W fiber optic coupled diode lasers from Spectra Physics Lasers. These lasers operated at 811 nm, and the power level could be controlled through an externally applied analog voltage. Each laser consists of two 30W diode bars that are connected to fiber optic bundles. The fiber bundle from each diode is routed to a fiber optic splice and from there into an optical connector with an SMA-905 type output connection for linking up to a fiber optic pigtail. Typical losses in the SMA type connector are ~ 1.0 dB. The fiber optic pigtails used are 1000 μm diameter pure silica core fibers, 3.5 m in length with a 1400 μm coating diameter[3]. Power pigtails were used for final power delivery to allow for flexibility in laser placement due to pigtail length, and more importantly, as a means of protecting the fiber optics on the laser units. If a fiber pigtail is damaged in handling or operation, the fiber was simply removed and replaced with a new unit[4]. If the fiber optics on the laser unit were damaged, the whole system would have to be returned to the manufacturer for repair and replacement.

The fiber pigtails used were of two primary types. One type had a cleaved tip end and the other had a full radius tip. The cleaved tip fiber produced an output beam divergence of 12° included angle. The radius tip fiber produced a $170 - 180°$ beam divergence resulting in a much expanded illumination pattern, but the resulting beam was so divergent that it was impossible to limit the illumination spot to the surface of the device only, so losses were very high.

The objective in the design is to minimize the number of optical components and interfaces. The fiber pigtails are a required item, but all other components were avoided for efficiency reasons. The total laser power in the system is very high and losses incurred through use of additional optics must be avoided at all costs. Optics are available with low reflectivity coatings, but at the chosen wavelength, these optics are non-standard and very expensive. Furthermore, additional optics require mounts, focusing and cleaning in order to keep losses to a minimum. The system is designed with consideration for the manufacturing environment. The test head where this system is designed to be mounted is subject to vibrations and possibly high shock loads as devices are loaded and unloaded from the test socket. Keeping precise focus on optics mounted in this region would be very hard and a major problem in obtaining long term reliability goals. These design requirements result in low cost fiber optic pigtails being the optimal solution for illuminating the surface of the device under

[3]Power pigtails are a standard off the shelf components from Newport Optics

[4]Approximate cost - $100/unit.

test.

Laser output is controlled by a 0-5V analog output generated in a control module in the DAQ system. Each laser can be individually controlled. Details of the control system are covered in the control section of this chapter.

5.1.3 System Assembly

The nozzle assembly is supported on four threaded rods that are mounted in the aluminum base. Two support plates are mounted on either side of the nozzle assembly. These plates provide mounting points for fiber optics support stands. These fiber optic clamps allow two fibers to be run through the slots of the nozzle modules. Either fiber can be positioned in any slot, either vertically or at an angle. This allows a great deal of flexibility in positioning the fiber optics over the test socket. Moving each fiber closer to the device surface reduces the size of the illumination spot. The maximum spot size is limited by how far the end of the fiber can be positioned from the surface. If the fiber is pulled back too far, either the laser beam will intersect with the end of the nozzles or the beam will be shielded by the side of the nozzle modules. The design becomes a trade off between small nozzle spacing in order to obtain maximum convective cooling performance and large laser illumination spot size. A schematic drawing of the assembled system is shown in Fig. 5-2

5.2 Data Acquisition System

The data acquisition system is based around an Agilent HP34970A data acquisition/DMM system. The unit has three module slots that can handle a wide range of data acquisition/control modules. Two slots are used for data acquisition and the third slot is used for a control module and will be discussed in the next section. The two data acquisition slots are filled with 20 channel multiplexer[5] units used for temperature measurements.

The data channels that have to be monitored consist of temperature measurements from the RTD's mounted on the die structure of each thermal test vehicle. The P848ACY die has 26 RTD's on the die, only 13 of which are routed to external pins and the DAQ system. Each RTD is a four wire system with a nominal 900 Ω resistance. The Pinetop TTV has 12 RTD's on the die structure with 10 routed to

[5]Agilent HP34901A 20-Channel Armature Mutliplexer Units

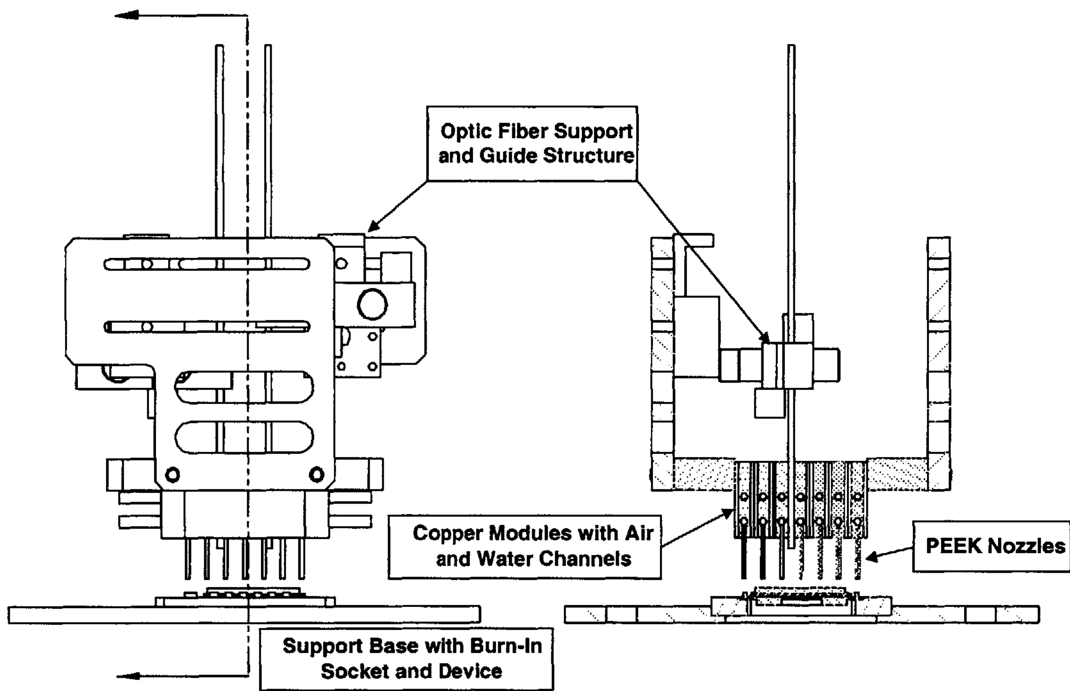

Figure 5-2: Side view and cross sectional view of assembled laser/convection system. Manifold system and base support structure not shown.

external pin connections and the DAQ system for four wire resistance measurement. Nominal resistance for each RTD is either 195 Ω or 50 Ω depending on the position of the sensor.

Each routed RTD is connected for 4 wire measurement of the resistance. Each four wire measurement requires two channels in the multiplexer module, so 10 channels can be routed through either module. The remaining channels are available for monitoring of thermocouples. Each multiplexer module has a built in cold-junction reference accurate to 0.8°C [22] and repeatable to 0.1°C. To reduce measurement error, all thermocouples are connected to the same multiplexer module. Four wire resistance measurements are accurate to .007% of full scale (10 kΩ full scale).

5.3 Power Supply and Control System

The thermal test vehicles are connected to an Agilent 6627A 4 channel DC power supply. Each channel is capable of producing 40 W at a peak voltage of 50 V at 0.8 A[23]. The actual wiring depends on which TTV is being run and under which configuration. The Pinetop TTV has a single configuration where two of the DC output channels are slaved together. This provides 1.6 A of current at a common voltage to the single die heater. The voltage is set in the power supply control input, and remote sensing lines are used for control to account for line resistance between the power supply and pin connections on the test socket.

The P858ACY TTV has two configurations. In the common configuration, DC supply channels 1 and 2 are slaved together and channels 3 and 4 are slaved together. One of these outputs is connected to die heaters 2 and 3 that are in parallel, while the other output channel is connected to die heaters 1 and 4 in parallel. This configuration allows for uniform high power dissipation in the die at total power levels up to 140 W. The other configuration the P858ACY TTV is for each die to be connected to a single DC output channel. This allows for varying power dissipation across the die structure, but with different peak power levels on each die. Again, the line voltage is specified and sensing lines are used to compensate for line resistance between the power supply and the test socket connections.

System control is based on a GPIB[6] interfaced computer system. This systems operates under HP-VEE control architecture and provides local control of the DAQ,

[6] General Purpose Interface Bus

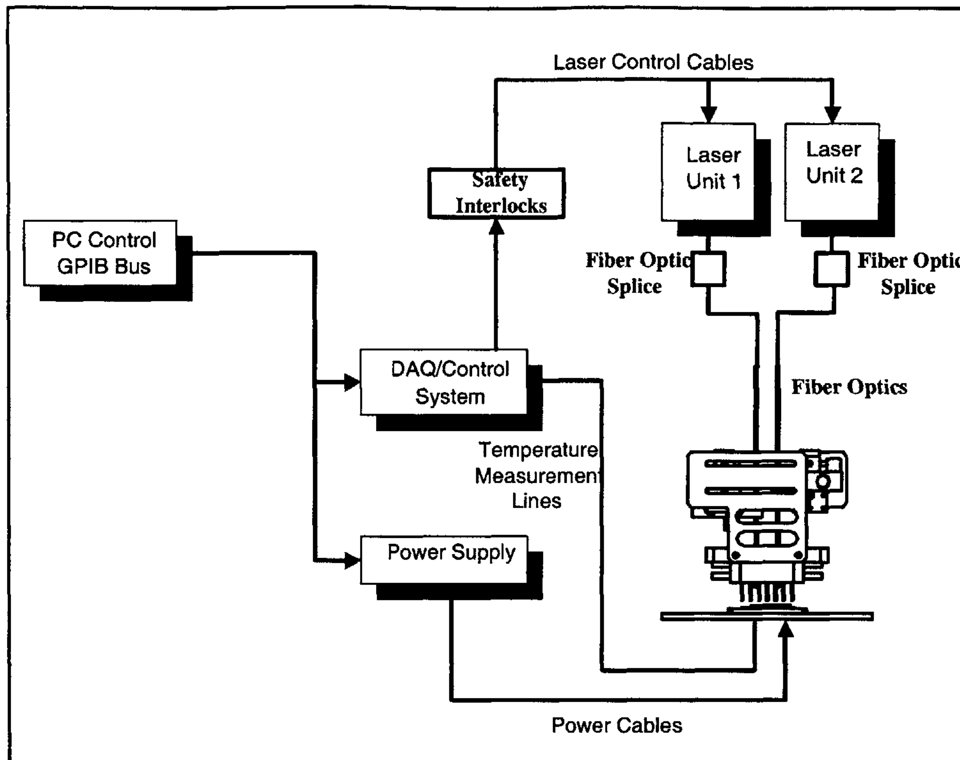

Figure 5-3: Schematic diagram of control and data acquisition system for laser/convection prototype system.

power supply, and laser systems. The control program has built in safety interlocks for the laser system. The power supply and DAQ system are connected to the controlling computer using daisy-chained GPIB interface cables. A general schematic drawing of the control and DAQ system is shown in Fig. 5-3.

5.4 Calibration and Test Procedures

This section describes the calibration procedures, operational procedures and limits of the system.

5.4.1 TTV Calibration

The thermal test vehicles must be calibrated for temperature measurement and for thin film resistance. The RTD's on both TTV's are non-standard and must be calibrated. This is done by measuring the resistance of each RTD at two reference

temperatures. The two reference temperatures used for calibration are room temperature and a hot temperature close to the expected maximum operating temperature of the system[7]. In order to reduce the error in the calibration measurement, an insulated chamber was constructed that the entire base, socket and device could be place in. This chamber was completely sealed from outside air for room temperature calibration points. The system was allowed to reach equilibrium overnight in a sealed room with all sources of air movement turned off. The next morning, resistance readings from each RTD were taken at a rate of 1 per second over 15 minutes. These resistance values for each channel were averaged and used for the room temperature data point. Four T type thermocouples were also mounted in the chamber to provide the reference room temperature.

The high temperature reference point was obtained by connecting the sealed chamber to an air forcing unit. The unit was capable of providing air at a constant high temperature within ±0.5°C. A small vent hole was opened up on the chamber, and the whole system was turned on and allowed to run for 6-8 hours to reach equilibrium. At this point, resistance and temperature measurements were taken over a 15 minute period and averaged values were used as the high temperature calibration point[8]. The two data points were then used to generate a scaling and offset value for each RTD on a given TTV assembly. This data for each TTV was used to generate a calibration file that is loaded each time the TTV in the test socket is changed. This file is written to the DAQ system where the resistance measurements are automatically converted into temperature measurements before being stored in memory.

Along with calibrating the resistance of the RTD's on each die, the resistance of each thin film heater on each die has to be calibrated. The power supply is capable of being voltage or current driven, but not power level driven. The resistance of each thin film heater could change quite a bit over the temperature range of interest, so knowledge of the film resistance is required if the level of power dissipation is to be known to any level of accuracy. In the same manner and at the same time as RTD resistances, the resistance of each thin film heater was measured at two reference

[7]The peak operating temperature at all tests was around 85°C. This temperature was deliberately kept lower than the maximum rating of the individual components for system reliability issues. The tests sockets represent a massive expenditure of time and resources, and reducing the peak temperatures reduced the risk of system damage. Hook-up wiring was rated to 105°C and no rating was available for the test sockets, so a conservative maximum test temperature of 85°C was chosen.

[8]The actual high temperature point varied over the range of devices due to external losses. The range varied from 70 to 75°C with an air forcing temperature of 85°C.

temperature points to obtain calibration information on the variation of die resistance with temperature. This information was used to generate a voltage driving file for a specified die temperature and power profile. This causes some error, especially in the case where no temperature control is used and the die temperature can vary by 20°C to 30°C over the test sequence. In the case where the temperature is controlled and the temperature only varies by 2°C to 3°C, the error in device power is substantially reduced. Real time measurement of the device power was not possible due to the high currents and limited DAQ channel availability.

TTV Temperature Measurement Accuracy

The accuracy of temperature measurement on the TTV die structures is a function of a number of factors. Since the measurement of interest is temperature change, absolute errors in temperature will be neglected. The rms error in temperature change will be a function of the following:

- Resolution and accuracy of resistance measurement.
- Accuracy of calibration files.

For an individual channel, the temperature is given by

$$T = m \cdot R_M + b \tag{5.1}$$

where R_M is the measured resistance, m is the slope from the calibration and b is the calibration intercept. The error in the temperature can be calculated from [24]

$$\frac{\partial T}{T} = \sqrt{\left(\frac{\partial b}{b} + \frac{\partial m}{m}\right)^2 + \left(\frac{\partial R_m}{R_M}\right)^2} \tag{5.2}$$

where the errors in the slope and intercept have to be determined from the calibration procedure.

The slope and intercept for each channel is determined from two reference points where

$$m = \frac{T_{R2} - T_{R1}}{R_2 - R_1} \tag{5.3}$$

and

$$b = T_{R1} - R_1 \cdot m \tag{5.4}$$

where T_{R1} and T_{R2} are the two temperature reference points and R_1 and R_2 are the corresponding resistance measurements. The error in m can be written as

$$\frac{\partial m}{m} = \sqrt{\left(\frac{\partial T_{R2} + \partial T_{R1}}{T_{R2} - T_{R1}}\right)^2 + \left(\frac{\partial R_2 + \partial R_1}{R_2 - R_1}\right)^2} \tag{5.5}$$

and the error in b can be written as

$$\partial b = \partial T_{R1} + R_1 \cdot m \left(\frac{\partial m}{m} + \frac{\partial R_1}{R_1}\right) \tag{5.6}$$

so now all errors can be expressed in terms of errors in the reference temperatures and resistances. Since multiple readings[9] were used to determine the reference temperatures and resistances, the errors in the measurements can be expressed as twice the standard deviation of the mean [24] of the measured value.

The actual error for each channel will depend on the specific calibration data. Rather than trying to present all the data for all the temperature sensors on all the devices, a typical channel will be considered. Using calibration data for a Pinetop TTV, the errors in calibration temperatures and resistances are

$$\partial T_{R2} = 2\sigma_{\overline{T}_{R2}} = 0.00098°\text{C} \qquad T_{R2} = 71.68°\text{C} \tag{5.7}$$

$$\partial T_{R1} = 2\sigma_{\overline{T}_{R1}} = 0.000022°\text{C} \qquad T_{R1} = 22.51°\text{C} \tag{5.8}$$

$$\partial R_2 = 2\sigma_{\overline{R}_2} = 0.00071\ \Omega \qquad R_2 = 220.78\ \Omega \tag{5.9}$$

$$\partial R_1 = 2\sigma_{\overline{R}_1} = 0.00027\ \Omega \qquad R_1 = 187.30\ \Omega \tag{5.10}$$

so the errors in the slope and intercept can be calculated as

$$m = 1.468 \qquad \frac{\delta m}{m} = 3.566 \times 10^{-5} \tag{5.11}$$

$$b = -252.45 \qquad \frac{|\delta b|}{b} = 0.006899 \tag{5.12}$$

[9] 900–1000 readings per channel.

Now the error in the temperature measurement can be found. Using the published data on the DAQ system accuracy for a single resistance measurement as $\partial R_m / R_M = 0.00007$, the temperature error becomes

$$\frac{\partial T}{T} = \sqrt{(6.899 \times 10^{-3} + 3.566 \times 10^{-5})^2 + 0.00007^2} = 8.465 \times 10^{-5} \tag{5.13}$$

so at a high temperature of 85°C, the error in the temperature from resistance measurement and calibration would be 0.01°C which is in line with typically cited measurement accuracy for commercially available RTD assemblies.

TTV Power Accuracy

The error in the power profile can be calculated in a similar manner, but there is the additional complication that the error is greater for larger temperature deviations (i.e., test runs where temperature control in not used or is not effective). In a similar manner to the RTD resistance, calibration values can be obtained for the resistances of the thin film heaters. This resistance is a function of temperature with resistance increasing with increasing temperature. At the same time as the RTD's resistances, the resistance values of the thin film heaters were measured. The goal is to find the slope and intercept of an equation such that the resistance is known as a function of temperature.

$$R_f = m_r \cdot T + R_0 \tag{5.14}$$

The error in m_r and R_0 can be found using standard propagation of error methods.

$$\frac{\partial m_r}{m_r} = \sqrt{\left(\frac{\partial T_{R2} + \partial T_{R1}}{T_{R2} - T_{R1}}\right)^2 + \left(\frac{\partial R_1 + \partial R_2}{R_2 - R_1}\right)^2} \tag{5.15}$$

$$\partial R_0 = \partial R_1 + m_r \cdot T_{R1} \left(\frac{\partial m_r}{m_r} + \frac{\partial T_{R1}}{T_{R1}}\right) \tag{5.16}$$

The error in the resistance at temperature T becomes

$$\frac{\partial R_f}{R_f} = \frac{\partial R_0}{R_0} + \sqrt{\left(\frac{\partial m_r}{m_r}\right)^2 + \left(\frac{\partial T}{T}\right)^2} \tag{5.17}$$

The power in the device is given by

$$P_{TTV} = I \cdot V_{die} = \frac{V_{die}^2}{R_f} \tag{5.18}$$

where V_{die} is the die voltage and is specified by the power supply driving function. This value is known to an accuracy of 50 mV [23].

The error in the temperature is the largest source of error in the calculation of the device power because of the effect on the die resistance. While the calibration for the resistance may be fairly good, the actual operating temperature is not generally known until after a couple of runs have been made, and then only to within 2°C. The problem really arises when making data runs with no form of temperature control, where the temperature can vary by 20°C to 30°C over the run. The system has to be configured for a power profile at a certain die temperature and while this is possible with a small amount of iteration during temperature controlled tests, the power dissipated in uncontrolled tests can have a high error compared with the desired 'ideal' power profile. As an example, for one of the Pinetop TTV's, the die resistance at 22.5°C is 22.52 Ω while the resistance at 71.7°C is 26.10 Ω. This results in a slope of $m_r = 0.073$ Ω/°C and an intercept of 20.88 Ω. The resulting errors are $\partial m_r/m_r = 0.01$ and $\partial R_0/R_0 = 0.00086$. If it is assumed that the error in the die temperature is 2°C at $T = 40$°C, then the error in R_f becomes

$$\frac{\partial R_f}{R_f} = 0.01 + \sqrt{0.01^2 + 0.05^2} = 0.061 \tag{5.19}$$

and the error in the die power becomes

$$\frac{\partial P_{TTV}}{P_{TTV}} = \sqrt{\left(2\frac{\partial V_{die}}{V_{die}}\right)^2 + \left(\frac{\partial R_f}{R_f}\right)^2} = 0.061 \tag{5.20}$$

If the temperature error becomes 10°C, then $\partial R_f/R_f = .26$ and the power error become $\partial P_{TTV}/P_{TTV} = 0.26$ or 26% error. This term is dominated by the uncertainty in die temperature when setting up the driving file for the power supply. Fortunately this error is much smaller ($\sim$ 6%) when temperature control is exerted.

5.4.2 Test Procedures

As stated earlier, the entire system is run from a single PC operating under the HP-VEE architecture. Tests are run from a graphical user interface where all parameters are established before a test begins. General procedure is as follows:

1. Set-up all DAQ parameters. The channels to be monitored, sampling rate, test duration are all set on the user interface.
2. Select driving files for power supply and laser systems. The files selected for controlling the power supply output and laser system outputs are constructed before the test and written to the disk drive on the control system.
3. Turn air supply on and seal the test facility. This engages the safety interlocks on the laser systems and allows them to power up in standby mode. Lasers are allowed to warm up for at least 30 seconds before the test is started.
4. Start test sequence. The computer puts the laser systems into ready mode and writes the data acquisition program to the DAQ system. The computer must receive input confirmation from the user before laser emission is allowed.
5. Once the test sequence is started, the controlling computer writes voltage and laser output values to the appropriate system. The DAQ program runs in stand alone mode once started and all data is stored in the DAQ for retrieval at a later time. The maximum rate that commands can be written to the GPIB bus is at 10 signals per second[10].
6. Once the test sequence is complete, the control computer automatically retrieves the test data from the DAQ system and writes the information to a data file. Real time monitoring of the die temperature is not possible without significantly restricting the rate at which control signals can be sent to the lasers and power supply.
7. After the test, the system is shut down and laser safety interlocks are disengaged and the air supply is turned off.

This is the general test sequence used on all data runs. Due to the high power lasers used in this equipment, all tests were always run from a remote terminal.

[10]Ten full command sequences per second. A command sequence consists of control data for the power supply and both lasers.

Chapter 6

Convective Cooling

In order to maximize the effectiveness of combined convection/radiation temperature control and to extend the operating range of the whole system, high performance convective cooling is required.

6.1 Convective Cooling Theory

In order to dissipate the thermal load of a device under test, the convective heat transfer needs to be as high as possible. The working fluid is restricted to gases, and is further restricted to air or N_2 due to commercial plant equipment limitations and cost considerations. The basic equation for heat transfer from a device is simply $Q = \overline{h_c} A \Delta T$. To increase the total heat transfer Q, we can increase average convective heat transfer coefficient $\overline{h_c}$ and the available temperature defect ΔT, but not A since the exposed surface area is fixed for a given device. Increasing the heat transfer by increasing the temperature defect ΔT is an option, but there are practical limits to this method. If the required ΔT is too large, expensive air chillers may be required. Also as ΔT is increased, since T_{hot} is specified, T_{cold} might be depressed to the point where condensation and frost formation within the system becomes a problem. Therefore the best way to increase Q is to maximize the convective transfer coefficient $\overline{h_c}$. There are two primary methods to doing this. One method is with high velocity cross-flow cooling, the other is with impingement cooling.

For the small sizes typical of electronic devices (3 cm x 3 cm at the largest), cross-flow cooling[1] can produce $\overline{h_c}$ values on the order of 500 W/m^2 K for Mach numbers

[1] Calculation based on fully turbulent flow over entire width of device.

less than around 0.5 [17]. At flow speeds greater than $M = 0.5$, noise generation of the system becomes excessive [25]. The small scale of devices and the need for some type of device retainer can make cross flow cooling very hard to implement, and cross-flow cooling tends to produce non-uniform cooling across the surface of the device. For this reason, and because initial calculations demonstrate h_c values 2-3 times greater are possible with impingement cooling, the decision was made to focus the research on impingement cooling.

Gas impingement heat transfer has been studied fairly extensively. Martin [26] has compiled an extensive summary of the work done on gas impingement cooling. A well established correlation for an array of round nozzles impinging on an flat plate yields

$$\frac{\overline{\mathrm{Nu}}}{\mathrm{Pr}^{.42}} = \left[1 + \left(\frac{H/D}{.6/\sqrt{f}}\right)^6\right]^{-.05} \sqrt{f}\frac{1 - 2.2\sqrt{f}}{1 + .2\,(H/D - 6)\,\sqrt{f}}\mathrm{Re}_D^{\frac{2}{3}} \tag{6.1}$$

where $\overline{\mathrm{Nu}} = \overline{h_c}D/k_a$ is the average Nusselt number, Pr is the Prandlt number, H is the nozzle to plate spacing, D is the nozzle diameter, and k_a is the conductivity of the air. The geometric factor, f, is calculated from

$$f = \frac{\pi}{4}\left(\frac{D}{L_t}\right)^2 \tag{6.2}$$

for an orthogonal array with nozzle to nozzle spacing of L_t and

$$f = \frac{\pi}{2\sqrt{3}}\left(\frac{D}{L_D}\right)^2 \tag{6.3}$$

for a hexagonal array of nozzles with spacing L_D. This correlation is valid under the following conditions:

$$2000 \leq \mathrm{Re_D} \leq 100000 \tag{6.4}$$

$$0.004 \leq f \leq 0.04 \tag{6.5}$$

$$2 \leq \frac{H}{D} \leq 12 \tag{6.6}$$

For parameters outside this range, then the solution for the Nusselt number becomes a function of three parameters. The equation for the Nusselt number is

$$\frac{\overline{\mathrm{Nu}}}{\mathrm{Pr}^{.42}} = K_A\left(H/D, f\right) \cdot G\left(H/D, f\right) \cdot F\left(\mathrm{Re_D}\right) \tag{6.7}$$

where the parameters are given by the following set of equations:

$$2000 < \mathrm{Re_D} < 30000 \qquad F(\mathrm{Re_D}) = 1.36 \cdot \mathrm{Re_D}^{0.574} \tag{6.8}$$

$$30000 < \mathrm{Re_D} < 120000 \qquad F(\mathrm{Re_D}) = 0.54 \cdot \mathrm{Re_D}^{0.667} \tag{6.9}$$

$$1200000 < \mathrm{Re_D} < 400000 \qquad F(\mathrm{Re_D}) = 0.151 \cdot \mathrm{Re_D}^{0.775} \tag{6.10}$$

$$K_A\left(\frac{H/D}{0.6/\sqrt{f}}\right) = \begin{bmatrix} 1 & \text{for } \frac{\mathrm{H/D}}{0.6/\sqrt{\mathrm{f}}} < 1 \\ \left(\frac{H/D}{0.6/\sqrt{f}}\right)^{-0.3} & \text{for } \frac{\mathrm{H/D}}{0.6/\sqrt{\mathrm{f}}} \geq 1 \end{bmatrix} \tag{6.11}$$

$$G(f, H/D) = 2\sqrt{f}\frac{1 - 2.2\sqrt{f}}{1 + 0.2(H/D - 6)\sqrt{f}} \tag{6.12}$$

Eqn. 6.1 can be optimized for a given pumping power, defined as

$$P.P. = \Delta P\dot{V}/A_{\mathrm{plate}} \tag{6.13}$$

where ΔP is the pressure drop, $\dot{V}$ is the volumetric flow rate, and A_{plate} is the area of the target plate. For optimization based on a fixed nozzle to plate spacing of H, maximum $\overline{\mathrm{Nu}}$ can be obtained by setting $H/D = 5.6$ and $H/L_t = 1.432$. Based on this correlation, $\overline{h_c}$ values on the order of 1200 W/m^{2}K to 1500 W/m^{2}K can be easily obtained for $M < 0.5$.

6.2 Convective Cooling Experimental Prototype

The correlation presented in eqn. 6.1 is for impingement on an infinite flat plate, but actual operating conditions for cooling of electronic devices differ from this. Devices under test have exposed side edges, and must be retained by some type of holder which will restrict the nozzle flow. This holder will also provide an additional conduction path for heat transfer from the device. In order to evaluate these effects, a test apparatus was designed and built (Fig. 6-1). The test rig was designed to test impingement cooling over various side edge configurations, for comparison of device holders made from different materials, and for comparison to heat transfer without a holder present. A schematic drawing of the entire system is shown in Fig. 6-2. The test rig was constructed around a thin film heater placed between a copper block and a low conductivity pedestal. By accurately measuring the voltage and current applied to the thin film heater, the total power dissipated could be calculated. All

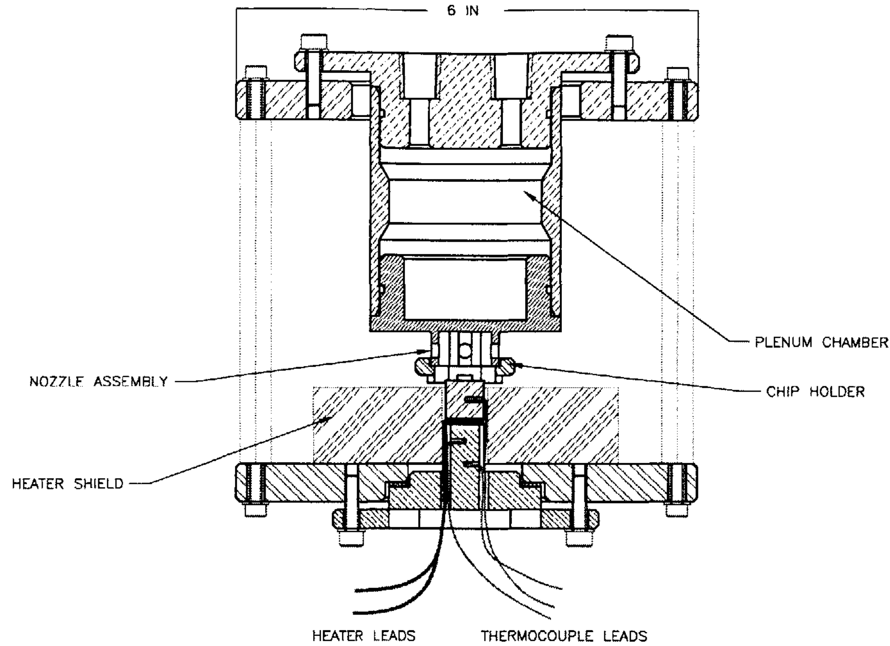

Figure 6-1: Test apparatus for measuring convective transfer coefficients on a simulated electronic device.

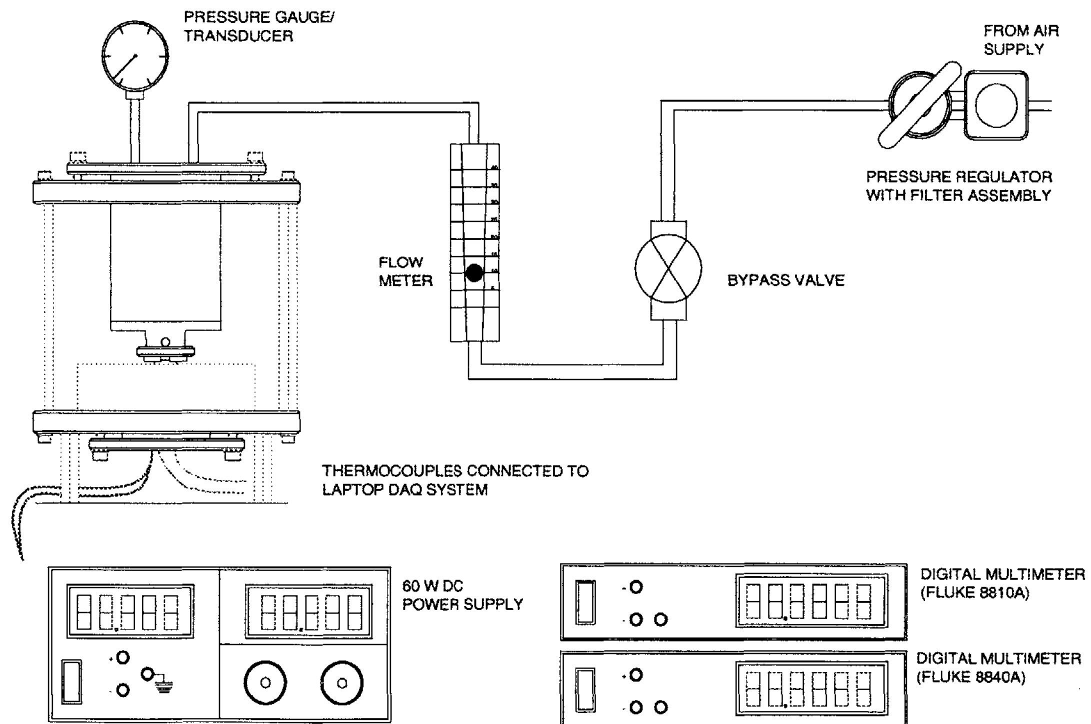

Figure 6-2: Schematic drawing of nozzle test system.

of this energy is either conducted through the copper block which is subjected to convection on the surface, or through the low conductivity pedestal. By sensing the temperature at two places on the pedestal, the flux through the mount can be calculated. The pedestal is constructed from PEEK[2] plastic, which is a high temperature, low conductivity[3] material. Low conductivity reduces the energy loss through the pedestal, but also reduces the error in measurement of the flux through the pedestal. For a given flux, the temperature drop through a low conductivity material will be greater than for a high conductivity material. Since there is a fixed, finite error in the T-type thermocouples used, the larger the temperature difference that is measured, the smaller the percent error in ΔT, and the more accurate the measurement of the total flux.

The entire pedestal, heater, copper block assembly is surrounded by a block of low conductivity plastic with a 1 mm gap between the edges of the pedestal/heater assembly and the surrounding plastic block. This small gap prevents conduction losses directly from the pedestal/copper block into the surrounding plastic, and the small aspect ratio of the gap prevents natural convection cells from forming. This leaves the only form of loss as conduction through the small air gap, which can be easily calculated from the basic conduction law. The top of this gap is sealed using 0.02 mm thick Kapton tape that seals against the edge of the copper block and surrounding block of plastic. This tape prevents the air jets from producing any air circulation in the narrow gap and the small cross sectional area of the tape combined with the very low conductivity of Kapton produces almost no conduction losses through the tape[4]. A detailed view of the heater/pedestal/copper block assembly can be seen in Fig. 6-3. This figure also shows the assembly with and without a holder present. The entire heater/pedestal assembly can be moved in and out to expose more or less of the side edge of the carrier.

The device holder was designed to simulate a holding/aligning fixture that is required under actual device testing conditions. The holder contacts the copper block over 1 mm^2 contact points on each corner. Three holders were manufactured to identical dimensions, but out of three different materials. One was made from PEEK (k = 0.2 W/m^{2}K), one from 316 stainless steel (k = 15 W/m^{2}K), and one from

[2]Polyether Ether Ketone

[3]k=0.2 W/m K

[4]The calculated conduction heat transfer through the tape under the worst conditions is an order of magnitude less than the measured error in the thin film heater energy dissipation.

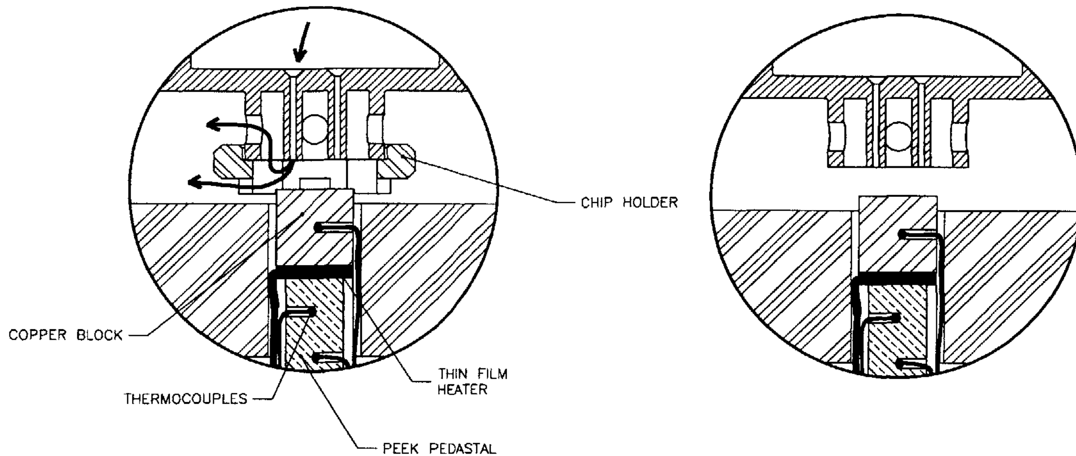

Figure 6-3: Detailed view of the heater section of the nozzle test assembly. Views are shown with and without a device holder.

copper ($k = 385$ W/m^{2}K) so a wide range of holder conductivities could be tested.

The nozzle system consists of 4 nozzles with a 1.01 mm internal diameter and 10 mm long. The nozzles are spaced 3.95 mm apart in a square array. The nozzles are surrounded by a ring of aluminum with holes in it. This ring is present to protect the nozzles from damage and the holes allow spent air to escape. The thin film heater is sandwiched between the copper block and PEEK pedestal. A small amount of silicon thermal paste is used on the heater in order to reduce the thermal resistance between the heater and copper block. Two T-type 30 AWG thermocouples are mounted 1.0 cm apart in the PEEK pedestal. The temperature measurements from these thermocouples can be used to calculate the flux through the pedestal. A single T-type thermocouple is mounted in the center of the copper block. The total power dissipated in the heater is calculated by measuring the applied voltage and current. Since the amount of power being conducted down through the pedestal is known, the remaining power must be conducted through the copper block and into the air stream.

A known supply pressure is applied to the plenum chamber and the air temperature is measured just above the nozzle entrances using a K-Type thermocouple probe. The mass flow of air is calculated using a rotameter. All temperature measurements are taken using a PCMCIA DAQ card in a laptop computer. The system can handle up to six temperature channels and has built in cold junction reference. All tests were run under steady state conditions, after all transient effects had died out.

The average convective heat transfer coefficient could be calculated by measuring the copper block temperature, air temperature, and total convective flux. The $\overline{h_c}$ value is calculated from

$$\overline{h_c} = \frac{Q_{cu}}{A_s \left(T_{cu} - T_{\text{air}} \right)} \tag{6.14}$$

where Q_{cu} is simply the difference between the heater power and pedestal flux. The pedestal flux is calculated from simple conduction and is given by

$$Q_{\text{pedestal}} = \frac{k_{\text{PEEK}} \cdot A_{\text{ped}}}{L_{TC}} \left(T_{UT} - T_{LC} \right) \tag{6.15}$$

where A_{ped} is the cross sectional area of the pedestal, L_{TC} is the distance between the thermocouples, and T_{UT} and T_{LC} are the temperature readings on the upper and lower thermocouples respectively.

The copper block temperature must be corrected to account for flux through the block itself. The temperature is measured in the middle of the block, but the temperature of interest to measure the convective coefficient is at the surface of the block. This difference is very small at low power levels and the error introduced is generally much smaller than the error from other sources, but at higher power levels the temperature difference across the block can be quite large. To eliminate this error, the copper temperature T_{cu} used in eqn. 6.14 is a corrected surface temperature that is calculated based on the flux through the copper block.

$$T_{cu} = T_{\text{measured}} - \frac{Q_{cu} * L_{cu}}{k A_{cu}} \tag{6.16}$$

In this equation, L_{cu} is the half thickness of the block and A_{cu} is the cross sectional area of the copper.

6.3 Experimental Data

6.3.1 Impingement Surface Convection

Experiments have shown that eqn. 6.1 is a valid approximation in the design of a nozzle assembly. Figure 6-4 plots experimental data and the correlation for an array of round nozzles. As can be seen, the agreement between the experimental data is very good for $\text{Re}_d < 35000$. While the convection coefficient is independent of the power dissipated in the thin film heater, the error in measurement of h is a function of the power used. This can be seen in Fig. 6-5. At very low powers, the error in

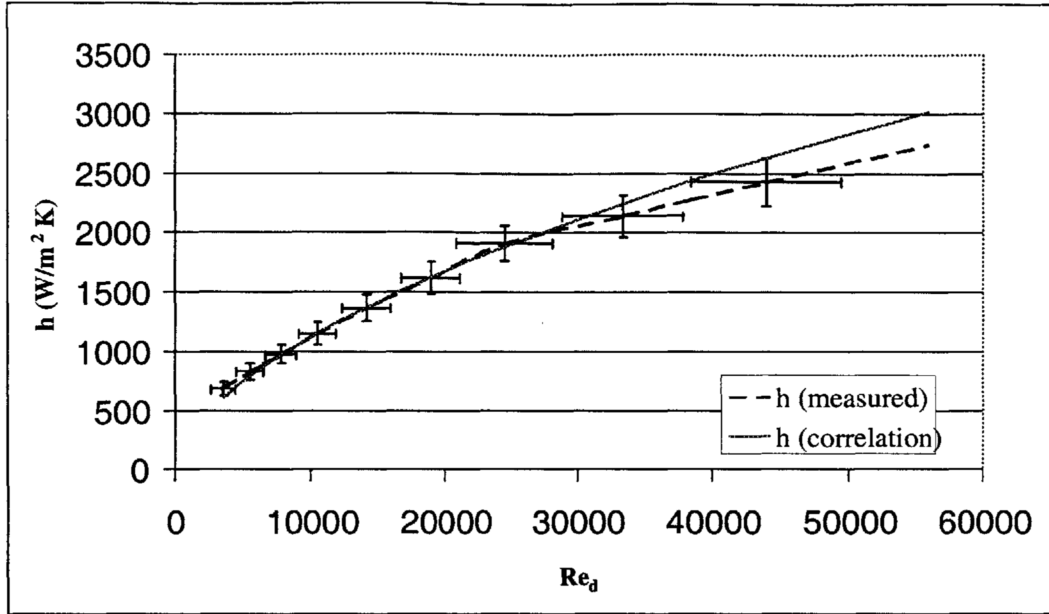

Figure 6-4: Correlation and experimental data for Reynolds number versus the convection coefficient $\overline{h}_c$ for the nozzle test rig. Error bars show the experimental measurement errors in $\mathrm{Re_d}$ and $\overline{h}_c$. Data is for a flat face conduction plate configuration (no side edges exposed) with no device holder present.

measurement of small temperature defects produce large errors in the measure value of h. At higher power levels, the magnitude of the errors are significantly reduced and the values converge on the correlation values.

The effect of changing the nozzle to target spacing can be evaluated using the experimental data. As stated in the theory section, the convective cooling coefficient can be optimized based on minimum pumping power to obtain an optimal H/D ratio. As this ratio is changed, the value of $\overline{h}_c$ increases for decreasing H/D ratio. Figure 6-6 shows correlation and experimental data for various H/D ratios. It is useful to note that higher $\overline{h}_c$ values can be obtained if the pumping power (eqn. 6.13) is not critical and a higher pressure drop and mass flow rate can be accommodated by the system.

6.3.2 Side Edge Convection

The value of the average heat transfer coefficient on the exposed side faces can also be measured. By keeping the nozzle to convection face spacing constant and increasing

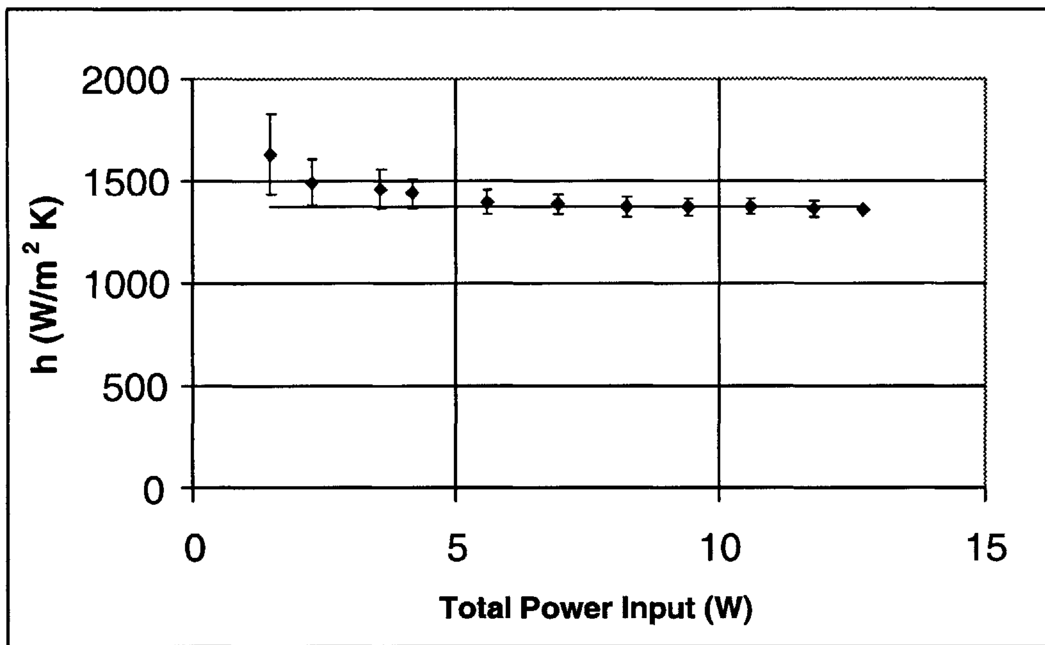

Figure 6-5: Measured values of h for increasing power dissipation levels at $\mathrm{Re_d}$ = 14500. Correlation value is $\overline{h}_c = 1400$ W/m^{2}K. Flat face configuration with no device holder present.

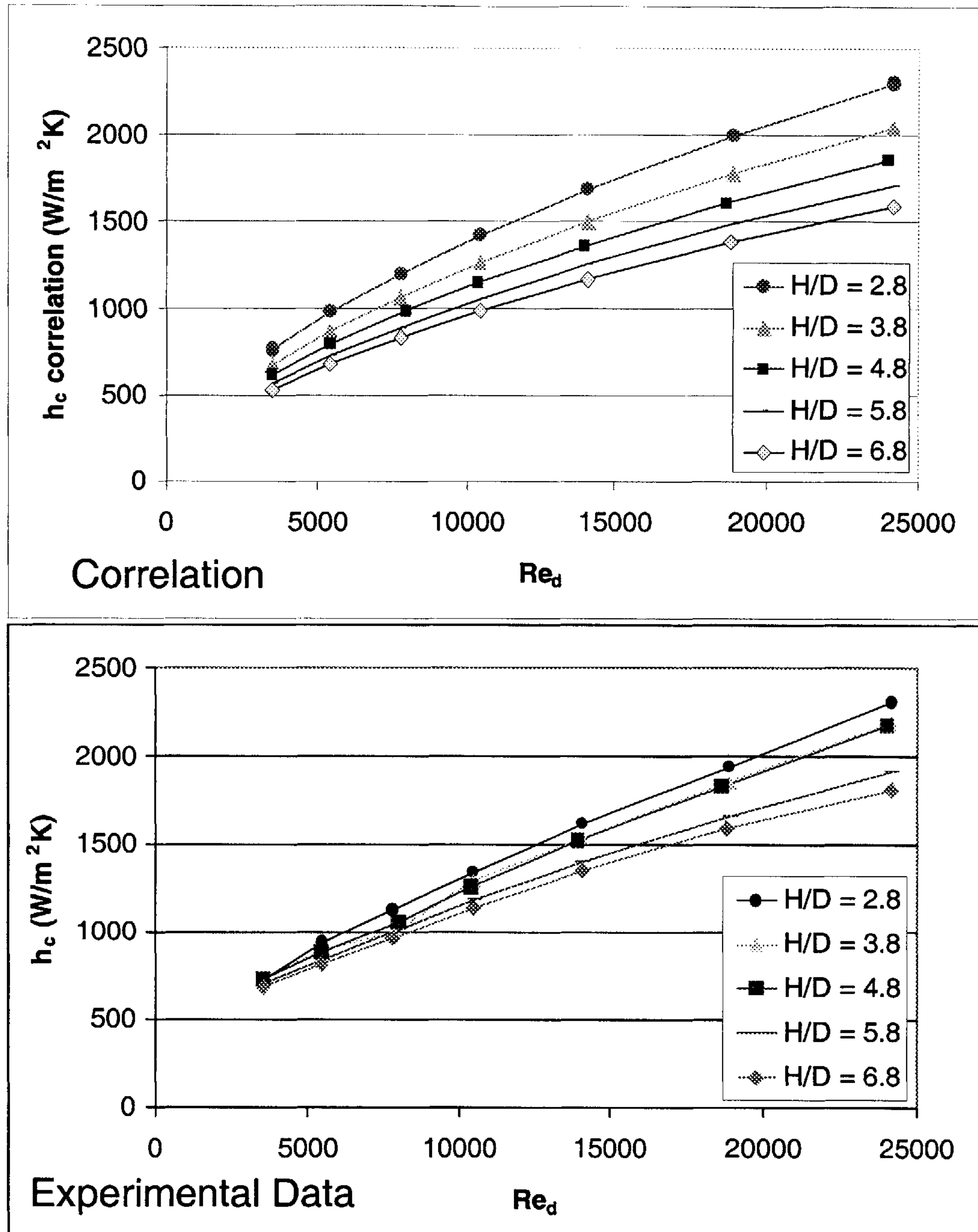

Figure 6-6: Correlation and experimental $\overline{h}_c$ values for multiple H/D ratios. Experimental data is for no exposed side edges and no holder present.

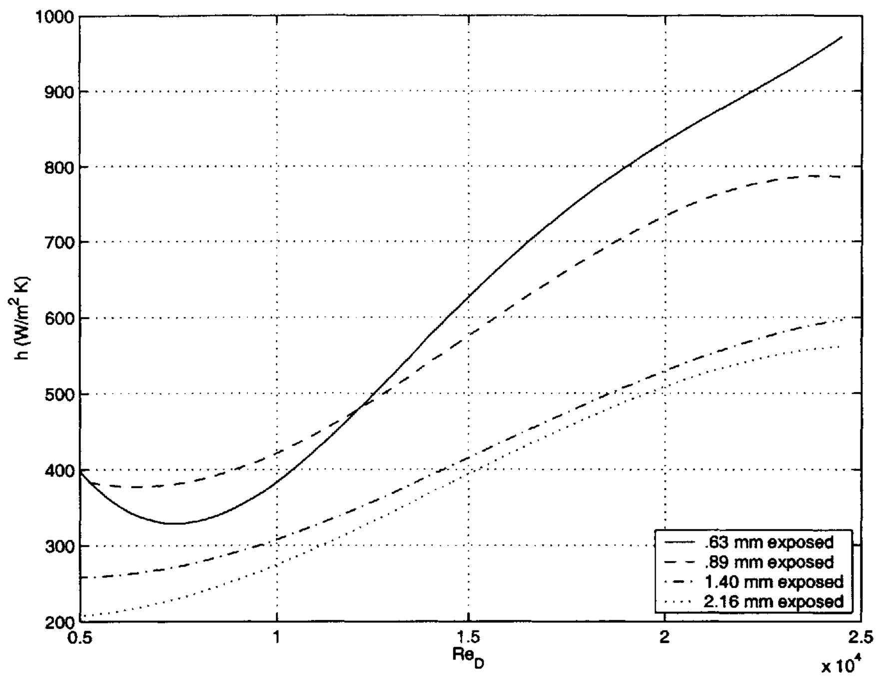

Figure 6-7: Average side edge convective heat transfer coefficients for various exposed side face heights.

the amount of edge face exposed, data can be obtained that can be used to evaluate the effective average convection coefficient from the side face. Assuming the average convection coefficient for the front face does not change as more of the side edge is exposed, the value of the average side face convection coefficient can be calculated by comparison of the results for no side edge exposure using the equation

$$\overline{h}_{\text{side}} = \frac{\overline{h}_{\text{meas}}\left(A_{\text{face}} + A_{\text{side}}\right) - \overline{h}_{\text{face}} A_{\text{face}}}{A_{\text{side}}} \tag{6.17}$$

where $\overline{h}_{\text{meas}}$ is the measured average convective heat transfer coefficient for combined front and side face exposure, and $\overline{h}_{\text{face}}$ is the convective transfer coefficient measured under identical conditions[5] with no side edges exposed. Figure 6-7 plots $\overline{h}_{\text{side}}$ for four different exposed side areas. The values of the side edge $\overline{h}_c$ are 20-40% of the surface values with increasing values for shorter edge exposure lengths. In each application, the actual value of the side edge convective transfer coefficient will depend on the nozzle spacing, nozzle size, nozzle position with respect to the edge, and edge height. Experimental measurements will have to be made to obtain the precise value for each case if required, but this data provides a general scaling for initial rough engineering design.

So far all data presented has been for measurements with no device holder in place. The presence of a device holder will change the flow pattern of the air because the exhaust air will no longer be able to flow freely away in all directions. The system is not designed for use of the holder with no side edges exposed, therefore the change in $\overline{h}_c$ is only defined for cases where side edges are exposed. The holder is used to simulate a device holder/alignment system that will hold the device under test against the test socket. The holder has recessed grooves that fit over each corner of the copper block. Figure 6-8 shows a detailed view of the device holder. There are air exits on each side and the top is open for the nozzles and air exit. The minimum exposed side edge for use with a holder is 0.89 mm.

6.3.3 Effect of Device Holder

In order to evaluate the effect of the holder on the heat transfer, a new effective convective heat transfer coefficient is defined as

[5] Nozzle spacing, supply pressure and air/copper temperature defect identical.

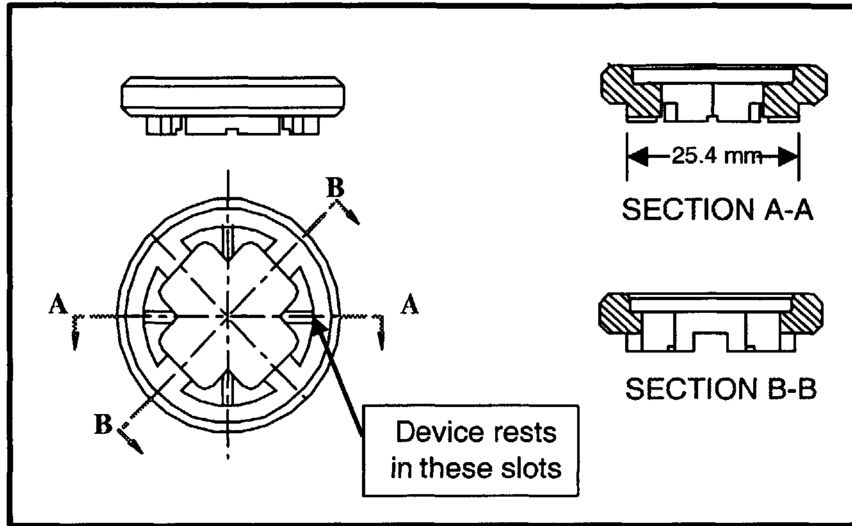

Figure 6-8: Detailed view of simulated die holder for convection experiments. The recessed grooves mount on the four corners of the copper block.

$$\overline{h}_e = \frac{Q_{\text{tot}}}{A_{\text{face}}\left(T_{CU} - T_{\text{air}}\right)} \tag{6.18}$$

where Q_{tot} is the total convective energy transfer from the surface and the side edges while A_{face} is the surface area of the impingement face and does not include the side area. Using this definition of the convective heat transfer coefficient, data for various heights of side face exposure was obtained for cases where no holder was present and where a low conductivity PEEK holder was present. This data is shown in Fig. 6-9. It can be seen that for a given side edge exposure, the presence of the holder reduces the effective convective heat transfer coefficient for a given Reynolds number. This data can be further reduced by taking the difference between the $\overline{h}_e$ values with the holder present and without the holder present and dividing the change by the original $\overline{h}_e$ value where no holder is present. The resulting data is presented in Fig. 6-10. The holder reduces $\overline{h}_e$ by 6-10% at all Reynolds numbers.

The holder material type will have a large effect on the convective heat transfer. For the low conductivity PEEK holder, the presence of the holder reduced $\overline{h}_e$ by 6-10%, but if a higher conductivity holder is used, then it can actually increase the effective heat transfer coefficient by acting as a fin heat sink. Device holders made from 304 stainless steel and OFC copper were tested to see the effect on convection,

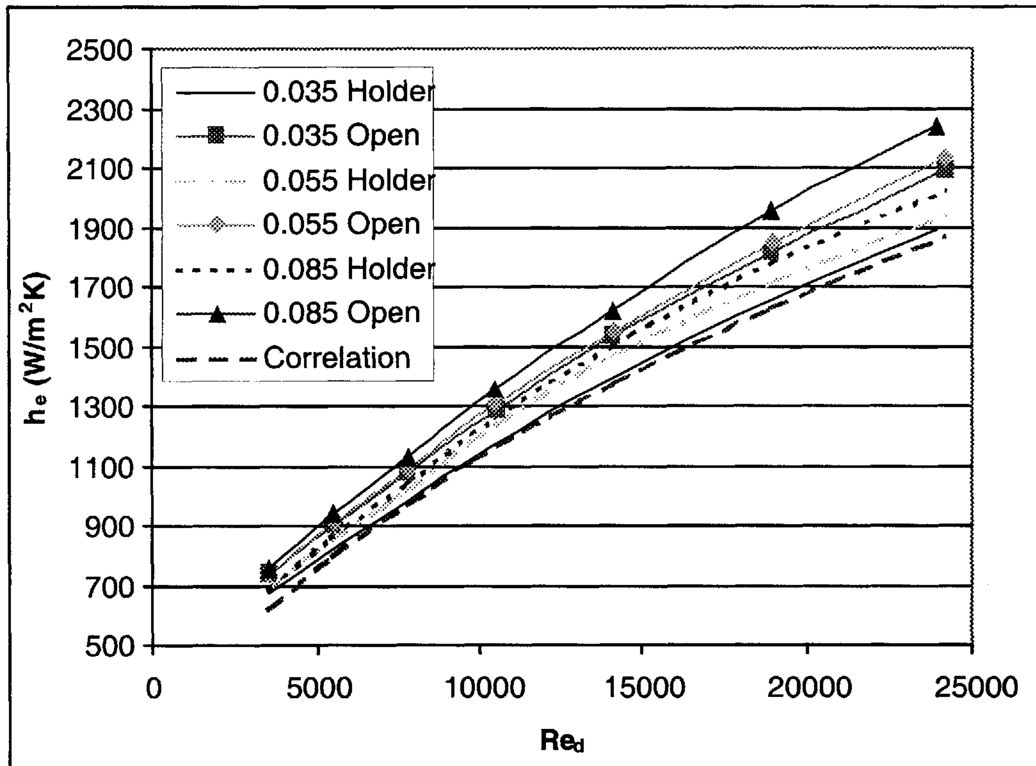

Figure 6-9: Effective heat transfer coefficient for various side edge exposure heights with no device holder and with PEEK device holder present.

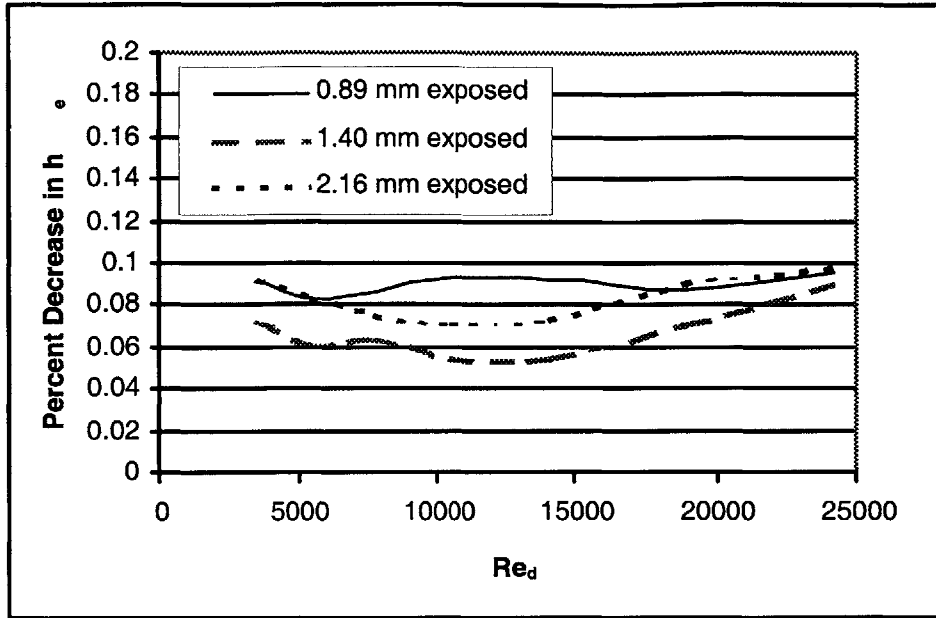

Figure 6-10: Percent decrease in $\overline{h}_e$ when a PEEK device holder is added for a specified exposed edge height.

the results are shown in Fig. 6-11. Still using the same definition for the effective heat transfer coefficient (eqn. 6.18), $\overline{h}_e$ can be greatly increased by using a high conductivity device holder. This is important when a large thermal load has to be dissipated[6].

6.3.4 System Noise

The noise generated by the nozzle system is of interest as there is a limit to the noise pollution that a system can generate as specified by OSHA. Just to obtain some baseline data, the noise level was measured at a position 1 cm away from the nozzle region at various supply pressures. The Radio Shack hand held noise meter was set for measuring A filtered noise as per OSHA standards, and there was no shielding between the meter and the exiting air stream. The noise data is shown in Fig. 6-12. The level of noise that is important is the sound level on the outside of the final tester, so noise level measurements right at the nozzle are not very useful for making the

[6]This will be useful for device to be developed over the next several years where even $\overline{h}_c$ on the order of 2000 W/m^2K will be unable to provide sufficient cooling for the device under test conditions.

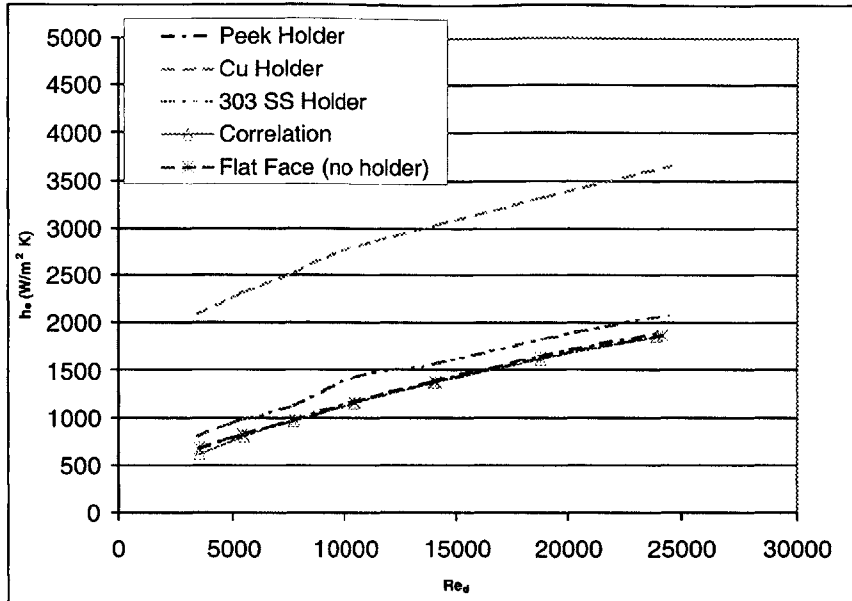

Figure 6-11: Measured $\overline{h}_e$ for various holder materials and flat plate configuration with no holder.

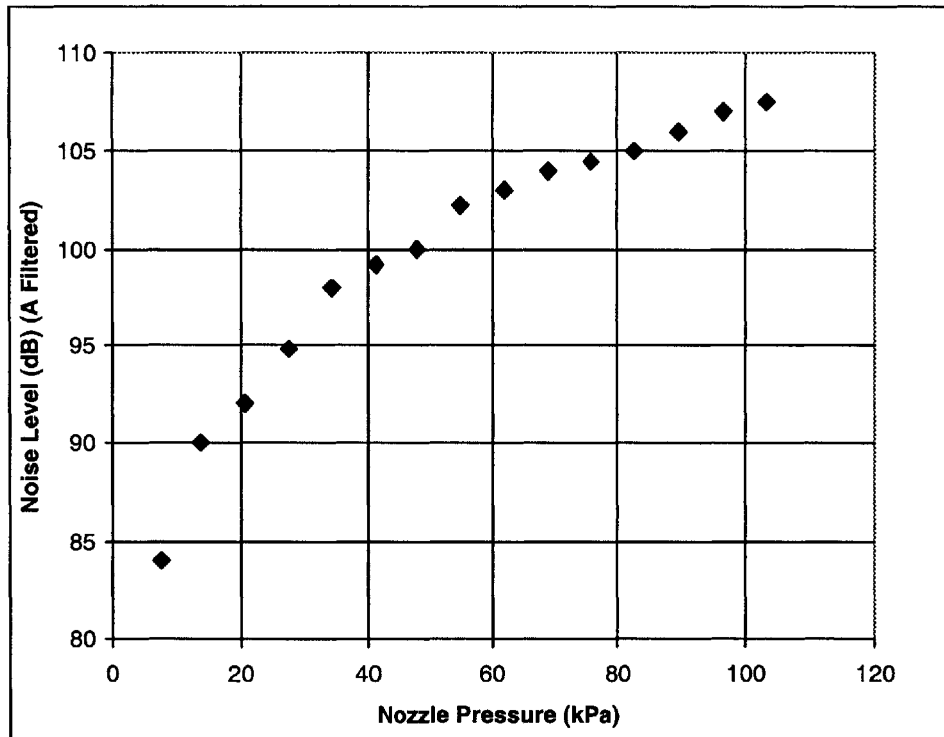

Figure 6-12: Noise level at a position 1 cm from the nozzle assembly.

statement that the system is too loud. Sufficient damping must be installed in the final assembly to reduce the noise to tolerable levels as specified by OSHA[27] and company guidelines.

6.4 Error Propagation and Analysis

The value of the convective heat transfer coefficient $\overline{h}_c$ can be calculated from the equation:

$$\overline{h}_c = \frac{Q}{A\left(T_{\text{surface}} - T_{\text{air}}\right)} \tag{6.19}$$

where Q is the flux and A is the convective surface area. The actual measurement of $\overline{h}_c$ involves several measurements and the error in the measurement takes a number of terms to calculate. A standard propagation of errors method [24] can be used to estimate the total error in the measured $\overline{h}_c$ values. The error can be written as

$$\left|\frac{\delta h_c}{h_c}\right| = \sqrt{\left(\frac{\delta A}{A}\right)^2 + \left(\frac{\delta Q}{Q}\right)^2 + \left(\frac{\delta \Delta T}{\Delta T}\right)^2} \tag{6.20}$$

where each of these measurements involves the error from other measurements. The error in the area can be calculated from

$$\frac{\delta A}{A} = \frac{A_f}{A_f + A_s} \cdot \frac{2\delta L}{L} + \frac{A_s}{A_f + A_s}\sqrt{\left(\frac{\delta L}{L}\right)^2 + \left(\frac{\delta s}{s}\right)^2} \tag{6.21}$$

where A_f is the face area exposed to direct impingement, A_s is the exposed side area, L is the square dimension of the device[7], and s is the height of the exposed side edge.

The error in the temperature defect is simply

$$\frac{\delta \Delta T}{\Delta T} = \frac{\delta T_{\text{surf}} + \delta T_{\text{air}}}{T_{\text{surf}} - T_{\text{air}}} \tag{6.22}$$

but the temperature of the surface T_{surf} cannot be measured directly. Instead the temperature at the center of the copper block can be measured and this value combined with the flux to derive the surface temperature. The surface temperature can be calculated using

$$T_{\text{surf}} = T_c - \frac{QL}{2k_{cu}L^2} = T_c - \frac{Q}{2k_{cu}L} \tag{6.23}$$

[7]The copper block is $L = 12.5$ mm by $L = 12.5$ mm in dimension.

so the error in the surface temperature can be written as

$$\frac{\delta T_{\mathrm{surf}}}{T_{\mathrm{surf}}} = \sqrt{\left(\frac{\delta T_c}{T_c}\right)^2 + \left(\frac{\delta Q}{Q}\right)^2 + \left(\frac{\delta k_{cu}}{k_{cu}}\right)^2} \tag{6.24}$$

The error in the flux is a function of the error in the measured power dissipated in the thin film heater and the error in measuring the flux through the pedestal. The total power dissipated in the heater is $P = IV$ where I is the measured current and V is the measured voltage. The error in this measurement is simply the error of the current and voltage added in quadrature.

$$\frac{\delta P}{P} = \sqrt{\left(\frac{\delta I}{I}\right)^2 + \left(\frac{\delta V}{V}\right)^2} \tag{6.25}$$

The convective flux is this power minus the losses down the pedestal. The losses down the pedestal can be calculated from

$$Q_L = \frac{k_p A_p}{L_p} \cdot (\Delta T_p) \tag{6.26}$$

so the error in the losses down the pedestal is

$$\frac{\delta Q_L}{Q_L} = \sqrt{\left(\frac{\delta k_p}{k_p}\right)^2 + \left(\frac{\delta A_p}{A_p}\right)^2 + \left(\frac{\delta L_p}{L_p}\right)^2 + \left(\frac{|\delta T_{\mathrm{high}}| + |\delta T_{\mathrm{low}}|}{T_{\mathrm{high}} - T_{\mathrm{low}}}\right)^2} \tag{6.27}$$

where k_p is the conductivity of the pedestal, A_p is the cross sectional area of the pedestal, L_c is the distance between the thermocouples mounted in the pedestals and the T_{high} and T_{low} are the temperatures of the those thermocouples.

A similar analysis can be performed in the calculation of the Reynolds number. With

$$Re = \frac{\rho V d}{\mu} = \frac{\dot{m}}{\mu \pi d} \tag{6.28}$$

and neglecting errors in the viscosity μ, the error in the Reynolds becomes

$$\frac{\delta \mathrm{Re}}{\mathrm{Re}} = \sqrt{\left(\frac{\delta \dot{m}}{\dot{m}}\right)^2 + \left(\frac{\delta d}{d}\right)^2} \tag{6.29}$$

where $\dot{m}$ is the mass flow rate and d is the nozzle diameter. The mass flow rate is calculated from a volumetric flow rate using $\dot{m} = \rho \dot{Q}$ and the density is found using $\rho = \rho_{\mathrm{atm}} P / P_{\mathrm{atm}}$ where P is the measured pressure at the flow meter. Again, all errors are independent so the errors add in quadrature.

Typical values used in the error evaluation are as follows:

$$\delta d = 0.07 \text{ mm} \tag{6.30}$$

$$\delta L = 0.1 \text{ mm} \tag{6.31}$$

$$\delta T = 0.2°\text{C} \tag{6.32}$$

$$\delta k_p = 0.01 \text{ W/mK} \tag{6.33}$$

$$\delta L_p = 0.2 \text{ mm} \tag{6.34}$$

$$\delta V = 0.005 \text{ V} \tag{6.35}$$

$$\delta I = 0.01 \text{ A} \tag{6.36}$$

$$\delta s = 0.2 \text{ mm} \tag{6.37}$$

$$\delta \dot{Q} = 2 \text{ L/min} \tag{6.38}$$

$$\delta P = 1370 \text{ Pa} \tag{6.39}$$

It turns out that the largest source of error is in the temperature measurements. All values were measured at steady state conditions to eliminate transient conduction errors and contact resistance problems. The relative magnitude of the temperature error could be reduced by operating at higher ΔT values, which is why the error bars in Fig. 6-5 decrease with increasing values of total power.

6.5 Conclusions

Theory and experiment show that convective heat transfer coefficients on the order of 1200 W/m^{2}K to 1500 W/m^{2}K can be obtained fairly easily using impinging nozzles on the surface of a device using a compressed air supply. Higher values up to $\overline{h}_c =$ 2000 W/m^{2}K can be obtained at higher pressures and the effective value of h_e can be increased by using high conductivity device holders.

Chapter 7

Laser/Convection System Experimental Results

This chapter presents the experimental data from the Laser/Convection prototype system. The first section covers device response to die inputs with no laser/temperature control. The second section presents data when active temperature control is used. The final section presents data related to the control limits of the device as well as data on use of the laser system to pre-heat the devices prior to testing and data on running multiple die at different power levels.

7.1 Baseline Data

This section covers data for both TTV devices without any temperature control in place. It presents the temperature response of both devices to the Intel power sequence at various scaling factors. Figure 7-1 presents the correlation $\overline{h}_c$ value as a function of manifold pressure for the prototype system. This plot is valid for both the P858ACY TTV and the Pinetop TTV as the nozzle configuration is the same[1]. Volumetric flow rate as a function of manifold pressure is plotted for both TTV setups in Fig. 7-2. The flow is presented at standard conditions (101.36 kPa & 21.4°C).

[1]The number of nozzles for each TTV is different, but the spacing, nozzle diameter, and offsets are the same, so for the same Reynolds number (same manifold pressure) the convective coefficient is the same.

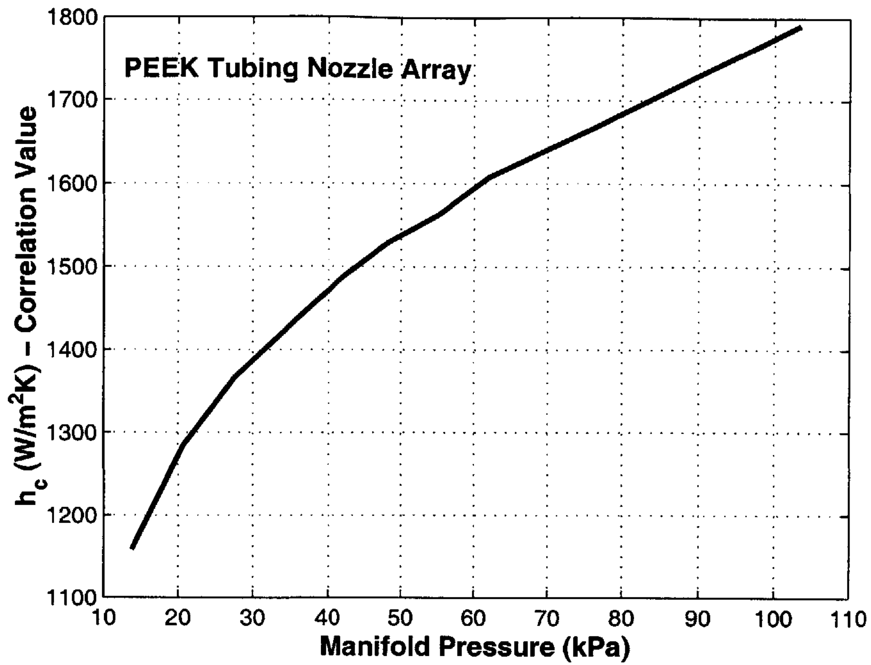

Figure 7-1: Manifold pressure versus $\overline{h}_c$ for the prototype system.

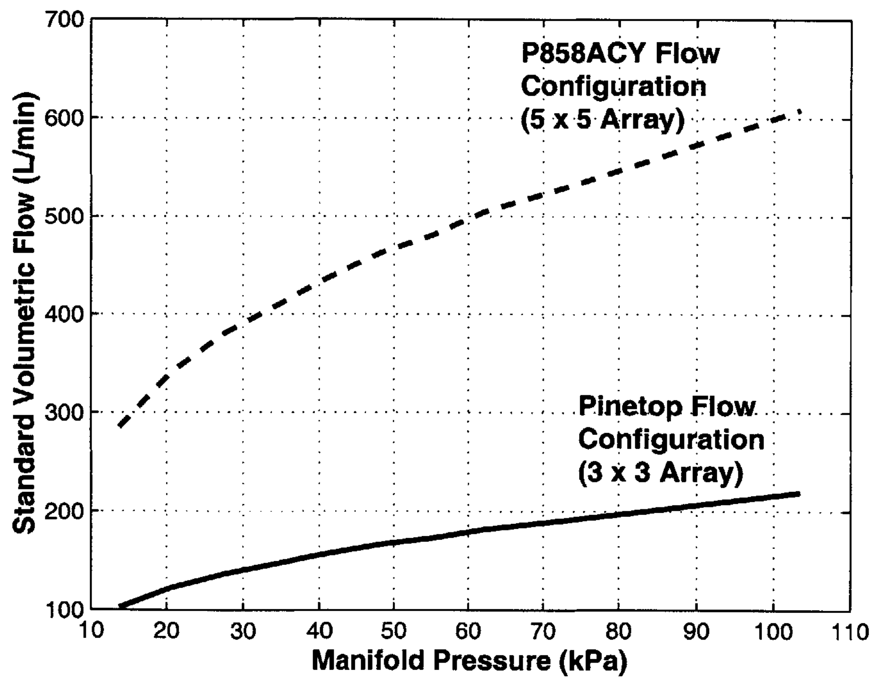

Figure 7-2: Volumetric flow rate under standard conditions versus manifold pressure.

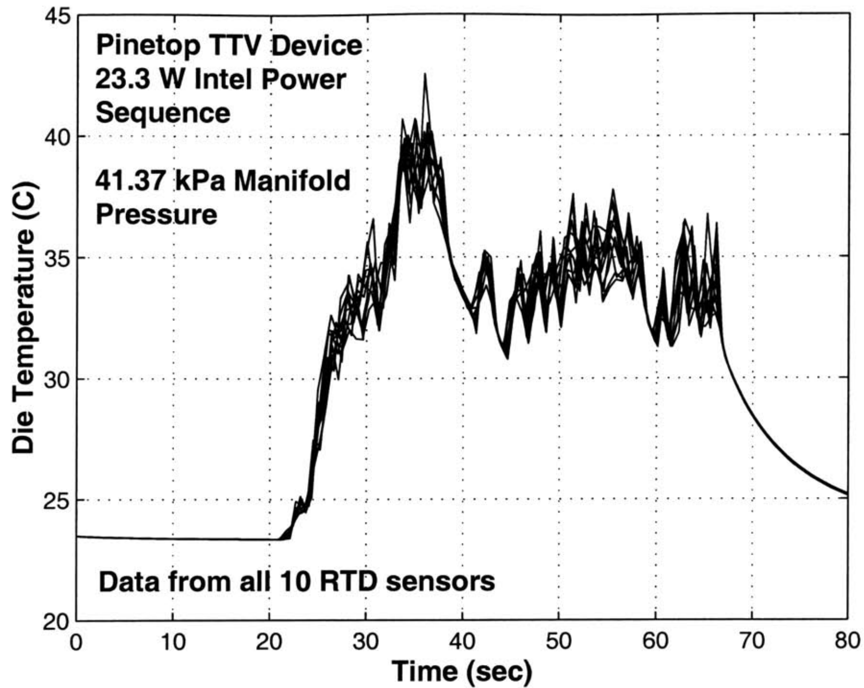

Figure 7-3: Die temperature for Pinetop TTV subject to a 23.3 W Intel test sequence.

7.1.1 Pinetop TTV

As stated in the Chapter 5, the Pinetop TTV is designed for low to medium power levels at much higher densities than the P858ACY TTV device. There is a single die structure and nominal resistance is 30 Ω. The peak electrical power run through the die is 56 W. Figure 7-3 shows the response of a Pinetop TTV to a 23.3 W peak power Intel test sequence with the manifold pressure set at 41.37 kPa. The data acquisition rate when acquiring on all RTD channels is on the order of 1-1.5 Hz. In order to examine the response of the die in detail, a single channel can be sampled at 30-40 Hz. A detailed measurement of the die temperature to a 23.3 W Intel sequence is shown in Fig. 7-4. For comparison, the temperature response of a Pinetop TTV to a 14 W Intel power sequence with no forced convection is shown in Fig. 7-5.

The Intel test sequence can be scaled up and down to see the effect of changing the peak power level. Figure 7-6 shows the temperature response of a Pinetop TTV with a fixed manifold pressure, as the peak power is changed. The effect of changing the manifold pressure with a constant power sequence is shown in Fig. 7-7.

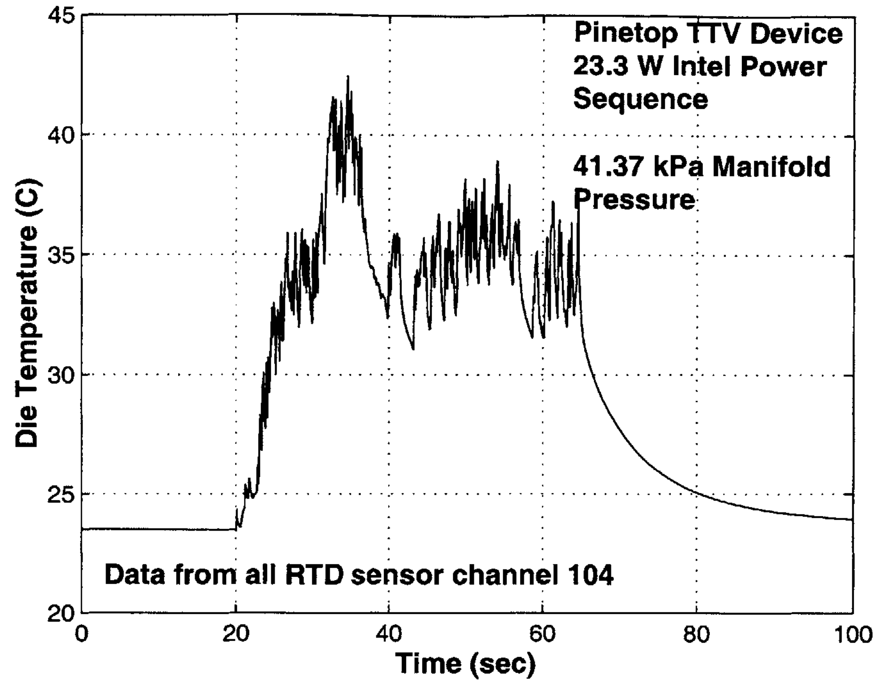

Figure 7-4: Single channel data for Pinetop TTV subject to 23.3 W Intel test sequence.

7.1.2 P858ACY TTV

The P858ACY TTV is designed for medium to high power levels at lower densities than the Pinetop TTV device. There are four die structures which can be run independently, but for all applications in this thesis, the four dies are connected as a single structure and are run with the same power densities. The peak electrical power run through the die is 92 W. Figure 7-8 shows the response of a P858ACY TTV to a 46.7 W peak power Intel test sequence with the manifold pressure set at 41.37 kPa.

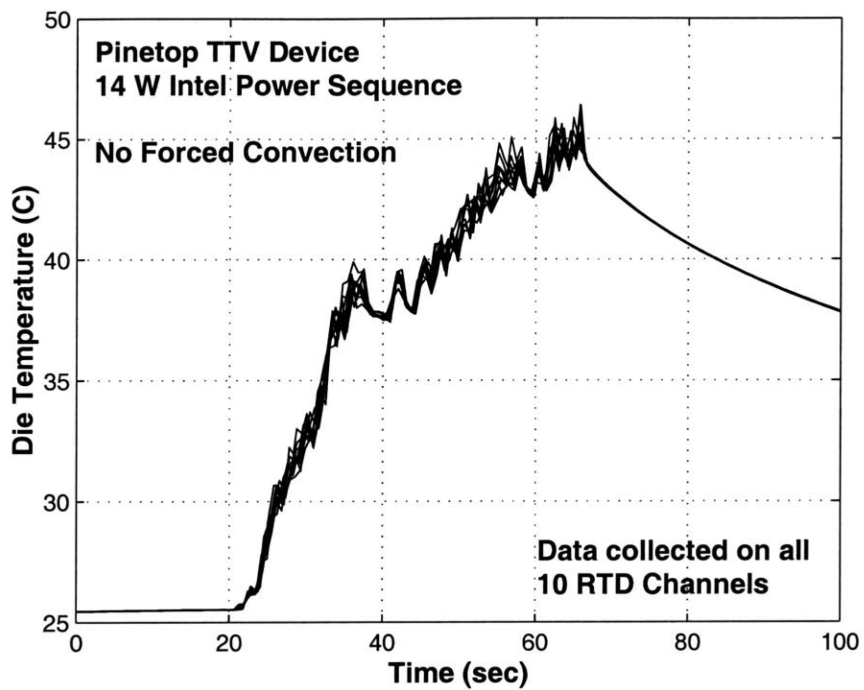

Figure 7-5: Temperature response of Pinetop TTV subject to a 14 W Intel power sequence with no forced convection.

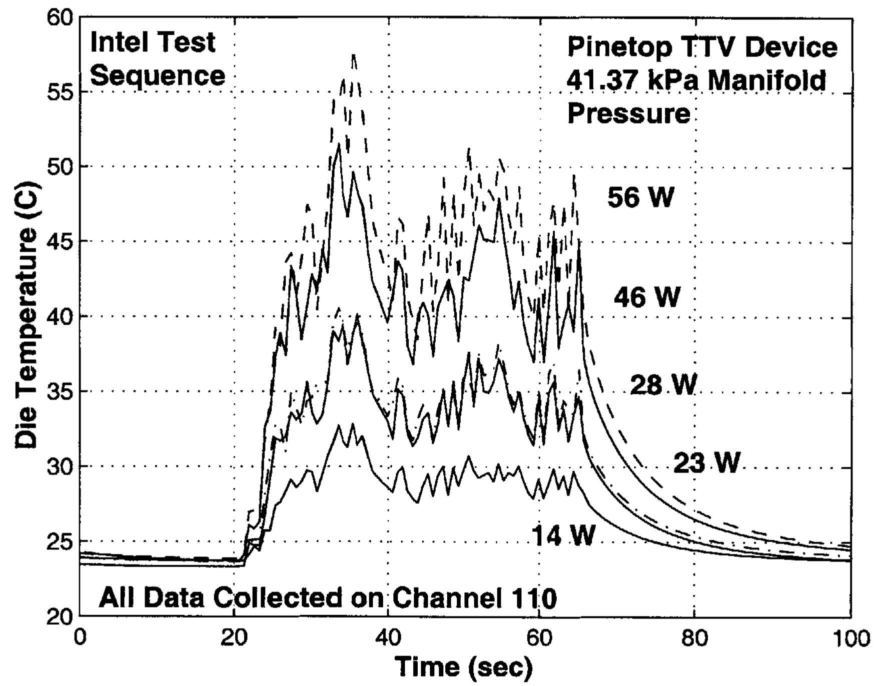

Figure 7-6: Temperature response of Pinetop TTV to scaled Intel test sequences with constant manifold pressure.

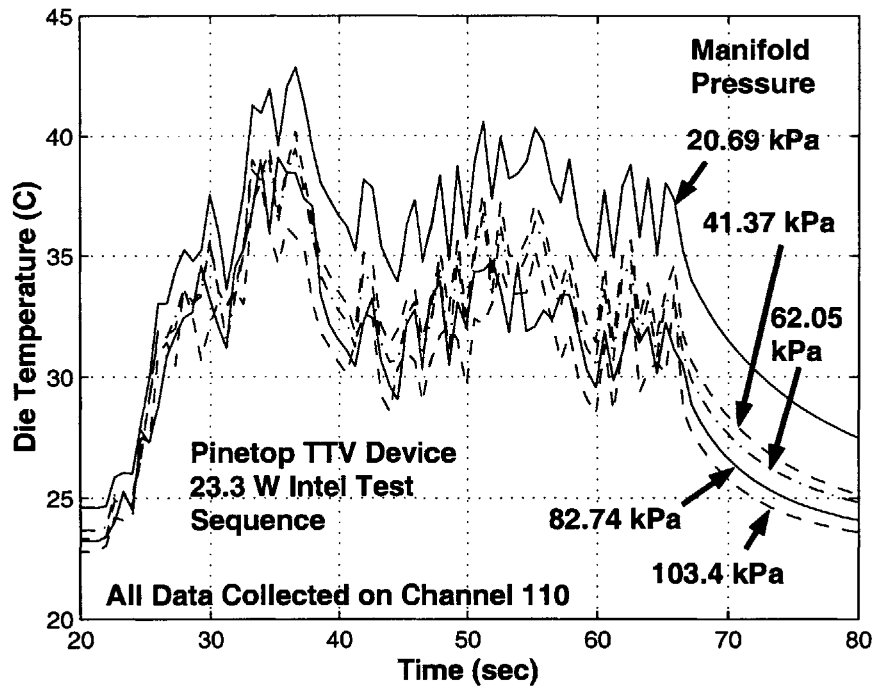

Figure 7-7: Temperature response of Pinetop TTV for a 23 W Intel test sequence at multiple manifold pressures.

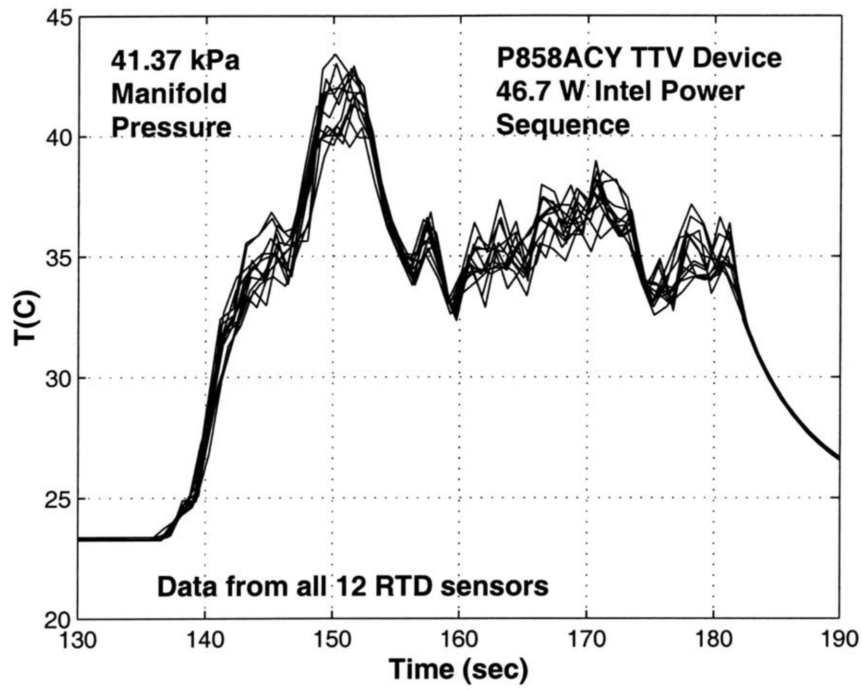

Figure 7-8: Die temperature for a P858ACY TTV subject to a 46.7 W Intel test sequence.

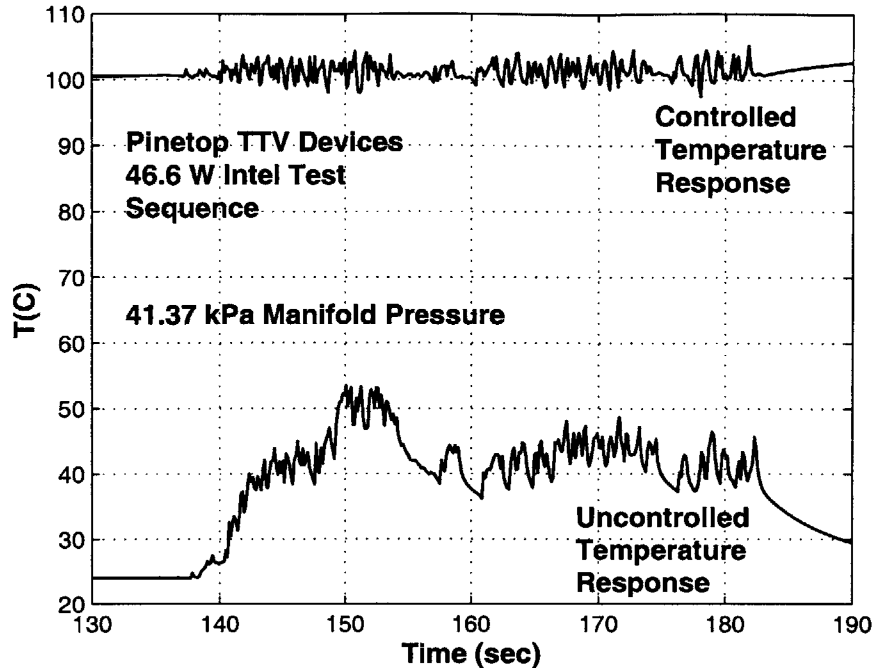

Figure 7-9: Uncontrolled and controlled temperature response of a Pinetop TTV to a 46.7 W Intel test sequence.

7.2 Temperature Control Data

7.2.1 Pinetop TTV

Figure 7-9 plots the temperature response with and without active temperature control for a Pinetop TTV subjected to a 46.7 W Intel test sequence. This plot clearly shows the effectiveness of the laser/convection temperature control system. The minimum temperature of each sequence would be adjusted to the target temperature (e.g. 100°C for example) by changing either the air temperature or the manifold pressure. The objective of the control system is to minimize the die temperature variation above this minimum temperature. In the uncontrolled case, this represents a temperature change of $\sim$ 29°C, while the control variation is less than 4°C.

A detailed view of the temperature response of a Pinetop TTV to a 23.3 W Intel sequence is shown in Fig. 7-10. The control sequence used to obtain this response is shown in Fig. 7-11. The effect of changing the manifold pressure on the temperature response of the DUT is shown in Fig. 7-12. Changing the supply pressure changes the mean temperature, but has almost no effect on the temperature range of the die.

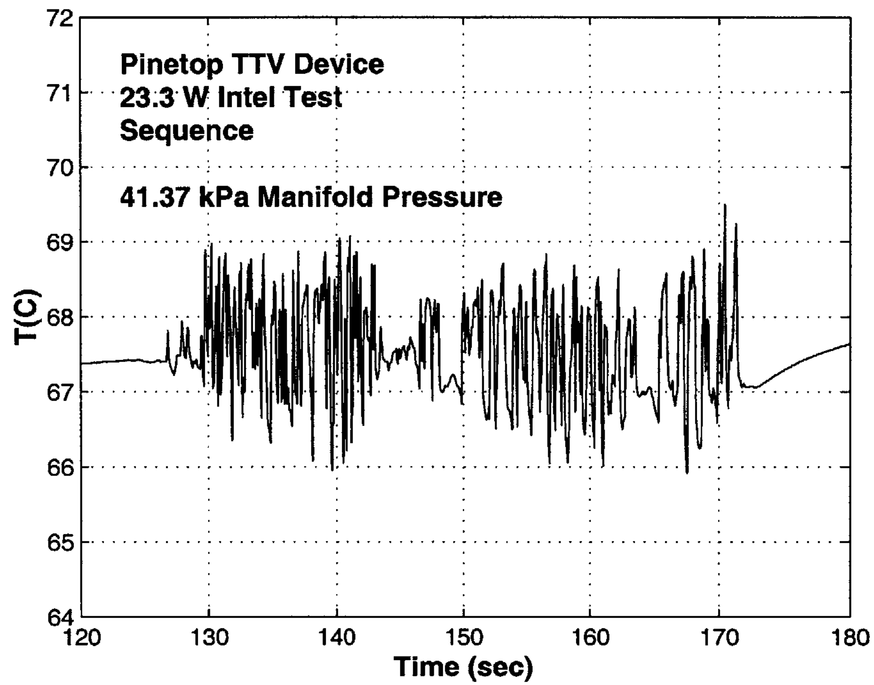

Figure 7-10: Controlled temperature response of a Pinetop TTV to a 23.3 W Intel test sequence.

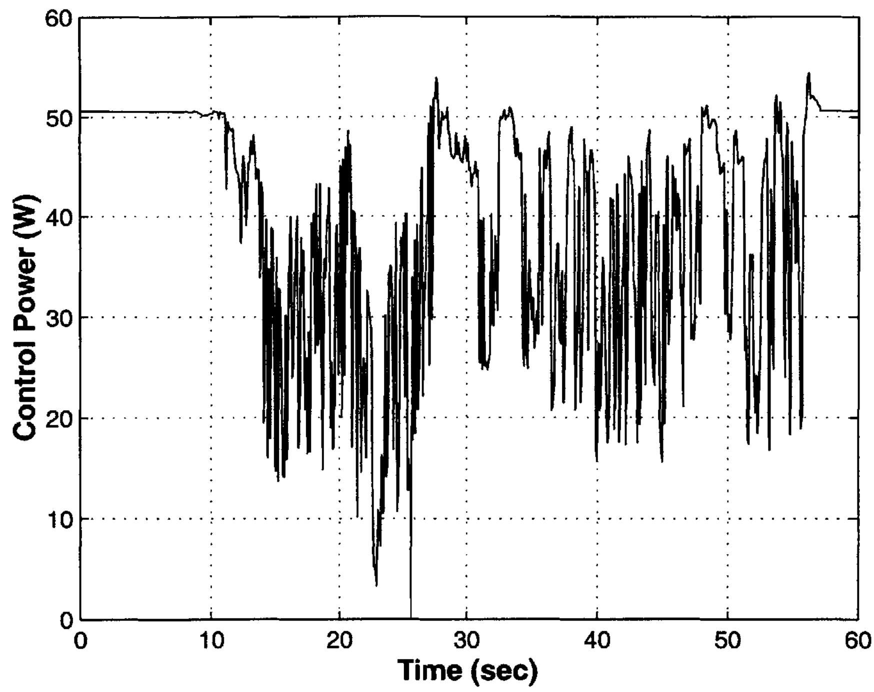

Figure 7-11: Control power sequence for Pinetop die temperature response shown in Fig. 7-10.

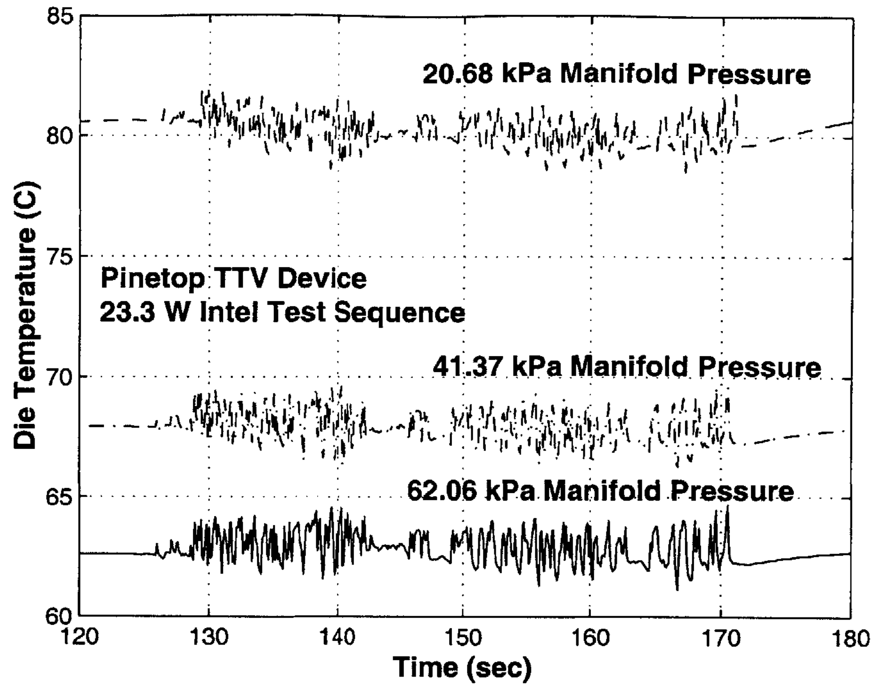

Figure 7-12: Controlled die temperature response to 23.3 W Intel test sequence at multiple manifold pressures.

7.2.2 P858ACY TTV

Figure 7-13 plots the temperature response with and without active temperature control for a P858ACY TTV subjected to a 46.7 W Intel test sequence. Again, this plot shows the effectiveness of the laser/convection temperature control system. The uncontrolled temperature change of the die is 20°C, while the controlled temperature response of the die is 1.6°C.

A detailed view of the temperature response of a P858ACY TTV to a 46.7 W Intel sequence is shown in Fig. 7-14. The control sequence used to obtain this response is shown in Fig. 7-15.

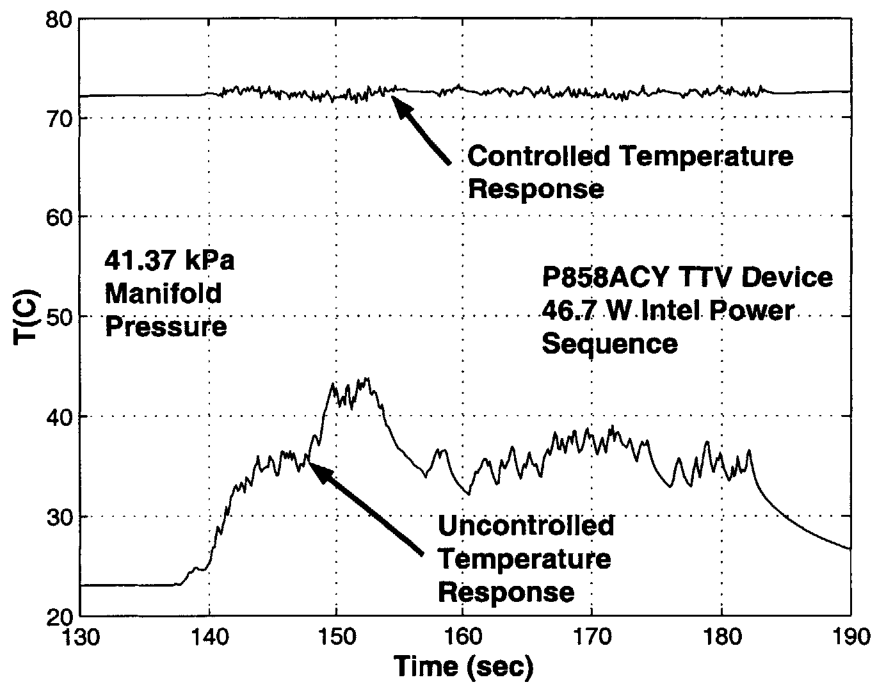

Figure 7-13: Uncontrolled and controlled temperature response of a Pinetop TTV to a 46.7 W Intel test sequence.

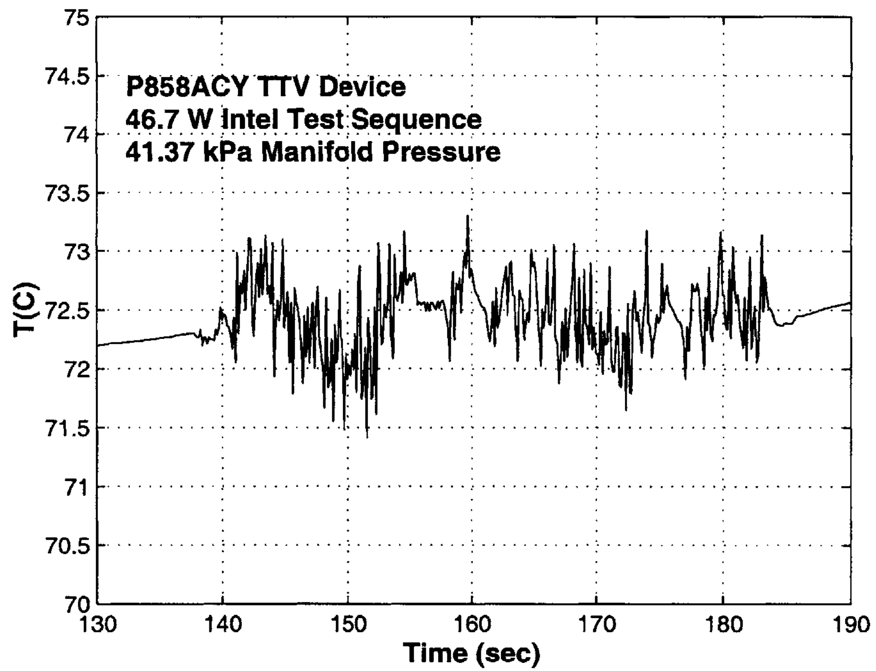

Figure 7-14: Controlled temperature response of a P858ACY TTV to a 46.7 W Intel test sequence.

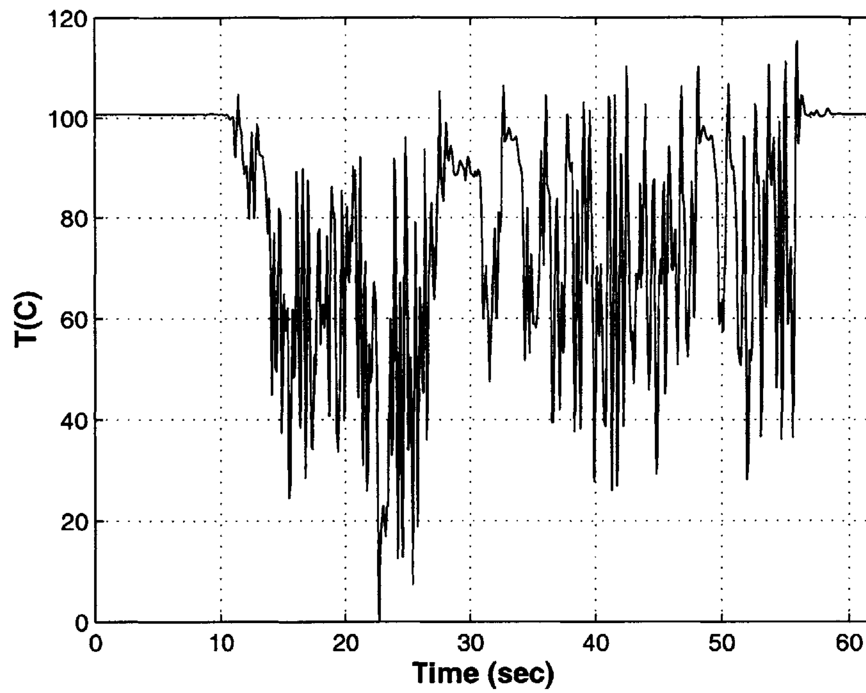

Figure 7-15: Control power sequence for P858ACY TTV die temperature response shown in Fig. 7-14.

7.3 Control Limits

The prototype system can be used to examine the temperature control limits of the thermal test vehicles. The Intel test sequence can be decomposed into a 5 second average, a 1 second average and all remaining terms such that if the three sequences are added together the original Intel test sequence is obtained. These three test sequences can then be used to examine the control limits to difference types of test sequences. Figure 7-16 shows the decomposition of the Intel test sequence. The 1 second average and remainder sequences can be offset such that the minimum power is zero.

This method of filtering is effectively the same as using two low pass filters[2] to remove the 5 second and 1 second averages. Because these filters overlap there is some duplication of energy in each of the average power sequences. A more sophisticated method of filtering would be to design a digital filter that provided a breakdown of energy into specific bandwidth regions, with no overlap between the regions. For the prototype system, the moving average provides adequate and valuable information for testing of the temperature control theory.

7.3.1 Five Second Average Power Sequence.

The 5 second average power sequence can be scaled up and down and the limits of control can be found experimentally. The uncontrolled and controlled temperature response for a Pinetop TTV to the 5 second power sequence is shown in Fig. 7-17. The same tests can be run by scaling this sequence and the limits of control can be found. The results are shown in Fig. 7-18 for a range of power levels up to 50.2 W. The peak control power required to obtain the optimal temperature control can also be plotted versus peak die power as shown in Fig. 7-19. The powers scale linearly with a total[3] laser power to die power ratio of 2.16. There is some temperature variation across the die due to non-uniform conduction and laser illumination effects in the integrated heat spreader. The variation across the die is shown for controlled and uncontrolled test sequences in Fig. 7-20. The die power profile and control power profile used to control the temperature for the 50.2-W 5-second average power profile is shown in Fig. 7-21. How this control profile is generated is described in the final

[2]The low pass filters are from the 5 second moving average and 1 second moving average.

[3]This is the power emitted at the laser. Power at the device will be approximately 60% of this power due to optical losses and surface reflections.

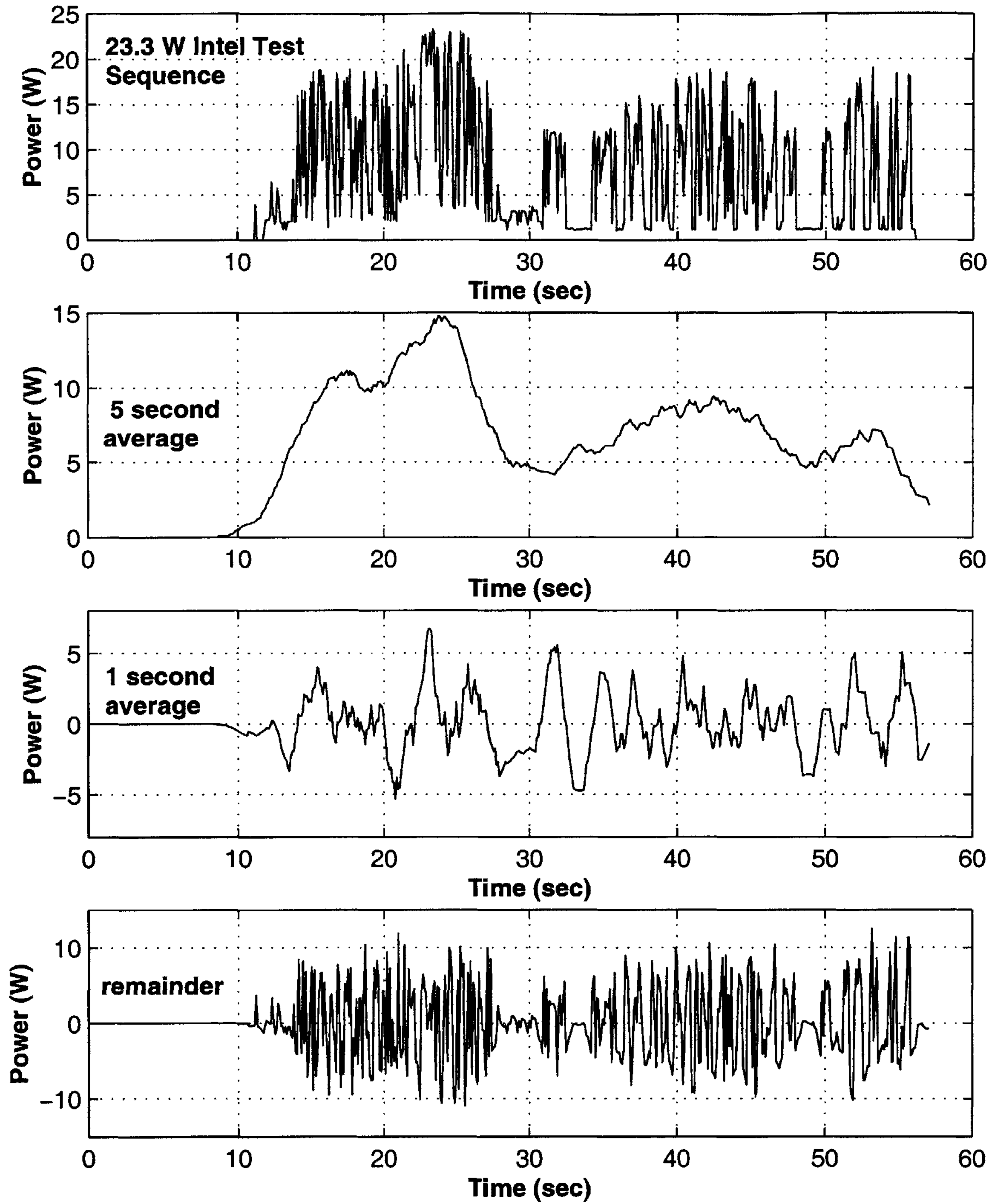

Figure 7-16: Decomposition of Intel test sequence.

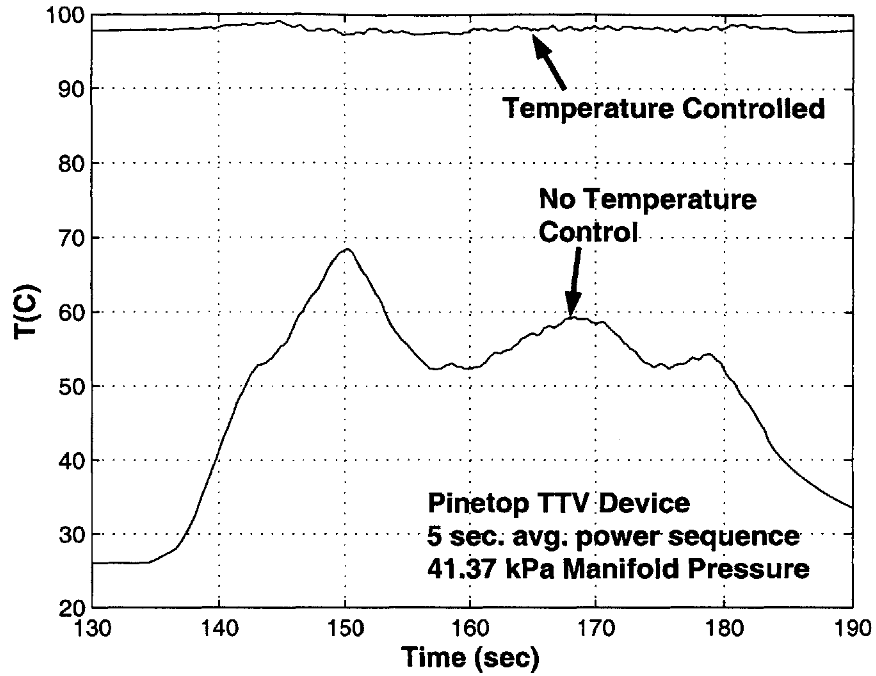

Figure 7-17: Uncontrolled and controlled temperature profile of a Pinetop TTV to the 5 second average power profile with a peak power at 50.2 W.

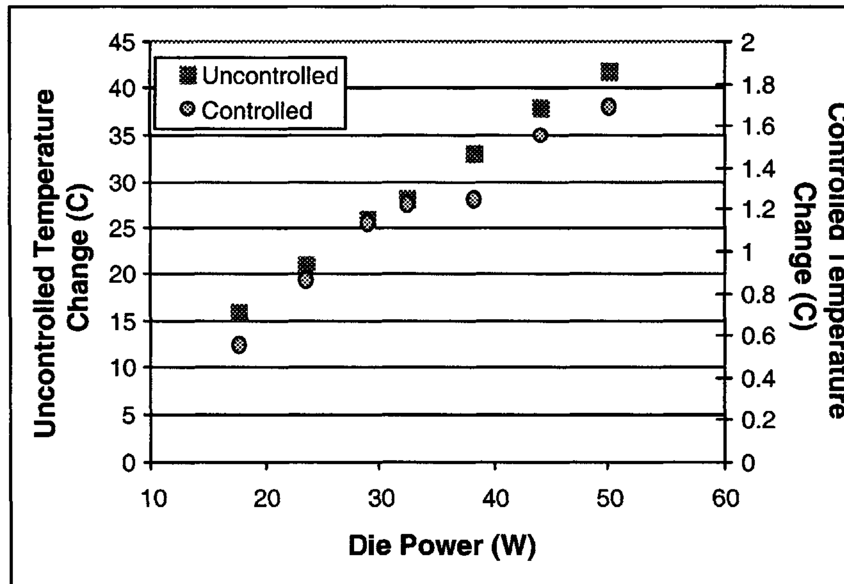

Figure 7-18: Experimental limits of temperature control for 5 second power average with Pinetop TTV.

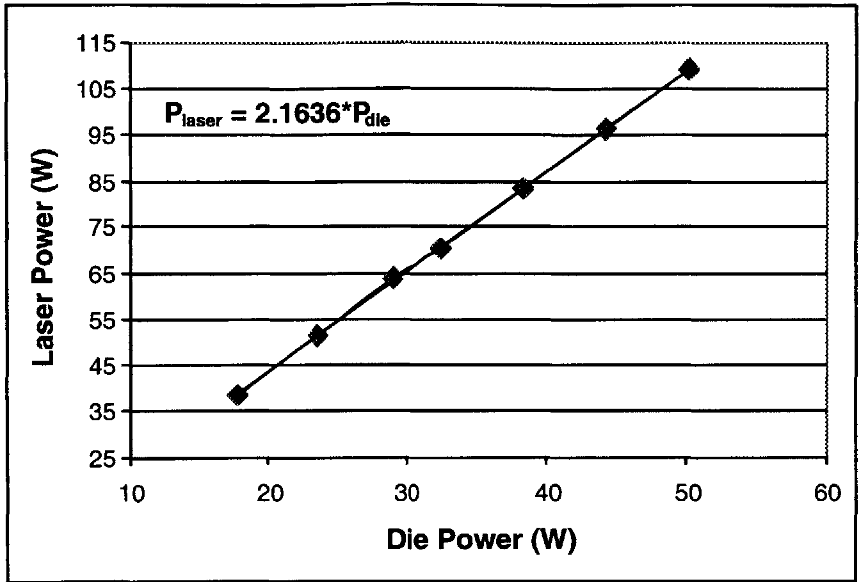

Figure 7-19: Peak control power versus peak die power for 5 second average power sequence on a Pinetop TTV.

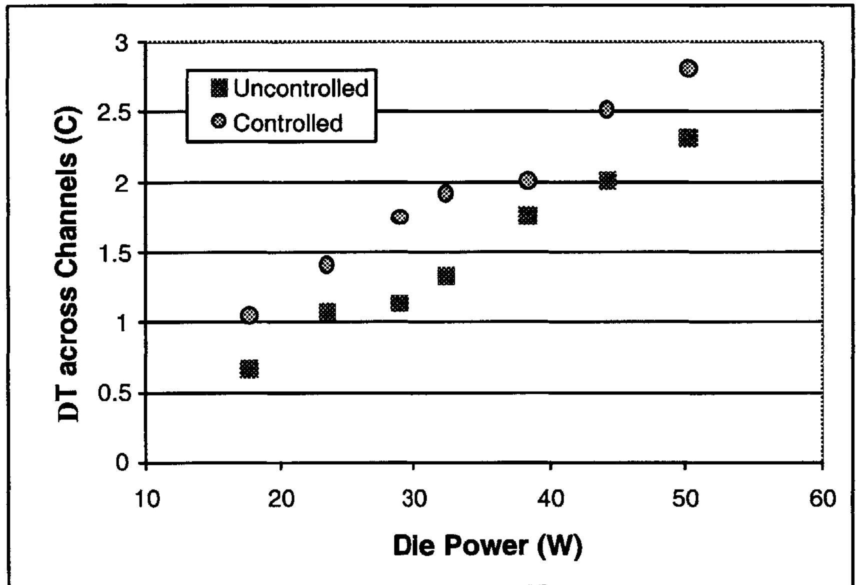

Figure 7-20: Temperature variation across the die for controlled and uncontrolled 5 second average test sequences.

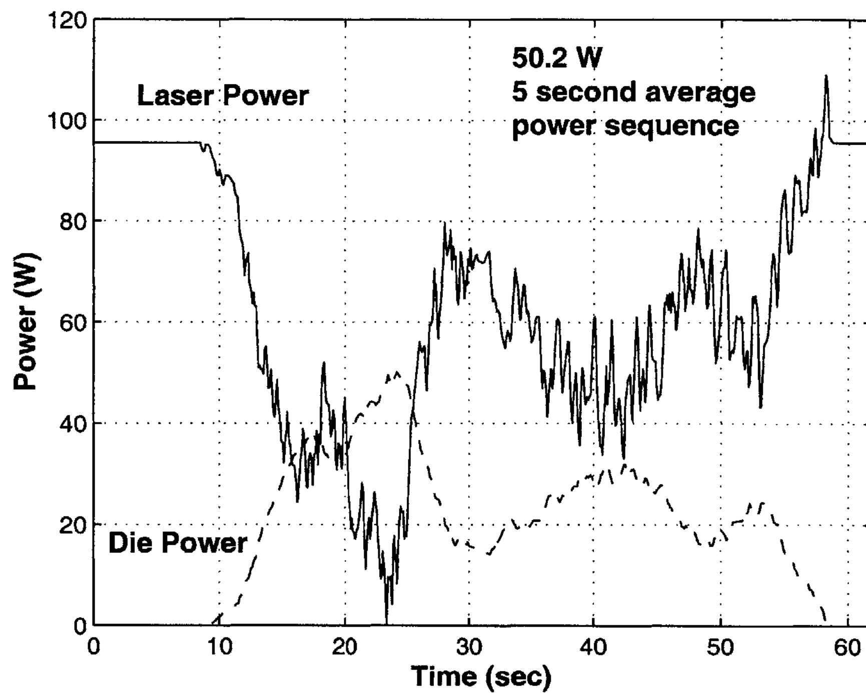

Figure 7-21: Die power and laser power as a function of time for temperature control of a Pinetop TTV with a 5 second average power sequence.

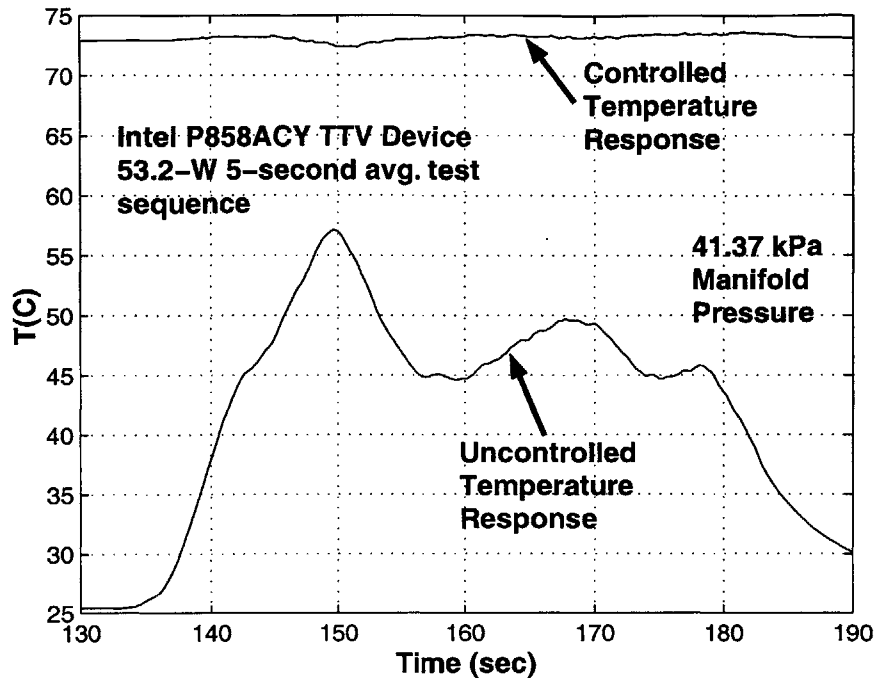

Figure 7-22: Uncontrolled and controlled temperature profile of a P858ACY TTV to the 5 second average power profile with a peak power at 53.2 W.

section of this chapter.

The uncontrolled and controlled temperature response for a P858ACY TTV to the 5 second power sequence is shown in Fig. 7-22. The same tests can be run by scaling this sequence and the limits of control can be found. The results are shown in Fig. 7-23 for a range of power levels up to 53.2 W. The peak control power required to obtain the optimal temperature control can also be plotted versus peak die power as shown in Fig. 7-24. The powers scale linearly with a total laser power to die power ratio of 2.04. There is some temperature variation across the die due to non-uniform conduction and laser illumination effects in the integrated heat spreader. The variation across the die is shown for controlled and uncontrolled test sequences in Fig. 7-25. The die power profile and control power profile used to control the temperature for the 53.2-W 5-second average power profile is shown in Fig. 7-26.

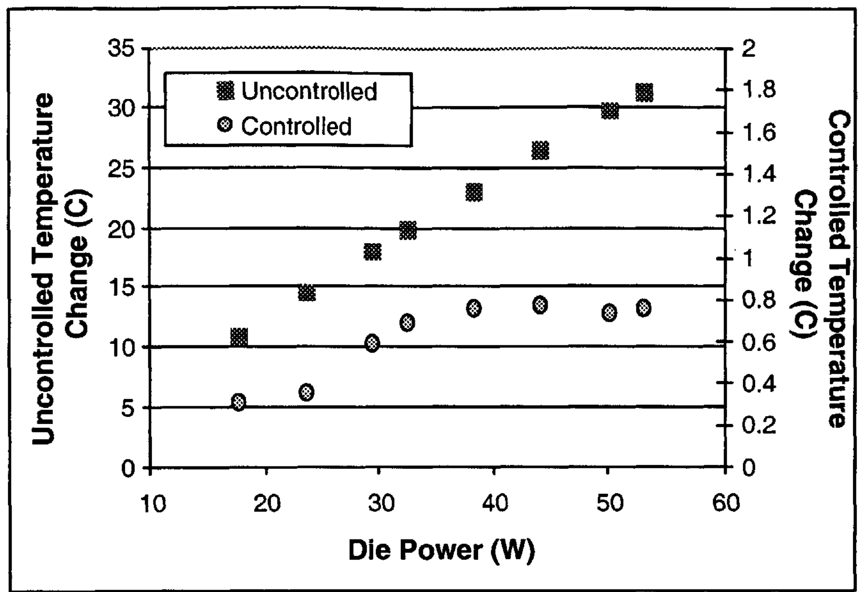

Figure 7-23: Experimental limits of temperature control for 5 second power average with P858ACY TTV.

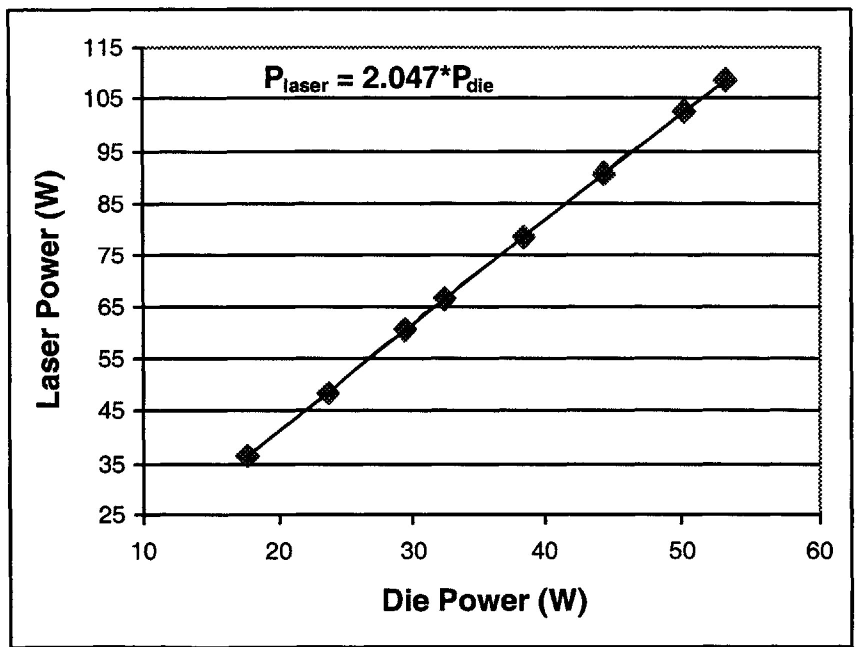

Figure 7-24: Peak control power versus peak die power for 5 second average power sequence on a P858ACY TTV.

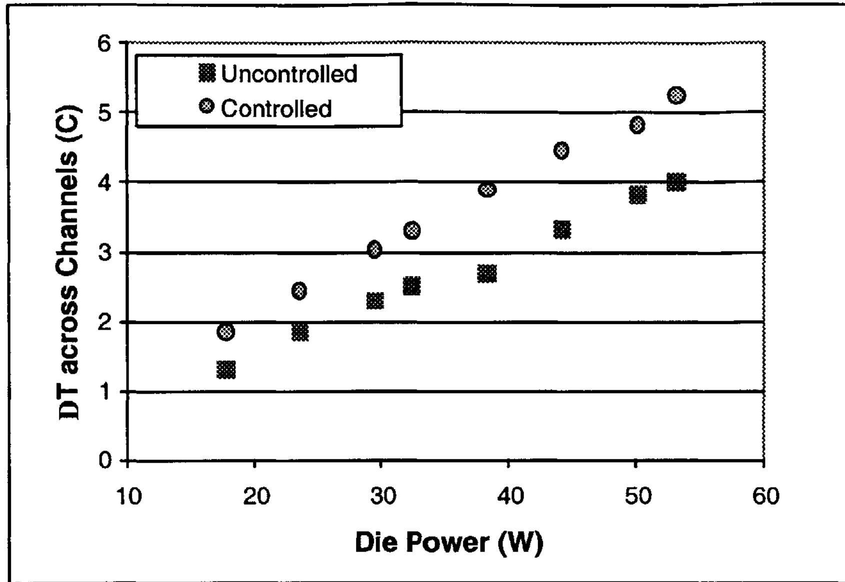

Figure 7-25: P858ACY TTV temperature variation across the die for controlled and uncontrolled 5 second average test sequences.

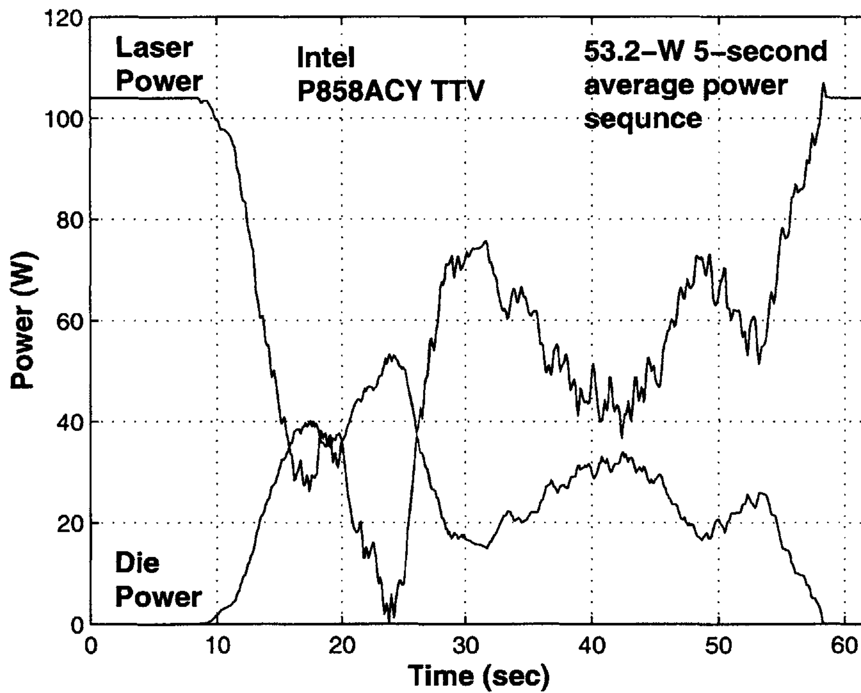

Figure 7-26: Die power and laser power as a function of time for temperature control of a P858ACY TTV with a 5 second average power sequence.

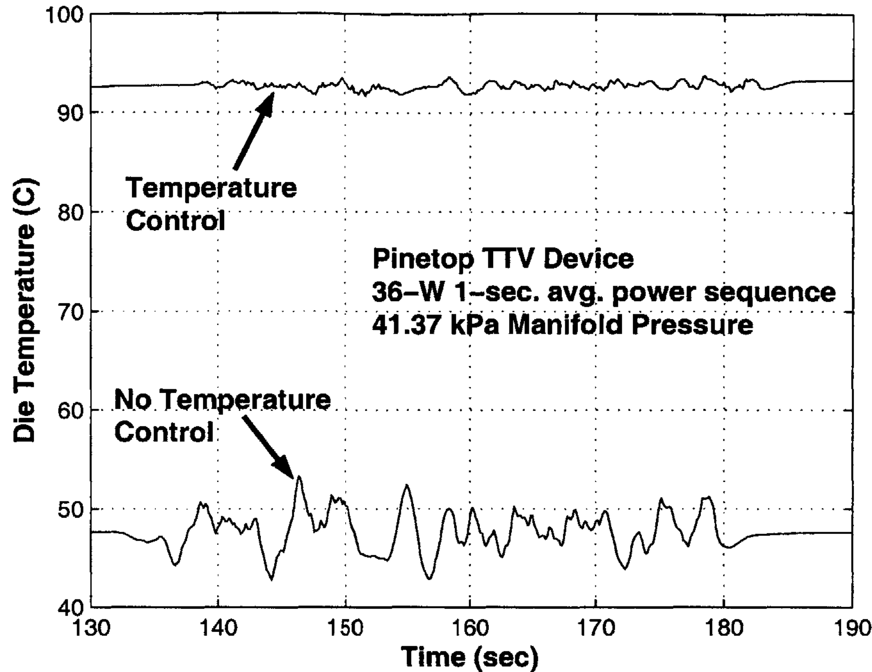

Figure 7-27: Uncontrolled and controlled temperature profile of a Pinetop TTV to the 1 second average power profile with a peak power at 36.0 W.

7.3.2 One Second Average Power Sequence

The 1 second average power sequence can also be scaled up and down and the limits of control can be found experimentally. The uncontrolled and controlled temperature response for a Pinetop TTV to the 1 second power sequence is shown in Fig. 7-27. The die and laser power sequences in this case are offset so the minimum power is zero[4] The same tests can be run by scaling this sequence and the limits of control can be found. The results are shown in Fig. 7-28. The peak control power required to obtain the optimal temperature control can also be plotted versus peak die power as shown in Fig. 7-29. The powers scale linearly with a total laser power to die power ratio of 2.95. The die power profile and control power profile used to control the temperature for the 36-W 1-second average power profile is shown in Fig. 7-30.

The uncontrolled and controlled temperature response for a P858ACY TTV to the 1 second power sequence is shown in Fig. 7-31. The same tests can be run by

[4]The decomposition of the original Intel test sequence results in the 1 second average power sequence as having both positive and negative values. Negative powers are not possible so an offset is added to the power sequence.

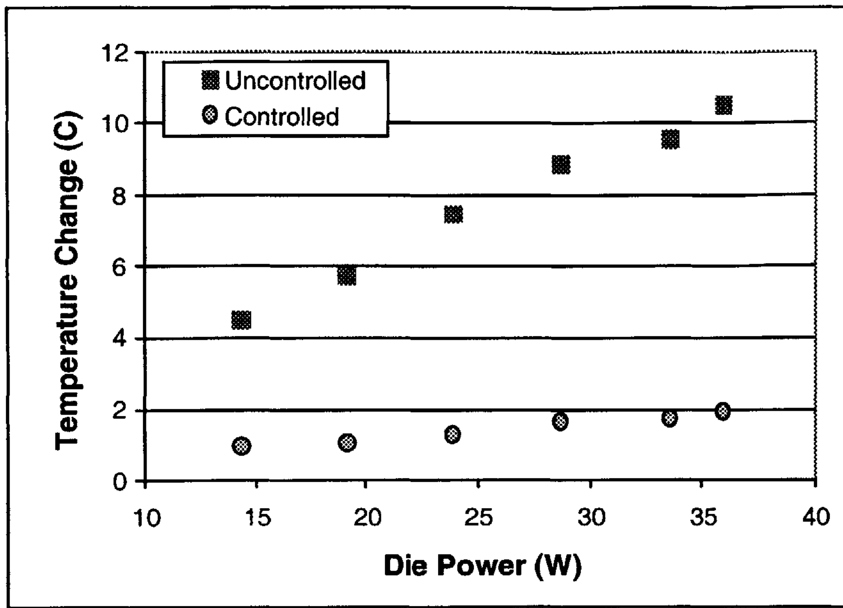

Figure 7-28: Experimental limits of temperature control for the 1 second power average with Pinetop TTV.

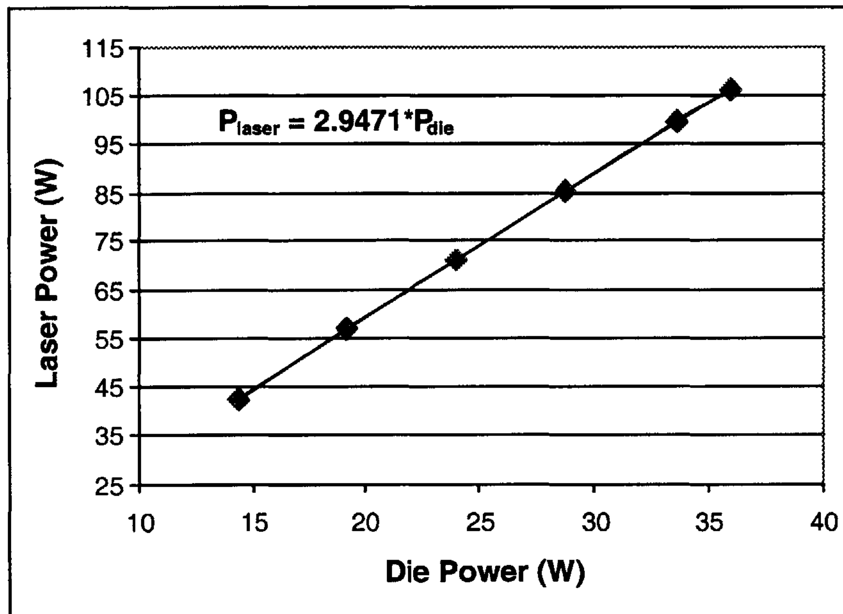

Figure 7-29: Peak control power versus peak die power for the 1 second average power sequence on a Pinetop TTV.

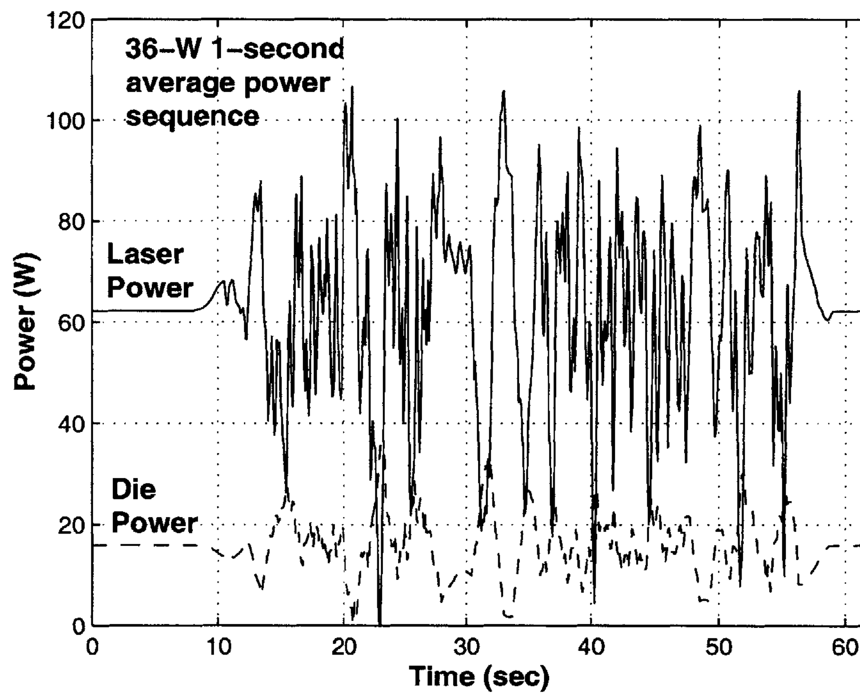

Figure 7-30: Die power and laser power as a function of time for temperature control of a Pinetop TTV with a 1 second average power sequence.

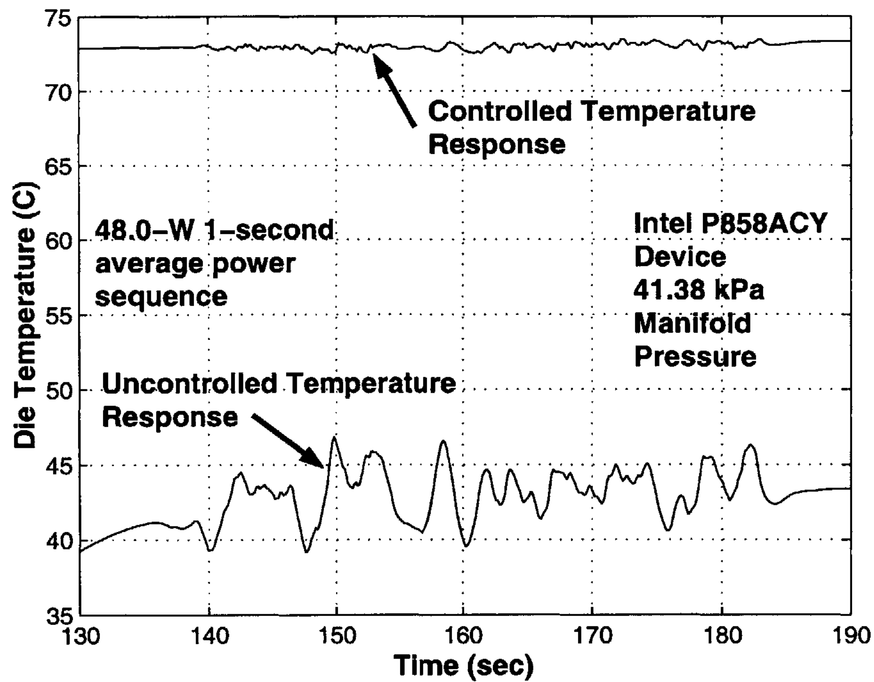

Figure 7-31: Uncontrolled and controlled temperature profile of a P858ACY TTV to the 1 second average power profile with a peak power at 48.0 W.

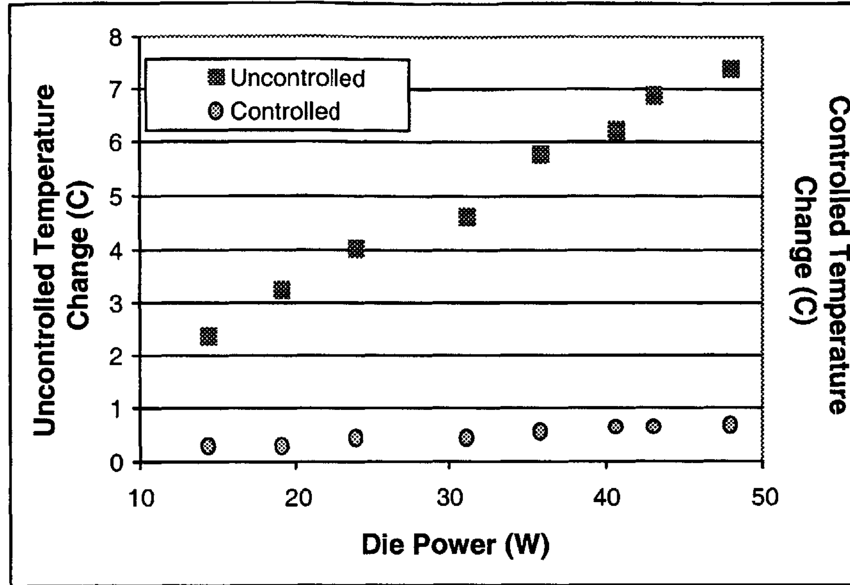

Figure 7-32: Experimental limits of temperature control for the 1 second power average with a P858ACY TTV.

scaling this sequence and the limits of control can be found. The results are shown in Fig. 7-32. The powers scale linearly with a total laser power to die power ratio of 2.25. The die power profile and control power profile used to control the temperature for the 48-W 1-second average power profile is shown in Fig. 7-34.

7.3.3 Remainder Power Sequence

The remainder power sequence consists of higher frequency power fluctuations. A detailed view of the remainder power sequence is shown in Fig. 7-35. The power sequence consists primarily of 5 Hz square waves. Attempts to control the temperature response of the die to this power sequence is fairly difficult due to the large rapid changes in the die power, but also because the limits of the prototype system are being reached. As will be shown in the next chapter, the required phase shift between the control signal and die signal is on the order of 70° to 80°. At 5 Hz, this corresponds to a time lead of around 0.04 seconds. The hardware in the prototype system is not capable of this level of control with the roughest time step being 0.1 seconds. This makes experimental implementation of temperature control on the remainder very difficult with the current prototype system. The uncontrolled and controlled

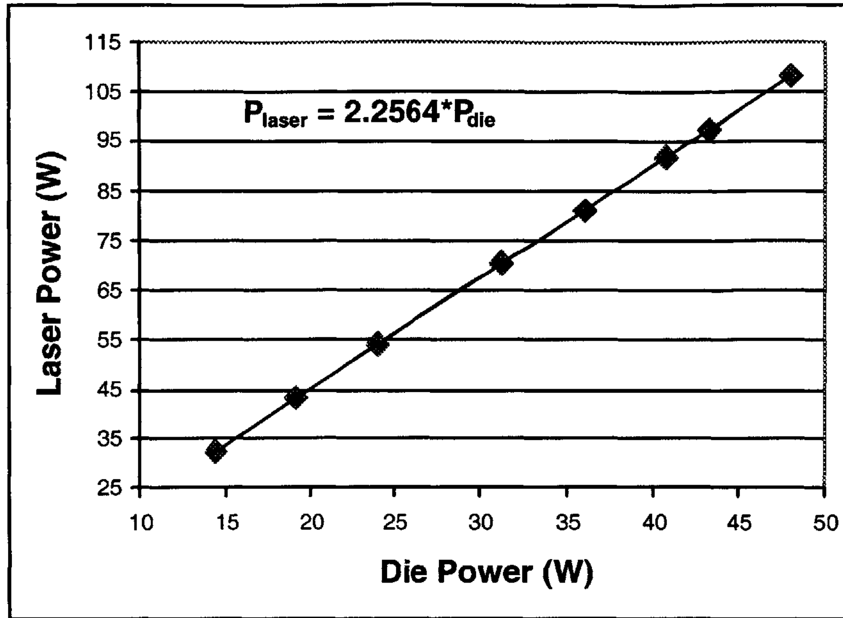

Figure 7-33: Peak control power versus peak die power for the 1 second average power sequence on a P858ACY TTV.

temperature response of a Pinetop TTV to the remainder power sequence is shown in Fig. 7-36. The control sequence has had a slight effect on the temperature of the die, but not very much. The uncontrolled and controlled temperature response of a P858ACY TTV to the remainder power sequence is shown in Fig. 7-37. The attempt at control of the remainder power sequence is more successful for the P858ACY TTV device, but the uncontrolled variation for this device is also less than for the Pinetop TTV device. This is due to much low power densities in the P858ACY device than the Pinetop device.

7.4 Control Sequence Generation

The generation of the control sequence for a given device test sequence is a multi-step process. As has been shown already, the test sequence can be decomposed into a series of component power profiles. The control sequence for each of these profiles can be generated separately and then combined to generate the control sequence for the final test program. The generation of the control signal for the high frequency component is fairly complex because transient conduction through the integrated

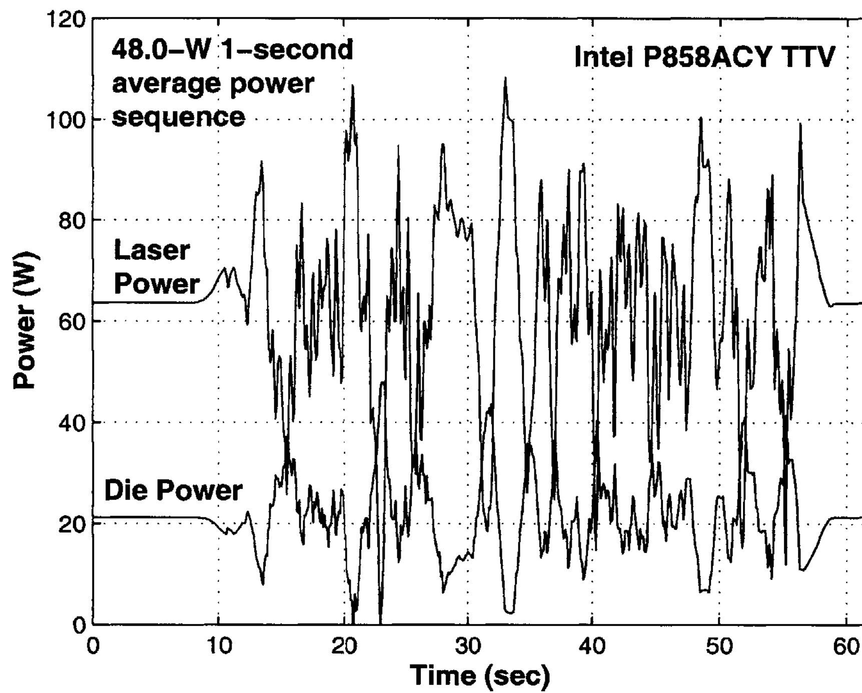

Figure 7-34: Die power and laser power as a function of time for temperature control of a P858ACY TTV with a 1 second average power sequence.

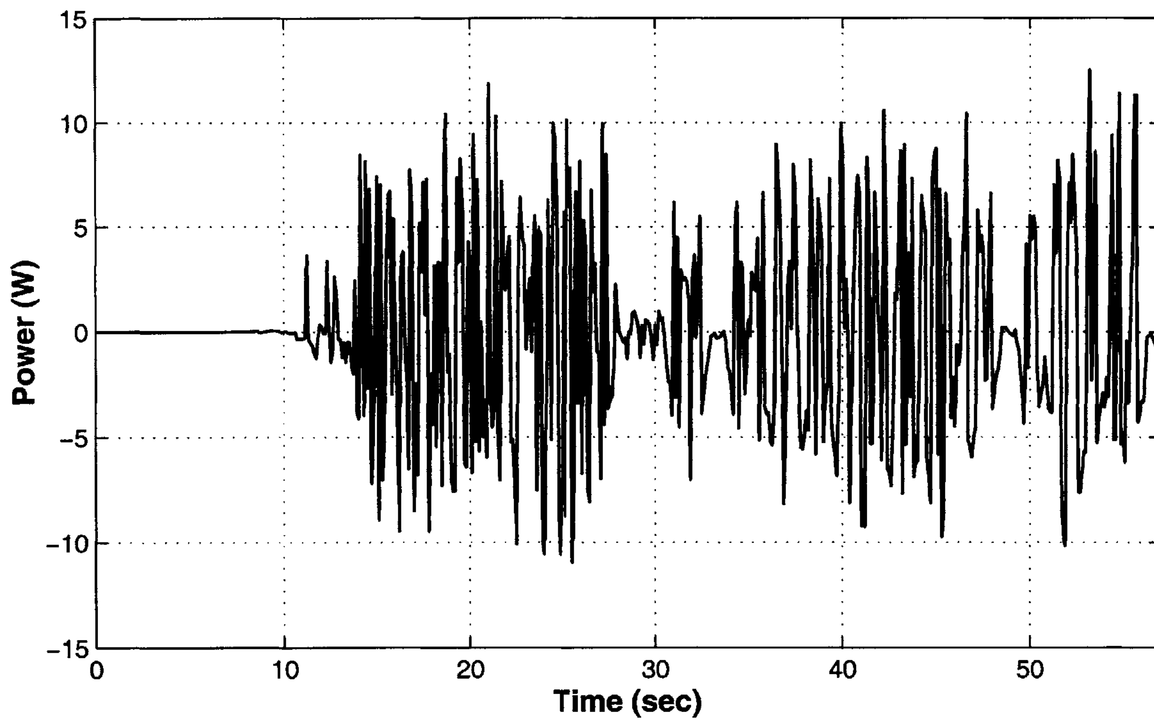

Figure 7-35: Detailed view of remainder power sequence.

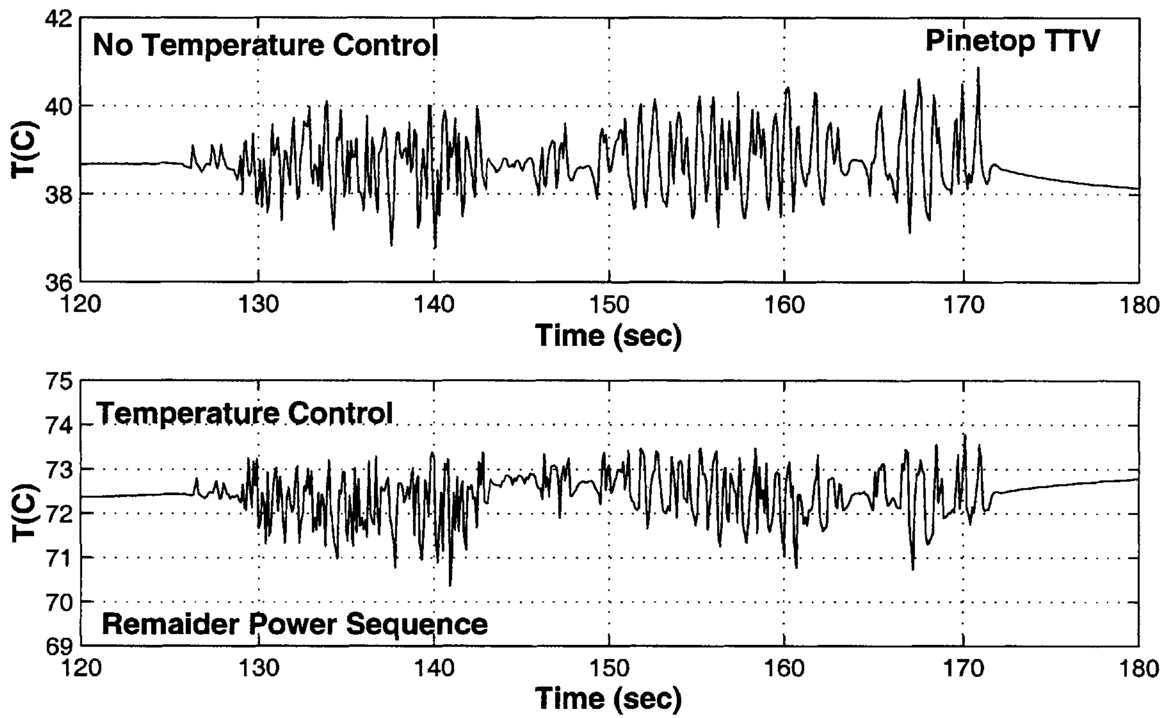

Figure 7-36: Controlled and uncontrolled temperature response of Pinetop TTV die to the remainder power sequence.

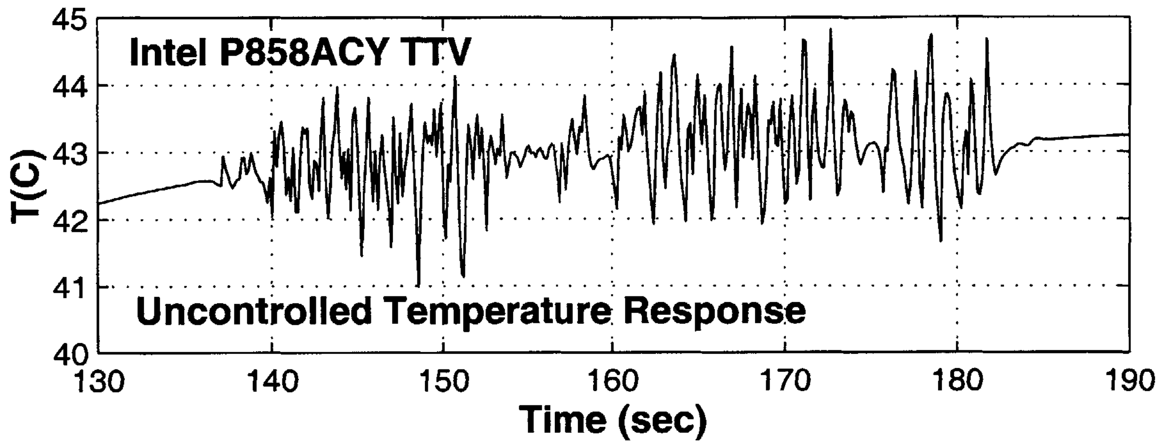

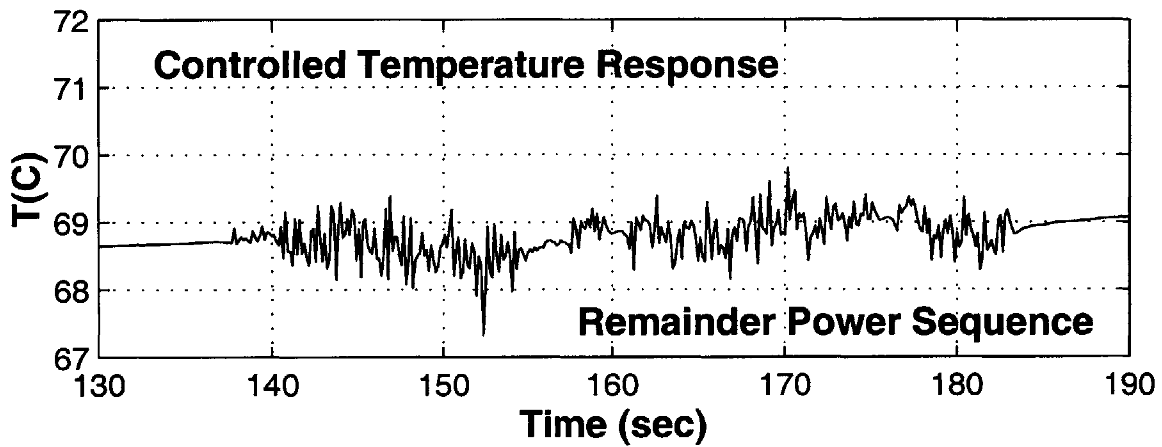

Figure 7-37: Controlled and uncontrolled temperature response of P858ACY TTV die to the remainder power sequence.

heat spreader must be considered. The generation of the required control power and control timing for this high frequency component is covered in detail in the next chapter. The remaining two component power profiles are for the one second and five second average power sequences. The control sequence for each of these profiles can be calculated using energy balance.

A basic model of the system can be generated by assuming the integrated heat spreader is isothermal at any given time. Assuming the temperature of the die remains constant, conservation of energy can be written as

$$Q_d(t) + Q_c(t) + mc_p \frac{dT_{\text{IHS}}(t)}{dt} = hA_s \left(T_{\text{IHS}}(t) - T_{\text{air}}\right) \tag{7.1}$$

where Q_d is the die power, Q_c is the control power, mc_p is the thermal mass of the integrated heat spreader, and h is the convective heat transfer coefficient acting over area A_s. Since the temperature of the die is assumed constant, the equation for conduction between the die and the IHS can be written as

$$Q_{\text{conduction}} = Q_d(t) = \frac{T_{\text{die}} - TIHS(t)}{R_t} \tag{7.2}$$

where R_t is the effective thermal contact resistance between the die and the IHS. This equation can be differentiated with respect to time to obtain an expression for the rate of change of the temperature of the IHS.

$$\frac{dT_{\text{IHS}}(t)}{dt} = -R_t \frac{dQ_d(t)}{dt} \tag{7.3}$$

The remaining unknowns in eqn. 7.1 are the temperature of the IHS and the temperature of the die. The temperature of the IHS can be expressed by rearranging eqn. 7.2 as $T_{\text{IHS}}(t) = T_{\text{die}} - R_t Q_d(t)$ so an expression for the temperature is the only factor missing.

The objective of the temperature control system is to keep the die temperature constant, so if the die temperature can be found at a single instant in time, then the die temperature for all times is known. The absolute minimum die temperature can be found be considering the peak die power. Under steady state conditions at the peak power, the temperature of the die is

$$T_{\text{die}} = \frac{Q_d^{\max}}{hA_s + \frac{1}{R_t}} + T_{\text{air}} \tag{7.4}$$

and the temperature for the IHS can be written as

$$T_{\text{IHS}}(t) = \frac{Q_d^{\max}}{hA_s + \frac{1}{R_t}} + T_{\text{air}} - Q_d R_t \tag{7.5}$$

These definitions can be substituted back into eqn. 7.1 and the results rearranged to obtain the control power.

$$Q_c(t) = hA_s \left[\frac{Q_d^{\max}}{hA_s + \frac{1}{R_t}} - R_t Q_d(t) \right] - mc_p R_t \frac{dQ_d(t)}{dt} - Q_d(t) \tag{7.6}$$

This equation can now be used to calculate the required control profile for any specified test sequence, but the end results will not be perfect and some calibration is required.

The parameters that are unknown in eqn. 7.6 are the thermal mass of the IHS and the effective value of the hA_s term. These values change due to lateral conduction into the edges of integrated heat spreader. A power sequence with a long characteristic time is more affected by lateral conduction than a test sequence with a short characteristic time. The correction factor for this effect can be handled through a series of calibration runs. Taking the base mc_p and hA_s values as the mass and surface area of the IHS directly over the top of the die structure, the values are then changed over a given range until the temperature response of the die to a given power sequence is optimized. It typically took 6-8 runs to optimize the required values for each sequence[5]. For the Pinetop TTV, a thermal mass multiplier of 3.5 was found for the 5 second average, and a thermal mass multiplier of 1.5 was found for the 1 second average. For the P858ACY TTV, the thermal mass multiplier was found to be 1.0 for both 1 and 5 second time average signals. No iteration was required to determine the correct value for the hA_s term. For both TTV devices, using the value corresponding to the correlation value for h (eqn. 6.1) and the area of the die for A_s produce satisfactory results.

One additional parameter was added to the control sequence calculation and calibration. It was found that by adding a multiplier to the derivative term in eqn. 7.6, the end result was easier to calibrate with better results. This multiplier was found to be 1.5 the Pinetop TTV device and 1.1 for the P858ACY device.

7.5 Conclusions

The experimental data clearly shows that the die temperature of a device under test conditions can be controlled using the laser/convection system developed in this

[5]Data was obtained for both TTV devices and for the 5 second and 1 second average power seqences.

thesis. The level of temperature control is a function of device power, power density, laser power, and test sequence design. Any test sequence can be decomposed into a 5 second average, a 1 second average, and a remainder signal. The 5 second and 1 second average control signals can be easily found by inverting the die power signal, correcting for reflection losses, and offsetting the resulting profile by 0.3 seconds for the 5 second average and 0.1 seconds for the 1 second average power signal. Control of the remainder power signal is not really possible with the current prototype system due to control signal propagation speed, but theory will be developed in the next chapter that will present the ideal solution for these high frequency power profiles.

Chapter 8

Thermal Model

This chapter covers the development of theoretical models to examine the control limits of a device under test. The chapter starts with a brief justification for some modeling approximations and then provides two quick solutions for basic control analysis that can be used in rough engineering design work. The chapter then goes on to develop a very detailed model for control limits and discusses the effect of steady state conduction on the overall die temperature solution.

8.1 Isothermal Die Temperature

The temperature of the die is assumed to be isothermal under all conditions. This can be justified by considering an equivalent Biot number for die. Rather than the traditional definition of the Biot number

$$Bi = \frac{h_c L}{k} \tag{8.1}$$

where h_c is the convective heat transfer coefficient, L is an effective thickness of the die, and k conductivity of the die material, the Biot number can be redefined as

$$Bi_R = \frac{L}{R_T A k} \tag{8.2}$$

where R_T is the contact resistance between the die and the integrated heat spreader, A is the die surface area in contact with the IHS[1]. Even taking L as the entire thickness of the die, $L = 200\ \mu\text{m}$, the effective Biot number calculates as

$$Bi_R = \frac{0.2 \times 10^{-4}\ \text{m}}{0.4\ \text{K/W} \cdot 1 \times 10^{-4}\ \text{m}^2 \cdot 148\ \text{W/mK}} = 0.034 \tag{8.3}$$

[1]Integrated heat spreader.

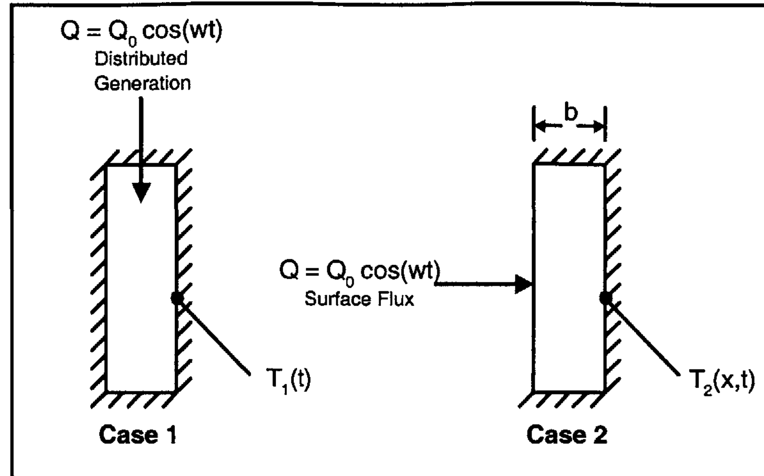

Figure 8-1: Comparison models for proof of isothermal die assumption.

which is far less than the traditional cut-off value of $Bi = 1/6$ below which a mass can be considered isothermal for a lumped capacitance model.

This analysis can be taken one step further. The low effective Biot number indicates that the die temperature can be taken as isothermal in comparison to the temperature between the die and the back face of the integrated heat spreader. This analysis is valid under steady state conditions, but under highly transient die power conditions the temperature profile across the die needs to be considered. The object is to define the conditions where the assumption of isothermal die temperature is valid. To do this, the two extremes will be considered. Both cases will consider an adiabatic die subject to a sinusoidal power profile. One case will assume fully distributed, uniform internal generation within the die, the other case assumes all the energy enters through one face of the die. The temperature response of the die on the contacting face with the IHS will be calculated for both cases and compare. Figure 8-1 shows these two cases. The distributed generation (Case 1) is the ideal isothermal die case and the and the surface flux assumption (Case 2) represents the worst case deviation from the isothermal die assumption. The solution for the temperature profile on the die side surface of Case 1 is easy and straight forward. The temperature profile is simply

$$T_1 = \frac{Q_0}{mc_p\omega} \cos(\omega t) \tag{8.4}$$

where m is the mass of the die, c_p is the specific heat, and ω is the sinusoidal frequency.

The solution for the temperature in case 2 is a little more complicated. The

temperature profile across the die in this case can be written as:

$$T_2(x,t) = \frac{2Q}{kL\left[D^2+E^2\right]}$$
$$\left(\mathrm{e}^{-xL}\left[D\cos\left(\omega t-xL\right)+E\sin\left(\omega t-xL\right)\right]+e^{xl}\left[D\cos\left(\omega t+xL\right)+E\sin\left(\omega t+xL\right)\right]\right) \tag{8.5}$$

where the coefficients D and E are calculated from

$$D = \mathrm{e}^{bL}\left[\cos\left(bL\right)-\sin\left(bL\right)\right]-\mathrm{e}^{-bL}\left[\cos\left(bL\right)+\sin\left(bL\right)\right] \tag{8.6}$$

$$E = \mathrm{e}^{b*L}\left[cos\left(bL\right)+\sin\left(bL\right)\right]-\mathrm{e}^{-bL}\left[\cos\left(bL\right)-\sin\left(bL\right)\right] \tag{8.7}$$

where b is the thickness of the die. By comparing the magnitude of the temperature fluctuation on the IHS side of the die, the assumption of isothermal die can be checked. Figure 8-2 shows the magnitude of the temperature fluctuation on the IHS side surface of the die for both cases. The only noticeable difference between the two cases starts to occur around 300 Hz, so the assumption of isothermal die is valid up to at least 300 Hz. There is a phase shift between the power signal and the temperature profile for both cases. For the distributed generation case, this phase shift is constant at 90° for all frequencies. For the case with surface flux, the phase shift becomes a function of frequency. This phase shift is plotted against frequency in Fig. 8-3.

The assumption of isothermal die temperature is valid up to sinusoidal power frequencies of at least 300 Hz. As will be shown later, this frequency is well above the signal frequency that needs to be considered for the hardware used in this project. The phase shift between the power signal and die temperature need to be considered at frequencies greater than $\sim$ 200 Hz.

8.2 Surface Absorption of Incident Radiation

For the devices considered in this thesis, the top surface upon which the radiation is incident upon is nickel coated copper. Ordal et.al. [7] has found the surface reflectivity of this surface to be on the order of 0.6 for the wavelength of the lasers used ($\lambda =$ 0.81 μm). The actual value will depend on the surface conditions of each device. The absorption coefficient for nickel coated copper is 10^5 cm^{-1}. Recalling from the infrared heating section, the incident radiation absorption over a material length s is

$$I_a = (1-\rho_\lambda)I_0(1-\mathrm{e}^{-\kappa_\lambda s}) \tag{8.8}$$

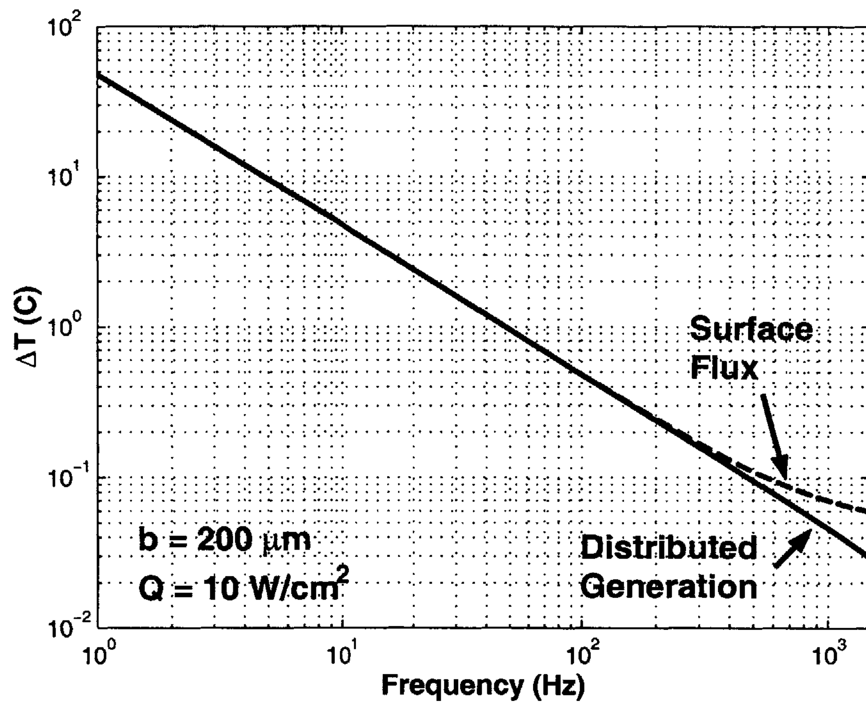

Figure 8-2: Magnitude of temperature fluctuation for distributed generation and surface flux on adiabatic die structure.

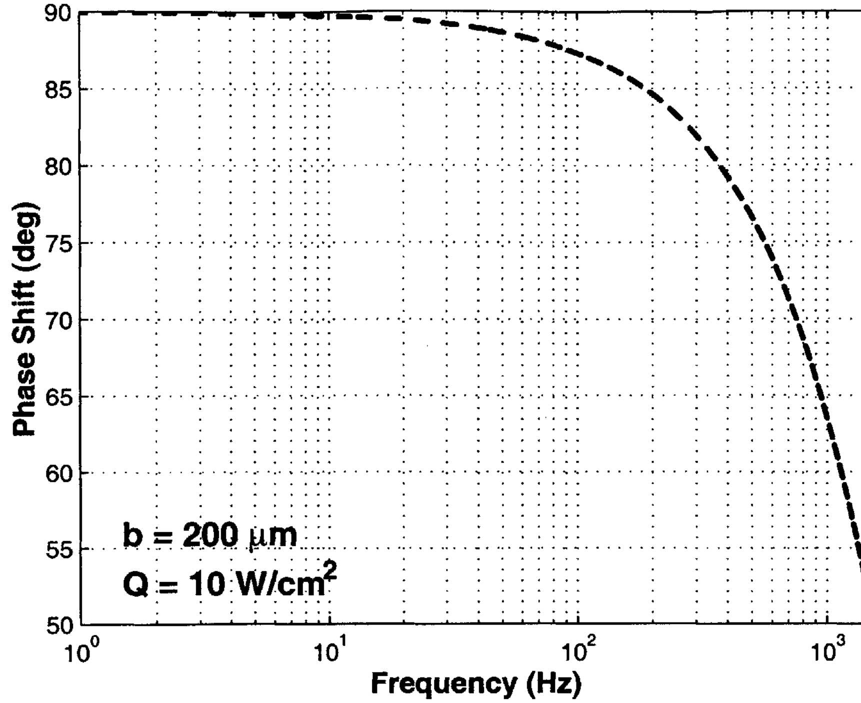

Figure 8-3: Phase shift of IHS side temperature for surface flux case.

where κ_λ is the spectral absorption coefficient, ρ_λ is the spectral surface reflectivity, and I_0 is the incident radiation intensity. Taking $I_s = I_0(1 - \rho_\lambda)$ as the surface radiation that enters the material, the material length over which 99.9% of the radiation is absorbed can be found using

$$s = \frac{-\ln\left(1 - \frac{I_a}{I_s}\right)}{\kappa_\lambda} \tag{8.9}$$

For the nickel coated copper heat spreaders, the material depth over which 99.9% of the surface radiation is absorbed is 6.9 μm. This is much smaller than the thickness of the heater spreaders ($\sim$ 1.8 mm) so the assumption that all of the radiation is absorbed at the surface of the device is reasonable. This calculation will hold true for all metals and wavelengths, but may have to be reconsidered for non-metallic surface materials.

8.3 Control Limits

8.3.1 Die Cut Off Frequency

There is a die power frequency above which no control is necessary because the temperature of the die will not vary beyond the limits of stated control goals. This cut off frequency is dependent on the mass of the die, specific heat of the die, input power, and resistance to surrounding thermal masses. To determine this cut off frequency, the input power profile is assumed to be a step function of magnitude Q that lasts for time t. The mass of the die is m with a specific heat c_p, and R_T is the thermal resistance from the die to the surrounding environment. For this analysis, the surrounding environment is assumed to be at a constant isothermal temperature. The tolerance goal for temperature control is ΔT with the ambient temperature taken to be zero for convenience. The differential equation describing the temperature of the die with these assumptions is

$$mc_p \frac{dT}{dt} = Q - \frac{T}{R_T} \tag{8.10}$$

which can be easily solved using an integrating factor of the form $\exp(t/mc_pR_T)$ and integrated from time zero to t to get

$$\Delta T = Q \cdot R_T \left(1 - e^{\frac{-t}{mc_pRT}}\right) \tag{8.11}$$

which can be solved for the maximum length of time for a given maximum ΔT. Solving for this time results in

$$t = mc_pR_T \ln\left(1 + \frac{\Delta T}{Q \cdot R_T}\right) \tag{8.12}$$

which, when inverted, will produce a frequency above which control does not have to be considered.

For the Intel P858ACY TTV, this cut off frequency can be calculated based on a die mass of 0.20 g. Taking the thermal resistance between the die and the integrated heat spreader as 0.42 Kcm^2/W, the die cut off frequency can be plotted versus die power (Fig. 8-4) for a number of temperature tolerance levels. A similar plot for the Intel Pine-Top TTV is shown in Fig. 8-5. As is expected, the Pine-Top TTV die has a greater cut off frequency than the P858ACY TTV at all power levels and temperature tolerances. This indicates that the Pine-Top TTV is more sensitive to changes in internal generation than the P858ACY TTV. This is expected since the Pine-Top TTV has a smaller thermal mass than the P858ACY TTV.

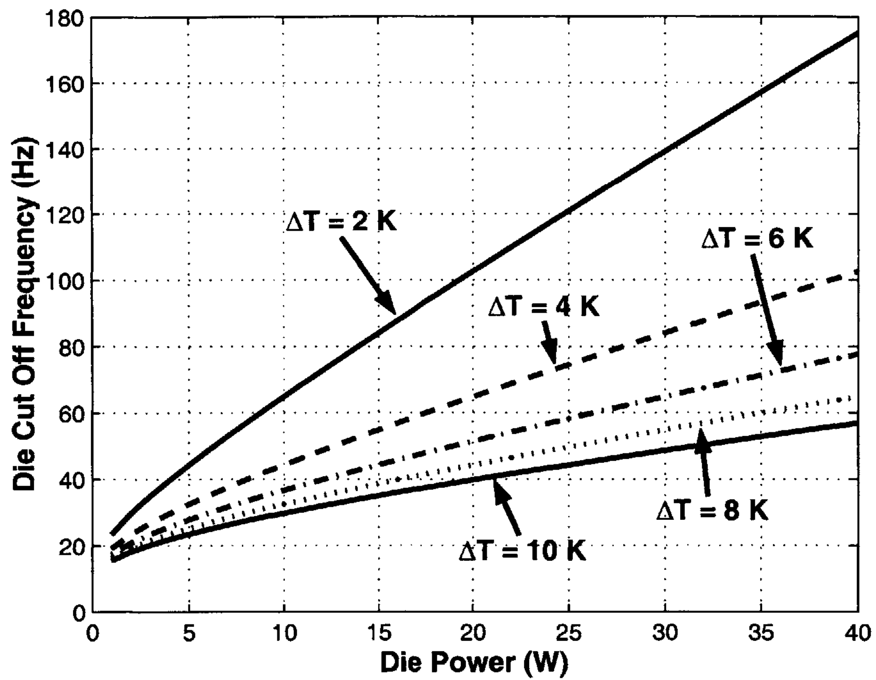

Figure 8-4: Die cut off frequency for the Intel P858ACY TTV at various temperature tolerance levels and power levels.

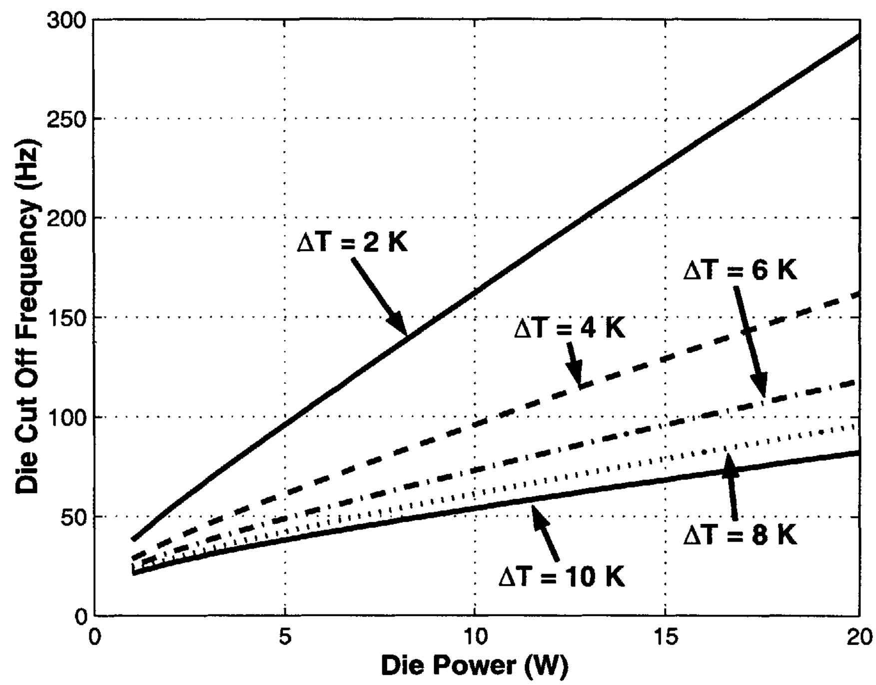

Figure 8-5: Die cut off frequency for the Intel Pine-Top TTV at various temperature tolerance levels and power levels.

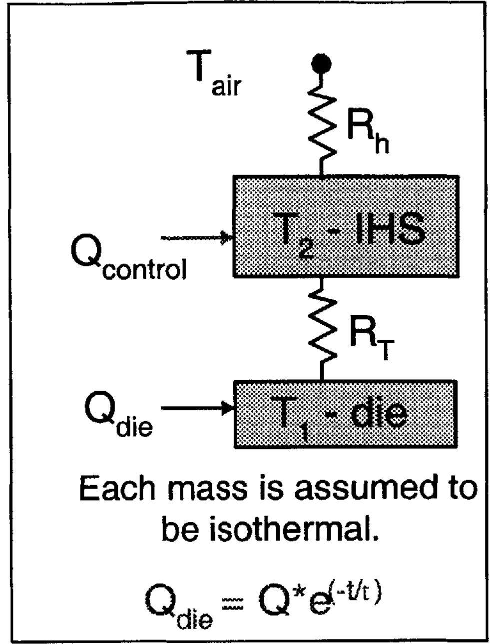

Figure 8-6: Physical model for die power to control power ratio calculation.

8.3.2 Die Power to Control Power Estimation

Along with a frequency response, information is needed to determine how the control power needs to scale compared to the die power. This section describes a quick method to determine a rough scaling for ideal temperature control[2]. It has already been shown that the die can be assumed isothermal. The integrated heat spreader cannot in general be assumed isothermal because of the highly transient conduction through it's thickness. A detailed analysis of this conduction will be performed in section 8.4, but a quick estimate of the control power required for a specified die power can be made if the IHS is assumed to be isothermal.

Now the die and integrated heat spreader are considered to be two isothermal masses as shown in Fig. 8-6. The die power input is assumed to be a negative exponential step profile[3] with magnitude Q with an associated time constant τ. The differential equation describing the temperature of the die in Fig. 8-6 can be written

[2]Ideal temperature control meaning the temperature change of the die is zero.

[3]An exponential step profile is a change between two power levels, with an exponential decay between the values with some characteristic time constant.

as:

$$K_1 K_2 R_T \frac{d^2 T_1}{dt^2} + \left(K_1 + K_2 + \frac{K_1 R_T}{R_h} \right) \frac{dT_1}{dt} + \frac{T_1}{R_h} = Q_2 + Q_1 \left(1 + \frac{R_t}{R_h} \right) + K_2 R_T \frac{dQ_1}{dt} + \frac{T_{air}}{R_h} \tag{8.13}$$

For this equation, $K_1 = m_1 \cdot c_{p_1}$ and similarly $K_2 = m_2 \cdot c_{p_2}$. By setting all derivatives of T_1 to zero and solving for the control power profile Q_2 yields

$$Q_2(t) = \frac{T_1 - T_{air}}{R_h} - Q_1 \left(1 - \frac{K_2 R_T}{\tau} \right) \exp\left(\frac{-t}{\tau} \right) + \frac{Q_1 R_T}{R_h} \exp\left(\frac{-t}{\tau} \right) \tag{8.14}$$

if the control input is assumed to be of the form $q_1 = Q_1(1 - \exp(-t/\tau))$. The first term in eqn. 8.14 is the final steady state value of the control power. By setting $t = 0$, the peak control power required can be calculated as

$$Q_2 = \frac{T_1 - T_{air}}{R_h} - Q_1 + \frac{Q_1 R_T}{R_h} + \frac{K_2 R_T Q_1}{\tau} \tag{8.15}$$

The most important term in eqn. 8.15 is the last term which has τ in the denominator. As the exponential time constant of the die power decreases, the control power increases. The control power ratio for the Pine-Top TTV is shown in Fig. 8-7.

As can be seen, based on this model the power ratios become very large for short time constants, with the ratio increasing as $m_2 c_{p_2} R_T / \tau$ increases. This parameter is independent of the control method or convection conditions of the surface and is strictly a function of the physical parameters of the device. As the applied die power signal approaches a step function[4], the control power required quickly becomes too large to be considered reasonable. The resulting power profile for a 1 W step in die power with a time constant of 0.025 seconds in presented in Fig. 8-8.

The model in Fig. 8-6 can also be used to estimate the temperature response of the die to a prescribed set of die and control power profiles. The Laplace transform $\mathbb{L}$ and Laplace operator s are defined as [28]:

$$\mathbb{F}(s) = \mathbb{L}(f(x), s) = \int_0^\infty f(x)\, e^{-sx}\, dx \tag{8.16}$$

Then in Laplace form, the solution to the temperature of the die takes on the form of

$$\mathbb{T}_1(s) = \frac{C \mathbb{L}(q_2)}{s^2 + As + B} - \frac{[D - sE] \mathbb{L}(q_1)}{s^2 + As + B} + \frac{B \cdot T_{air}}{s [s^2 + As + B]} \tag{8.17}$$

[4] τ gets smaller

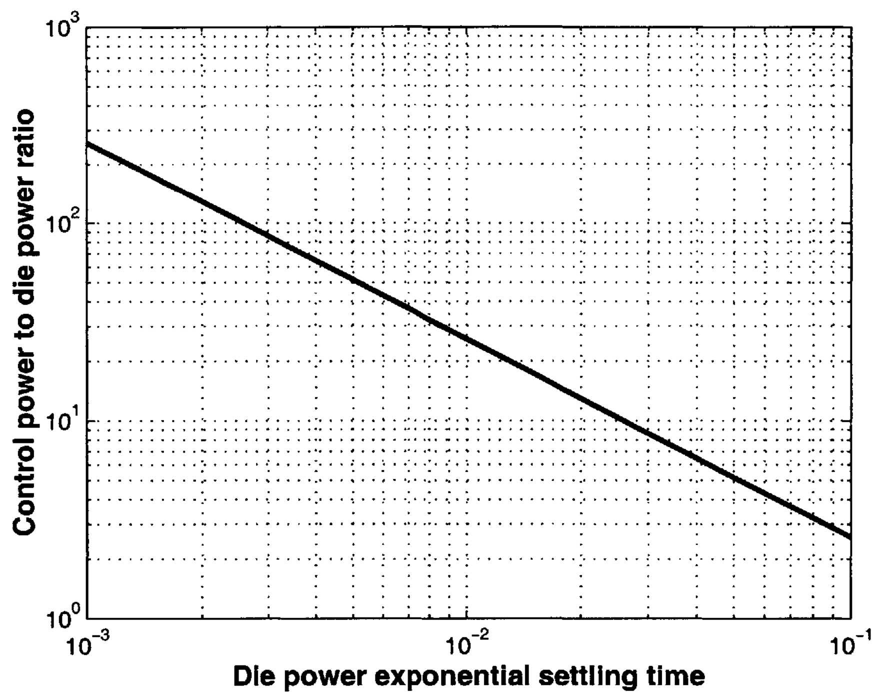

Figure 8-7: Control power to die power ratio versus exponential settling times of the die power for the Intel Pinetop TTV.

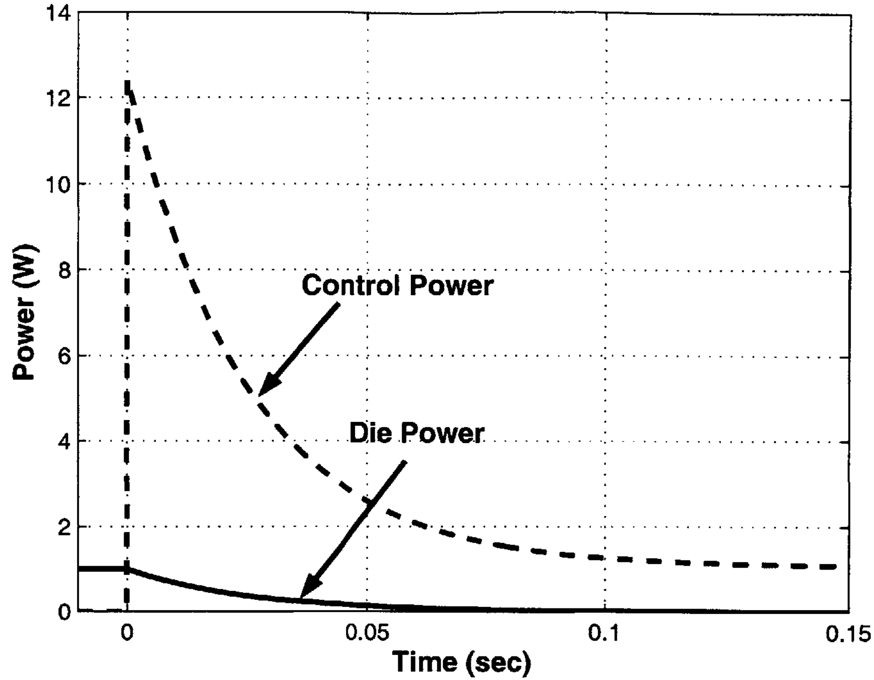

Figure 8-8: Die power and control power for dual mass model based on $\tau = 0.025$ sec.

where the parameters are given by:

$$A = \frac{K_1 + K_2 + \frac{R_T \cdot K_1}{R_h}}{K_1 \cdot K_2 \cdot R_T} \tag{8.18}$$

$$B = \frac{1}{K_1 \cdot K_2 \cdot R_T \cdot R_h} \tag{8.19}$$

$$C = \frac{1}{K_1 \cdot K_2 \cdot R_T} \tag{8.20}$$

$$D = \frac{1 + \frac{R_T}{R_h}}{K_1 \cdot K_2 \cdot R_T} \tag{8.21}$$

$$E = \frac{1}{K_1} \tag{8.22}$$

Assuming the die power is of the form $q_1 = Q_1\,(1 - \exp(-t/\tau_1))$ and the control power is of the form $q_2 = Q_{2p}\exp(-t/\tau_2) + Q_{2ss}$, the resulting Laplace inversion of eqn. 8.17 will result in a solution consisting of a sum of four exponentials. Defining a_1 and a_2 as the solutions[5] to $s^2 + As + B = 0$, $b_1 = 1/\tau_1$, and $b_2 = 1/\tau_2$, the solution to the

[5]Solutions to the quadratic are assumed to be real and distinct.

die temperature can be written in the following general form:

$$
\begin{aligned}
T_1(t) = & \frac{C \cdot Q_{2p}\left[(a_2 - a_1) - a_2 \exp(-a_1 t) + a_1 \exp(-a_2 t)\right]}{a_1 a_2^2 - a_1^2 a_2} \\
& + \frac{C \cdot Q_{2ss}\left[(a_2 - a_1)\exp(-b_2 t) + (b_2 - a_2)\exp(-a_1 t) + (a_1 - b_2)\exp(-a_2 t)\right]}{(b_2 - a_1)\cdot(a_1 - a_2)\cdot(a_2 - b_2)} \\
& - \frac{Q_1 \cdot D\left[(a_2 - a_1)\exp(-b_1 t) + (b_1 - a_2)\exp(-a_1 t) + (a_1 - b_1)\exp(-a_2 t)\right]}{(b_1 - a_1)\cdot(a_1 - a_2)\cdot(a_2 - b_1)} \\
& - \frac{Q_1 \cdot E\left[b_1(a_1 - a_2)\exp(-b_1 t) + a_1(a_2 - b_1)\exp(-a_1 t) + a_2(b_1 - a_1)\exp(-a_2 t)\right]}{(b_1 - a_1)\cdot(a_1 - a_2)\cdot(a_2 - b_1)} \\
& + \frac{B \cdot T_{air}\left[(a_2 - a_1) - a_2 \exp(-a_1 t) + a_1 \exp(-a_2 t)\right]}{a_1 a_2^2 - a_1^2 a_2} \qquad (8.23)
\end{aligned}
$$

This equation is valid where the air temperature is set such that the initial die temperature is zero[6]. This equation can be used to find the temperature of the die if a non-ideal control power profile is used.

8.4 Transient Control Limits

The question arises as to whether a fundamental limit exists to the level of temperature control possible for a packaged device. This question can actually be broken into two separate parts that can be approached in different ways. The first question is whether temporal leading of the control power versus the die power will enable optimal control. This can be addressed by an analysis of temperature control limits when the die power profile in the test sequence is known in advance. This allows leading the control power in order to obtain optimal control. The second part of the control limit analysis will be for the situation where no prior knowledge of the die power profile exists, and all control must be maintained through traditional feedback methods.

8.4.1 Temperature Response to Die and Control Inputs

A full mathematical analysis of multi-dimensional transient conduction becomes very difficult, if not impossible, to solve in closed form. For this reason, a number of simplifying assumptions need to be made about the device under test and operating

[6]This requires a negative air temperature. This assumption simplifies the form of eqn. 8.23 and the solution can be simply offset up or down to match desired operating temperatures. $T_f(t) = T_1(t) + T_{\text{air}}$

conditions. The goal of this analysis is to determine the limits of temperature control under typical transient die power fluctuations, so only transient effects will be considered. The steady state (DC component) of the temperature response of the system will be neglected. The system is assumed to be one-dimensional. This assumption is equivalent to neglecting the effect of lateral conduction in the integrated heat spreader. A justification and a correction factor for this approximation will be presented at the end of this section. Conduction from the die into the interposer assembly will be neglected. The interface resistance between the die and the integrated heat spreader is known, but the thermal mass of the interface material used to produce this interface is neglected. The die is assumed to be isothermal with uniform internal generation.

The system has now been reduced to the system shown in Fig. 8-9. There is a die power profile that is assumed to be sinusoidal at a fixed frequency and magnitude. There is a control profile that is also sinusoidal, at the same frequency with some specified phase shift and magnitude. The front face of the integrated heat spreader is also subjected to a convective heat transfer condition that is assumed constant in time.

To start the analysis, just the temperature profile within the integrated heat spreader (IHS) will be considered. This problem can be further broken down into two parts, the results of which can be combined using superposition. The first part is for the IHS with an adiabatic back face[7] and a front surface subject to convection and the control power profile. The second part is for the IHS with an imposed surface flux from the die on one face and convection on the other face. These two problems and the coordinate systems used in the solution are shown in Fig. 8-10.

The steady periodic transient response to case 1 and 2 can be calculated using a number of methods. The method chosen for this analysis is a complex temperature approach. A full description of this method can be found in Carslaw and Jaeger [8]. The solution for case 1 takes on the form[8]

$$T_1(x,t) = \frac{Q_d \cdot e^{-x \cdot L}}{P_1^2 + R_1^2} \left[U_1 \cdot \cos\left(\omega t - x \cdot L\right) - V_1 \sin\left(\omega t - x \cdot L\right) \right] + \frac{Q_d \cdot e^{x \cdot L}}{P_1^2 + R_1^2} \left[P_1 \cos\left(\omega t + x \cdot L\right) + R_1 \sin\left(\omega t + x \cdot L\right) \right] \quad (8.24)$$

where Q_d is the transient die flux in W/m^2. The parameters in this equation are as

[7] Die side face is assumed adiabatic.

[8] Derivation of the solution is shown in Appendix A.

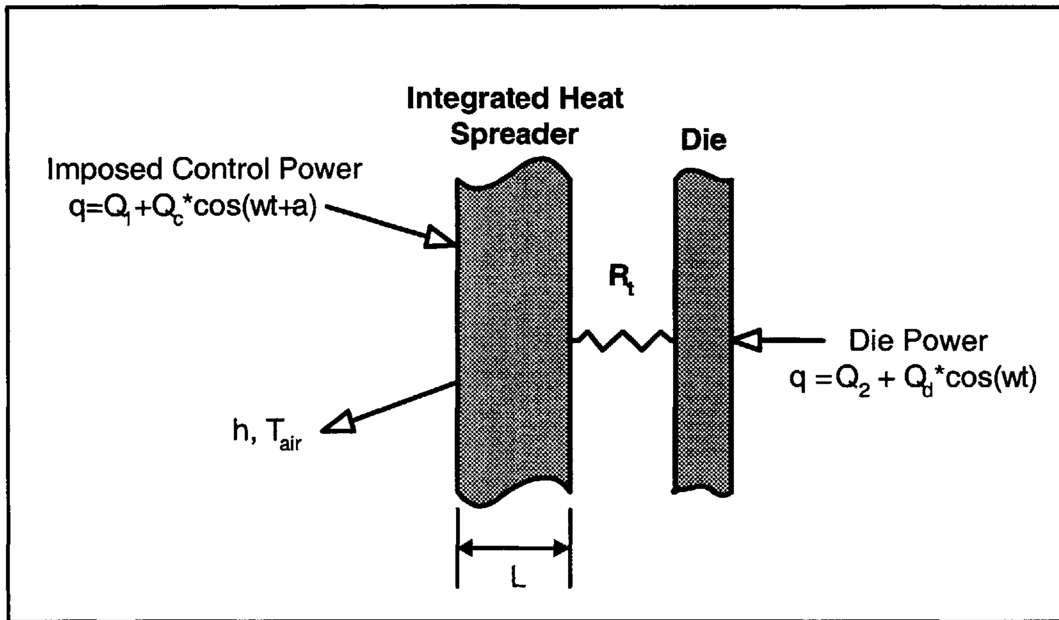

Figure 8-9: Schematic diagram of simplified device for transient analysis. Q_c is the magnitude of the control input and a is the phase shift of the control input. Q_d is the magnitude of the die power profile.

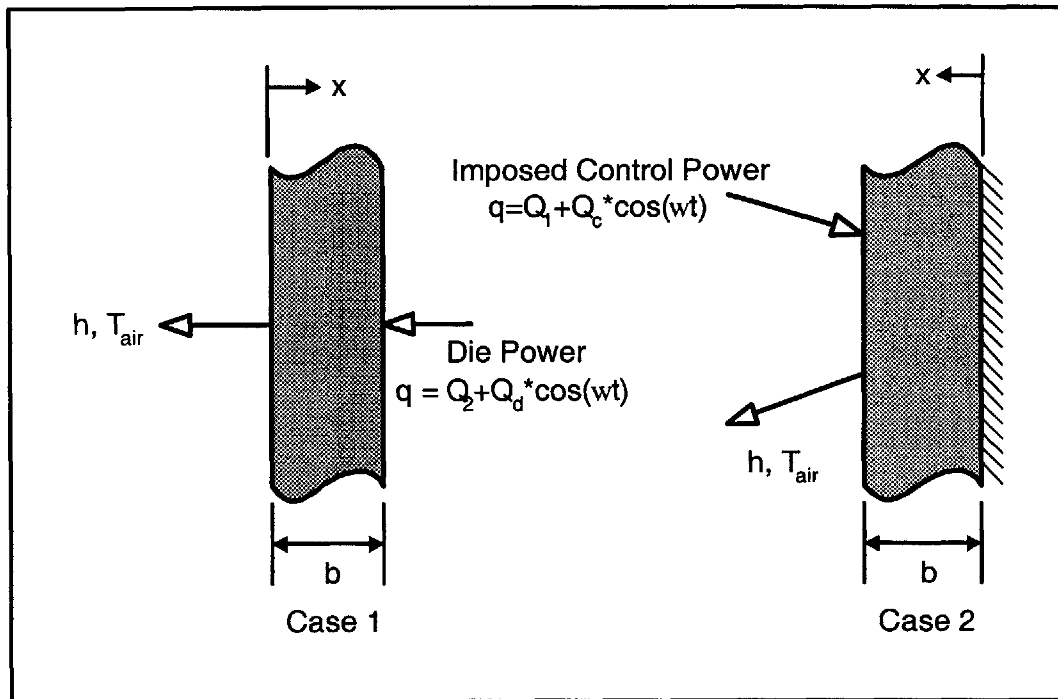

Figure 8-10: Schematic drawing of decomposition for solution to transient temperature profile in integrated heat spreader.

follows:

$$L = \sqrt{\frac{\omega}{2a_t}} \tag{8.25}$$

$$A_1 = h + k \cdot L \tag{8.26}$$

$$B_1 = k \cdot L - h \tag{8.27}$$

$$D_1 = A_1^2 + (k \cdot L)^2 \tag{8.28}$$

$$E_1 = A_1 \cdot B_1 + (k \cdot L)^2 \tag{8.29}$$

$$F_1 = A_1 \cdot k \cdot L - B_1 \cdot k \cdot L \tag{8.30}$$

$$M_1 = E_1 - F_1 \tag{8.31}$$

$$N_1 = E_1 + F_1 \tag{8.32}$$

$$P_1 = k \cdot L \cdot e^{b \cdot L} [\cos(b \cdot L) - \sin(b \cdot L)] - \frac{k \cdot L \cdot e^{-b \cdot L}}{D_1} [M_1 \cos(b \cdot L) + N_1 \sin(b \cdot L)] \tag{8.33}$$

$$R_1 = k \cdot L \cdot e^{b \cdot L} [\sin(b \cdot L) + \cos(b \cdot L)] + \frac{k \cdot L \cdot e^{-b \cdot L}}{D_1} [M_1 \sin(b \cdot L) - N_1 \cos(b \cdot L)] \tag{8.34}$$

$$U_1 = \frac{P_1 \cdot E_1 + R_1 \cdot F_1}{1} \tag{8.35}$$

$$V_1 = \frac{P_1 \cdot F_1 - E_1 \cdot R_1}{D_1} \tag{8.36}$$

The solution for case 2 takes on the form

$$T_2(x,t) = \frac{Q_c \cdot e^{b \cdot L - x \cdot L}}{A_2^2 + B_2^2} [A_2 \cos(\omega t - x \cdot L) + B_2 \sin(\omega t - x \cdot L)] + \frac{Q_c \cdot e^{b \cdot L + x \cdot L}}{A_2^2 + B_2^2} [A_2 \cos(\omega t + x \cdot L) + B_2 \sin(\omega t + x \cdot L)] \tag{8.37}$$

$$A_2 = h\, e^{-b \cdot L} \cos(b \cdot L) + h\, e^{b \cdot L} \cos(b \cdot L) - kL\, e^{-b \cdot L} \cos(b \cdot L) - kL\, e^{-b \cdot L} \sin(b \cdot L) + kL\, e^{b \cdot L} \cos(b \cdot L) - kL\, e^{b \cdot L} \sin(b \cdot L) \tag{8.38}$$

$$B_2 = -h\, e^{-b \cdot L} \sin(b \cdot L) + h\, e^{b \cdot L} \sin(b \cdot L) - kL\, e^{-b \cdot L} \cos(b \cdot L) + kL\, e^{-b \cdot L} \sin(b \cdot L) + kL\, e^{b \cdot L} \sin(b \cdot L) + kL\, e^{b \cdot L} \sin(b \cdot L) \tag{8.39}$$

where $L = \sqrt{\omega / 2a_t}$ as in the solution for case 1.

The solution for the combined systems can be obtained simply by adding[9] the results from eqn. 8.24 and eqn. 8.37. With this result, for any specified die flux Q_d, the required control power profile can be calculated for any desired temperature profile at a given point. The information required to determine the control power profile is the magnitude Q_c and the phase shift α between the control input and the die input. For example, to obtain a constant temperature at the die contact point on the integrated heat spreader, the magnitude and phase shift of the control signal can be found by solving the equation:

$$\begin{aligned}[PS_2 \cdot A_2 \cos(\alpha) + PS_2 \cdot B_2 \sin(\alpha)] \cdot Q_c \cos(\omega t) + PS_1 \cdot U_1 \, \mathrm{e}^{-b \cdot L} \cos(b \cdot L) \cos(\omega t) \\ + PS_1 \cdot V_1 \, \mathrm{e}^{-b \cdot L} \sin(b \cdot L) \cos(\omega t) + PS_1 \cdot P_1 \, \mathrm{e}^{b \cdot L} \cos(b \cdot L) \cos(\omega t) \\ + PS_1 \cdot R_2 \, \mathrm{e}^{b \cdot L} \sin(b \cdot L) \cos(\omega t) \\ + [PS_2 \cdot B_2 \cos(\alpha) - PS_2 \cdot A_2 \sin(\alpha)] \cdot Q_c \sin(\omega t) + PS_1 \cdot U_1 \, \mathrm{e}^{-b \cdot L} \sin(b \cdot L) \sin(\omega t) \\ - PS_1 \cdot V_1 \, \mathrm{e}^{-b \cdot L} \cos(b \cdot L) \sin(\omega t) - PS_1 \cdot P_1 \, \mathrm{e}^{b \cdot L} \sin(b \cdot L) \sin(\omega t) \\ + PS_1 \cdot R_1 \, \mathrm{e}^{b \cdot L} \cos(b \cdot L) \sin(\omega t) = 0 \quad (8.40)\end{aligned}$$

$$PS_1 = \frac{Q_d}{P_1^2 + R_1^2} \quad (8.41)$$

$$PS2 = \frac{2 \, \mathrm{e}^{b \cdot L}}{A_2^2 + B_2^2} \quad (8.42)$$

This equation must hold for any time t, so solution for Q_c and α may be obtained by looking at the sine and cosine terms of eqn. 8.40 separately. Separating eqn. 8.40 into it's component sine and cosine terms yields the following set of equations:

$$\begin{aligned}[PS_2 \cdot A_2 \sin(\alpha) + PS_2 \cdot B_2 \sin(\alpha)] \cdot Q_c = -R_t \cdot Q_d \\ - PS_1 \cdot U_1 \, \mathrm{e}^{-b \cdot L} \cos(b \cdot L) - PS_1 \cdot V_1 \, \mathrm{e}^{-b \cdot L} \sin(b \cdot L) \\ - PS_1 \cdot P_1 \, \mathrm{e}^{b \cdot L} \cos(b \cdot L) - PS_1 \cdot R_1 \, \mathrm{e}^{b \cdot L} \sin(b \cdot L) \quad (8.43)\end{aligned}$$

$$\begin{aligned}[-PS_2 \cdot A_2 \sin(\alpha) + PS_2 \cdot B_2 \cos(\alpha)] \cdot Q_c = \\ - PS_1 \cdot U_1 \, \mathrm{e}^{-b \cdot L} \sin(b \cdot L) + PS_1 \cdot V_1 \, \mathrm{e}^{-b \cdot L} \cos(b \cdot L) \\ + PS_1 \cdot P_1 \, \mathrm{e}^{b \cdot L} \sin(b \cdot L) - PS_2 \cdot R_1 \, \mathrm{e}^{b \cdot L} \cos(b \cdot L) \quad (8.44)\end{aligned}$$

[9] Care must be taken when adding the results as the coordinate systems of the two solutions are different.

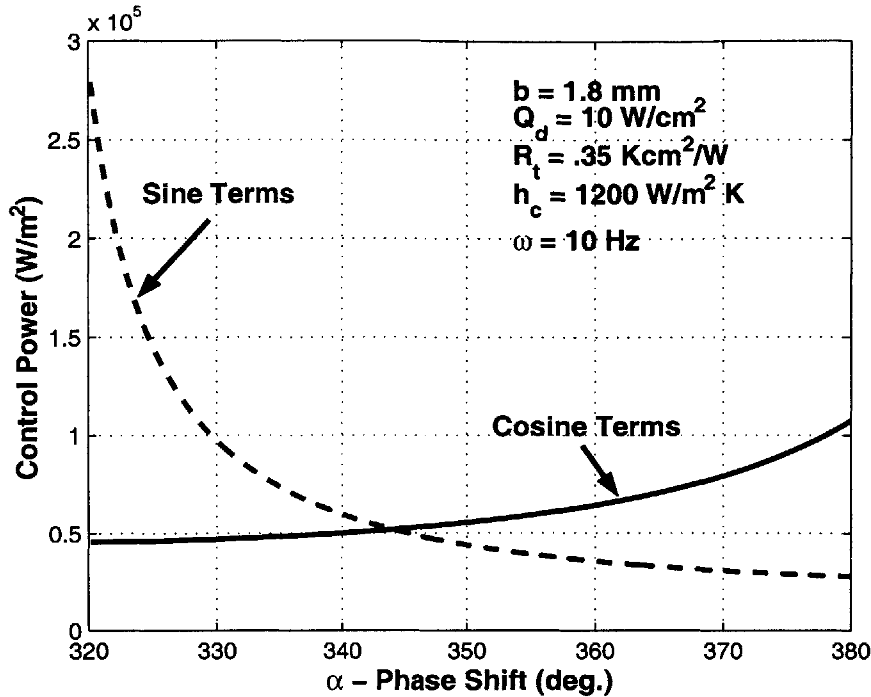

Figure 8-11: Graphical solution for phase shift and magnitude of control power profile.

The easiest solution method for these equations is through graphical methods. Plotting the sine and cosine terms as a function of α will produce solutions for α and Q_c by finding the intersection of the two curves.

An example of this solution in shown in Fig. 8-11. As can be seen, for the stated conditions, one solution for the control power profile is a phase shift of 344.1° with magnitude of 5.2×10^4 W/m^2. The results from this plot can then be used to generate the temperature profile in the IHS under steady periodic conditions. Figure 8-12 presents the temperature response in the IHS if only the die power profile is imposed. A steady state response of the temperature distribution has been added to the steady periodic solution. This steady state response is from the conduction law and the profile is simply calculated from

$$T(x) = \frac{Q_d \cdot x}{k} \tag{8.45}$$

where x is measured from the convection side face[10], b is the IHS thickness and Q_d is the half amplitude sine wave flux in W/m^2. As can be seen, the temperature of

[10]Steady state temperature at the convection side face is taken as zero.

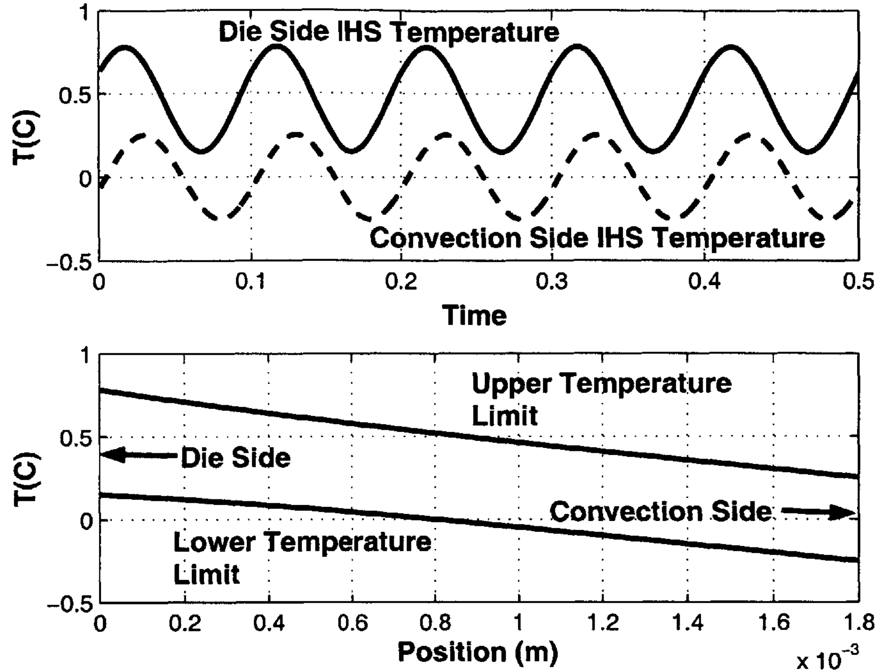

Figure 8-12: Temperature response of IHS to a 10 Hz die power profile with Q_d = 10 W/cm^2. For this system, h_c = 1200 W/cm^2 and the IHS is 1.8 mm thick.

the IHS at the die interface fluctuates at 10 Hz, as does the convection side of the IHS. The maximum and minimum temperatures through the IHS are plotted in the bottom plot of Fig. 8-12. There is a phase shift between the temperatures on the two faces, and the amplitude on the die side is slightly larger than the convection side. If a control profile of magnitude 5.2×10^4 W/m^2 and phase lag of 344.1° is applied to the convection side of the IHS, the resulting temperature profile is seen in Fig. 8-13. Obviously it is possible to control the back-face temperature of the IHS for a given die power profile, so now the question becomes one of how to control the temperature of the die itself.

It has already been demonstrated that the die can be assumed to be isothermal. Based on this, the differential equation describing the temperature of the die can be written as

$$m \cdot c_p \frac{dT_{die}}{dt} = Q_d \cdot \cos(\omega t) - \frac{T - T_{BF}}{R_t} \tag{8.46}$$

where T_{BF} is the die side surface temperature of the integrated heat spreader. This equation is based on the assumption that the thermal interface material between the die and the IHS has no mass. This equation can be solved for T_{BF} based on the desired

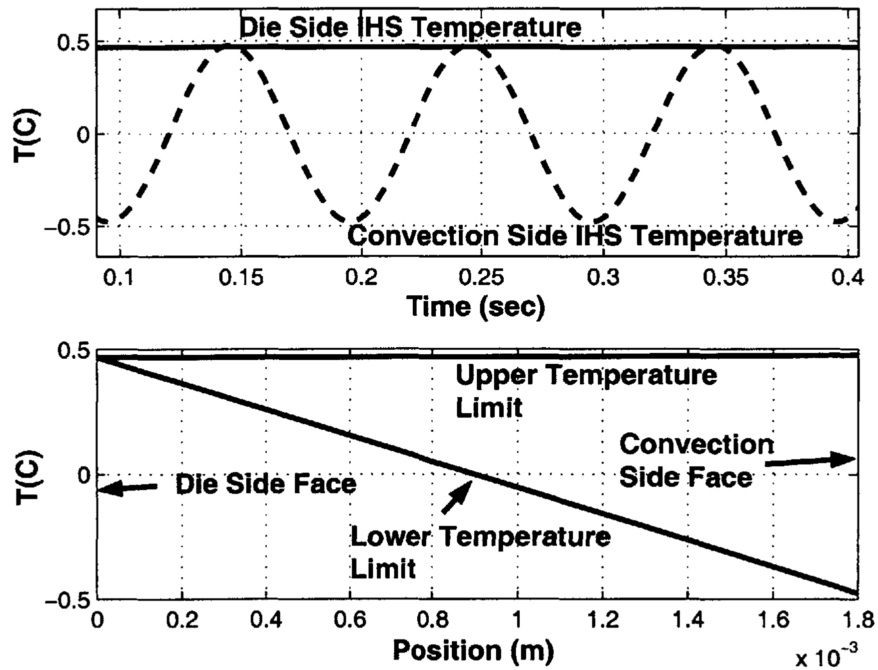

Figure 8-13: Temperature response of IHS to a 10 Hz die power profile with $Q_d = 10\ \mathrm{W/cm^2}$ and a control power profile imposed on the front face.

temperature of the die. For ideal temperature control where there is no change in die temperature and assuming the desired die temperature is zero[11], the equation for the IHS back face temperature becomes:

$$T_{BF} = -Q_d \cdot R_t \cos(\omega t) = Q_d \cdot R_t \cos(\omega t + \pi) \tag{8.47}$$

The second expression clearly shows that for ideal temperature control, the desired IHS back face temperature is 180° out of phase with the die power profile with a magnitude that depends on Q_d and the thermal interface resistance R_t. Returning to the example in Fig. 8-12, to obtain constant die temperature, the desired back-face temperature must be obtained by appropriate scaling of the control profile. To find this control profile, eqn. 8.40 must be solved, but instead of zero on the righthand side of the equation, the term $(-Q_d \cdot R_t \cos(\omega t))$ must be used. Again by matching sine and cosine terms and plotting the results, the solution to the power profile can be found. Figure 8-14 shows the desired control profile phase shift to be 283.42° with a magnitude of $17.30 \times 10^5 \mathrm{W/m^2}$. The phase shift calculated here is a phase lag between the die input and the control input. For steady periodic conditions this is the same as a phase lead shifted by 360°. In other words, the calculated phase lag of 283.42° is the same as the control power profile leading the die power profile by 76.58°. This is important when the analysis starts to consider control limits for a die power profile.

Using these results, the temperature profile in the IHS can again be calculated. Figure 8-15 plots the IHS temperature as a function of time and position, as well as the die power profile and the target T_{BF} temperature. Again, the target temperature can be obtained, but there is a significant cost compared to the previous case where T_{BF} was kept constant. The ratio of control power to die power has gone from 0.52 to 17.30. This is because the entire mass of the IHS has to be driven over a much wider temperature range and the forcing function to obtain this range has to come from the control power profile. A similar analysis can be performed over the full range of frequencies and powers.

So far an analysis has been performed which can be used to generate the control profile for the case where either the die temperature is constant or where the temperature of the back face of the IHS is held constant. Neither of these cases is really what is needed. What is needed is an analysis that will calculate the required control

[11] This assumption is made for mathematical convenience. Any desired temperature can be used and will simply add a steady state offset to the solution.

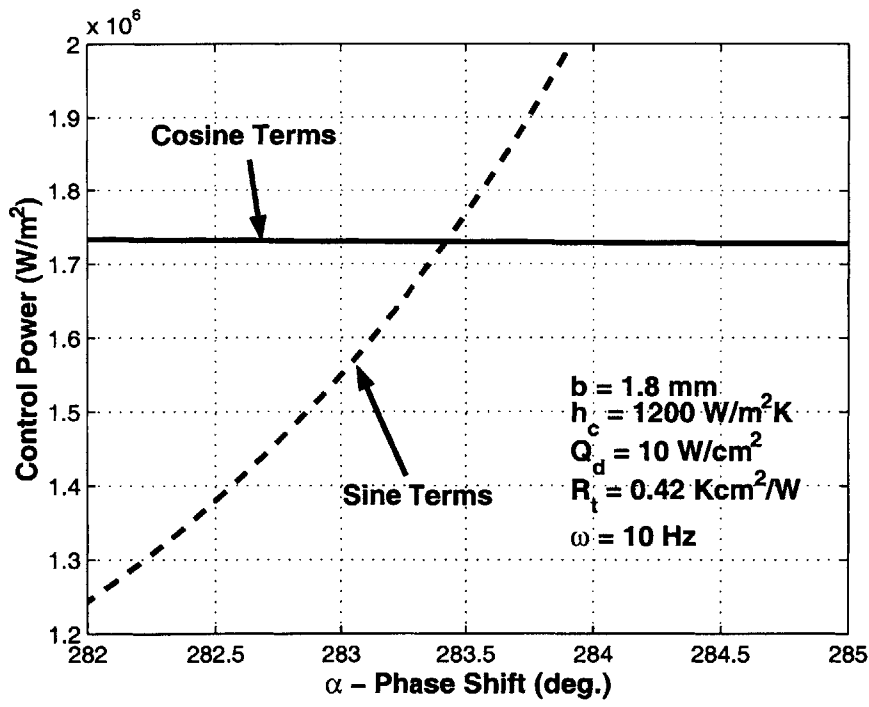

Figure 8-14: Solution for phase shift and control magnitude for ideal temperature control of die.

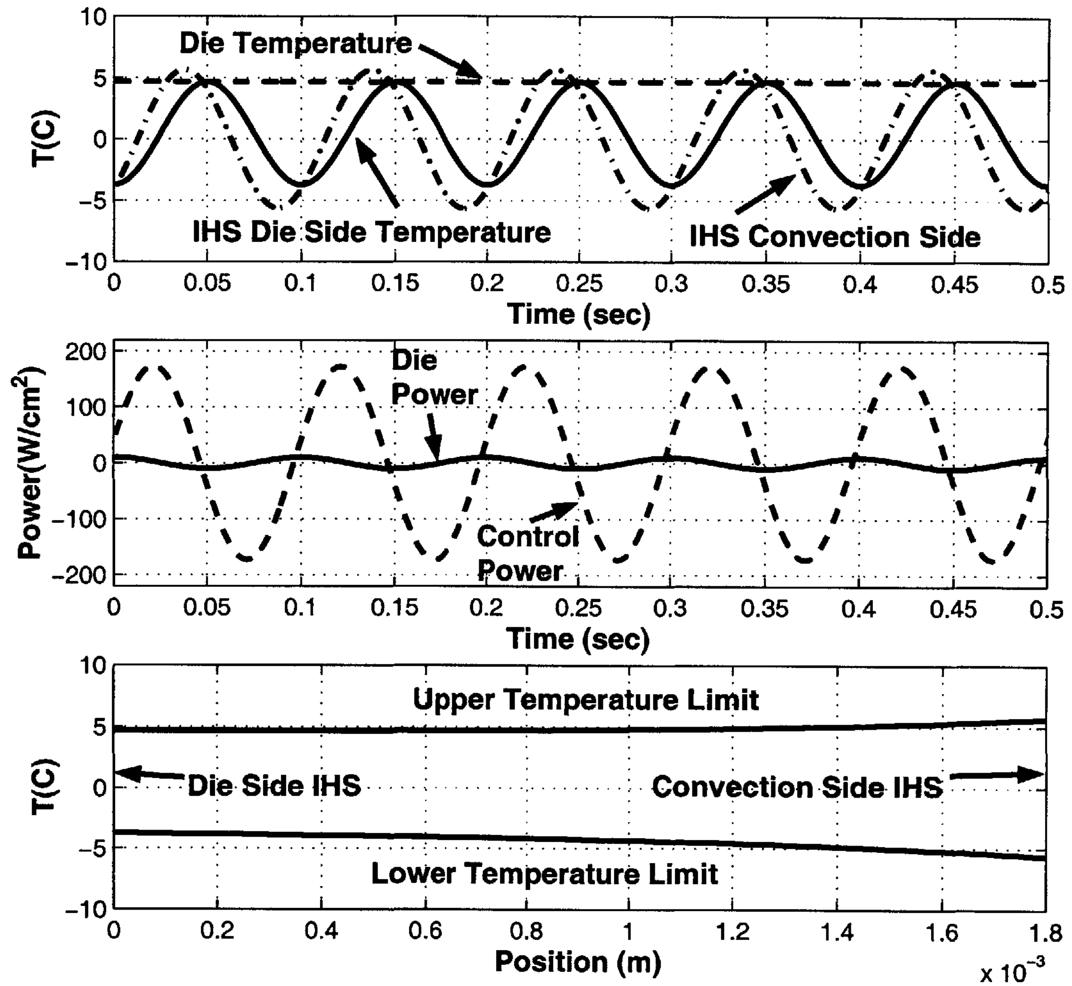

Figure 8-15: IHS temperature profile for ideal control of die temperatures.

profile for a given die power profile and an allowed range of die temperature. This analysis will be built on the previous analysis for ideal control of the die temperature.

Starting with the differential equation for the temperature of the die (eqn. 8.46), now this differential equation must be integrated to find a discrete solution for the die temperature. For ideal temperature control, it has been shown that $T_{BF} = -R_t \cdot Q_d \cos(\omega t)$. For non-ideal control, it is assumed that the back face temperature of the die will take on the form

$$T_{BF} = M \cdot R_t \cdot Q_d \cos(\omega t + \beta) \tag{8.48}$$

where the scaling factor M takes on a value between 0 and 1. Using the identity, $\cos(\omega t + \beta) = \cos(\beta)\cos(\omega t) - \sin(\beta)\sin(\omega t)$, eqn. 8.46 can be expressed in the form

$$\frac{dT}{dt} + \frac{T}{mc_pR_t} = \frac{Q_d}{mc_p}\cos(\omega t)\cdot\cos\beta\cdot(1 - M\cdot cos(\beta)) - \frac{Q_d}{mc_p}\sin(\omega t)\cdot\sin\beta \tag{8.49}$$

which can be integrated using an integration factor e^{t/mc_pR_t}. The solution for the temperature of the die becomes:

$$T_{die} = \frac{Q_d\,(1 + M\cos(\beta))}{mc_p\,(\lambda^2+\omega^2)}\left[\lambda\cos(\omega t) + \omega\sin(\omega t)\right] - \frac{Q_d\sin(\beta)}{mc_p\,(\lambda^2+\omega^2)}\left[\lambda\sin(\omega t) - \omega\cos(\omega t)\right] \tag{8.50}$$

where $\lambda = 1/mc_pR_t$. Of interest here is the magnitude of the fluctuation of T_{die}. By setting this magnitude equal to the allowed ΔT of the die, the scaling factor M and the phase shift β can be found.

So far there is one equation in two unknowns, but a second equation can be found by recognizing that the goal is to minimize M for a given die power profile. The smaller the value of M, the small the required control power. Setting the magnitude of eqn. 8.50 equal to ΔT and solving for M produces:

$$M = \frac{1}{2Q_d}\left[-2\cos\beta\cdot Q_d \pm \sqrt{4\cos^2\beta\cdot Q_d^2 + (mc_p\omega\Delta T)^2 - 4Q_d^2 + (mc_p\lambda\Delta T)^2}\right] \tag{8.51}$$

This equation can be differentiated with respect to β

$$\frac{dM}{d\beta} = \sin\beta \mp \frac{4Q_d^2\cos\beta\sin\beta}{\sqrt{4\cos^2\beta\cdot Q_d^2 + (mc_p\cdot\omega\Delta T)^2 - 4Q_d^2 + (mc_p\lambda\Delta T)^2}} = 0 \tag{8.52}$$

which yields the obvious solution of $\beta = 0, \pi$. For $\Delta T = 0$, the solution should be $M = 1$, not $M = -1$, so the solution for β must be $\beta = \pi$. The result for M is now

$$M = 1 - \frac{mc_p\Delta T}{Q}\sqrt{\lambda^2+\omega^2} \tag{8.53}$$

so now the magnitude of the fluctuation of T_{BF} is known.

One more step needs to be taken before solving for the temperature profile in the integrated heat spreader and the control power profile. The flux from the die into the heat spreader is no longer the equal to the die power profile. Some of the energy from the die power profile will be stored in the die in the form of a steady periodic die temperature change. The die temperature profile is

$$T_{die} = \frac{Q_d(1-M)}{mc_p\left(\lambda^2+\omega^2\right)}\left[\lambda\cos(\omega t)+\omega\sin(\omega t)\right] \tag{8.54}$$

which can be used to calculate the flux from the die into the heat spreader.

$$Q_{da} = \frac{T_{BF}-T_{die}}{R_t} = \left(\frac{Q_d\lambda(1-M)}{mc_pR_t\left(\lambda^2+\omega^2\right)} - MQ_d\right)\cos(\omega t) + \frac{Q_d\omega(1-M)}{mc_p\left(\lambda^2+\omega^2\right)}\sin(\omega t) \tag{8.55}$$

where Q_{da} is an adjusted die flux which can be rewritten in the form

$$Q_{da} = \left(MQ_d - \frac{Q_d\lambda^2(1-M)}{\lambda^2+\omega^2}\right)\cdot\cos\left(\omega t+\gamma\right) \tag{8.56}$$

where the phase shift can be calculated from:

$$\gamma = \tan^{-1}\left[\frac{mc_p\omega Q_d(1-M)}{mc_pMQ_d\left(\lambda^2+\omega^2\right)-Q_d\lambda^2(1-M)}\right] \tag{8.57}$$

The flux from the die into the integrated heat spreader is reduced in magnitude and shift by a phase lag of magnitude γ.

With this revised solution for the magnitude and phase shift of the flux and the target temperature for the die contact face of the IHS, the temperature profile of the IHS can be calculated along with the desired control profile using

$$\begin{aligned}
&[PS_2\cdot A_2\cos(\alpha)+PS_2\cdot B_2\sin(\alpha)]\cdot Q_c\cos(\omega t)+PS_1\cdot U_1\,\mathrm{e}^{-b\cdot L}\cos(b\cdot L+\gamma)\cos(\omega t)\\
&\quad+PS_1\cdot V_1\,\mathrm{e}^{-b\cdot L}\sin(b\cdot L+\gamma)\cos(\omega t)+PS_1\cdot P_1\,\mathrm{e}^{b\cdot L}\cos(b\cdot L+\gamma)\cos(\omega t)\\
&\quad+PS_1\cdot R_2\,\mathrm{e}^{b\cdot L}\sin(b\cdot L+\gamma)\cos(\omega t)\\
&+[PS_2\cdot B_2\cos(\alpha)-PS_2\cdot A_2\sin(\alpha)]\cdot Q_c\sin(\omega t)+PS_1\cdot U_1\,\mathrm{e}^{-b\cdot L}\sin(b\cdot L+\gamma)\sin(\omega t)\\
&\quad-PS_1\cdot V_1\,\mathrm{e}^{-b\cdot L}\cos(b\cdot L+\gamma)\sin(\omega t)-PS_1\cdot P_1\,\mathrm{e}^{b\cdot L}\sin(b\cdot L+\gamma)\sin(\omega t)\\
&\quad+PS_1\cdot R_1\,\mathrm{e}^{b\cdot L}\cos(b\cdot L+\gamma)\sin(\omega t)=-R_tM\cdot Q_d\cos(\omega t)
\end{aligned} \tag{8.58}$$

where PS_1 has been redefined as

$$PS_1 = \frac{Q_{da}}{P_1^2+R_1^2} \tag{8.59}$$

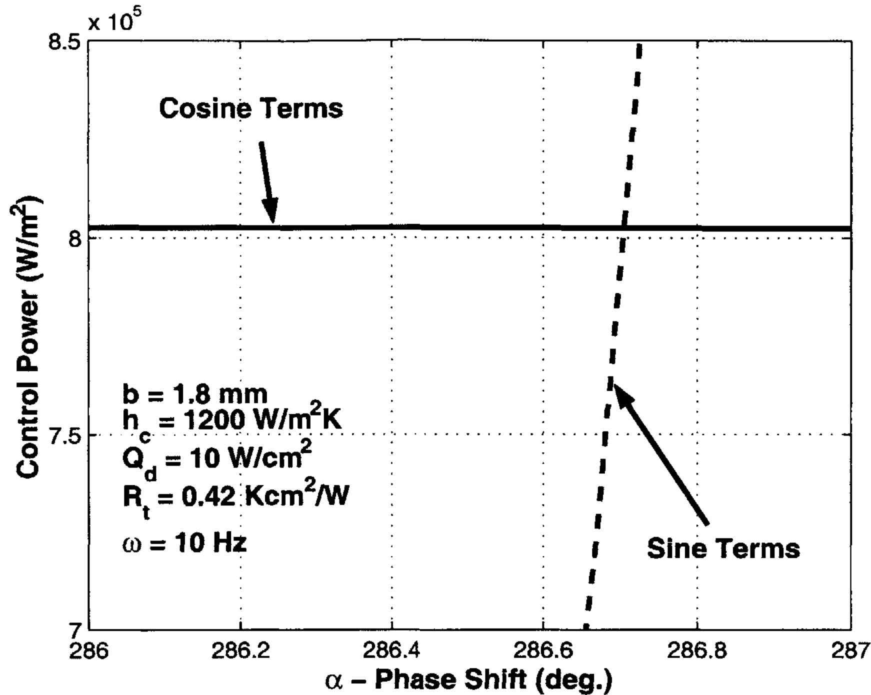

Figure 8-16: Magnitude and phase shift of control profile to maintain die temperature within 4 K for a 10 Hz die power profile with $Q_d = 10$ W/cm^2.

This equation can be solved in the same way as eqn. 8.40, where the equation is separated into sine and cosine terms, and then solved graphically. Solving for $Q_d = 10$ W/cm^2 with $\Delta T = 4$ K, the solution for control magnitude and phase shift can be taken from Fig. 8-16. where it can be seen that the desired phase shift is 286.95° with a control magnitude of 61.19 W/cm^2. These results are much better than the ideal temperature control case where the control magnitude was calculated as 173.0 W/cm^2. The resulting temperature profile in the die and the IHS is shown in Fig. 8-17.

8.4.2 Model Confirmation

A method of confirming the analytic model developed in the previous section is needed, if for no other reason than the solution is long and complex, and it is very easy to make mathematical errors in the solution process. In order to provide an independent solution, a finite difference model of the die/heat spreader system was constructed. Using an implicit method [17] and breaking the heat spreader into N sections, the equation describing the temperature response of the system can be written

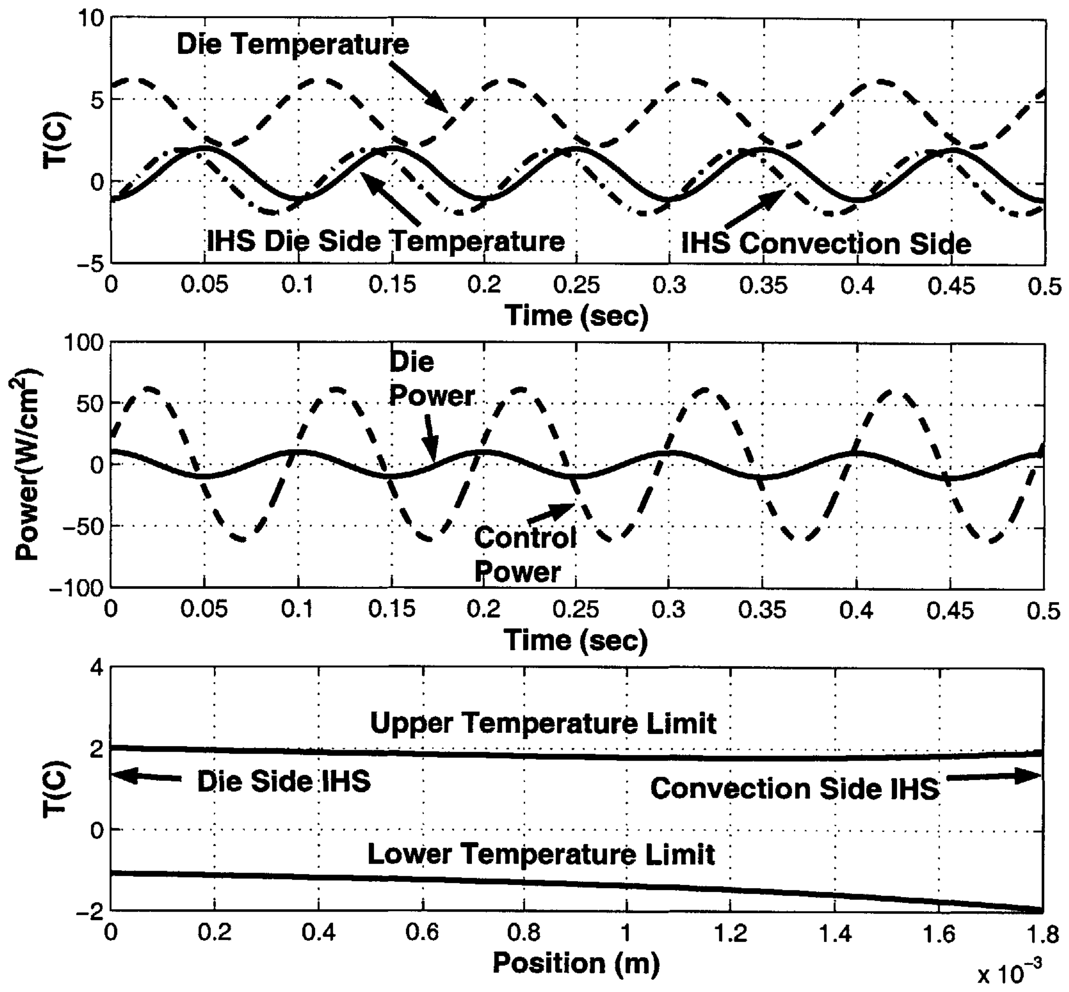

Figure 8-17: Temperature profile in die and IHS for 10 Hz die power profile with magnitude of 10 W/cm^2 with $\Delta T = 4$ K.

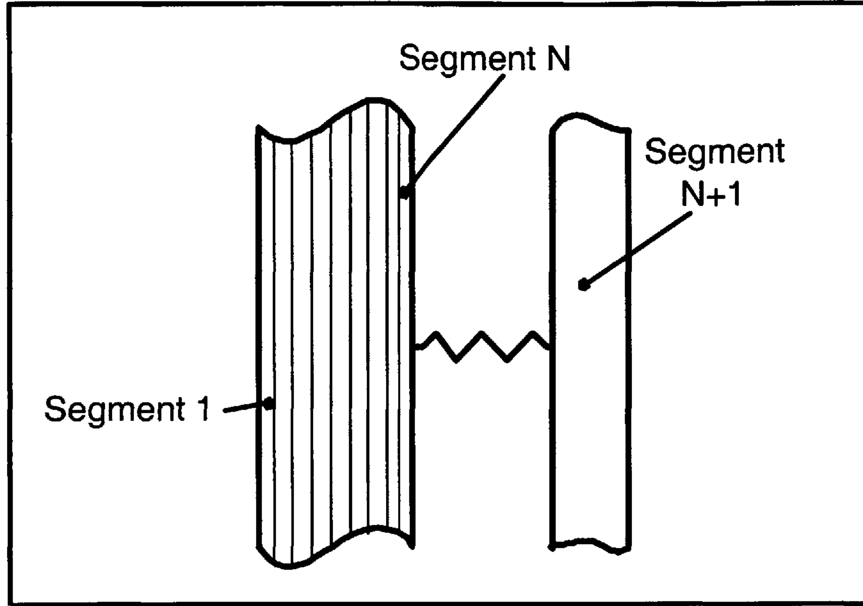

Figure 8-18: Incremental segment break-down for finite difference confirmation model.

as

$$\mathbf{A} \cdot \mathbf{T}^{i+1} = \mathbf{T}_i + \mathbf{F} \tag{8.60}$$

where $\mathbf{T}$ is an N+1 temperature array of the heat spreader and die[12] temperatures, $\mathbf{F}$ is the forcing function, and $\mathbf{A}$ is a characteristic matrix. The indices i and $i+1$ indicate the temperature at time steps i and $i+1$. The forcing function of the system is an N+1 array with all elements zero except for the first and last elements. The first element is given by

$$\mathbf{F}_1 = \frac{T_{air} h_c \Delta t}{m_1 c_p} + \frac{Q_c^i \Delta t}{m_1 c_p} \tag{8.61}$$

where Δt is the time step, m_1 is the mass of the surface incremental section as shown in Fig. 8-18, and Q_c is the control input for time step i. The last element is given by

$$\mathbf{F}_{N+1} = \frac{Q_d^i \Delta t}{m_{die} c_p} \tag{8.62}$$

[12]Section N+1 is the die.

where m_{die} is the mass of the die and Q_d is the die input for time step i. The characteristic matrix is calculated from

$$\begin{bmatrix} 1+\frac{h\Delta x\Delta t+k\Delta t}{m_1 c_p \Delta x} & \frac{-k\Delta t}{m_1 c_p \Delta x} & 0 & 0 & \cdots & 0 \\ \frac{-k\Delta t}{m_2 c_p \Delta x} & 1+\frac{2k\Delta t}{m_2 c_p \Delta x} & \frac{-k\Delta t}{m_2 c_p \Delta x} & 0 & \cdots & 0 \\ 0 & \cdots & \frac{-k\Delta t}{m_n c_p \Delta x} & 1+\frac{2k\Delta t}{m_n c_p \Delta x} & \frac{-k\Delta t}{m_n c_p \Delta x} & 0 \\ \cdots & \cdots & \cdots & \cdots & \cdots & \cdots \\ 0 & \cdots & 0 & \frac{-k\Delta t}{m_N c_p \Delta x} & 1+\frac{k\Delta t R_t+\Delta x\Delta t}{m_N c_p \Delta x \Delta t} & \frac{-\Delta t}{m_N c_p R_t} \\ 0 & \cdots & \cdots & 0 & \frac{-\Delta t}{m_{die} c_p R_t} & 1+\frac{\Delta t}{m_{die} c_p R_t} \end{bmatrix} \tag{8.63}$$

This is a sparse matrix and can be easily inverted. The temperature of the system at time step $i+1$ can now be calculated from

$$\mathbf{T}^{i+1} = \mathbf{A}^{-1}\mathbf{T}^{i} + \mathbf{A}^{-1}\mathbf{F} \tag{8.64}$$

based on the temperature at time step i. This model is not useful for solving for the required control input magnitude and phase shift, but is very useful for checking the results from the analytical solution.

Figure 8-19 shows the results for the die temperature using the finite difference model for a 10 Hz die signal with Q_d = 10 W/cm^2. The control input has Q_c = 61.2 W/cm^2 and a phase shift of 286.95°. This is the specified control input to control the die temperature to a 4 K range. As can be seen, the finite difference model confirms that the control input does control the temperature of the die to the desired level.

8.5 Control of Non-Sinusoidal Die Power Profile

So far only sinusoidal power profiles have been considered, but any power profile can be decomposed into a Fourier series of sine terms that can be used to calculated the required control profile using superposition. The Fourier series for a square wave can be written as [28]

$$Q_{sq}(t) = \frac{4Q}{\pi} \sum_{n=1,3,5\ldots} \frac{1}{n} \sin\left(\frac{2n\pi t}{\tau}\right) \tag{8.65}$$

where Q is the magnitude of the square wave[13] and τ is the period of the square wave. Each of these components can now be analyzed using the method developed

[13]Half the peak to peak amplictude.

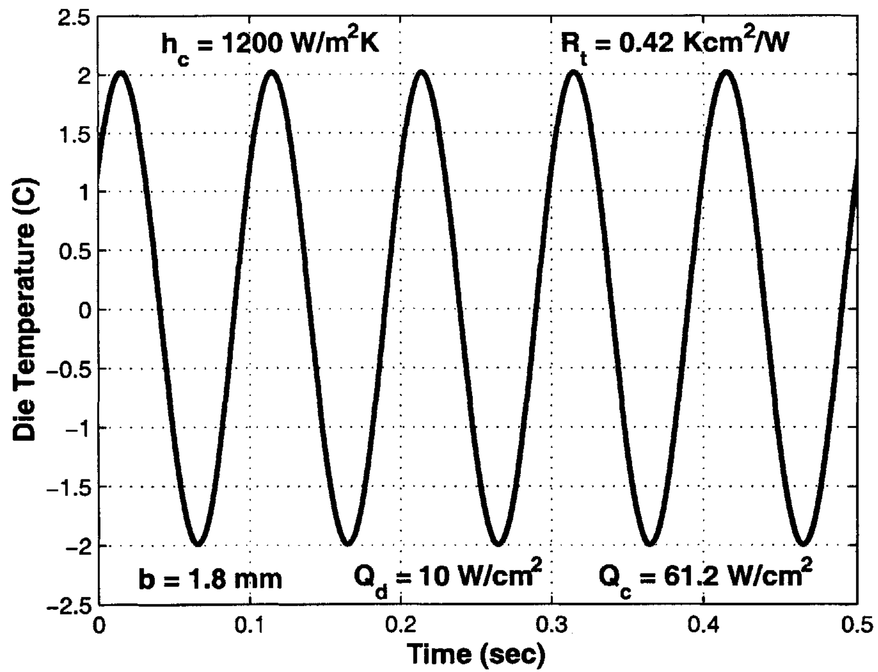

Figure 8-19: Calculated die temperature using finite difference model to confirm analytic solution for control input.

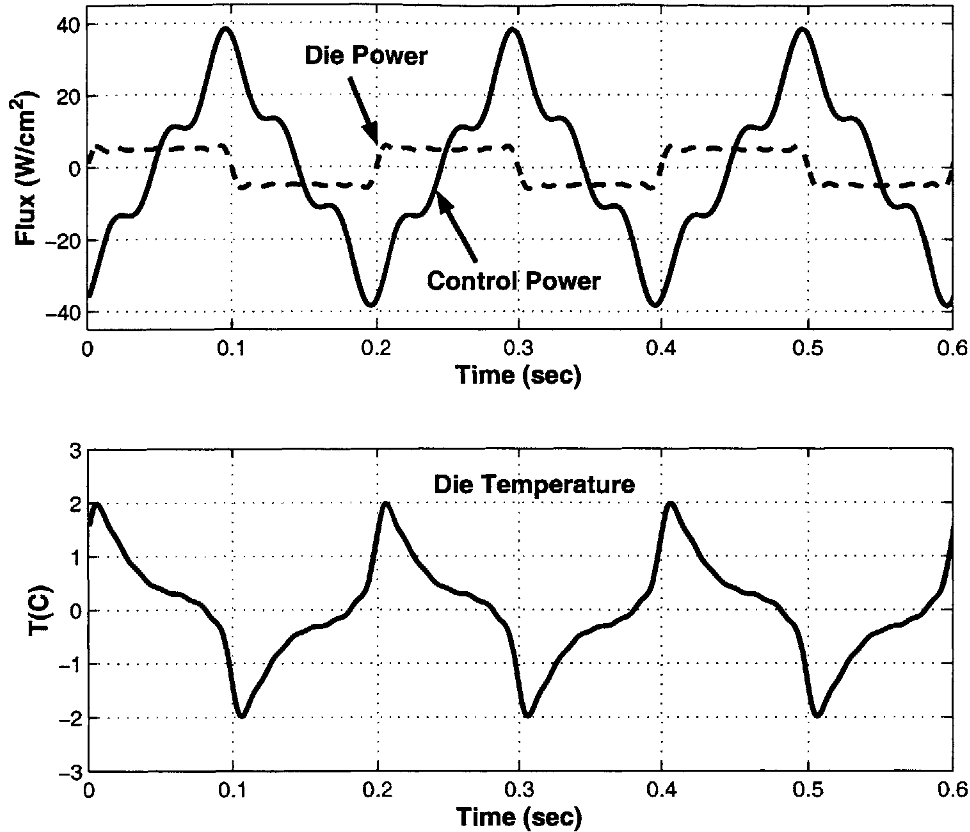

Figure 8-20: Control input and die temperature for square wave die power profile.

in the previous section in order to determine the required control input to maintain the specified ΔT of the die. The sum of the ΔT's for each component will then provide an approximate total ΔT for the die once the signals are recomposed. Some iteration in the solution is required to obtain the desired results with the minimum in control input. For example, with a desired ΔT_{die} of 4 K, the control input may be broken down into an allowed ΔT of 1 K for the first frequency component of the decomposition, 1 K for the second component, 1 K for the third and 1 K for the fourth. Using this as the base of analysis, it can quickly be shown that the third and fourth components produce die fluctuations much lower than the target values of ΔT = 1 K, so no control is required. So now the analysis can be redone with $\Delta T = 2$ K on the first and second components, or $\Delta T = 3$ K on the first component and 1 K on the second component. Multiple iterations are generally required to find the optimal solution. The results for a 5 Hz square wave are shown in Fig. 8-20.

A similar type of analysis can be performed for power profiles of any shape. A

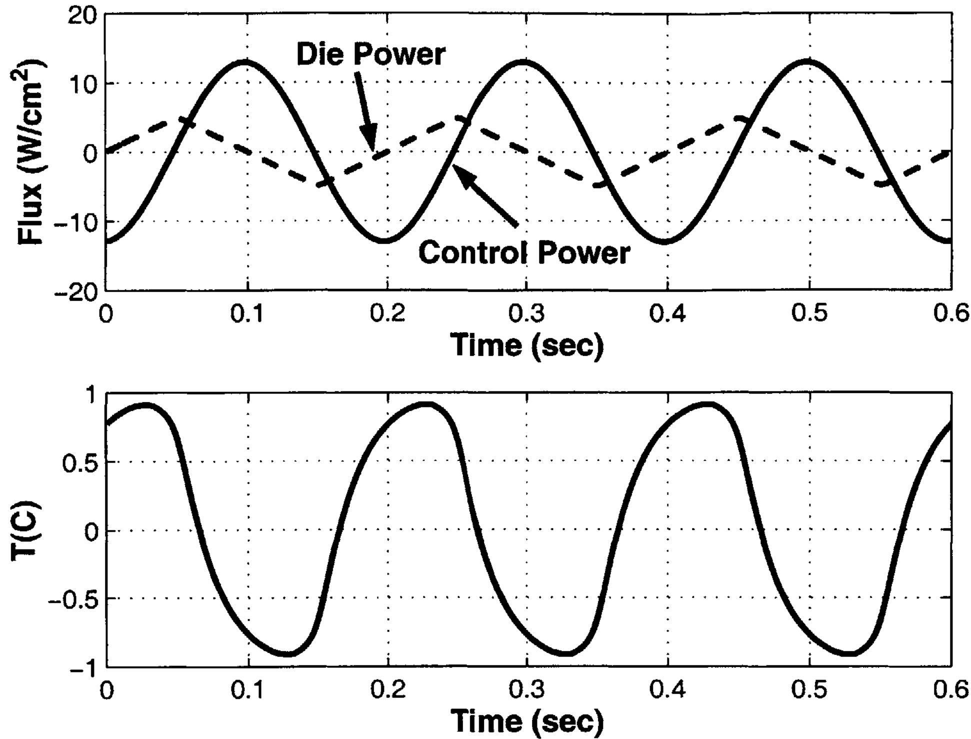

Figure 8-21: Control input and die temperature for triangular wave die power profile.

triangular wave can be expressed as the Fourier series [28]

$$Q_{tr}(t) = \frac{8Q}{\pi^2} \sum_{n=1,3,5...} \frac{(-1)^{\frac{n-1}{2}}}{n^2} \sin\left(\frac{2n\pi t}{\tau}\right) \tag{8.66}$$

Using this decomposition, the control input for a desired level of die temperature control can be calculated. The results for a triangular wave decomposition are shown in Fig. 8-21. Note the big difference in control power required between the triangular wave and square wave die power profiles. The square wave needs almost 8:1 control to die power ratio to control the die temperature to within 4 K while the triangular wave requires only a 2.4:1 ratio to maintain a 2 K temperature tolerance. Sudden step changes in die power profiles require much more control power to a given level of temperature tolerance than a continuous power profile such as the triangular wave pattern.

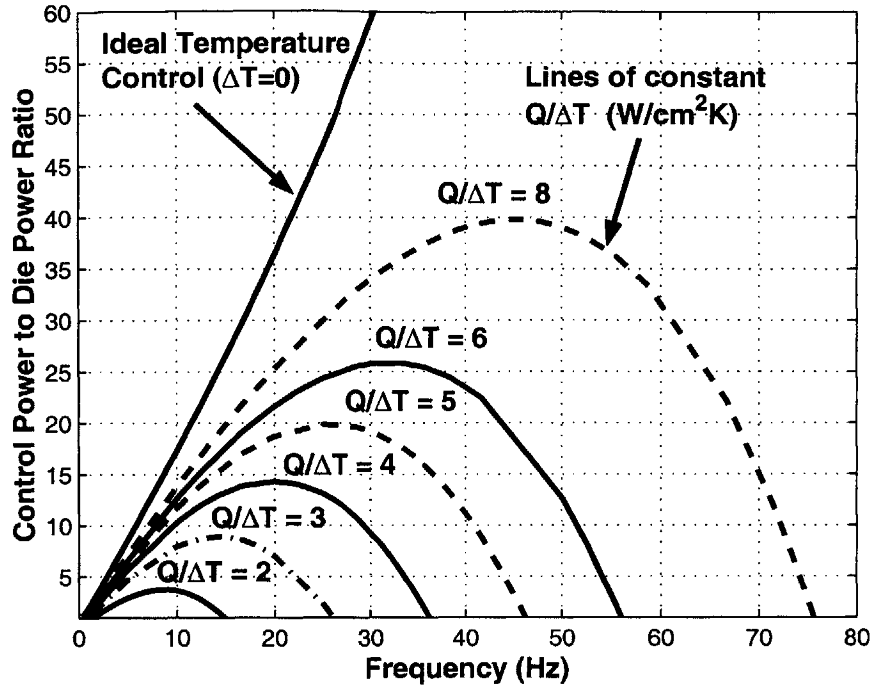

Figure 8-22: Control limits for specified die power profile.

8.6 Limits to Control with known Die Power Profile

The previous analysis to determine the required control power profile for a given temperature tolerance in the die can be used to define control limits for a given system. For a given die power magnitude and a limited control power to die power ratio, there is a finite limit to the controllability of the die temperature. At a given die power frequency, the control power ratio can be found for a given die temperature tolerance. Figure 8-22 shows the control limits for a die with a 200 μm thick die structure, with a 1.8 mm thick IHS and a $h_c = 1200$ W/m^{2}K. A detailed view of the same data is shown in Fig. 8-23. These figures illustrate the limits of control. There are three regions in Fig. 8-23, each representing different region of operation. The area to the left of the lines represents a region where the temperature of the die can be controlled by applying the specified control profile. The region to the right of the lines represents the region where the die power frequency is so high that no control is required to maintain the temperature tolerance limits on the die. The region in between represents the region where the specified control cannot be attained with the

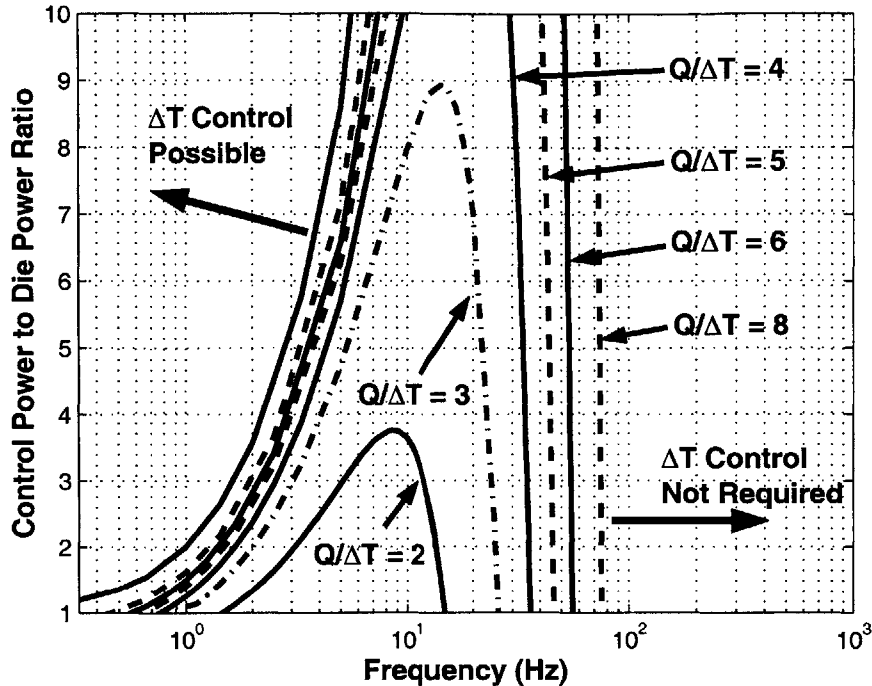

Figure 8-23: Control limits for specified die power profile.

specified control power/die power ratio.

It can be seen in Fig. 8-22 that any desired flux to temperature tolerance can be obtained so there is no theoretical limit to temperature control. On a practical level, power ratios over 3 or 4 quickly become impractical. Remember this analysis was for steady periodic profiles. To implement these profiles in practice, the control and die profile magnitudes have to be added to the system as there is no such thing as a negative flux. So now Fig. 8-23 really does show that there are limits to temperature control and the results provide some very important points. The position of the lines on the left hand side of the plot are defined by the physical system of the heat spreader (thickness, conductivity etc) while the line positions on the right are defined by the mass of the die, frequency of the die profile, and thermal interface resistance between the die and IHS. One way to obtained the desired level of temperature control may be to change the test sequence such that the die power profile always lies to the right side of the figure.

This analysis method can be used to evaluate the effect of design changes on the integrated heat spreader and thermal interface between the die and IHS. Figure 8-24 shows the effect on control limits of changing the value of the convective transfer

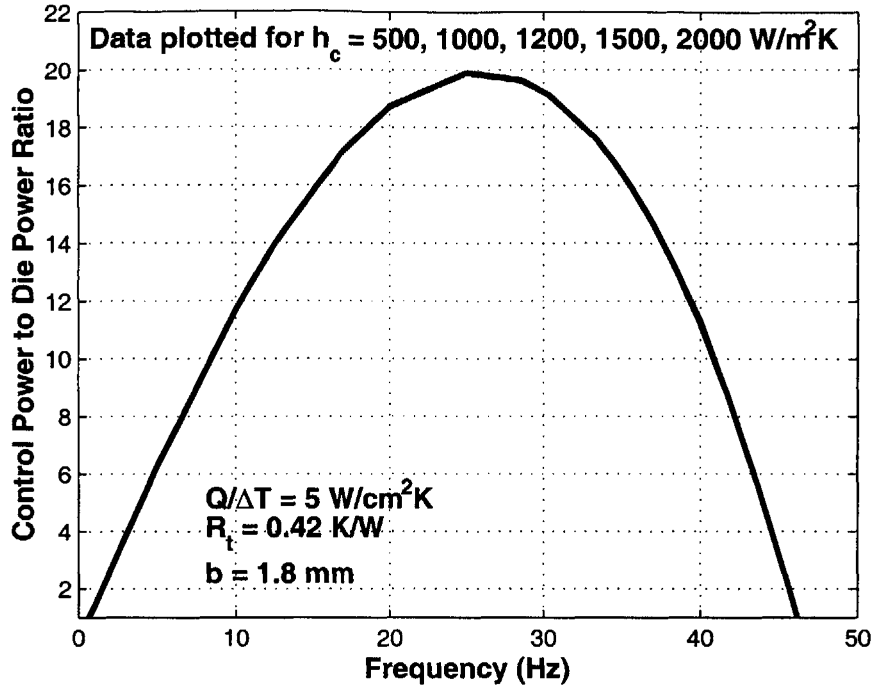

Figure 8-24: Limits of control for multiple values of the convective heat transfer coefficient h_c.

coefficient h_c. As can be seen, changing the value of h_c has no effect on the control limit curve. Changing the value of the thermal resistance between the die and the IHS can have a more profound effect on the control limits at higher power ratios. This can be seen in Fig. 8-25 for $Q/\Delta T = 5$ W/cm^{2}K. The effects of changing the thickness of the integrated heat spreader and die are shown in Fig. 8-26 and Fig. 8-27 respectively. Changing the mass of the die itself by changing the thickness of the die has the largest impact on the control limits of the device. The effect of changing the thickness(i.e. mass) of the IHS can be taken as the analogous situation to the control system adding mass to the system. If the control system adds thermal mass to the system, the power required for the same level of control.

8.7 Feedback Control Limits

If there is no prior knowledge of the die power profile then classic feedback control is required for temperature control of the die. Using the same assumption of a one dimensional transient problem as for the steady periodic solution, a transfer function

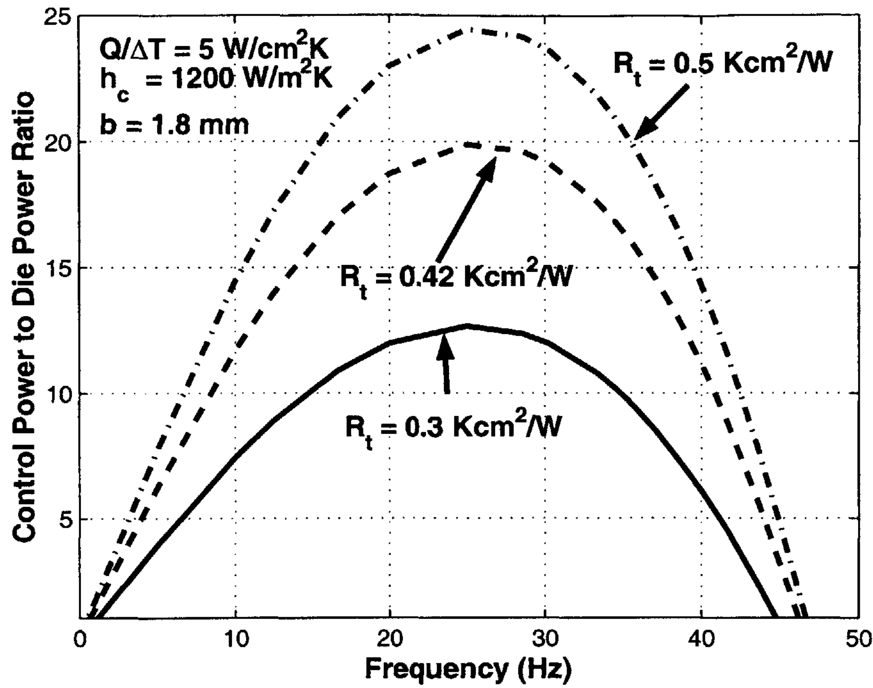

Figure 8-25: Effect of die to IHS thermal resistance on control limits.

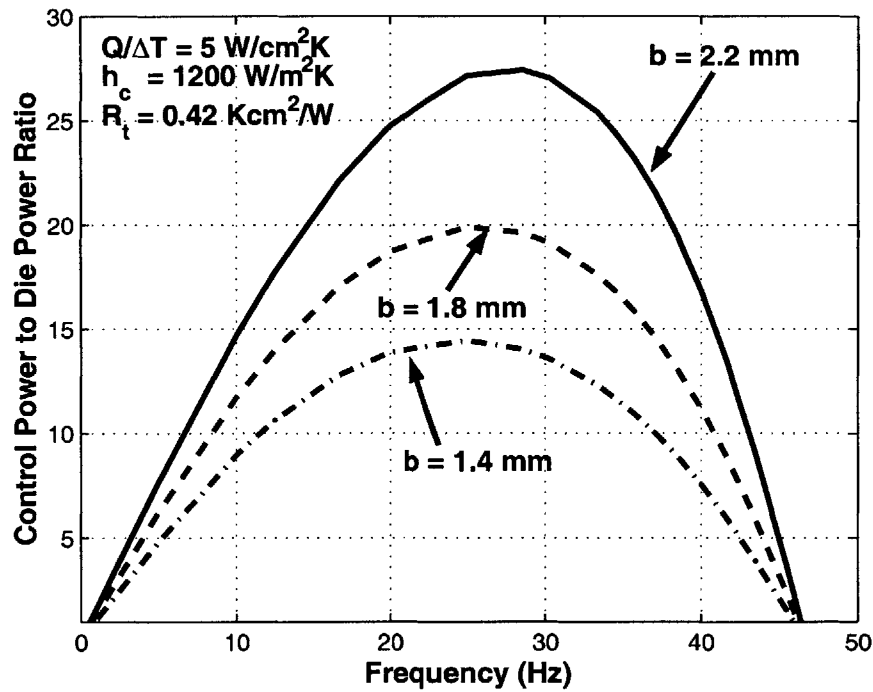

Figure 8-26: Effect of IHS thickness on control limits.

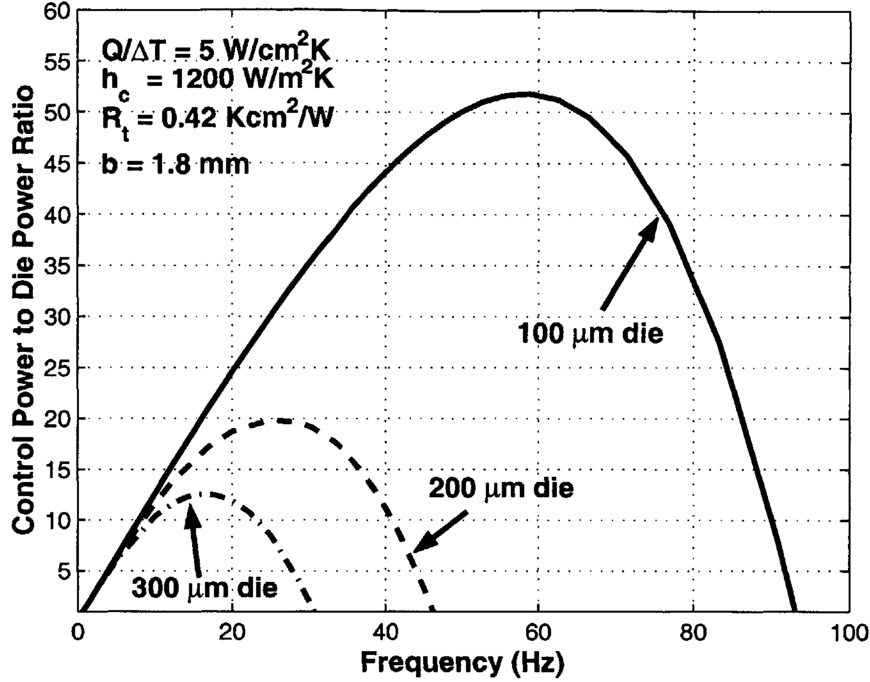

Figure 8-27: Effect of die thickness on control limits.

for the die temperature as a function of the die and control powers can be calculated. In Laplace form, the equation becomes

$$\mathbb{T}_{die}(s) = \frac{K\mathbb{Q}_d(s)}{s+\lambda} + \frac{K}{s+\lambda}\left(1 + \mathbb{Q}_c(s) + \mathrm{e}^{-2pb}\left(\frac{kp-h}{kp+h}\right)\right) \times \left[\frac{-\mathbb{Q}_c(s)(kp+h)\left[s - pkR_t(s+\lambda)\right] - K\mathbb{Q}_d(s)}{(kp+h)\left[s+pkR_t(s+\lambda)\right] + (kp-h)\,\mathrm{e}^{-2pb}\left[s - pkR_t(s+\lambda)\right]}\right] \quad (8.67)$$

where s is the Laplace operator, $K = mc_p$ of the die, $\lambda = 1/mc_pR_t$, and $p = \sqrt{s/a_t}$ where a_t is the thermal diffusivity of the IHS. The inversion of this equation into the time domain is dependent on the form of the die and control inputs as well as on the feedback control system used. Rather than attempting to solve for the entire feedback system, the fundamental limits of feedback control will be studied.

There is a finite time between the application of a control signal on the front face of the IHS until an effect of this control signal propagates through the IHS to the back face where it can have some effect on the die temperature. During this period of time, the die is effectively uncontrolled and the temperature will vary according to the form of the die power. This uncontrolled time period can be calculated based on the solution of the temperature profile propagation in a semi-infinite solid, as until the

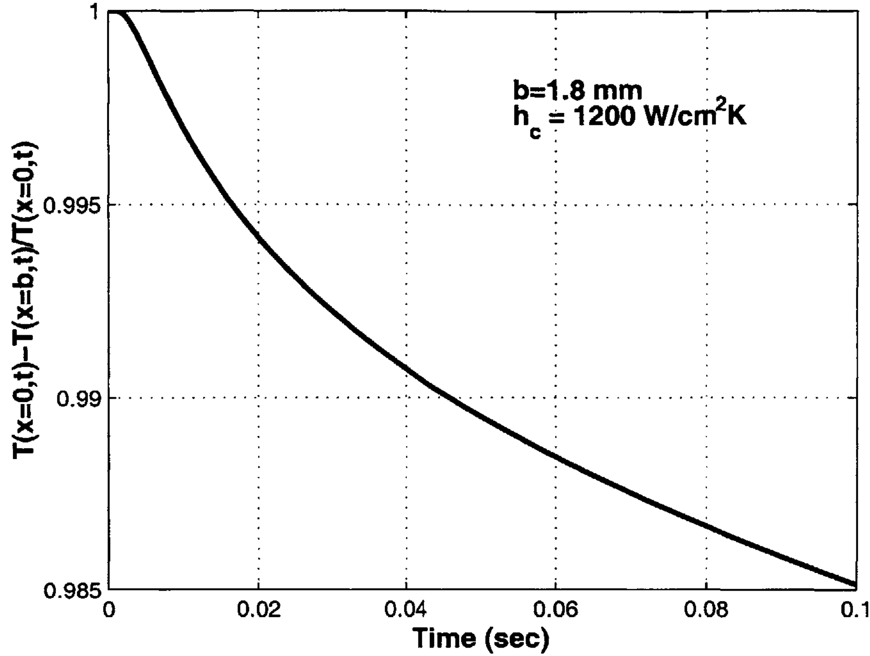

Figure 8-28: Solution for temperature profile propagation time for integrated heat spreader.

change in surface conditions propagates through to the back face, the IHS behaves just like a semi-infinite solid. For a solid subject to a surface flux and convective conditions, the temperature profile within the solid becomes [8]

$$T(x,t) = \left(\frac{Q_c + hT_{air}}{h}\right)\left(\operatorname{erfc}\frac{x}{2\sqrt{a_t t}} - e^{\left[\frac{hx}{k}+a_t t\frac{h^2}{k^2}\right]}\operatorname{erfc}\left[\frac{x}{2\sqrt{a_t t}} + \frac{h}{k}\sqrt{a_t t}\right]\right) \quad (8.68)$$

By defining an penetration depth δ as the point where

$$\frac{T(x=0,t) - T(x=\delta,t)}{T(x=0,t)} = 0.99 \quad (8.69)$$

and by setting $\delta = b$, the thickness of the IHS, a propagation time can be calculated. This time is the minimum time required for a temperature change to propagate through the IHS. Figure 8-28 shows the solution for this propagation time with the given conditions to be 0.042 seconds. This time can now be used to estimate the temperature change in the die based on the specified die power profile. The integral equation describing the temperature of the die becomes

$$T\,e^{\lambda t} = \int_0^{t_p} \frac{Q_{die}}{mc_p} e^{\lambda t}\,dt + \int_0^{t_p} \lambda T_{BF}\,e^{\lambda t}\,dt \quad (8.70)$$

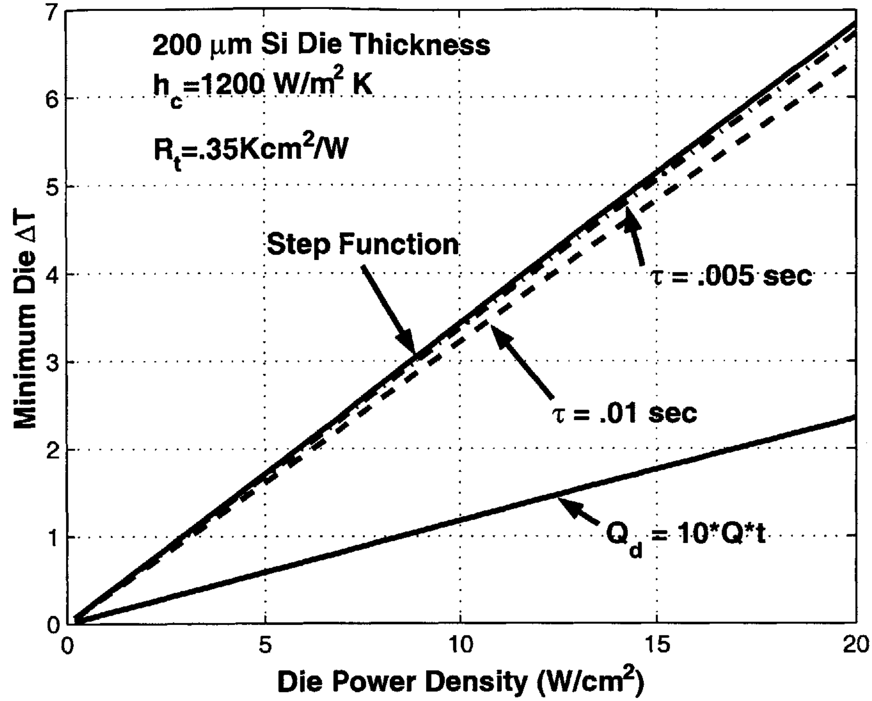

Figure 8-29: Minimum changed in die temperature for under ideal feedback control conditions.

where $\lambda = 1/mc_pR_t$. This equation can be easily solved for any given die power profile. If the die profile is a step function and taking $T_{BF} = 0$, the temperature of the die becomes

$$T = R_tQ_d\left(1 - \mathrm{e}^{-\lambda t_p}\right) \tag{8.71}$$

If the die power profile is a step function with an exponential rise time τ, the temperature of the die becomes

$$T = R_tQ_d\left(1 - \mathrm{e}^{-\lambda t}\right) - \frac{Q_d}{mc_p\left(\lambda - \frac{1}{\tau}\right)}\left[\mathrm{e}^{-t/\tau} - \mathrm{e}^{-\lambda t}\right] \tag{8.72}$$

If the die power is a ramp function of some magnitude $Q_d = A \cdot t$, the temperature becomes

$$T = \frac{A}{mc_p}\left[\frac{\lambda t - 1}{\lambda^2} + \frac{\mathrm{e}^{-\lambda t}}{\lambda^2}\right] \tag{8.73}$$

The results of these calculations are plotted in Fig. 8-29 for a range of die power profile intensities. This plot represents the absolute minimum ΔT of the die when using feedback control. It assumes there is no delay in sensing the die temperature

and feeding back the results into the control power. It puts no limit on the magnitude of the control power and assumes that just being able to propagate a control signal through the IHS to the back face implies control of the die temperature.

Feedback control is not a viable means of temperature control in the case of most high power packaged devices. The resulting delay between temperature sensing and control application to the die causes too large a temperature deviation in the die under all conditions except at very low power levels. To enable temperature control of devices under test conditions, prior knowledge of the power sequence is required in most cases. Where feedback control can be useful is for correction for variation between devices. Even if the power sequence is known in advance, this represents an ideal power sequence and manufacturing variation in devices will result in variations in the actual power sequences. Typical variation across devices will be on the order of $\pm 5\%$. For low to mid-level power devices, feedback control now becomes a viable option for correcting the temperature response due to these variations in power levels. At high power levels, feedback control is not able to handle even this 5% variation in power sequences and some new type of control is required. Figure 8-30 shows the typical variation in temperature response to a common power sequence. One possible option is the utilization of a training signal for the first 1-2 seconds of the test cycle. This short sequence would consist of two or three power levels that could be used for temperature measurement for use in developing a correction factor. This correction factor would then be used to forward correct the remaining power sequence.

8.8 Transient Lateral Conduction

So far the models that have been developed have all been one dimensional, considering only the device section consisting of the die and the integrated heat spreader directly over the die. Using this analysis is useful for determining the important parameters for control, but the effects on the remaining parts of the device need to be considered. Lateral conduction into the integrated heat spreader that is not directly over the die will have an effect on the required control profile and temperature response of the die.

Calculating the Biot number for the heat spreader that is not over the die shows that this section of the heat spreader can be treated as a fin except at very high

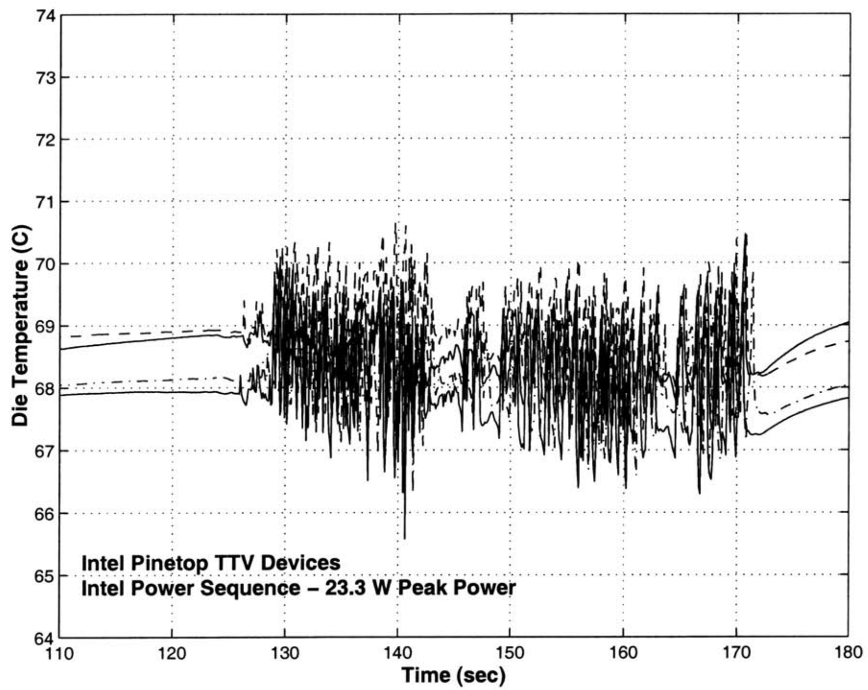

Figure 8-30: Device to device variation in temperature response for common power sequence.

convection values. Even at $h_c = 2000$ W/m^{2}K, the Biot number calculates as

$$Bi_{\text{IHS}} = \frac{h_c b}{k} = \frac{2000 \text{ W/m}^2\text{K} \cdot 0.0018 \text{ m}}{385 \text{ W/mK}} = 0.009 \tag{8.74}$$

which is much less than $Bi = 1/6$ where the temperature variation across the die can be neglected. The equation describing the temperature variation in the IHS can now be written. For the heat spreader not directly over the die, conservation of energy equation requires

$$\frac{\partial^2 \Theta}{\partial x^2} + \frac{2\alpha b}{A(x)} \frac{\partial \Theta}{\partial x} - \frac{hP}{kA(x)} \Theta = \frac{1}{a_t} \frac{\partial \Theta}{\partial t} \tag{8.75}$$

where $\Theta = T - T_{air}$, P is the perimeter subject to convection, $A(x)$ is the cross sectional area, and a_t is the thermal diffusivity. The α term in eqn. 8.75 represents the changing cross sectional area of the heat spreader as distance from the die increases. This term is simply the slope of the line separating symmetric segments. A square heat spreader with a square die can be broken into four segments with a base thickness equal to the width of the die and with $\alpha = 0.5$. The area of the heat spreader can now be expressed as $A(x) = A_0 + 2\alpha bx$ where A_0 is the area of the fin at the contact point with the die. Unfortunately this partial differential is very hard if not impossible to solve, except under some very restrictive boundary conditions or under steady state conditions. Instead, the equation will be solved using discrete methods. The two main items of interest from the solution are the resulting flux and the temperature invasion depth as a function of time for a change in base temperature[14].

In a method similar to the model confirmation for the transient analysis, the temperature of a fin section can be written as

$$\mathbf{A} \cdot \mathbf{T}^{i+1} = \mathbf{T}^i + \mathbf{F} \tag{8.76}$$

where for the N sections shown in Fig. 8-31, the forcing function and characteristic matrix are as follows:

$$\mathbf{F} = \begin{bmatrix} \frac{2kA_0\Delta t}{m_1 c_p \Delta x} T_b^i + \frac{hP_1\Delta t}{m_1 c_p} T_{air} \\ \frac{hP_2\Delta t}{m_2 c_p} T_{air} \\ \cdots \\ \frac{hP_n\Delta t}{m_n c_p} T_{air} \\ \cdots \\ \frac{hP_N\Delta t}{m_N c_p} T_{air} \end{bmatrix} \tag{8.77}$$

[14]The base temperature is the temperature of the IHS directly over the die structure.

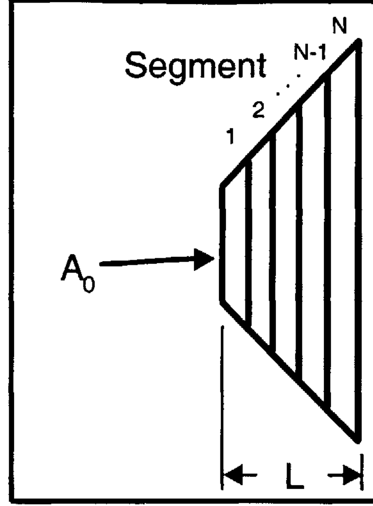

Figure 8-31: Segmentation of IHS for lateral conduction calculations.

$$\mathbf{A}_{1,1} = 1 + \frac{(kA_1 + 2kA_0 + hP_1\Delta x)\,\Delta t}{m_1 c_p \Delta x} \tag{8.78}$$

$$\mathbf{A}_{1,2} = \frac{-kA_1\Delta t}{m_1 c_p \Delta x} \tag{8.79}$$

$$\mathbf{A}_{n,n-1} = \frac{kA_{n-1}\Delta t}{m_n c_p \Delta x} \quad \text{for } 2 \leq \text{n} \leq \text{N} - 1 \tag{8.80}$$

$$\mathbf{A}_{n,n} = 1 + \frac{(kA_{n-1} + kA_n + hP_n\Delta x)\,\Delta t}{m_n c_p \Delta x} \quad \text{for } 2 \leq \text{n} \leq \text{N} - 1 \tag{8.81}$$

$$\mathbf{A}_{n,n+1} \frac{-kA_n\Delta t}{m_n c_p \Delta x} \quad \text{for } 2 \leq \text{n} \leq \text{N} - 1 \tag{8.82}$$

$$\mathbf{A}_{N,N-1} = \frac{-kA_{N-1}\Delta t}{m_N c_{p_{die}} \Delta x} \tag{8.83}$$

$$\mathbf{A}_{N,N} = 1 + \frac{(kA_{N-1} + kP_N\Delta x)\,\Delta t}{m_N c_{p_{die}} \Delta x} \tag{8.84}$$

$$\text{all other } \mathbf{A} = 0 \tag{8.85}$$

where $A_n = A_0 + 2\Delta x \alpha n b/N$, $P_n = 2\Delta x(x_0 + \alpha n \Delta x)$, $\Delta x = L/N$ and L is the length of the fin.

The solution for temperature profile in the fin at time step $i + 1$ becomes

$$\mathbf{T}^{i+1} = \mathbf{A}^{-1} \cdot \mathbf{T}^{i} + \mathbf{A}^{-1} \cdot \mathbf{F} \tag{8.86}$$

which can now be used to determine the temperature profile in the fin as a function of time subject to changing base temperature T_b. This temperature is never uniform

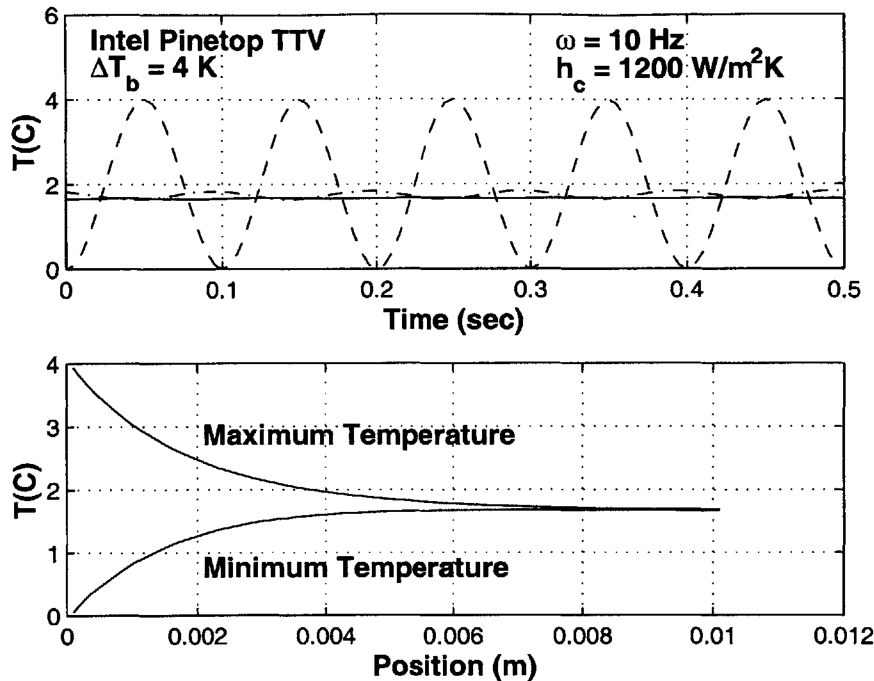

Figure 8-32: Transient fin temperature profile for Pinetop TTV with $\Delta T_b = 4$ K at 10 Hz. Top figure represents temperature profile at base, middle and tip of fin. Bottom figure represents maximum temperature defect along the length of the fin.

across the depth of the heat spreader, but the temperature varies over a very specified range and a bounding value can be used to examine the effective worst case losses into the surrounding fin structures.

As stated earlier, the information of interest is the losses associated with the variation in base temperature and the depth of invasion of the temperature profile into the fin structure. The energy loss associated with a sinusoidal variation in base temperature can be calculated by simply calculating the flux through the base structure and integrating over time. This energy loss represents the energy that is lost due to leakage from the IHS over the die into the surrounding IHS. This can be thought of as lost control energy. A plot of the temperature in the IHS fin for a Pinetop TTV is shown in Fig. 8-32. The energy transport associated with this temperature profile is 0.38 W per fin, or a total transport of 1.52 W for all four fins. A similar analysis can be performed for multiple base temperature fluctuations and with different h_c values. Figure 8-33 plots the total loss associated with base temperature fluctuation in the Intel Pinetop TTV. Figure 8-34 plots the loss as a function of h_c for the P858ACY

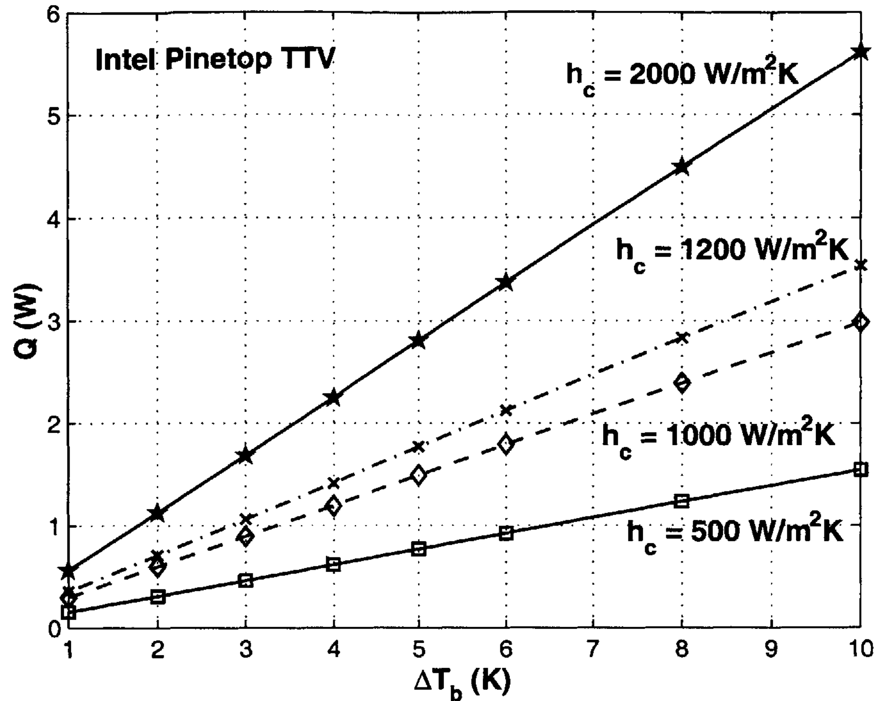

Figure 8-33: Lateral conduction into Pinetop TTV IHS for multiple frequencies with h_c = 1200 W/m^{2}K. Q represents the total energy loss due to transient conduction into the edges of the IHS. ΔT_b represents the magnitude of the fluctuation of the temperature of the IHS directly over the die structure.

TTV. Both plots are independent of the sinusoidal frequency as the results are for a periodic steady state solution.

The information from this analysis can be used in one of two ways to correct for the lateral conduction losses. Either these losses can simply be added to the total control power, or the IHS can be over illuminated such that the temperature profile invasion depth never propagates to the IHS region over the die structure. This second option is only really possible for higher frequency signals because at lower frequencies the invasion depth is of the same order of magnitude as the width of the die. If the invasion depth is defined as the length between the base of the fin and the point where the fluctuation in temperature is less than 0.1°C, then the invasion depth for the temperature profile shown in Fig. 8-32 is 6.1 mm. This is over half the width of the die structure for the Pinetop TTV. Illuminating the die area covers 1.17 cm^2, illuminating the die area and a sufficient edge area to prevent lateral conduction

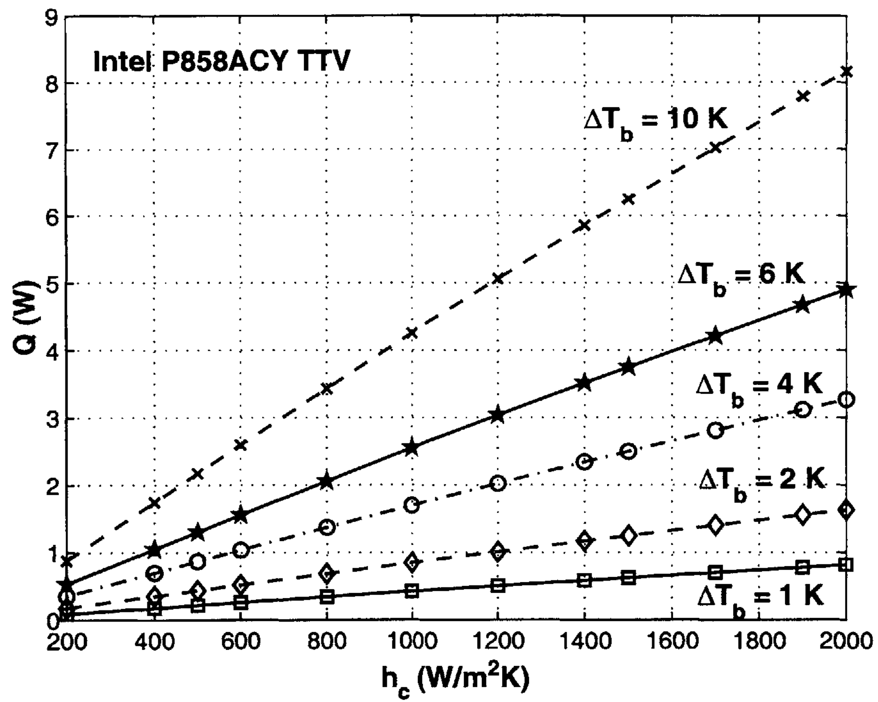

Figure 8-34: Lateral conduction (Q) into Pinetop TTV IHS for a range of h_c values for a 10 Hz base temperature fluctuation of ΔT_b.

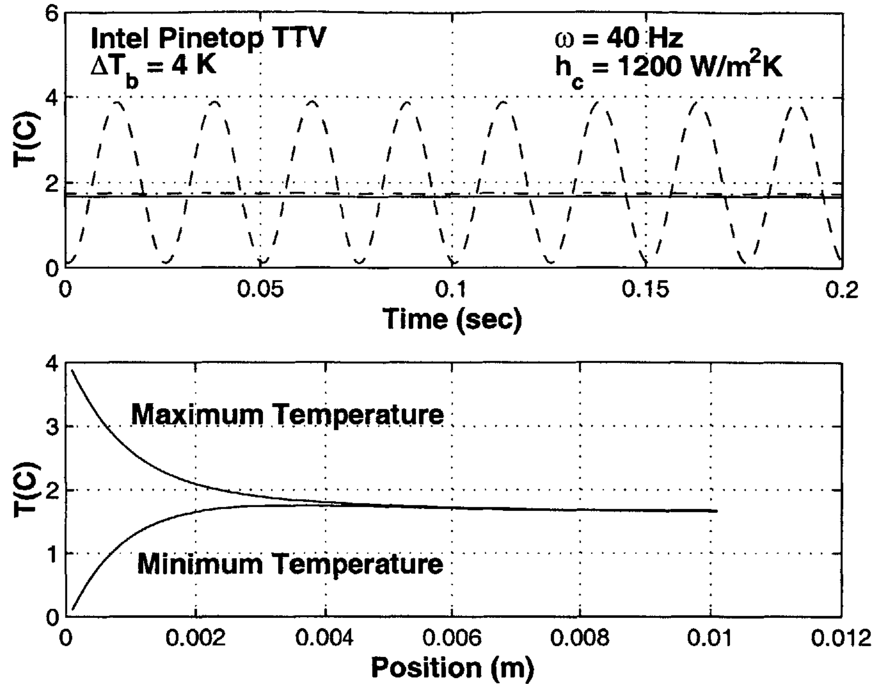

Figure 8-35: Transient fin temperature profile for Pinetop TTV with $\Delta T_b = 4$ K at 40 Hz. Top plot represents temperature profile at base, middle, and tip of fin. Bottom plot represents maximum temperature defect along the length of the fin.

effects on the die area requires illumination of 5.3 cm^2. The temperature response for the Pinetop TTV system subject to a 40 Hz signal is shown in Fig. 8-35. The invasion depth is now 3.4 mm and over illumination covers 2.90 cm^2. For a 100 Hz signal, the invasion depth becomes 2.1 mm and over illumination covers 2.25 cm^2. Assuming the radiant intensity is uniform over the entire illumination area, over illumination requires 4.5 times more radiant power at 10 Hz, 2.5 times more at 40 Hz and 1.9 times the power at 100 Hz.

If the effect of lateral conduction is compensated by adding more power to the illumination directly over the die and not increasing the illumination area, then the additional power required can simply be taken from Figures 8-33 and 8-34. Unless the devices are operating at extremely low powers, increasing the power level of the radiant energy over the die structure will always be more efficient than increasing the illumination area at constant intensity, when the control frequency is less than 100 Hz. For signals over 100 Hz, all power levels considered so far are below the point where control is actually required to maintain stated temperature control limits.

8.9 Steady State Temperature Profile

A temperature profile is associated with the effective steady state component that can be superimposed on all the transient solutions calculated so far. The DC temperature profile can be broken down into the response from the die input and the response from the control input.

8.9.1 Control Input Steady State Response

The solution for the steady state temperature profile can be facilitated by considering the die and IHS as circular structures and solving for the temperature profile in radial coordinates. Taking the outer diameter of the IHS as r_2 and the diameter of the illumination spot[15] as r_1, the temperature profile in the IHS can be calculated from

$$T(z,r) - T_{air} = \frac{Q}{\pi h r_2^2} + \sum_{n=1}^{\infty} C_n \mathrm{J}_0\left(\alpha_\mathrm{n} \mathrm{r}\right) \cosh\left(\alpha_\mathrm{n} \mathrm{z}\right) \tag{8.87}$$

where J_0 is the Bessel function of the first kind of order 0, Q is the total control power, r is measured from the IHS centerline, and z is measured from the die face. The parameter C_n is calculated from

$$C_n = \frac{2Q\mathrm{J}_1\left(\alpha_\mathrm{n} \mathrm{r}_1\right)}{\pi r_1 r_2^2 \alpha_n \left[h \cosh\left(\alpha_n b\right) + k\alpha_n \sinh\left(\alpha_n b\right)\right]} \tag{8.88}$$

where b is the thickness of the IHS, and J_1 is the Bessel function of the first kind of order 1. The parameter α_n comes from the solution to the equation

$$\mathrm{J}_1\left(\alpha_\mathrm{n} \mathrm{r}_2\right) = 0 \tag{8.89}$$

Figure 8-36 shows the steady state temperature response for an 20 W control input to the IHS on the P858ACY TTV with h_c = 1200 W/m^{2}K. The effect of changing the convective transport coefficient is shown in Fig. 8-37. Figure 8-38 is a plot of the temperature profile in the IHS of the P858ACY TTV with a 20 W control input. The main difference between the results for the Pinetop TTV and P858ACY TTV is the average temperature for a 20 W input. The actual temperature change in the IHS over the die structure is $\sim$ 0.2°C in both cases despite different die sizes and power densities.

The illumination spot size is not always ideal and will not match the die size in all situations. The effect of the illumination area can will have an effect on the

[15]Illumination is assumed uniform over the illumination spot/

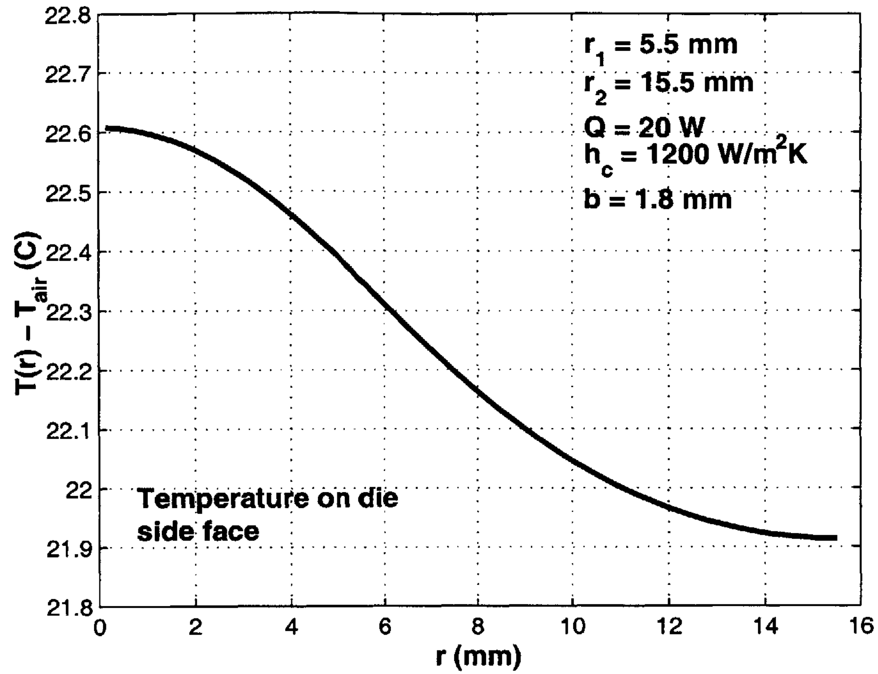

Figure 8-36: Steady state temperature profile for Pinetop TTV.

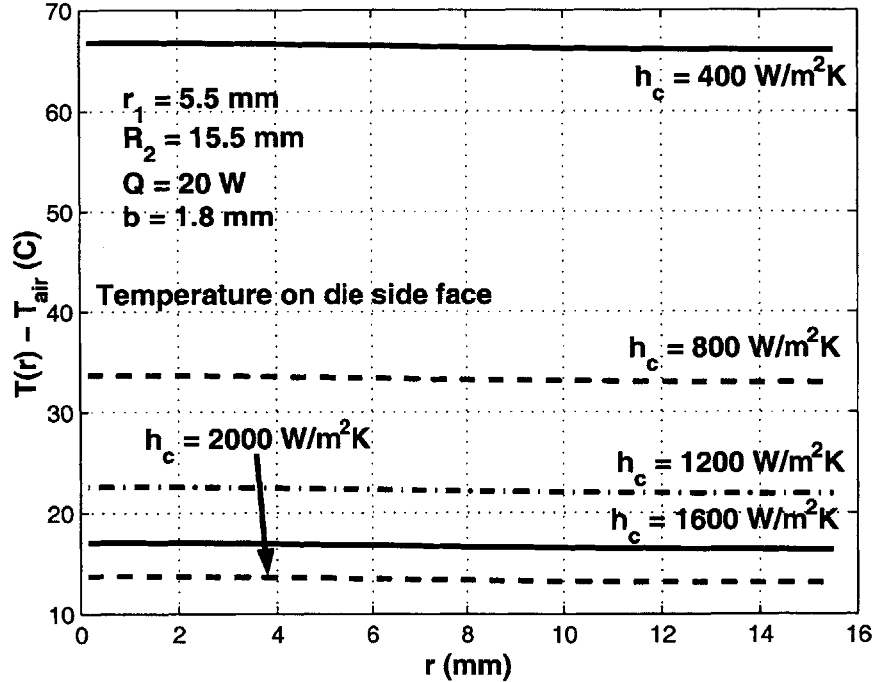

Figure 8-37: IHS temperature as a function of h_c for 20 W control power input.

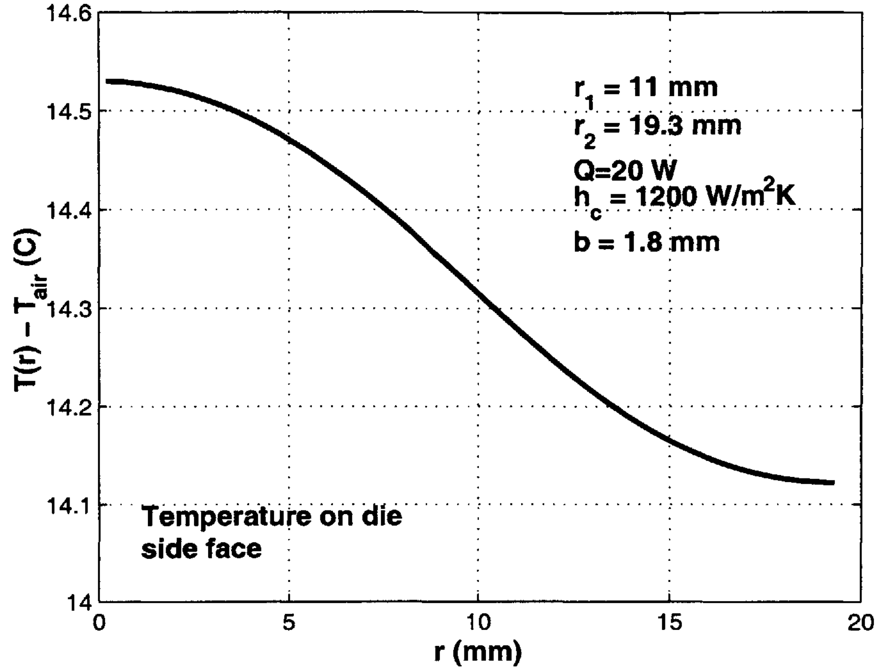

Figure 8-38: Steady state temperature profile for P858ACY TTV.

temperature distribution of the IHS over the die structure. Figure 8-39 plots the temperature distribution on the top and bottom surface of the IHS for a 1 mm diameter illumination spot. This plot is not significantly different than the plot for a 11 mm diameter illumination spot size. The temperature range over the die structure is now 0.7°C versus 0.2°C.

8.9.2 Die Input Steady State Response

Based on the same assumptions as before, the solution for the temperature profile in a round IHS based on a round die of radius r_d can be written as

$$T(r,z) - T_{air} = \frac{Q\left[k+hb\right]}{\pi k r_2^2 h} +$$

$$\sum_{n=1}^{\infty} C_n \mathrm{J}_0\left(\alpha_\mathrm{n}\mathrm{r}\right)\left[\cosh\left(\alpha_\mathrm{n}\mathrm{z}\right) - \left(\frac{\mathrm{h}\cosh\left(\alpha_\mathrm{n}\mathrm{b}\right) + \mathrm{k}\alpha_\mathrm{n}\sinh\left(\alpha_\mathrm{n}\mathrm{b}\right)}{\mathrm{k}\alpha_\mathrm{n}\cosh\left(\alpha_\mathrm{n}\mathrm{b}\right) + \mathrm{h}\sinh\left(\alpha_\mathrm{n}\mathrm{b}\right)}\right)\sinh\left(\alpha_\mathrm{n}\mathrm{z}\right)\right] \quad (8.90)$$

where the constant C_n is calculated from

$$C_n = \frac{2Q_d \mathrm{J}_1\left(\alpha_\mathrm{n}\mathrm{r}_\mathrm{die}\right)\left[\mathrm{k}\alpha_\mathrm{n}\cosh\left(\alpha_\mathrm{n}\mathrm{b}\right) + \mathrm{h}\sinh\left(\alpha_\mathrm{n}\mathrm{b}\right)\right]}{\pi k r_{die}\alpha_n^2 r_2^2 \mathrm{J}_0^2\left(\alpha_\mathrm{n}\mathrm{r}_2\right)\left[\mathrm{h}\cosh\left(\alpha_\mathrm{n}\mathrm{b}\right) + \mathrm{k}\alpha_\mathrm{n}\sinh\left(\alpha_\mathrm{n}\mathrm{b}\right)\right]} \quad (8.91)$$

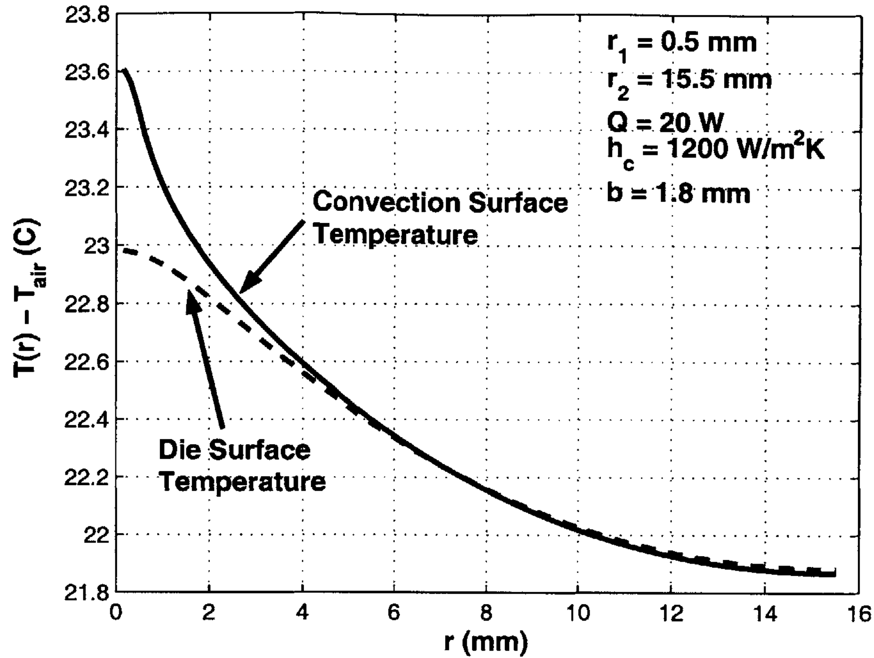

Figure 8-39: IHS temperature distribution for small illumination spot size on the Pinetop TTV.

where Q_d is the total die power, b is the thickness of the IHS, and the parameter α_n can be found from the solution to

$$\mathrm{J_1}\left(\alpha_\mathrm{n}\mathrm{r_2}\right) = 0 \tag{8.92}$$

The coordinate system in eqn. 8.90 is the same as eqn. 8.87 where $z = 0$ corresponds to the die side face of the IHS. Figure 8-40 shows the temperature profile in the IHS of the Pinetop TTV for a 20 W die input. The main difference between this response and the response for a 20 W control input is the temperature distribution over the die structure. With the control input the temperature range across the die area changed by $\sim$ 0.2°C, but with a die input the temperature range increases to almost 2°C. Figure 8-41 plots the IHS temperature profile for a 20 W die input to the P858ACY TTV. The temperature range across the die for the P858ACY is about 1.7°C for a 20 W die input.

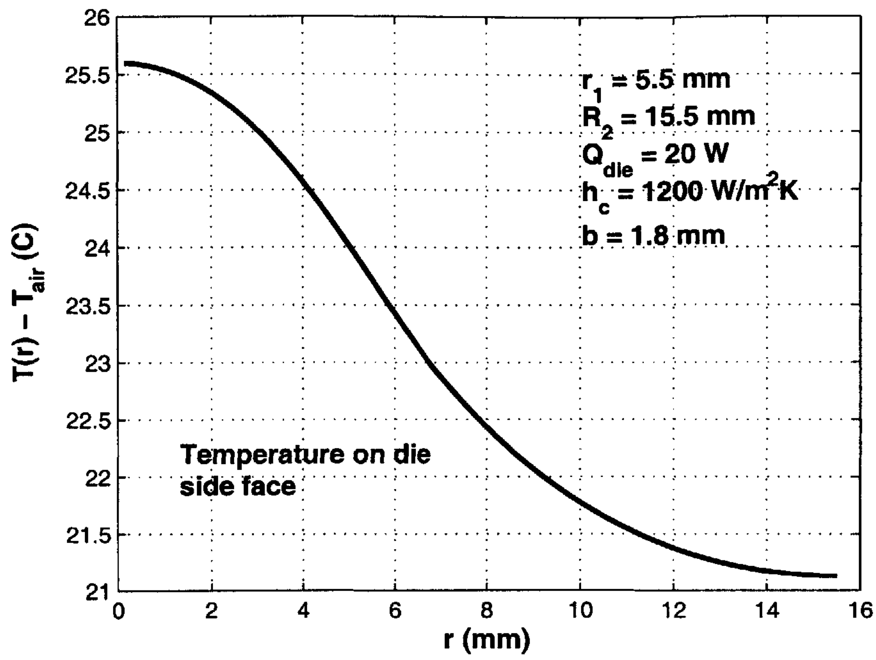

Figure 8-40: IHS temperature profile for Pinetop TTV with 20 W die input.

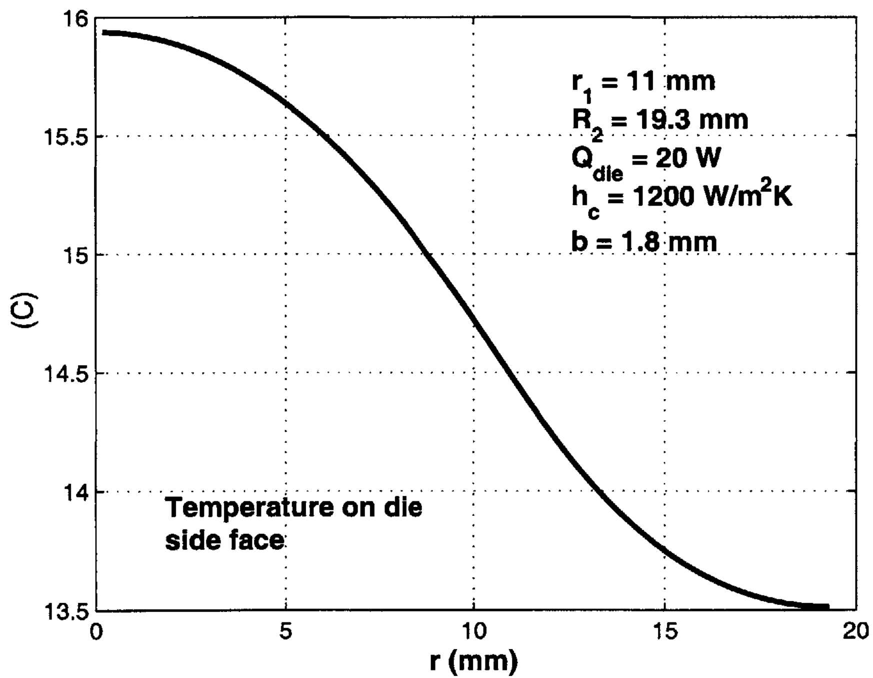

Figure 8-41: IHS temperature profile for P858ACY TTV with 20 W die input.

8.9.3 Combined Steady State Solution

The results from the die input steady state solution and control input steady state solution can be added using superposition. The main goal is the temperature of the die structure, so the temperature of interest is the heat spreader directly over the die. With this temperature profile and the thermal resistance between the die and IHS known, the maximum power limit for a device configuration can be determined based on a specified temperature defect and convection state. Assuming the maximum h_c value is on the order of 2000 W/m^{2}K and peak temperature defect[16] is 160°C, the maximum combined steady state thermal load for the P858ACY TTV is 302 W and 162 W for the Pinetop TTV. These load limits can be increased by increasing the surface area of the integrated heat spreaders, increasing the h_c maximum or decreasing the die to IHS thermal resistance R_t. Figure 8-42 plots the resulting IHS temperature profile for a 20 W die and 20 W control input with the Pinetop TTV. Figure 8-43 presents the same plot for the P858ACY TTV.

8.10 Solution Approach

The final temperature profile in a device under test conditions is a function of several independent solutions covering the transient and steady state solutions to the temperature profiles in the die and integrated heat spreader. While it would be possible to determine a single expression for the approximate temperature profile in the die structure, the resulting equation would be very bulky with little practical use. The recommended approach is to solve for each facet of the final temperature separately and compared to the desired state of temperature tolerance on the die. The following chart (Table 8.10) shows the appropriate equations to be solved for calculating the required control inputs, and steady state die/IHS temperature response.

[16]This ΔT represents a device die temperature of 100°C and an air temperature of −60°C. The minimum air temperature of −60°C is based on the capability of currently available commercial air chillers units, and is hard to implement due to frost formation issues. These numbers represent a best case scenario and actual numbers can be expected to be worse than those stated here.

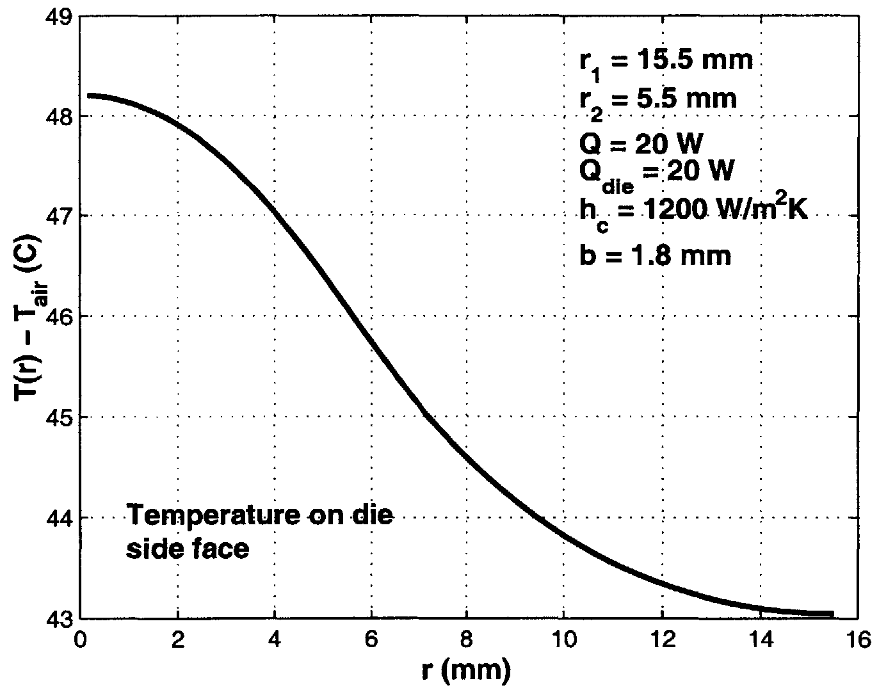

Figure 8-42: IHS temperature profile for Pinetop TTV with 20 W die and 20 W control input.

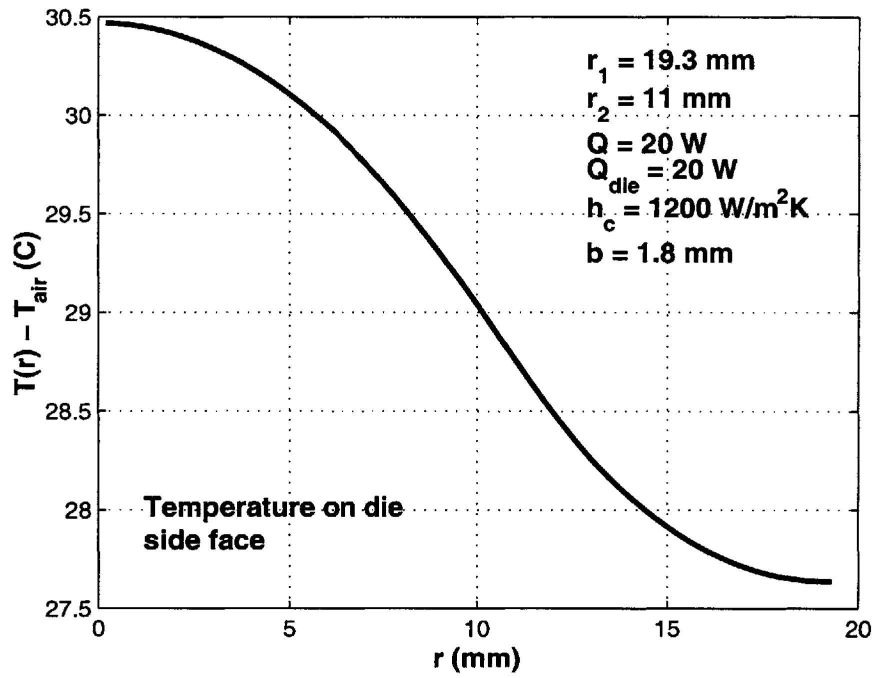

Figure 8-43: IHS temperature profile for P858ACY TTV with 20 W die and 20 W control input.

Table 8.10: Solution method for transient and steady state temperature profile of a device under test.

Solution to required control power profile.	
Decomposition of die power profile into sinusoidal profiles.	Equation 8.65 Equation 8.66
Solution to required control phase shift and magnitude for specified die input.	Graphical Solution to Equation 8.58
Effective flux from die to IHS.	Equation 8.56
Transient control input losses due to lateral conduction in IHS.	Equation 8.86
Steady state temperature solution.	
IHS temperature profile from die power profile.	Equation 8.90
IHS temperature profile from control power profile.	Equation 8.87

8.11 Conclusions

A number of conclusions can be drawn from the modeling results of this chapter. The conclusions are as follows[17]:

1. The temperature of the die can be considered uniform across the depth of the die - eqn. 8.3.

2. For a specified die temperature limit and die power level, there exists a control signal which will keep the die temperature within the tolerance levels - eqn. 8.58.

3. For a specified control power to die power ratio, there exist a set of frequencies such that for a signal frequency below a certain level, the desired die temperature range can be maintained. Above an upper frequency cut-off, no control is required to maintain the desired temperature tolerance. In the region in between these frequencies, the desired level of control cannot be maintained. The test sequence should be designed with these limiting frequencies in mind.

[17]Where appropriate, the relevant equations are referenced.

4. Any die power signal can be decomposed into a sine series. This series can be used to determine the required control power sequence - eqn. 8.65 & eqn. 8.66.

5. Step changes in die power require much more control power to maintain a specified temperature tolerance than a continuous die power profile.

6. Adding mass to the die/IHS system in the form of the control system will increase the power required for control.

7. Adding mass directly to the die will lower the die cut-off frequency.

8. High power devices cannot be controlled using feedback. Some type of feed-forward control that requires prior knowledge of the test sequence is needed, except at very low powers - eqn. 8.71 thru eqn. 8.73.

9. Feedback control may be usable for correcting for temperature deviations due to device to device variation.

10. Lateral conduction effects have a limited effect on required control power levels.

11. Steady state lateral conduction in the IHS can be modeled using radial coordinates. The resulting temperature profiles can be super-imposed on the transient solution - eqn. 8.87 & eqn. 8.90.

Chapter 9

Theoretical versus Experimental Results

Experimental data for tests performed on the thermal test vehicles have been presented in Chapter 7 and a theory for limits of control has been presented in Chapter 8. Confirmation of the theory is possible using the experimental data from a few key points.

9.1 Control Plots for Intel Thermal Test Vehicles

The set of control plots presented in Chapter 8 were generated before all the information was available on the physical dimensions of the TTV's. The die thickness of both TTV's turned out to be thicker than the standard 200 μm used in most of the plots. The actual thickness of the die structure turned out to be 750 μm. The power densities of the Pinetop TTV was also much higher for a specified ΔT than the numbers presented in Chapter 8. The control plots have been recalculated based on peak powers of 46.7 W for the P858ACY TTV and the Pinetop TTV with a temperature tolerance of $\Delta T = 2°$C. This plot is presented in Fig. 9-1. Recall that the die area for the Pinetop TTV is 1.17 cm^2 and the die area for the P858ACY TTV is 4.2 cm^2. As can be seen, while the power levels of the two devices are the same, the power densities on the dies are very different (39.9 W/cm^2 vs. 11.1 W/cm^2) and this has a large effect on the power required for control.

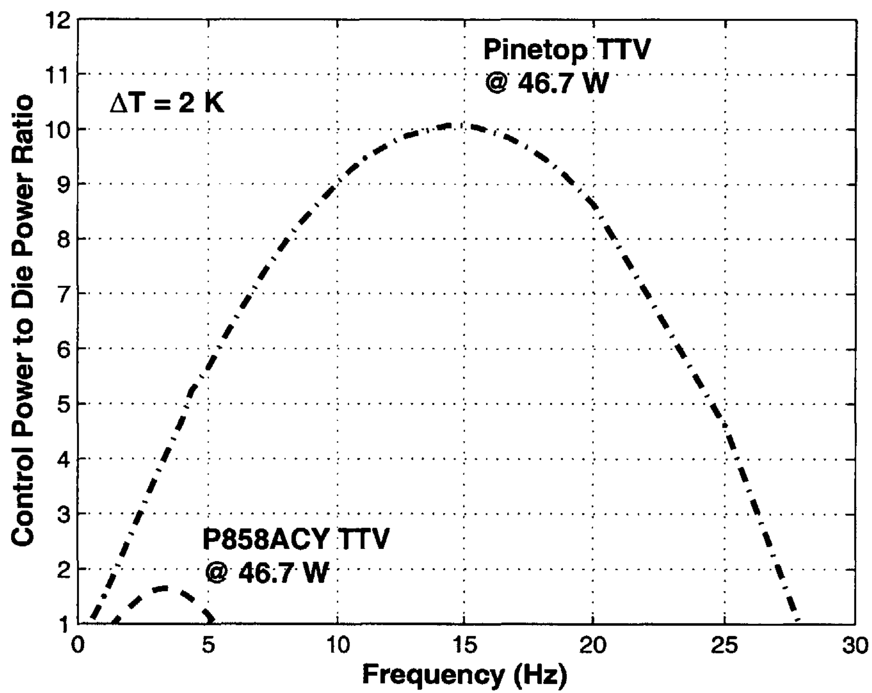

Figure 9-1: Control limit plot for Intel Pinetop TTV and P858ACY TTV for 46.7 W peak power and $\Delta T = 2°C$.

9.2 Experimental Data Correlation to Control Limit Model

Actual fitting of experimental data to the control limit model is difficult for a couple of reasons. First, the control limit model assumes that the control power profile is applied at a specific phase lead based on the magnitude and frequency of the die power profile. In the experimental prototype, very limited control over the phase shift was possible, making it difficult or impossible to match the required phase shift of the model. Second, the exact frequency content of the test sequence is not fully known. This can be addressed by the decomposition data, but even then the problem of a finite limited time step in the control and die power sequence arises.

The control limit theory shows that for a given die to control power ratio, the lower power density device should have better control of temperature for all frequencies. This can be confirmed by looking at the limits of temperature control of both the Pinetop and P858ACY TTV's subject to the same test sequence. Fig. 9-2 shows the best obtainable temperature response of each device using the prototype control system. The peak laser power in both cases was about the same, 115.2 W for the P858ACY TTV and 119.1 W for the Pinetop TTV, so the control power to die power ratio for the two devices is about the same. There is a very noticeable difference between the two devices. The offset between the mean die temperatures of the two devices is due to the increased IHS surface area on the P858ACY device. This lowers the temperature defect associated with convective heat transfer, so the large temperature difference between the devices can be ignored. The interesting point of this figure is the high frequency temperature changes. The variation of the P858ACY die temperature is significantly less than the variation in the Pinetop die temperature. This confirms that the lower power density devices are easier to control, despite having total power levels that may be the same as smaller, higher power density devices. This provides qualitative proof that the control limits model holds for the Intel TTV devices.

9.2.1 1 Second and 5 Second Decomposed Power Profile

A better match of data to experiment can be obtained by using the data results for the decomposed power profiles. Even here the data won't exactly match the results from the control limits model because each decomposed profile contains power at a

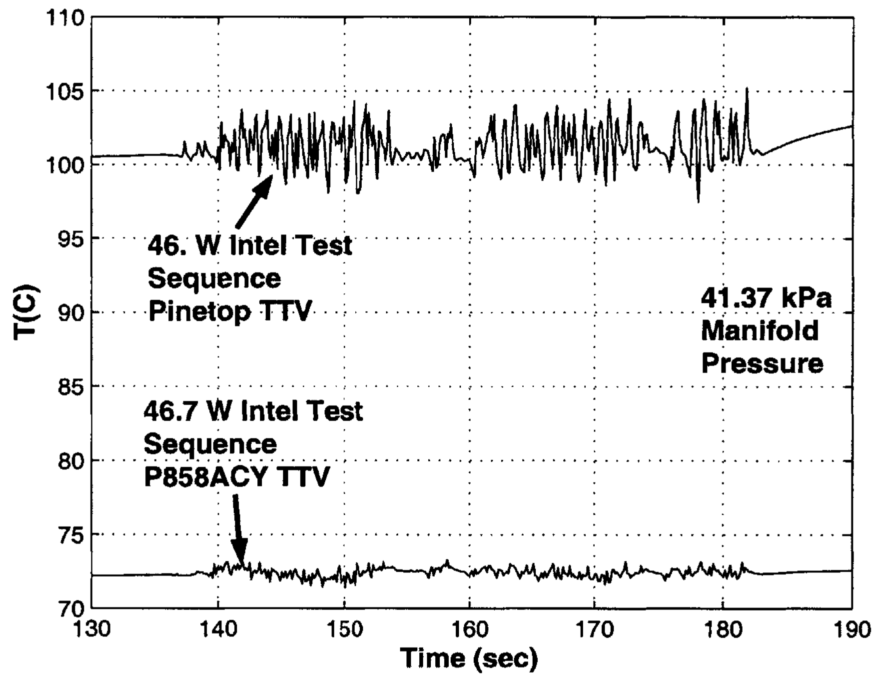

Figure 9-2: Comparison of temperature control limits of Pinetop TTV and P858ACY TTV for a 46.7 W Intel test sequence.

number of frequencies. A discrete Fourier transform can be performed on each power profile to examine the exact frequency content. The results of a DFT analysis for each decomposed power profile is shown in Fig. 9-3. Most of the energy in the 5 second average power profile is contained in the zero[1] to 2 Hz range. The 1 second average power sequence has most of the power contained in the 0 Hz to 8 Hz range and the remnant power sequence has almost all of the power in a band above 5 Hz. In none of these power sequences is there a single dominating frequency so fitting experimental data to an exact point on the control limits curve is not possible. There are ranges of frequencies for the 1 second and 5 second average power sequences that can be used to bound the data.

Data from the 1 second and 5 second average power sequences are presented in Fig. 9-4. While this data is somewhat scattered, there are two average trends that stand out. One set of data is focused around 15 W/cm^2K and the other set is around 25 W/cm^2K. Control plots can be generated for these power density/temperature tolerance levels from the 0.5 Hz to 10 Hz range. Data points from the 5 second and 1 second average power sequences can now be plotted on these curves. Taken from Figures 7-19, 7-24, 7-29, and 7-33, the required laser power to die power ratio for each device is given in Table 9.2.1. The question remains as to which frequency to plot the power ratio data points. The discrete Fourier transform provided data as to the frequency content of each power sequence, but as stated earlier, there is no single characteristic frequency for either the 1 second or 5 second power sequence. Using 1 Hz as a representative frequency of the 5 second power sequence and 1.5 Hz[2] as a representative frequency of the 1 second power profile, the experimental data points are plotted in Fig. 9-5 along with the results from the control limit theory. The data roughly fits the control curves, with data deviation from theory for the 1 second average, which has a broader range of frequency content than the 5 second average. The trend in the data as the representative frequency is increased is correct. As the representative frequency is increased, the difference between the lower power density and higher power density data increases.

[1]Zero Hz is the net DC component of the signal.

[2]1.5 Hz is the location of the first peak in Fig. 9-3 for the 1 second power profile.

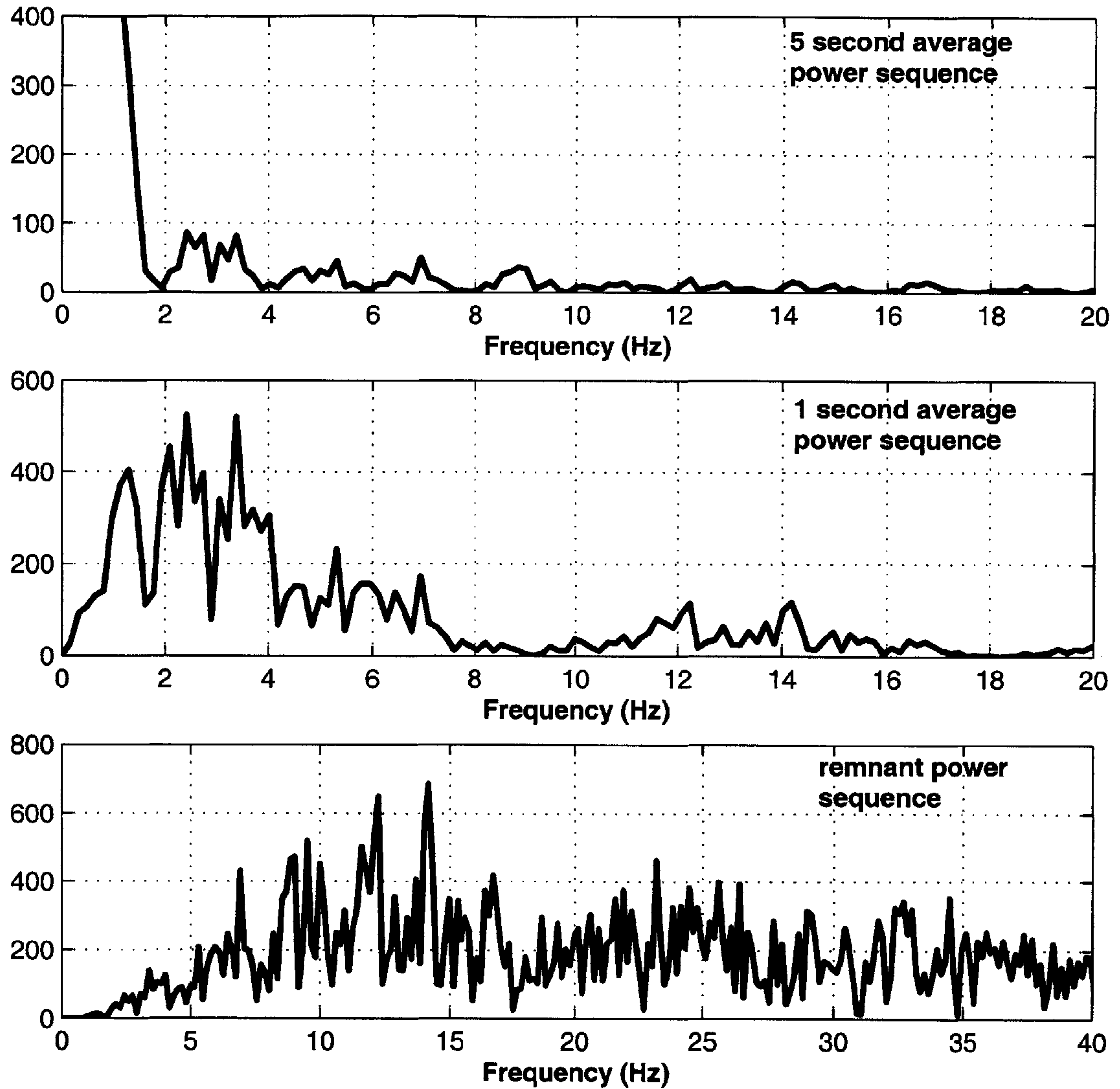

Figure 9-3: Results of a discrete Fourier transform on each of the decomposed power profiles.

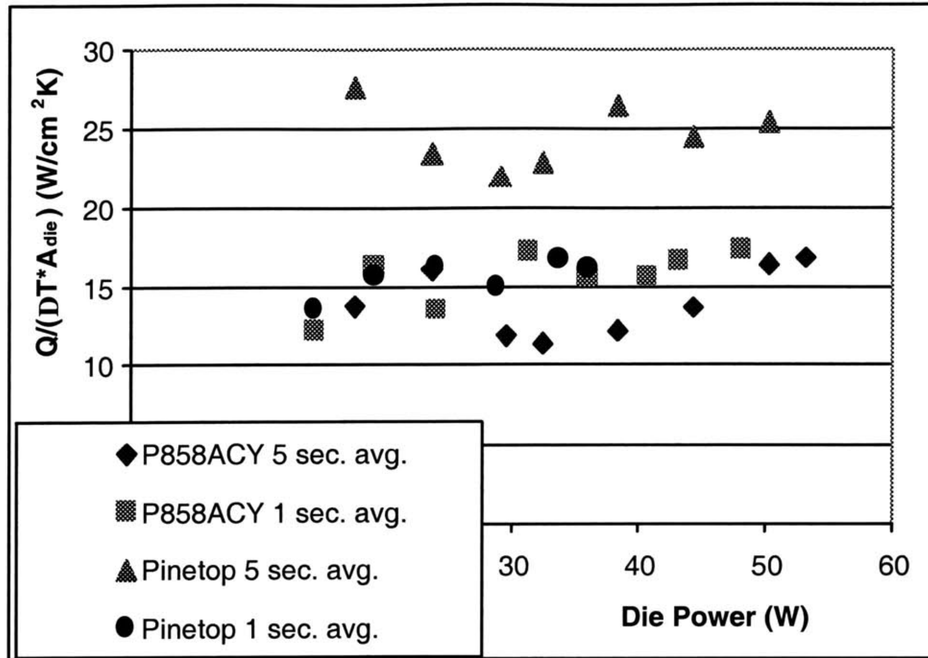

Figure 9-4: Experimental data for P858ACY TTV and Pinetop TTV for comparison with control limit theory.

Table 9.2.1: Laser Power/Die Power ratio for decomposed power profiles.

	Total Laser Power to Die Power Ratio	Loss Corrected[a] Laser Power to to Die Power Ratio
P858ACY 5 sec. avg.	2.05	1.44
Pinetop 5 sec. avg.	2.16	1.51
P858ACY 1 sec. avg.	2.26	1.58
Pinetop 1 sec. avg.	2.95	2.06

[a]This is the laser power than is actually absorbed at the device surface. Losses are incurred in the optical path from the laser units to the fiber optic tip and from surface reflection losses. Absorbed power is approximately 70% of total power.

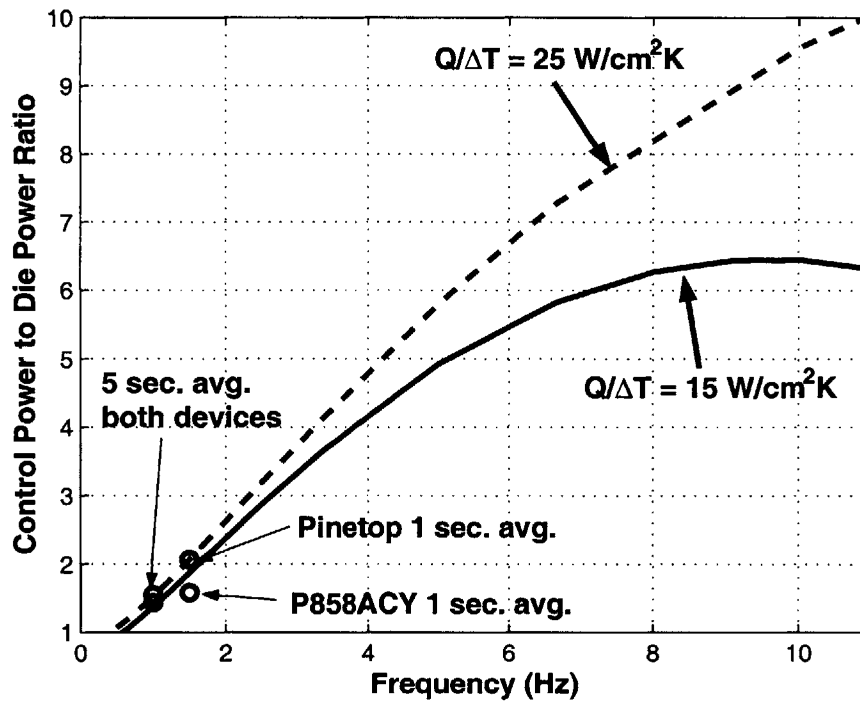

Figure 9-5: Experimental data versus control limit theory for 1 second and 5 second power profile sequences.

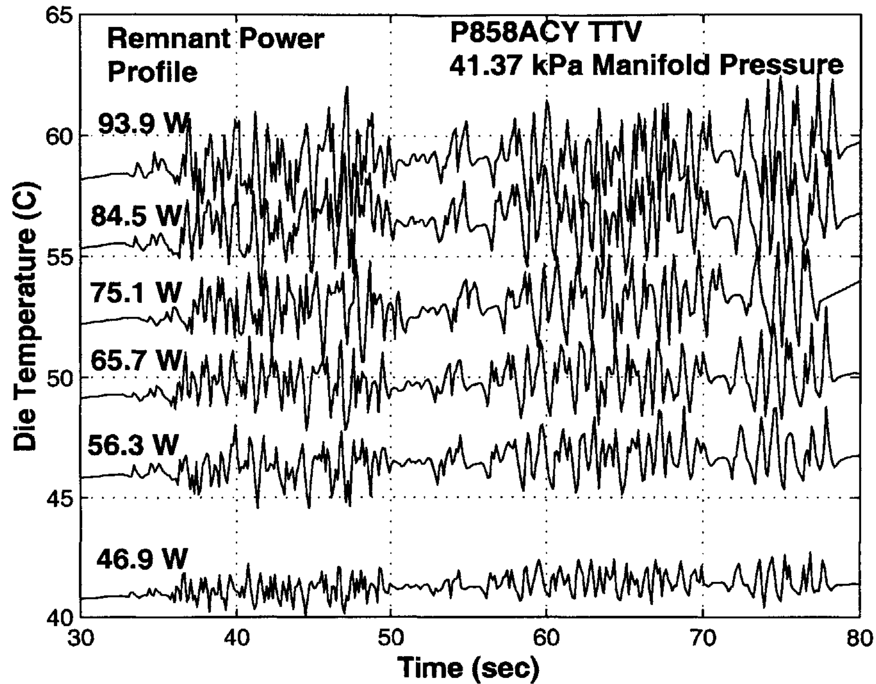

Figure 9-6: P858ACY TTV uncontrolled temperature response to scaled remnant power profiles.

9.2.2 Remnant Power Profile

The experimental data from the remnant power profile cannot be used to confirm the control limit in the same way as the data from the 1 and 5 second power profiles. This is because the required power levels for the control of the higher frequency components are beyond the range of the prototype system and because proper timing and phase lead of the control signal is even more difficult at the higher frequencies than at the lower frequencies. Instead, the remnant power profile can be used to examine the higher frequency cut off values where no control is required. The remnant power profile can be scaled up and down and the ΔT of the die can be measured for no control applied. Since the frequency content of the signal doesn't change as the profile is scaled, then the ratio of $Q/\Delta T$ should be constant. Fig. 9-6 shows the uncontrolled temperature response of the P858ACY TTV to a range of scaled remnant power profiles. The die power versus $Q/\Delta T$ is plotted in Fig. 9-7. Again, the data is not perfect, but a definite trend towards a straight line exists.

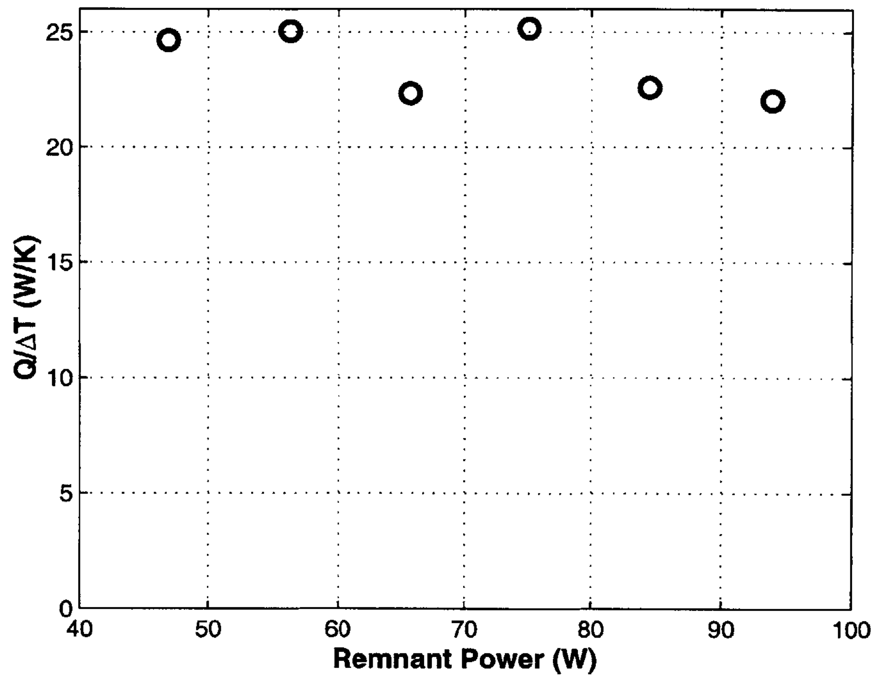

Figure 9-7: Uncontrolled temperature limits for P858ACY to scaled remnant power profile.

9.3 Conclusions

The experimental data validates the control limits model in a qualitative sense, but more data at very specific power frequencies is needed for additional quantitative validation. The current prototype system is not capable of running as these specific frequency due to command signal limitations. Square waves could be used to validate the signal, except square die power waves require non-square control power profiles for optimal control and the prototype limitations prevent this at all but the lowest frequencies. At very low frequencies, less than 1 Hz, the one dimensional approximation used to generate the control limit theory no longer holds as lateral conduction into the edges of the heat spreader begin to dominate the temperature profile.

Chapter 10

Conclusions and Future Work

This chapter presents the conclusions of this thesis, a set of recommendations about the technology that has been developed, and some suggestions for future work in the area of thermal control systems for testing of electronics.

10.1 IR Heating of Bulk Devices

10.1.1 Conclusions

Proper implementation of low IR heating units can produce very effective repeatable results in the heating of many types of bulk devices. The method depends on accurate design of the heating chamber and selection of IR source and can be applied to almost any type of device and carrier. The system is low cost and very low volume which provides a large amount of flexibility in engineering implementation of the devices. The limits in heating are generally imposed by conduction and maximum material temperature limits on the device itself, rather than the available power. The following is a list of basic design guidelines that need to be considered in the implementation of IR heating of devices.

- Select an IR heater/bulb assembly such that the entire width of the carrier can be covered by the center 90% of the bulb[1].

- Make sure the devices are not transparent to the emission band of the source.

[1] 90% is a minimum, depending on the IR manufacturer specification, 80% may be more appropriate.

- Calculate relative thermal masses of components and carrier. If either mass dominates, design the IR system to bring that mass to test temperature. If masses are of same order of magnitude, design system around the components and then calculate settling times.
- Evaluate the maximum component and carrier temperatures. If maximum exceeds specified limits, reduce radiation intensity and reduce velocity or increase exposure distance (i.e. add a second heater).

10.1.2 Future Work

The next step in the development of the IR heating system is in the design and integration of a system with a test handler that has a hot chamber that the heater can be mounted up against. A specific heating goal for a specific device and carrier needs to be established in order to drive the design process. The models developed in this thesis can provide a baseline analysis for selection of the IR source and design of the heating chamber, but more work needs to be performed in the integration hardware and system packaging areas before the IR method is incorporated at a production level.

10.2 Laser/Convection Thermal Control of an Active Device

10.2.1 Conclusions

The experimental results clearly show that the laser/convection system is capable of controlling the temperature of an electronic device under test. The system provides a method of maintaining the temperature of the die within a specified limit. The power required for control is a function of the physical parameters of the system (mass, dimensions etc.) and also of the test sequence. There exists a range of frequencies of the test sequence where control cannot be maintained for a specified control to die power ratio. Careful design of the test sequence to avoid this region is needed if the temperature tolerance of the die is to be maintained with a reasonable control power.

An analytic method has been developed that allows calculation of the power and phase shift required for a control signal to obtain the desired die temperature profile.

This method is also applicable to other types of systems that have a discrete mass which must be controlled, where the control has to be exerted on a remote part of the system.

10.2.2 Future Work

There is a significant amount of research that can still be done on this system. This work includes but is not limited to:

- High power lasers. The available technology in high power laser systems is changing rapidly and new products are being developed and introduced to the market on a fairly regular basis. The goal is to develop a low cost fiber coupled system that operates at wavelengths with very low reflectivities on device surfaces. Increased efficiency and dependability are very important.

- Structured illumination using custom ground fiber optics. The goal is to obtain very specific illumination structures without the use of additional optical components that will increase losses in the optical path.

- Specific tuning of nozzle and optical array. Model and develop design methods that allow a multi-component die to be run at multiple power densities at the same die temperature.

- Develop specific methods for noise abatement for high Mach number nozzle assemblies. This will allow extension of the convective cooling coefficient past the 2000 W/m^2K range.

- Control and feedback algorithms. A very rough estimate of performance of temperature feedback has been presented in this thesis. More work needs to be done to develop the actual feedback mechanism and control algorithm.

- Develop a digital filter to allow specific breakdown of the control sequence into specified frequency bands without the overlap problems associated with the moving averages used in this thesis. This will allow improved control profile generation and comparison of theoretical and experimental data.

- Implementation of the system on an actual testing system.

Bibliography

[1] A.C. Pfahnl, J.H. Lienhard V, and A.H. Slocum. Temperature control of a handler test interface. *Proc. IEEE Intl. Test Conf.*, 1998.

[2] A.C. Pfahnl, J.H. Lienhard V, and A.H. Slocum. Thermal management and control in testing packaged integrated circuit devices. *Proc. 34th Intersociety Energy Conversion Conf.*, 1999.

[3] J. Tustantswkyj and J.B. Babcock. Temperature control system for an electronic device which achieves a quick response by interposing a heater between the device and a heat sink. U.S. Patent #5,821,505, Oct. 13 1998.

[4] M.F. Modest. *Radiative Heat Transfer.* McGraw-Hill, Inc., New York, 1993.

[5] Y.S. Touloukian and D.P. Dewitt. *Thermophysical Properties of Matter Vol 8: Thermal Radiative Properties: Non-metallic Solids.* IFI - Plenum, New York, 1970.

[6] Y. Wang, Y. Abe, Y. Matsuura, M. Miyagi, and H. Uyama. Refractive indicies and extinction coefficients of polymers for the mid-infrared region. *Applied Optics*, 37(30):7091–7095, 1998.

[7] M.A. Ordal, L.L. Long, R.J. Bell, S.E. Bell, R.R. Bell, R.W. Alexander, and C.A. Ward. Optical properties of the metals Al, Co, Cu, Au, Fe, Pb, Ni, Pd, Pt Ag, Ti, and W in the infrared and far infrared. *Applied Optics*, 22(7):1099–1119, 1983.

[8] H.S. Carslaw and J.C. Jaeger. *Conduction of Heat in Solids.* Oxford University Press, Oxford, 1959.

[9] K. Weed and A. Kirkpatrick. An experimental investigation of the emissivity of various electonic packages. *Proceedings of the Twelfth IEEE SEMI-THERM Symposium*, pages 59–64, 1996.

[10] J.H. Lienhard IV and J.H. Lienhard V. *A Heat Transfer Textbook.* Cambridge, 2000.

[11] M.M. Yovanovich and W.M. Rohsenow. Influence of surface roughness and waviness upon thermal contact resistance. In *Technical Report No. 76361-48.* MIT, Dept. of Mech. Eng., 1967.

[12] M.M. Yovanovich and V.W. Antonetti. Application of thermal contact resistance theory to electronic packages. In Avram Bar-Cohen and Allan D. Kraus, editors, *Advances in Thermal Modeling of Electronic Components and Systems*, volume 1, pages 79–128. Hemisphere Publishing, New York, 1988.

[13] A.D. Kraus and A. Bar-Cohen. *Thermal Analysis and Control of Electronic Equipment.* Hemisphere Publishing Corp., Washington, 1983.

[14] E. Oberg, F.D. Jones, and H.L. Horton. Machinery's handbook. In H.H. Ryffel and J.H. Geronimo, editors, *22nd Edition.* Industrial Press Inc., New York, 1985.

[15] G.R. Rugger. Weathering. In D.V. Rosato and R.T. Schwartz, editors, *Environmental Effects on Polymeric Materials.* Interscience Publishers, New York, 1968.

[16] M. Chanda and S.K. Roy. *Plastics Technology Handbook - 3rd Ed.* Marcel Dekker Inc., New York, 1998.

[17] A.F. Mills. *Heat and Mass Transfer.* Irwin, Chicago, 1995.

[18] W.E. Boyce and R.C. DiPrima. *Elementary Differential Equations and Boundary Value Problems.* John Wiley and Sons, New York, 1977.

[19] F.P. Incopera and D.P. DeWitt. *Fundamentals of Heat and Mass Transfer.* John Wiley & Sons, New York, 1990.

[20] J.A. Jr. Carpenter. Measurements of properties of materials in electronic packaging. In Deborah D.L. Chung, editor, *Materials for Electronic Packaging*, pages 341–360. Butterworth-Heinemann, Boston, 1995.

[21] V.S. Arpaci. *Conduction Heat Transfer.* Addison-Wesley, Reading, MA, 1966.

[22] *Agilent 34970A Data Acquisition/Switch Unit - User's Guide*, 1999.

[23] *Agilent 6627A Multiple Output Linear System DC Power Supply - User's Guide*, 2000.

[24] J.R. Taylor. *An Introduction to Error Analysis.* University Science Books, Mill Valley, CA, 1982.

[25] J.I. Tustaniwskyj and J.W. Babcock. Constant temperature control of a device under test (DUT) - Part 1. *Advances in Electronic Packaging*, 2:2031–2036, 1997.

[26] H. Martin. Heat and mass transfer between impinging gas jets and solid surfaces. In T. Irvine and J.P. Hartnett, editors, *Advances in Heat Transfer*, volume 13, pages 1–60. Academic Press, New York, 1977.

[27] *Occupational noise exposure. - 1910.95 (OHSA Regulations - Standards 29CFR).*

[28] J.S. Robertson, K. Bolinger, L.M. Glasser, N.J.A. Sloane, and R. Gross. Chapter 1: Analysis. In Daniel Zwillinger, editor, *CRC Standard Mathematical Tables and Formulae*, pages 1–74. CRC Press, Boca Raton, 1996.

[29] M. Sparks. Theory of laser heating of solids: Metals. *Journal of Applied Physics*, 47(3):837–849, 1976.

[30] M. Malinoski, J. Maveety, S. Knostman, and T. Jones. A test site thermal control system for at-speed manufacturing testing. In *International Test Conference*, pages 119–128. IEEE, 1998.

[31] R.J. Goldstein, A.I. Behbahani, and K. Kieger Heppelmann. Streamwise distribution of the recovery factor and the local heat transfer coefficient to an impinging circular air jet. *Int. J. Heat and Mass Transfer*, 29(8):1227–1235, 1986.

[32] G.B. Kromann. Thermal management of a C4/Ceramic-ball-grid array: The Motorola PowerPC 603 and PowerPC 604 RISC microprocessors. *Proceedings of the Twelfth IEEE SEMI-THERM Symposium*, pages 36–42, 1996.

[33] C.J.M. Lasance, H. Vinke, and H. Rosten. Thermal characterization of electronic devices with boundary condition independent compact models. *IEEE*

Transactions on Components, Packaging, and Manufacturing Technology - Part A, 18(4):723–731, 1995.

[34] A. Bar-Cohen and W.B. Krueger. Thermal characterization of chip packages - evolutionary development of compact models. *IEEE Transactions on Components, Packaging, and Manufacturing Technology - Part A*, 20(4):399–410, 1997.

[35] W.E. Pence and J.P. Krusius. Package thermal resistance: Geometrical effects in conventional and hybrid packages. *IEEE Transactions on Components, Hybrids, and Manufacturing Technology*, 13(2):245–251, 1990.

[36] A.M. Huber and R. Viskanta. Effect of jet-jet spacing on convective heat transfer to confined, impinging arrays of axisymmetric air jets. *Int. J. Heat and Mass Transfer*, 37(18):2859–2869, 1994.

[37] A.M. Huber and R. Viskanta. Comparison of convective heat transfer of perimeter and center jets in a confined, impinging array of axisymmetric air jets. *Int. J. Heat and Mass Transfer*, 37(18):3025–3030, 1994.

[38] D.C. O'Shea, W.R. Callen, and W.T. Rhodes. *Introduction to Lasers and their Applications*. Addison-Wesley, Reading, 1978.

[39] K.W. Van Treuren, Z. Wang, P.T. Ireland, and T.V. Jones. Detailed measurements of local heat transfer coefficient and adiabatic wall temperature beneath an array of impinging wall jets. *Journal of Turbomachinery*, 116:369–374, 1994.

[40] K. Jambunathan, E. Lai, M.A. Moss, and B.L. Button. A review of heat transfer data for single circular jet impingement. *Int. J. Heat and Fluid Flow*, 13(2):106–115, 1992.

[41] M.K. Premkumar. Al/SiC for power electronic packaging. *International Symposium on Advanced Packaging Materials*, pages 162–165, 1997.

[42] A.M. Huber and R. Viskanta. Convective heat transfer to a confined impinging array of air jets with spent air exits. *Journal of Heat Transfer*, 116:570–576, 1994.

Appendix A

Derivation of Temperature Solution

This appendix covers the derivation of the solution for the temperature profile in the integrated heat spreader for the two cases where a control input is applied and the back face is adiabatic, and the case where a die input is applied.

A.1 Temperature response to control input

Consider an infinite slab with one side adiabatic. The other face is subject to convective boundary conditions h with air temperature $T_{\text{air}} = 0$, and a control flux of form $Q(t) = Q_c \cos(\omega t)$. The coordinate system used corresponds to case 2 shown in Fig. 8-10. Using complex analysis methods, it is assumed that the solution to the temperature profile in the complex plane takes on the form:

$$W = X(x) \cdot \tau(t) \tag{A.1}$$

where $\tau(t) = \mathrm{e}^{i\omega t}$ and $i = \sqrt{-1}$ is the imaginary operator. The local conservation of energy equation in the integrated heat spreader is

$$\frac{\partial^2 W}{\partial x^2} = \frac{1}{a_t}\frac{\partial W}{\partial t} \tag{A.2}$$

so with the assumed solution of form eqn. A.1, this can be rewritten in the form:

$$\frac{\partial^2 X}{\partial x^2} = \frac{i\omega}{a_t} \tag{A.3}$$

This second order differential has the general solution of

$$X(x) = C_1 \, e^{-\sqrt{\frac{i\omega}{a_t}}x} + C_2 \, e^{\sqrt{\frac{i\omega}{a_t}}t} \tag{A.4}$$

The derivative of X can be written as:

$$\frac{dX}{dx} = -\sqrt{\frac{i\omega}{a_t}} C_1 \, e^{-\sqrt{\frac{i\omega}{a_t}}x} + \sqrt{\frac{i\omega}{a_t}} C_2 \, e^{\sqrt{\frac{i\omega}{a_t}}x} \tag{A.5}$$

The boundary conditions on eqn. A.3 are as follows:

$$x = 0 \qquad -k\frac{dX}{dx} + Q_c = hX \tag{A.6}$$

$$x = b \qquad \frac{dX}{dx} = 0 \tag{A.7}$$

Substituting the boundary condition at $x = 0$ into eqn. A.5 yields:

$$\frac{dX}{dx} = 0 = -\sqrt{\frac{i\omega}{a_t}} C_1 + \sqrt{\frac{i\omega}{a_t}} C_2 \tag{A.8}$$

which can be solved to show that $C_1 = C_2 = C$. Substituting the boundary condition at $x = b$ into eqn. A.5 produces the expression:

$$hC\left[e^{-bL(i+1)} + e^{bL(i+1)}\right] + kC\left[e^{-bL(i+1)} - e^{bL(i+1)}\right] L(i+1) = Q_c \tag{A.9}$$

where $L = \sqrt{\omega/2a_t}$. The objective is to solve this equation for C. Using the equalities [28]:

$$e^{i\omega x} = \cos\omega x + i\sin\omega x \tag{A.10}$$

$$e^{-i\omega x} = \cos\omega x - i\sin\omega x \tag{A.11}$$

to expand all exponential terms, eqn. A.9 can be written as:

$$C\left(A_2 + B_2 i\right) = Q_c \, e^{bL} \tag{A.12}$$

where

$$A_2 = h\cos(bL) + h\,e^{2bL}\cos(bL) - kL\cos(bL) - kL\sin bL + kL\,e^{2bL}\cos(bL) - kL\,e^{2bL}\sin bL \tag{A.13}$$

$$B_2 = -h\sin(bL) + h\,e^{2bL}\sin(bL) - kL\cos bL + kL\sin(bL) + kL\,e^{2bL}\cos(bL) + kL\,e^{2bL}\sin bL \tag{A.14}$$

Eqn. A.12 can now be solved for C by multiplying both side through by the complex conjugate. Substituting this value of C back into the original solution for X yields:

$$X = \frac{Q_c \, e^{bL} \left(A_2 - B_2 i\right)}{A_2^2 + B_2^2} \left[e^{-xL(i+1)} + e^{xL(i+1)}\right] \tag{A.15}$$

To find the solution to the temperature profile in the integrated heat spreader in the real domain versus the imaginary domain, the real part of $X\,e^{i\omega t}$ needs to be found.

$$T(x,t) = \mathrm{Re}\left(\mathrm{X}\,e^{i\omega t}\right) = \mathrm{Re}\left[\frac{\mathrm{Q_c}\,e^{\mathrm{bL}}\left(\mathrm{A_2} - \mathrm{B_2 i}\right)}{\mathrm{A_2^2 + B_2^2}}\left(e^{-\mathrm{xL}}\,e^{(\omega \mathrm{t} - \mathrm{xL})\mathrm{i}} + e^{\mathrm{xL}}\,e^{(\omega \mathrm{t} + \mathrm{xL})\mathrm{i}}\right)\right] \tag{A.16}$$

Expanding all imaginary exponentials in terms of identities eqn. A.11, and collecting terms yields the solution:

$$\begin{aligned} T(x,t) = {} & \frac{Q_c \, e^{bL-xL}}{A_2^2 + B_2^2}\left[A_2 \cos\left(\omega t - xL\right) + B_2 \sin\left(\omega t - xL\right)\right] \\ & + \frac{Q_c \, e^{bL+xL}}{A_2^2 + B_2^2}\left[A_2 \cos\left(\omega t + xL\right) + B_2 \sin\left(\omega t + xL\right)\right] \end{aligned} \tag{A.17}$$

A.2 Temperature response to die input

An identical approach can be used to solve for the temperature profile of the integrated heat spreader subject to a die input, but with different boundary conditions. Using the coordinate system shown for case 1 in Fig. 8-10, the boundary conditions are as follows:

$$x = 0 \qquad k\frac{dX}{dx} = hX \tag{A.18}$$

$$x = b \qquad Q_d = k\frac{dX}{dx} \tag{A.19}$$

Substituting the boundary condition at $x = 0$ into the solution for X (eqn. A.4) yields:

$$-kC_1\sqrt{\frac{i\omega}{a_t}} + kC_2\sqrt{\frac{i\omega}{a_t}} = hC_2 + hC_2 \tag{A.20}$$

which can be rearranged as

$$C_1\left[h + kL(i+1)\right] = C_2\left[kL(i+1) - h\right] \tag{A.21}$$

and defining

$$A_1 = h + kL$$

$$B_1 = kL - h$$

Eqn. A.20 can now be written as

$$C_1\left[A_1 + kLi\right] = C_2\left[B_1 + kLi\right] \tag{A.22}$$

which can now be solved to express C_1 in terms of C_2.

$$C_1 = C_2\frac{A_1B_1 + (kL)^2 + (A_1kL - B_1kL)\,i}{A_1^2 + (kL)^2} \tag{A.23}$$

Defining

$$\begin{aligned} D_1 &= A_1^2 + (kL)^2 \\ E_1 &= A_1B_1 + (kL)^2 \\ F - 1 &= A_1kL - B_1kL \end{aligned}$$

eqn. A.23 can be written as

$$C_1 = C_2\frac{\left[E_1 + F_1 i\right]}{D_1} \tag{A.24}$$

and the solution for X can now be expressed as

$$X = C\left[\frac{E_1 + F_1 i}{D}\,\mathrm{e}^{-\sqrt{\frac{i\omega}{a_t}}x} + \mathrm{e}^{\sqrt{\frac{i\omega}{a_t}}}\right] \tag{A.25}$$

Substituting this value for X into the boundary condition at $x = b$ produces:

$$Q_d = C\left[kL\,(i+1)\,\mathrm{e}^{bL}\,\mathrm{e}^{bLi} - \frac{kL}{D_1}\,\mathrm{e}^{-bL}\,(E_1 + F_1 i)\,(i+1)\,\mathrm{e}^{-bLi}\right] \tag{A.26}$$

Separating terms produces

$$\begin{aligned} \frac{Q_d}{C} &= kL\,\mathrm{e}^{bL}\left(\cos(bL) - \sin(bL)\right) - \frac{kL}{D_1}\,\mathrm{e}^{-bL}\left(M_1\cos(bL) + N - 1\sin(bL)\right) \\ &\quad + kL\,\mathrm{e}^{bL}\,i\left(\sin(bL) + \cos(bL)\right) - \frac{kL}{D_1}\,\mathrm{e}^{-bL}\,i\left(-M_1\sin(bL) + N_1\cos(bL)\right) \end{aligned} \tag{A.27}$$

where

$$\begin{aligned} M_1 &= E_1 - F_1 \\ N_1 &= E_1 + F_1 \end{aligned}$$

With the following definitions

$$P_1 = kL\,\mathrm{e}^{bL}\left[\cos(bL) - \sin(bL)\right] - \frac{kL\,\mathrm{e}^{-bL}}{D_1}\left[M_1\cos 9bL) + N_1\sin(bL)\right] \tag{A.28}$$

$$R_1 = kL\,e^{bL}\,[\sin(bL)+\cos(bL)] + \frac{kL\,e^{-bL}}{D_1}\,[M_1\sin(bL) - N_1\cos(bL)] \tag{A.29}$$

the solution for the constant C can be expressed as

$$C = \frac{Q_d\,(P_1 - R_1 i)}{P_1^2 + R_1^2} \tag{A.30}$$

and X now becomes

$$X = \frac{Q_d}{P_1^2 + R_1^2}\left[\frac{(P_1 - R_1 i)\,(E_1 + F_1 i)}{D_1}\,e^{-xL(i+1)} + (P_1 - R_1 i)\,e^{xL(i+1)}\right] \tag{A.31}$$

Defining

$$U_1 = \frac{P_1 E_1 + R_1 F_1}{D_1}$$
$$V_1 = \frac{P_1 F_1 - E_1 R_1}{D_1}$$

the solution for the temperature in the heat spreader can now be found by solving for the real part of the expression:

$$T(x,t) = \mathrm{Re}\left[\mathrm{X}\,e^{i\omega t}\right] \tag{A.32}$$

The final expression for the temperature of the heat spreader now becomes

$$T(x,t) = \frac{Q_d\,e^{-xL}}{P_1^2 + R_1^2}\,[U_1\cos(\omega t - xL) - V_1\sin(\omega t - xL)] + \frac{Q_d\,e^{xL}}{P_1^2 + R_1^2}\,[P_1\cos(\omega t + xL) + R_1\sin(\omega t + xL)] \tag{A.33}$$

A.3 Combined temperature response

The temperature response of the integrated heat spreader to both control and die inputs can be found using superposition. Of interest is the temperature on the die side contact face of the IHS. The requires adding the solution to the control input at $x = 0$ and the solution to the die input at $x = b$. A phase shift will be added to the solution for the control input in order to calculated the required magnitude and phase shift of the control input for a desired IHS temperature. This simply involves substituting $\omega t + \alpha$ for ωt in eqn. A.17. The final temperature profile at the die side

contact face of the IHS is:

$$\begin{aligned}T_{\text{IHS}} = {} & \frac{2Q_c\,\mathrm{e}^{bL}}{A_2^2+B_2^2}\left[A_2\cos(\alpha)+B_2\sin(\alpha)\right]\cos(\omega t) \\ & + \frac{2Q_c\,\mathrm{e}^{bL}}{A_2^2+B_2^2}\left[-A_2\sin(\alpha)+B_2\cos(\alpha)\right]\sin(\omega t) \\ & + \frac{Q_d\,\mathrm{e}^{-bL}}{P_1^2+R_1^2}\left[U_1\cos(bL)+V_1\sin(bL)\right]\cos(\omega t) \\ & + \frac{Q_d\,\mathrm{e}^{bL}}{P_1^2+R_1^2}\left[P_1\cos(bL)+R_1\sin(bL)\right]\cos(\omega t) \\ & + \frac{Q_d\,\mathrm{e}^{-bL}}{P_1^2+R_1^2}\left[U_1\sin(bL)-V_1\cos(bL)\right]\sin(\omega t) \\ & - \frac{Q_d\,\mathrm{e}^{bL}}{P_1^2+R_1^2}\left[P_1\sin(bL)-R_1\cos(bL)\right]\sin(\omega t) \qquad \text{(A.34)}\end{aligned}$$

In the case of ideal temperature control, the goal is to set $T_{\text{IHS}} = 0$ and solution to the value of Q_c and α in eqn. A.34 can be found be considering all sine and cosine terms separately. Since the equation must be valid at all times t, then at any given instant, all the sine terms must sum to zero and and all cosine terms must sum to zero. The graphical solution to these equations is described in Chapter 8. In the case where a temperature tolerance is specified for the die, the righthand side of eqn. A.34 is no longer zero, but is specified by eqn. 8.58. This does not change the solution for the sine terms, but adds one additional term to the cosine equation. Solution is still best performed graphically.

4493-71